Dynamics and Decoherence in the Central Spin Model

From a Quantum Mechanical to a Classical Description

Dissertation

zur Erlangung des Doktorgrades
der Naturwissenschaften
der Fakultät Physik
der Technischen Universität Dortmund

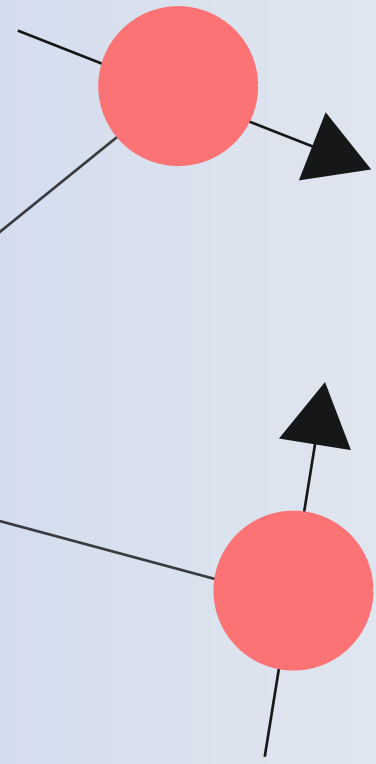

vorgelegt von

Daniel Stanek

aus Dortmund

Dezember 2013

Vorsitzender der Prüfungskommission:	Prof. Dr. Dr. Wolfgang Rhode
Erster Gutachter:	Prof. Dr. Götz S. Uhrig
Zweiter Gutachter:	Prof. Dr. Frithjof B. Anders
Vertreterin der wiss. Mitarbeiter:	Dr. Bärbel Siegmann
Tag der Disputation:	17. Februar 2014

Typeset using LaTeX and KOMA-Script.

Contents

Kurze Zusammenfassung

Lange Dekohärenzzeiten sind von enormer Bedeutung für die Quanteninformationsverarbeitung. Nur falls die Speicherdauer von Informationen in den Quantenbits lang genug ist und eine ausreichend große Anzahl an Operationen durchgeführt werden kann, können Quantenalgorithmen erfolgreich implementiert und die Vorteile gegenüber einem klassischen Computer ausgenutzt werden.

In dieser Dissertation wird die Dekohärenz eines Elektronenspins im Zentralspinmodell untersucht, in dem ein einzelner Spin an ein Bad aus nicht wechselwirkenden Spins gekoppelt ist. Das Zentralspinmodell hat sich innerhalb des letzten Jahrzehnts als eine effektive Beschreibung für die Dekohärenz eines einzelnen Elektronenspins in einem Quantenpunkt etabliert, welche im wesentlichen durch die Hyperfeinwechselwirkung zwischen dem Elektronenspin und den Kernspins der Umgebung verursacht wird.

Zur Beschreibung der Dekohärenz wird die Echtzeitdynamik im Zentralspinmodell mittels unterschiedlicher numerischer und analytischer Methoden berechnet. Ziel dieser Arbeit ist es, die Anwendbarkeit der Methoden zu verifizieren und mögliche Einschränkungen aufzuzeigen. Eine numerische Untersuchung des quantenmechanischen Zentralspinmodells wird auf Basis der Dichtematrix-Renormierungsgruppe durchgeführt, wodurch die Hyperfeinwechselwirkung zwischen dem Zentral- und den Badspins für beliebige externe Magnetfelder stets vollständig erfasst wird. Eine Beschränkung auf den Limes starker externer Felder ist im Gegensatz zu vielen anderen Methoden nicht erforderlich. Neben einer detaillierten Beschreibung der Implementierung des Algorithmus für ein Cluster von Spins, welches durch einen Zentralspin verbunden wird, liegt ein Schwerpunkt der vorliegenden Arbeit auf unterschiedliche Erweiterungen der Dichtematrix-Renormierungsgruppe zur Berechnung der Echtzeitentwicklung der Spins. Die exakte Berechnung der Spur der Operatoren im Hochtemperaturlimes erfolgt dabei immer mittels purifizierter Zustände. Beste Ergebnisse erhält man mit der adaptiven Methode, die auf der Trotter-Suzuki-Zerlegung des Zeitentwicklungsoperator basiert. Diese Methode liefert eine hohe Genauigkeit, welche mit einer relativ schnellen Laufzeit des Algorithmus kombiniert wird, so dass Systeme bestehend aus bis zu eintausend Badspins auf kurzen und mittleren Zeitskalen numerisch untersucht werden können.

Motiviert durch die numerischen Ergebnisse für das vollständig quantenmechanische Zentralspinmodell und durch einfache analytische Argumente, wird ein semiklassisches Modell für die Beschreibung der Zentralspindynamik eingeführt. Dabei wird das Bad durch eine klassisches zufällig fluktuierendes Feld ersetzt, während der Zentralspin weiterhin quantenmechanisch beschrieben wird. Das semiklassische Modell wird analytisch im Rahmen der Magnus-Entwicklung („Average Hamiltonian theory“) und mittels einer numerischen Simulation untersucht. Durch den Vergleich mit den quantenmechanischen Resultaten kann so gezeigt werden, dass der quasistatische Limes des Bades bereits in der Größenordnung von eintausend Badspins einsetzt. Außerdem wird die separate Behandlung von Erhaltungsgrößen anhand des erhaltenen Gesamtspins diskutiert, was zu einer spürbaren Verbesserung der numerischen Ergebnisse des semiklassischen Modells führt.

Als Alternative zur vollständig quantenmechanischen und semiklassischen Beschreibung werden die Bewegungsgleichungen des Zentralspinmodells zusätzlich auf klassischem Niveau diskutiert. Anders als im semiklassischen Modell ist in der vollständig klassischen Beschreibung die Berechnung der Badfluktuationen enthalten. Auf kurzen Zeitskalen ergibt sich eine bemerkenswerte Übereinstimmung mit den Ergebnissen der Dichtematrix-Renormierungsgruppe, so dass der Einfluss von Quantenfluktuationen vernachlässigbar ist. Für große Zeiten gewinnen die Quantenfluktuationen an Einfluss, was zu einer Reduktion der Autokorrelation des Zentralspins im quantenmechanischen Fall führt. Ein vollständiger Zerfall der Autokorrelation für große Zeiten kann ohne jegliches externes Feld nicht beobachtet werden. Bei einem endlichen Magnetfeld hängt die Qualität der klassischen Beschreibung von der Stärke des Feldes ab. Insgesamt suggerieren die Ergebnisse jedoch, dass für große Bäder eine Überstimmung zwischen klassischer und quantenmechanischer Beschreibung erreicht wird.

Zum Abschluss der Arbeit werden die Eigenschaften von optimierten Pulsen, die der Dephasierung des Elektronenspins entgegenwirken, im Rahmen des semiklassischen Modells für unterschiedliche Arten von Rauschen untersucht. Falls die Autokorrelationsfunktion des Rauschens der eines Ornstein-Uhlenbeck-Prozesses ähnelt, so ist die Unterdrückung der Dephasierung mittels optimierter Pulse stark eingeschränkt. Dieses Verhalten kann auf dem Niveau der Magnus-Entwicklung erklärt werden. Durch die Kuspe in der Autokorrelationsfunktion tritt eine zusätzliche Bedingung auf, welche bei der Optimierung von Pulsen standardmäßig nicht berücksichtigt wird.

Abstract

In the field of quantum information processing, long decoherence times of the quantum bits are essential. Only if sufficiently long computations can be performed, quantum algorithms, which exploit the special properties of a quantum computer, can be implemented successfully. This includes the storage of quantum information as well as the number of performable operations on the quantum bits.

In this thesis, we present a proof-of-principle study of the dynamics of an electron spin in the central spin model where a single spin interacts with a large number of non-interacting bath spins. During the last decade, the central spin model has proven to be a good description of the decoherence of a single electron spin confined in a quantum dot. There, the decoherence is dominated by the hyperfine interaction between the electron spin and the surrounding nuclear spins.

For studying the dynamics in the central spin model, we combine a variety of numerical and analytical tools. A numerical study of the quantum mechanical model is accomplished by the time-dependent density matrix renormalization group. This approach captures the full hyperfine interacting for arbitrary magnetic fields. Thus, it is not restricted to a certain regime such as many other methods. We demonstrate how the algorithm is adopted for a cluster of spins linked by a central spin. An exact calculation of the trace at infinite temperature is achieved by purifying the system. Furthermore, a detailed investigation of several approaches for calculating the real-time evolution is presented. Best results are obtained from the adaptive method based on the Trotter-Suzuki decomposition of the time-evolution operator. Thereby, systems containing up to thousand bath spins can be studied on short and on intermediate time scales.

Motivated by the results for the quantum model and by simple analytic arguments, a semiclassical description of the central spin problem is introduced. In this description, the spin bath is replaced by a classical fluctuating variable while the central spin is still treated on the quantum level. The semiclassical model is analyzed in the framework of average Hamiltonian theory and numerical simulations. By combing these results with the results from the quantum mechanical model, the convergence towards the static-bath

approximation is proven. Furthermore, the numerical simulations reveal that a separate treatment of the conserved quantities is crucial.

In addition, the central spin model is discussed on the level of classical spins comprising a self-consistent calculation of the bath fluctuations. On short time scales, the numerical results for the dynamics of the central spin are in remarkable agreement with the results obtained from the density matrix renormalization group. This implies that the influence of quantum fluctuations is negligible on the corresponding time scales. For larger times, quantum fluctuations arise inducing a slight reduction of the central spin autocorrelation functions. Without external field, the long-time behavior reveals a non-decaying fraction of the central spin. For a finite external field, the quality of the solution determined by the classical equations of motion depends on the regarded regime of the field.

Finally, pulses for pure dephasing are discussed in the framework of a semiclassical model for different types of noise. If the autocorrelation function of the noise resembles the one of an Ornstein-Uhlenbeck process, the Frobenius norm exhibits an unexpected dependence on the inverse pulse amplitude. Based on average Hamiltonian theory, we derive an additional condition which is not fulfilled for pulses derived from the standard conditions.

Outline

The present thesis is organized as follows. In Chapter 1, we motivate our study and introduce the central spin model. This includes a review of other approaches for studying the decoherence of a single electron spin in a quantum dot. Furthermore, a short introduction to pulses is given. The adaption of the density matrix renormalization group to the central spin model is presented in Chapter 2. Extensions for the calculation of the real-time evolution are introduced and verified. Additionally, the errors and limits of the Trotter-Suzuki approach are discussed in detail. The chapter closes with an analysis of the short time behavior in dependence of the external magnetic field. To access the long-time behavior, a semiclassical model is proposed in Chapter 3. The model is treated on the base of average Hamiltonian theory as well as on different stages of numerical simulations based on the sampling of Gaussian fluctuations. In Chapter 4, the transition to a completely classical description of the central spin model is presented. For this and the latter chapter, the results obtained from the density matrix renormalization group always serve as benchmark. Pulses for pure dephasing are discussed on the base of a semiclassical model in Chapter 5. The analysis in dependence of the type of noise is performed again numerically and analytically. Finally, our results are concluded.

Chapter 1

Introduction

Contents

In this chapter, we motivate the study presented in this thesis. Therefore, the basics of quantum information processing are recapitulated and a brief summary of possible candidates for the realization of a quantum computer is given in Sect. 1.1. For the success of a system as a quantum computer, a detailed understanding of the decoherence in the underlying system is essential. A for the present thesis relevant definition of all processes summarized under the term decoherence is given in Sect. 1.2. Great potential for the realization of a quantum computer is assigned to single electron spins in quantum dots which are the main focus of this thesis. After introducing the basic properties of a quantum dot in Sect. 1.3, we argue that the hyperfine interaction is the dominating mechanism for the decoherence. For an efficient description of the hyperfine interaction in a quantum dot, we employ the central spin model which is introduced in Sect. 1.4. An overview of applicable methods for the study of the decoherence in the central spin model and related models is given in Sect. 1.5. Finally, it is discussed in Sect. 1.6 how decoherence can be effectively delayed by the application of pulses and pulse sequences.

1.1 Motivation

The field of quantum information processing (QIP) [SS08, NC10] has been one of the most active research field in physics during the last two decades. By exploiting two fundamental principles of quantum mechanics, namely *superposition* and *entanglement*, a quantum computer is able to solve specific problems with much higher efficiency than a classical device. In a quantum computer, all information is stored in *quantum bits* or *qubits* which are quantum mechanical two-level systems. Two complex numbers can be stored in one single qubit. A set of N qubits is initialized in linear time and has 2^N basis states due to the superposition principle. In addition, a transformation can be applied to all qubits at the same time which saves 2^N steps compared to an individual application. In the literature, this feature is often discussed under the keyword *quantum parallelism*. On the contrary, a classical bit carries only one piece of information at a time and the same operation has to be applied successively to all bits. Thus, 2^N repetitions are required to complete an operation on all classical bits.

To exploit the advantages of a quantum computer, special quantum algorithms have been developed. A famous example is Shor's algorithm [Sho94, Sho97] which finds the integer factorization of a given number in polynomial time. This is an enormous speedup compared to the non-polynomial runtime of corresponding classical algorithms. Another example is the search in an unstructured database. In a classical implementation, the effort grows linearly with the number of entries. The Grover algorithm [Gro96, Gro97] reduces the effort on a quantum computer by the square root. Both the Shor [VSB+01] as well as the Grover algorithm [DMK03] have already been implemented for a quantum computer based on nuclear magnetic resonance (NMR).

During the past two decades, qubits have been realized in a variety of different systems. In the following, we summarize briefly a selection of different candidates. In liquid-state NMR [VC05, Jon11], the nuclear spins of a very large ensemble of molecules serves as qubit. In other implementations, atomic ions placed inside an ionic trap represent the qubits [LBMW03]. To avoid a fast relaxation to the ground state, either metastable states or sublevels of the electronic ground state of the ions define the two levels of the qubit. This approach can also be extended to neutral atoms located in optical traps. Other realizations are based on nitrogen and phosphorus atoms embedded in C_{60}-fullerenes [MTA+06], which serve as a trap on the nanoscale. Various ways exist to employ the nuclear as well as the electron spin of the embedded atoms as qubits. The implementation of two-level systems is also possible in superconducting materials [MSS01]. There, one distinguishes between *charge*, *flux*, and *phase qubits* which mainly differ by the form of the potential used for the definition of the energy levels.

Besides the realizations mentioned in the previous paragraph, several other implementations of qubits in solid-state physics are conceivable. In a famous proposal made by Kane [Kan98], it was suggested to study phosphorus-31 impurities in silicon where a two-dimensional subspace of the electron-nuclear spin system of the phosphorus donor is used as qubit. However, a complete implementation of the system including all required control mechanisms is sophisticated. But substantial progress has been made in the past years, see Ref. [ZDM+13] for a recent review. Alternatively, qubits can be defined in single nitrogen-vacancy centers in diamond [JGP+04]. Nitrogen-vacancy centers are located on two adjacent lattice sites of the crystal structure, where one carbon atom has been replaced with a nitrogen atom and the other site is vacant. The total spin of the defect is $S = 1$ and couples to the nuclear spins of the surrounding carbon-13 atoms via hyperfine interaction. Two levels of the $S = 1$ spin triplet are used for the implementation of the qubit.

Moreover, quantum dots are a very promising system for the realization of a qubit [LD98, SKL03]. Quantum dots are low-dimensional semiconducting structures on the nanoscale. For example, the spin of a single electron confined in quantum dot defines the two levels of a qubit. As this realization is the focus of the present thesis, a more detailed introduction to quantum dots is given in Sect. 1.3.

The requirements for an implementation of a quantum computer are summarized by the famous DiVincenzo's criteria [DiV00]:

1) Scalability and well-defined qubits.
2) Well-defined initialization of the qubits in a simple state.
3) Long decoherence times.
4) A universal set of quantum gates.
5) Measurement of selected qubits.

With respect to these five criteria, every candidate for a quantum computer has its own individual advantages and disadvantages. For example, liquid-state NMR suffers from the lack of scalability so that the number of qubits is significantly limited. Scalability is in general problematic since a large ensemble of qubits may behave differently than a small number of qubits. While all of DiVincenzo's criteria are of great importance, special attention in research is often paid to decoherence because it strongly limits the number of accomplishable operations. Only if the coherence time of the qubit is sufficiently long, information can be stored and an adequate number of computations can be executed.

Concerning the success of quantum information processing, a fundamental statement is made by Preskill's *threshold theorem* [Pre98]: If the average error rate of the quantum gates is kept below a critical value, arbitrary long computations will be possible due to quantum error correction. Thus, a lot of effort is put into the development of quantum error correction [Ste96a, Ste96b, Pre98, SS08, NC10]. Another strategy is to eliminate or to reduce the sources of errors. This implies a thorough investigation of the decoherence. With these insights, techniques can be established which diminish the influence of decoherence in the system under study.

In total, a detailed comprehension of decoherence is crucial. If the underlying mechanisms for the decoherence in a defined system are known, strategies can be developed to suppress it. Long coherence times are essential in QIP because decoherence limits the storage time of the information as well as the number of accomplishable operations. But quantum algorithms require a certain amount of operations to yield usable output. This motivates the study presented in this thesis, where we investigate the decoherence in a spin model applicable to quantum dots. The specification of a particular system is important because the mechanisms causing decoherence strongly depend on the system under study. With quantum dots, one of the most promising candidates for the realization of a quantum computer has been chosen.

For a single electron confined in a quantum dot, the hyperfine interaction between the electron spin and the nuclear spins is the dominating source of decoherence of the electron spin. The relevant physics is well described by the Gaudin model or *central spin model* [Gau76]. In this proof-of-principle study, we develop a twofold strategy for investigating the decoherence of the central spin. First, we introduce a numerical treatment of the central spin model based on the *density matrix renormalization group* (DMRG) [Whi92, Whi93, WF04, FW05] which fully captures the decoherence due to the hyperfine interaction with the surrounding bath spins. Thereby, large spin baths containing up to ≈ 1000 spins are accessible up to intermediate time scales. Second, semiclassical and classical approaches to the central spin problem are presented. They are verified with our DMRG results and give access to the long-time behavior. Finally, we address pulses, which extend the dephasing time of the electron spin, in the framework of a semiclassical model.

1.2 Decoherence

Coherence is essential for many areas in physics. For example, interference in classical wave optics is observed only when two waves are coherent. This implies a well-defined phase relation between the two waves. If the constant phase relation is lost, constructive or destructive interference is not possible anymore. The coupling to the environment induces decoherence and the ability for interference is gone. In quantum mechanics for example, decoherence involves the destruction of the relative phase of a superposition state, for example the superposition $|\Psi\rangle = a|\uparrow\rangle + b|\downarrow\rangle$ of a spin up and a spin down state. The processes which are summarized under the term decoherence strongly depend on the studied system and vary between different fields of physics. In the following, we define decoherence for spins in quantum dots.

The decoherence of a spin is characterized by different relaxation processes. Here, we adopt the definition of the different processes from NMR [Lev08]. The longitudinal relaxation time T_1 describes the decay of the magnetization of the spin, which is aligned in the direction of the magnetic field. In this thesis, the direction of the external magnetic field is taken as z-direction. After the time T_1 has passed, the polarization of an initially polarized system has decreased by a factor $1/\mathrm{e}$ towards its equilibrium, a mixture of spin up and spin down states. Then, quantum mechanically stored information is lost because a reliable measurement of the polarization is not possible anymore. In NMR, this process is often referred to as spin-lattice relaxation because it is caused by the interaction of the spin with its environment, for example the crystal lattice.

The time scale T_2 captures the decay of the magnetization in the transverse plane. This process is often called spin-spin relaxation or simply dephasing. It describes the duration of the phase coherence between a spin up and a spin down component. In QIP, the time scale T_2 characterizes the number of possible operations applicable to the qubit. In contrast to T_2, the transverse relaxation time T_2^* takes the static inhomogeneities between the various spins in an ensemble into account. The different time scales fulfill the inequality $T_2^* \leq T_2 \leq 2T_1$ [Lev08]. Usually, but not always, the strict inequality $T_2 < 2T_1$ holds. Consequently, dephasing is the limiting process of long-lasting coherence.

Throughout this thesis, the following nomenclature is used for the different processes: The longitudinal relaxation is usually abbreviated as relaxation, while the decay of the transverse magnetization is generally referred to as dephasing. Under the term decoherence, both processes are summarized.

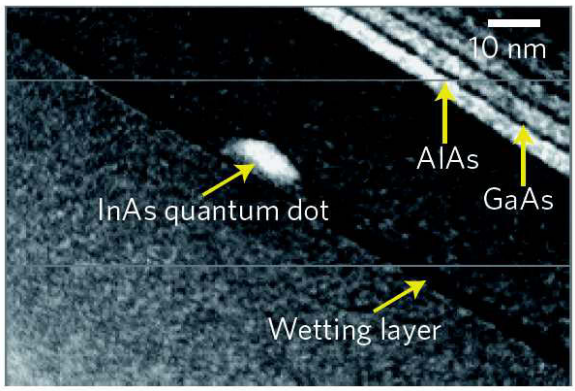

Fig. 1.1: Transmission electron microscopy image of a self-assembled InAs quantum dot grown in GaAs. The InAs/GaAs layers are embedded in a heterostructure to enable the control of the electronic population of the dot. Figure is taken from Ref. [War13].

1.3 Quantum dots

Quantum dots are small three dimensional structures on the nanoscale which are confined in all three spatial dimensions. Due to the confinement, the energy levels of an electron or a hole placed inside the dot are discrete, similar to a particle in a box or to the electronic levels of an atom. Thus, quantum dots are often referred as "artificial atoms". Besides their importance for QIP, quantum dots also play a big role in the field of spintronics [ŽFDS04]. In the following, we briefly present two different types of quantum dots relevant for QIP.

Self-assembled quantum dots grow randomly on a substrate [War13]. In Fig. 1.1, the transmission electron microscopy image of a typical InAs quantum dot embedded in GaAs is shown. Layer-by-layer, InAs is grown on the GaAs substrate. Thereby, InAs quantum dots form randomly which are capped by additional GaAs layers. To control the electronic occupation of the dot, they are integrated into an additional heterostructure to enable a tuning of the electronic levels by a gate voltage. The size of such a self-assembled quantum dot lies typically in the order of magnitude of ten nanometers. Due to its potential depth, a self-assembled quantum dot can be operated at fairly high temperatures $T \gtrsim 4\,\mathrm{K}$. The electron spin is controlled optically. The required laser pulses do not exceed a few picoseconds and enable ultrafast rotations of the spins with a high fidelity [GES$^+$09, War13]. Measurements are usually performed on an ensemble of randomly located quantum dots. Pump and probe spectroscopy revealed that the ensemble dephasing time T_2^* does not exceed a few nanoseconds [GYS$^+$06, HGB$^+$08]. But the dephasing time T_2 of a single dot lies in the scale of microseconds for temperatures $T <$ 15-20 K. The longitudinal relaxation time T_1 is much longer than the dephasing time T_2. At $T = 1\,\mathrm{K}$, it reaches values of $T_1 \approx 20\,\mathrm{ms}$ as long as the magnetic field is not too large [KDH$^+$04]. The properties of self-assembled

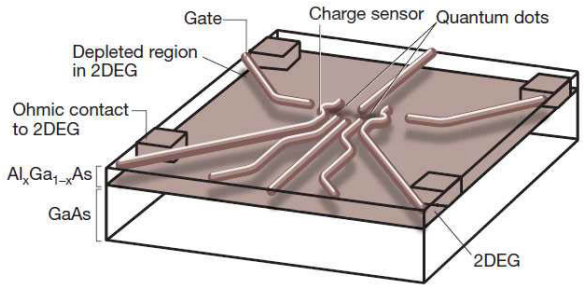

Fig. 1.2: Sketch of a typical lateral double quantum dot based on a GaAs/$Al_xGa_{1-x}As$ heterostructure. The two-dimensional electron gas (2DEG) forms at the interface of the GaAs and the $Al_xGa_{1-x}As$ layer. Figure is taken from Ref. [LJL+10].

quantum dots are defined by their size, their shape and their distribution inside the sample. These quantities are all of random nature which can be cumbersome. Consequently, each dot may have different optical properties [LJL+10].

Alternatively, electrostatically defined quantum dots are frequently examined [HKP+07]. The characteristic structure of such a lateral quantum dot is sketched in Fig. 1.2. Its foundation is based on a heterostructure of GaAs and $Al_xGa_{1-x}As$ fabricated by molecular beam epitaxy. $Al_xGa_{1-x}As$ is made from GaAs by replacing a fraction x of the Ga atoms with Al. The upper $Al_xGa_{1-x}As$ is doped with Si so that free electrons are induced which gather at the interface of the GaAs and the $Al_xGa_{1-x}As$ layer. This corresponds to the realization of a two-dimensional electron gas, where the free electrons are confined in the plane of the interface. By using electron-beam lithography, gate electrodes are placed onto the heterostructure. They are used to separate small regions of electrons inside the two-dimensional electron gas. The depleted areas confine potential minima which form the quantum dots. Their occupation is controlled by tuning the gate voltages. Since the separation of the energy levels is much smaller than in a self-assembled quantum dot, they have to be operated at temperatures below 1 K. Control of the electron spin is achieved via electron spin resonance using microwave radiation. Experimental measurements of the spin dephasing time revealed a fast dephasing $T_2* \approx 30\,\text{ns}$ [KNV08] compared to a fairly large spin relaxation time $T_1 \approx 1\,\text{ms}$ [EHWvB+04]. Using spin echo techniques, values up to $T_2 \approx 0.5\,\mu\text{s}$ were measured for the dephasing time of a single spin [KNV08].

With respect to the five DiVincenzo criteria [DiV00], quantum dots with electron spins as qubits indeed have a great potential for the realization of a quantum computer. The spin of an electron confined inside the dot is a *well-defined qubit*. Besides the identification of a single spin as qubit, it is also possible to define a qubit in the basis of two or three spins. Solid-state systems are *scalable* by construction, but the implementation of systems with a large number of qubits will certainly be challenging. The *initialization* of a lateral quantum

dot is achievable by relaxation or by populating the dots with selected spin states, which can be realized by adjusting the coupling to the reservoir [HKP+07]. For self-assembled quantum dots, reliable initialization is achieved by optical pumping [War13]. Both single lateral as well as single self-assembled quantum dots have relatively *long decoherence times*. By applying schemes from dynamic decoupling [Ban98, VL98, KL05, Uhr07, Lev08], the decoherence time can be increased further. In addition, the optical control of a single spin in a self-assembled quantum dot is very fast so that a large number of operations can be performed. For computations, a *universal set of quantum gates* is required which is represented by a single-qubit and a two-qubit gate [LD98]. A single-qubit gate corresponds to a rotation of the spin. As an example for the required two-qubit gate, one may consider the SWAP gate which exchanges the state of two spins. For a detailed review of possible realizations, see Ref. [LYS10] for self-assembled and Ref. [HKP+07] for lateral quantum dots. In combination, the single-qubit and the two-qubit gate can be used to implement arbitrary quantum gates. The *measurement* of qubits in lateral quantum dots is based on the conversion of the spin state to a charge state. The detection of a single charge is much easier than the measurement of a tiny magnetic moment so that this technique is the method of choice. For the spin-to-charge conversion, a variety of different methods has been proposed [HKP+07]. Spontaneous emission and Faraday rotation enable the optical measurement of spins in self-assembled quantum dots, see Ref. [War13] for a summary.

In total, the realization of a quantum computer with electron spins in quantum dots complies with DiVincenzo's criteria [DiV00] in many aspects. In the future, the experimental as well as the theoretical progress will certainly improve the situation further.

Alternatively, qubits in quantum dots are also realizable via excited electron-hole pairs (excitons) which are created with short laser pulses. For example, by creating a single exciton in two quantum dots, the basis states are used to define two qubits [BHH+01]. Furthermore, qubits can also be represented by hole spins [War13]. This is an independent and currently very active field in research.

In this theses, we discuss the realization of qubits in the two-levels of a single electron spin confined in a quantum dot. Hence, a qubit is always identified with an electron spin-1/2 and vice versa from now on. As mentioned above, the decoherence of the electron spin is an important issue in QIP. In the next sections, we discuss the underlying mechanisms and introduce an appropriate model.

1.3.1 Decoherence of an electron spin in a quantum dot

The dominating source for the decoherence of electron spins in solids is usually based on spin-orbit coupling. By spin-orbit interaction, the spin couples to the electronic degrees of freedom which are exposed to various perturbing effects such as impurity scattering or electron-phonon interaction. However, an analysis of the spin-flip rates [KN00, KN01] revealed that the relaxation of the electron spin due to spin-orbit coupling with electron-phonon coupling is strongly suppressed for electrons confined in an s-type conduction band of a quantum dot. In a consecutive investigation, the dephasing of the electron spin [GKL04] was included in the analysis of the spin-orbit interaction. Based on perturbation theory and a Markovian approximation, it was found that the transverse relaxation time T_2 exceeds the longitudinal relaxation time T_1 with $T_2 = 2T_1$. This result is general and does not depend on the nature of the fluctuations coupling to the orbital degrees of freedom. Hence, if spin orbit coupling alone was the dominating mechanism for the decoherence, a single electron spin confined in a quantum dot would exhibit very long dephasing times because $T_1 \approx$ 1-20 ms, see previous section.

However, experimental observations contradict with this theoretical result. Measurements revealed strongly reduced dephasing times compared to to relaxation time, see previous section. Thus, spin-orbit coupling alone cannot be the major source of decoherence. Instead, the decoherence is dominated by the Fermi contact hyperfine interaction between the electron spin and the nuclear spins in the dot. This is supported by the fact that common semiconducting materials such as GaAs or InAs have a substantial nuclear magnetic moment of the order of several nuclear magnetons [SKL03]. This is comparable to the scenario in single nitrogen-vacancy centers, where the hyperfine interaction between the spin of the nitrogen-vacancy center and the nuclear spins of the surrounding carbon-13 atoms is the dominating contribution to decoherence.

According to Fermi [Fer30], the hyperfine interaction is proportional to the probability $|\Psi(\vec{r}_j)|^2$ that the electron is at the site $\vec{r}_j$ of the nucleus. For a single nucleus, the Hamiltonian of the hyperfine interaction between the electron spin $\vec{S}_0$ and a single nuclear spin $\vec{I}_i$ is given by the expression [MER02, SKL03, CL06]

$$H_i = J_i \vec{S}_0 \cdot \vec{I}_i. \tag{1.1}$$

The coupling constant reads

$$J_i = \frac{6\pi}{3I} \mu_B \mu_{I_i} \left|\Psi(\vec{r}_i)\right|^2, \tag{1.2}$$

where μ_B stands for the Bohr magneton of the electron and μ_{I_i} for the magneton of the nucleus i. We assume that the electron is in its orbital ground state so that the hyperfine exchange can be regarded as isotropic. Placed inside a quantum dot, the electron spin interacts with about $N = 10^6$ nuclear spins [SKL03]. The sign of the interaction depends on the compound, for instance, it is antiferromagnetic for GaAs and InAs. The time scale for the decoherence of the electron spin is set by the total contribution J_q of all nuclear spins with $J_q^2 \sim \sum_{i=1}^{N} |\Psi(\vec{r}_i)|^4$ [MER02].

In addition to the hyperfine coupling, the nuclear spins interact with one another by dipole-dipole exchange. For two nuclear spins i and j, the dipolar interaction is described by the Hamiltonian [SKL03]

$$H_{ij} = -\frac{\mu_I^2}{I_i I_j} \frac{1}{r_{ij}^3} \left(\frac{3\left(\vec{I}_i \vec{r}_{ij}\right)\left(\vec{I}_j \vec{r}_{ij}\right)}{r_{ij}^2} - \vec{I}_i \cdot \vec{I}_j \right), \tag{1.3}$$

where $\vec{r}_{ij}$ is the spatial distance between the nuclei. The time scale of the hyperfine interaction is of the order 10^{-6} s, while the dipolar coupling affects the decoherence of the electron spin on a time scale which is roughly one or two orders of magnitudes larger. This time scale lies beyond the scope of the present thesis. Consequently, we will not consider the dipolar coupling further.

1.4 Central spin model

The previously introduced hyperfine interaction between a single electron spin and a bath of surrounding nuclear spins in a quantum dot is well captured by the central spin or Gaudin model [Gau76, Gau83]

$$\begin{aligned} H &= \vec{S}_0 \sum_{i=1}^{N} J_i \vec{S}_i \\ &= \sum_{i=1}^{N} J_i \left[S_0^z S_i^z + \frac{1}{2}\left(S_0^+ S_i^- + \text{h.c.} \right) \right]. \end{aligned} \tag{1.4}$$

The term Gaudin model refers originally to a class of integrable spin models first proposed by Gaudin in 1976 [Gau76]. This family of models is closely related to the pairing-model in the BCS THEORY of superconductivity, see for instance Ref. [vDP02] or the review in Ref. [DPS04] and the references therein.

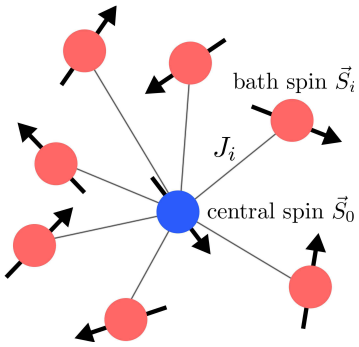

Fig. 1.3: Sketch of the star topology of the central spin model (1.4). The central spin $\vec{S}_0$ interacts with the bath spins $\vec{S}_i$ by hyperfine interaction. The corresponding exchange constants are denoted by J_i.

As illustrated in Fig. 1.3, the central spin model (1.4) has a star topology where a centered spin $\vec{S}_j$ interacts with N bath spins with coupling constants J_i. Throughout this thesis, the central spin always has the index $i = 0$. The dipolar interaction between the bath spins has been excluded, see the discussion in the previous section. For simplicity, we do not distinguish between electron and nuclear spins in our notation. The discussion in the present thesis is restricted to spin-1/2 objects. Higher values for the bath spins would result into larger local Hilbert spaces. But this should not affect most aspects of the qualitative physics of this model.

It is convenient to represent the bath by the operator

$$\vec{A} := \sum_{i=1}^{N} J_i \vec{S}_i, \tag{1.5a}$$

which acts on all bath spins weighted with their corresponding couplings constants. It can be interpreted as an effective three-dimensional field created by the bath spins which is often referred to as Overhauser field. Thereby, the Hamiltonian (1.4) simplifies to

$$H = \vec{S}_0 \cdot \vec{A}. \tag{1.5b}$$

In the course of this thesis, the central spin model in a magnetic field is discussed. The local fields h_i are applied in z-direction and the Hamiltonian is given as

$$\begin{aligned} H &= \vec{S}_0 \sum_{i=1}^{N} J_i \vec{S}_i - \sum_{i=0}^{N} h_i S_i^z \\ &= \vec{S}_0 \cdot \vec{A} - \sum_{i=0}^{N} h_i S_i^z. \end{aligned} \tag{1.6}$$

Usually, the field is applied either to the central spin or to the bath spins. With respect

to nuclear spins, magnetic fields are often neglected because the Zeeman splitting is very small due to the small magnetic moments of the nuclei. In contrast, the Bohr magneton of the electron is about three orders of magnitude larger. But fields applied to bath spins induce a dynamics in the bath which is exploited in the course of this thesis as simple example of an intrinsic bath dynamics.

The coupling constants J_i are inhomogeneous because they are defined by the probability $|\Psi(\vec{r}_i)|^2$ that the electron is present at the site of the nucleus i. As mentioned before, the time scale for the decoherence is defined by the total contribution of all nuclear spins. In the present thesis, we focus mainly on a completely disordered initial state where the first moment of the coupling constants does not contribute. Hence, it is advisable to define the time scale for the fast dynamics as $1/J_\mathrm{q}$ where J_q^2 is given by the quadratic sum of all couplings [MER02]

$$J_\mathrm{q}^2 := \sum_{i=1}^{N} J_i^2. \tag{1.7}$$

Note that we use units where $\hbar = 1$ so that J_q corresponds to an energy. The J_i are distributed randomly, since the nuclear spins are located randomly inside the dot. By employing experimentally measured values and an approximation for the wave function, it is possible to model the distribution of the exchange constants inside a spherical quantum dot, see for instance Ref. [SKL03].

In the present thesis, we refrain from discussing specific distributions relevant for a particular experimental situation. Rather we are interested in a proof-of-principle investigation of the central spin model. Hence, we discuss a generic uniform distribution $J_i \in [0, J_\mathrm{c}]$ where the cutoff J_c is determined by the total energy J_q. By picking equidistant couplings from the box $[0, J_\mathrm{c}]$

$$J_i = \sqrt{\frac{6N}{2N^2+3N+1}}\frac{N+1-i}{N} J_\mathrm{q}, \quad i \in \{1, \ldots, N\}, \tag{1.8}$$

the randomness is avoided in our calculation, see Fig. 1.4 for an illustration. This induces a systematic dependence of the results on N so that an improved investigation of the different numerical methods is enabled. Moreover, the choice from Eq. (1.8) fulfills the normalization constraint (1.7) so that the relaxation always takes place on the same time scale independent of the actual bath size. This allows for an easy comparison of different system sizes and a study of the convergence with N.

We stress once more that the central spin model (1.4) also captures the dynamics of the spin of single nitrogen-vacancy centers [JGP+04]. There, the decoherence of the spin is

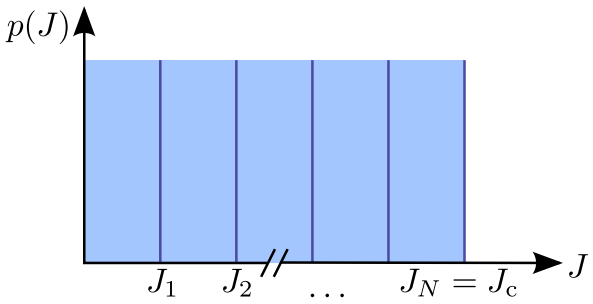

Fig. 1.4: Uniform probability distribution $p(J)$ of the coupling constants $J \in [0, J_c]$. To avoid the randomness in our calculation, we pick equidistant couplings J_i from the box $[0, J_c]$ for $i = 1, \ldots, N$, see Eq. (1.8).

dominated by the hyperfine interaction with the non-vanishing nuclear magnetic moment of the carbon-13 atoms. However, a corresponding theoretical study comprises a significant dipole-dipole interaction which induces stronger fluctuations in the bath [MTL08].

1.5 Overview of methods

First investigations of the central spin model (1.4) in the 1970s were based on the Bethe ansatz [Gau76, Gau83]. Over the years, the model has become very popular for the description of the hyperfine interaction of an electron spin in a quantum dot. Nowadays, the central spin model has been studied in the framework of many different methods. Besides standard techniques such as exact diagonalization, more elaborate methods such as *cluster expansion* [WdSDS05] or *non-Markovian master equation formalism* [CL04] have been applied to the model. These techniques give access to larger bath sizes, but often require additional approximations which limit the universality of the results. For example, many applications are restricted to the strong-field limit where spin-flips between the central spin and the bath can be neglected or treated perturbatively. For the sake of completeness, we also mention perturbative [KLG02, KLG03] and Markovian approaches [SMP02, dSDS03a, dSDS03b].

In practice, the method should be chosen with respect to the aim of study. For a full study of the decoherence the time evolution of the observables has to be calculated for a sizeable nuclear bath over a large period of time. In exact diagonalization, the reachable time scale is only limited by CPU time. However, only small systems with $N \approx 20$ bath sites can be implemented [SKL03, CDDS10]. Within the available amount of CPU resources, the accessible time scale is extended further by calculating the time evolution in the framework of Chebychev polynomials [DDR03, HA14].

Our study is based on the *density matrix renormalization group* (DMRG) [Whi92, Sch05a], which is introduced in the next chapter. There, we also present several extensions to *time-dependent DMRG* (tDMRG) [WF04, FW05, Sch05a]. The numerical treatment within the framework of tDMRG fully captures the hyperfine exchange between the central spin and the bath. Compared to exact diagonalization, the number of accessible bath spins is larger by up to two orders of magnitude, but the reachable time scales are more limited. In addition, a semiclassical and a classical model for the decoherence is introduced in the progress of this thesis. Both approaches can be combined to justify an effective description of the electron spin dynamics.

In this section, we briefly introduce a selection of different methods and describe their potential and limits. This short review does not claim to be complete; its purpose is to give a first impression of different treatments of the central spin model.

1.5.1 Bethe ansatz

The central spin model (1.4) is exactly solvable by Bethe ansatz [Gau76, Gau83]. However, finding the solutions is highly non-trivial and strongly depends on the initial state of the system. The Bethe ansatz gives access to the eigen decomposition of the Hamiltonian. To this end, the Bethe ansatz equations have to be solved. For the central spin model, the number of equations corresponds to the number M of flipped spins, starting from an entirely polarized state. In total, there are C_M^N different solutions, called Bethe roots, of the coupled Bethe ansatz equations where C_M^N stands for the binomial coefficient. The Bethe roots correspond to a complete representation of the eigenvalues and -vectors of the Hamiltonian. They are used to calculate the time dependence of the desired observables, for example the magnetization of the central spin.

As mentioned before, solving the Bethe ansatz is a highly complicated task. Thus, the solutions are usually restricted to initial states where the bath is either fully polarized or where only a small number of spins is flipped [BS07b, BS07a]. Especially the calculation of observables is costly because it requires the summation of C_M^N terms. However, it was demonstrated that the Bethe ansatz can be used to extract important features, for example the dominating frequencies in the spectral representation of the magnetization without summing over a very large number of contributions [BES$^+$10a]. Thereby, an estimate for the longitudinal relaxation time T_1 of the electron can be made. The results are valid even for low polarizations of the bath, depending on the exact properties of the distribution of the exchange constants. Furthermore, the Bethe ansatz was employed for a calculation of

the static magnetization profile and the static two-point correlation function of the central spin model [BES10b]. The corresponding Bethe ansatz result was combined with a classical approximation and exact diagonalization results. While the magnetization profile of the classical approximation is close to the one of the quantum mechanical model, the two-point correlation function shows significant contributions from quantum fluctuations.

Recently, a method combining the algebraic Bethe ansatz and Monte Carlo sampling was proposed [FS13a, FS13b]. In this variant, a restriction to a definite polarization of the bath is not necessary. So far, the real-time evolution of up to $N = 48$ spins was calculated up to long times $t \approx$ 100-1000 J_{q}^{-1}. As there is no restriction to states with a certain polarization, the calculation in combination with the Monte Carlo sampling approximates the complete trace in the Hilbert space. However, this approach can be applied only if the coupling constants are isotropic. In contrast, the XXZ version of the central spin model, where the coupling constants in z-direction differ from the ones in the xy-plane, may be investigated with the DMRG.

1.5.2 Cluster expansion techniques

Cluster expansions are used to study models which describe the decoherence due to *spectral diffusion*. Spectral diffusion implies that a dipolar interaction between the bath spins is the dominant mechanism for the decoherence of the central spin. In addition, a secular approximation is usually made. This corresponds to the neglection of spin-flips between the central spin and the bath. The approximation is justified in the strong-field limit relevant for many experimental studies. Consequently, only the transverse relaxation time T_2 can be studied within this approach. A longitudinal relaxation does not take place within this approximation.

For the cluster expansion developed by Witzel *et al.* [WdSDS05, WDS06], the fluctuations of the bath are approximated by sub-processes. To this end, the bath is separated into small disjoint clusters. The lowest order is given by all processes including two nuclear spins, because a single nuclear spin has no contribution. The number of involved spins is successively increased. Thus, contributions from clusters with three nuclear spins are taken into account followed by contributions from four nuclei which cannot be represented by sub-processes caused by the interaction of two nuclear spins. Consequently, the n-th order of the cluster expansion contains contributions of all clusters consisting of up to n spins. To obtain a result, the desired quantity has to be expanded in terms of the cluster contributions. Then, the individually calculated cluster contributions up to a certain order

are inserted to evaluate the expression. Convergence is achieved when the contribution of the clusters decreases quickly with their size. This is supported by the fact that the dipolar interaction between two randomly located nuclear spins with distance R decays extremely fast $\sim 1/R^3$. Hence, the contribution of spins with a large spatial distance only plays a minor role in the total contribution, while a contribution of neighbored spins is crucial.

Besides the technique sketched above, other variants of cluster expansions exist. Based on the original scheme [WdSDS05, WDS06], the *disjoint cluster approach* was introduced and applied to nitrogen-vacancy centers in diamond [MTL08]. The *correlated cluster expansion* developed by Yang and Liu [YL08a, YL09] is extremely suitable when contributions from larger clusters have to be taken into account. It has been applied successfully to study pulse sequences which extend the coherence time of the electron spin [DRZ$^+$09, ZWL11, ZHL12].

The main disadvantage of the cluster expansion techniques is the restriction to pure dephasing of the central spin. A modified version of the correlated cluster expansion includes spin-flips between central spin and bath on the level of a one-cluster contribution [WCCDS12], but the results are restricted to small time scales. Moreover, a very large number of clusters has to be taken into account when the size of the bath is large.

1.5.3 Non-Markovian master equation formalism

The decoherence of the electron spin in the central spin model shows strongly non-Markovian behavior [BBP04, CL04]. This is also underlined by the fact that the bath in the central spin model has no intrinsic dynamics. Hence, a derivation of the equations of motion based on a Markovian approximation is generally insufficient, see Sect. 1.5.5. The lack of non-Markovian contributions can be repaired by considering the application of non-Markovian master equations. Here, we follow the notation used in Refs. [BP07, FB07].

The non-Markovian master equation formalism is based on the Liouville or von Neumann equation of the density matrix. The density matrix ρ of the total system is projected onto the so-called "relevant part" $\mathcal{P}\rho$ by the application of a projection operator $\mathcal{P}$. The projection operator $\mathcal{P}$ is chosen in a way that all irrelevant degrees of freedom are eliminated.

A generic choice for the relevant part is $\mathcal{P}\rho = \mathrm{Tr}_\mathrm{E}(\rho) \otimes \rho_0$, where the partial trace is taken over the Hilbert space of the environment, for example the bath, with the fixed state ρ_0 of the environment. The remaining part of the Hilbert space is called the system. With

the superoperator $\mathcal{P}$ satisfying the condition $\mathcal{P}\rho(0) = \rho(0)$, one derives the NAKAJIMA-ZWANZIG EQUATION

$$\frac{\mathrm{d}}{\mathrm{d}t}\mathcal{P}\rho(t) = \int_0^t \mathrm{d}t_1 \, \mathcal{K}(t, t_1)\, \mathcal{P}\rho(t_1) \tag{1.9}$$

for the reduced density matrix where the so-called memory Kernel or self-energy $\mathcal{K}(t, t_1)$ induces the non-Markovian behavior. The Nakajima-Zwanzig equation is an integrodifferential equation for the effective dynamics of the quantum mechanical system defined by the "relevant part". In general, the obtained master equation cannot be solved in closed form. To this end, it is usually simplified further by applying additional approximations and a perturbative expansion of the kernel in powers of the interaction between the system and the bath. In the final step, the simplified master equation is often solved analytically.

Alternatively, the *time-convolutioness master* equation

$$\frac{\mathrm{d}}{\mathrm{d}t}\mathcal{P}\rho(t) = \mathcal{K}(t)\, \mathcal{P}\rho(t) \tag{1.10}$$

can be solved. It is also derived from the von Neumann equation. Compared to the Nakajima-Zwanzig equation, the dependence on the history of the relevant part has been eliminated by the employment of an exact backward propagator [BP07]. Thus, the time-convolutioness master equation is a time-local equation which is often preferred to the time-convolution in the Nakajima-Zwanzig equation. The superoperator $\mathcal{K}(t)$ is a time-dependent generator which introduces the non-Markovian behavior. Like the self-energy in Eq. (1.9), the generator $\mathcal{K}(t)$ is usually derived from a perturbative expansion in the interaction between system and bath.

In one of the first studies, a generalized master equation was derived by defining a superoperator which preserved all electron spin excitations [CL04]. Thereby, the solution for the relaxation and dephasing of the electron spin due to hyperfine coupling was found in the strong-field limit. In the zero-field limit, only a lower bound for the decaying fraction of the electron spin could be estimated. By comparing solutions from non-Markovian master equations with the exact result for the reduced dynamic of the electron spin in the central spin model with XX interaction, Breuer *et al.* [BBP04] demonstrated that both the Nakajima-Zwanzig as well as time-convolutioness master equation yield a good approximation for the short-time behavior. However, the approach failed for larger times where partially unphysical behavior occurred. The standard projection operator as introduced above reduces the total state to a tensor product state between system and bath. An advanced approach is based on correlated projection operators which partly preserve the correlation between system and bath [FB07]. The results were compared

to the exact solution of the central spin model with homogeneous coupling constants. Even in lowest order, a nice agreement between all results was found. For the model with non-uniform exchange constants, the same conclusion was reached for the short- and long-time behavior in the high-field limit [FBN$^+$08]. The study was based on the time-convolutioness master equation and correlated projection operators. In a more recent publication, a non-perturbative solution of the time-convolutioness master equation was presented by Barnes *et al.* [BCDS12]. After a resummation of all orders of the master equation, the solution can be written in a closed form. It is valid for inhomgeneous couplings as well as for a large number of different initial states. However, this calculation still requires a finite magnetic field and is restricted to a small time-scale defined by the inverse of the largest coupling constant.

In all, the non-Markovian master equation formalism captures the decoherence of the electron spin in the central spin model for finite magnetic fields on limited time-scales. Solutions for the long-time behavior are restricted to the strong-field regime. Furthermore, the employment of non-Markovian master equations provides access to an analytical treatment of the model. But master equations involve many approximations and the output depends on the assumptions made during their derivation .

1.5.4 Semiclassical and classical approaches

Semiclassical and classical models for the decoherence of an electron spin are frequently studied. The spins of the bath and/or the central spin are approximated either by classical spins or by an effective field. Note that the dynamics of classical spins is closely related to the one of quantum spins due to the isomorphism between the rotation group SO(3) and the group SU(2) of complex rotations.

Merkulov *et al.* [MER02] studied the hyperfine-induced decoherence of electron spins in a large ensemble of quantum dots without magnetic field and in the strong-field limit. Three different processes were identified which contribute to the decoherence of the electron spin with different impact. First, the electron spin precesses in the frozen hyperfine field of the nuclear spins. Second, fluctuations in the hyperfine field of the nuclear spins were discussed. They are induced by the precession of the nuclear spins in the hyperfine field of the electron, which is smaller by the factor $1/\sqrt{N}$ than the field acting on the electron spin. A third time scale is set by the dipolar coupling between the nuclear spins. But this effect was not included since many other mechanisms contribute to the decoherence on the long-time scale of the dipolar interaction. All equations of motion were treated on a classical level and estimates for the spin dephasing time T_2^* were calculated.

A similar approach was carried out by replacing the nuclear spins with an effective time-dependent nuclear field which varies slowly due to the effective field created by the electron spin [EN02, EN04]. The effective field of the nuclear spins was obtained from a semiclassical calculation where the average spin of the electron entered. The corresponding equations of motion were integrated numerically by splitting the nuclear spins into subsets defined by the strength of their coupling to the central spin. The results were calculated for randomly chosen initial values of the nuclear spins without external magnetic field. From the total contribution of the individual subsets, the long time behavior of the autocorrelation function of the central spin was calculated using the adiabatic approximation. In addition, an ensemble average over random initial conditions was discussed.

The employment of semiclassical equations of motion is indeed a valid approximation in the limit of a large number of bath spins. This was shown in Ref. [CBB07] where the equations of motion were derived from a spin coherent path integral. As already proposed in Ref. [EN04], this approach leads to an effective field inducing the precession of the electron spin. By replacing the electron spin by its time average, Chen *et al.* [CBB07] derived a set of reduced equations of motion for the dynamic of the nuclear spins. They discuss explicitly the influence of conserved quantities such as the total momentum and the energy. Thereby, they were able to study the asymptotic behavior of the central spin for a large number of bath spins ($N = 900$) and different initial configurations in the dependence of the shape of the electron wave function. For a Gaussian profile of the coupling constants, they found that the magnetization $\langle S_0^z(t)\rangle$ of the central spin decays $\sim 1/\ln t$.

For unpolarized baths, it was shown by Al-Hassanieh *et al.* that a method combining a time-dependent mean field theory with the P-representation of the density matrix yields reliable results [AHDDH06]. Within the P-representation, equations of motion were derived where the part describing the central spin coincides with the exact one. Note that the postulated set of equations of motion does not correspond to the exact set, neither to the fully quantum mechanical nor to the semiclassical equations. This method gives access to the long-time behavior for a large number $N > 1000$ bath spins. But its application is restricted to completely unpolarized states only. In a consecutive study, this approach was employed together with exact numerical results to study the influence of an external magnetic field on the relaxation of an electron spin located in a single quantum dot and on two electron spins located in two neighboring quantum dots [ZDAH$^+$06]. The dephasing in direction perpendicular to the external field was not investigated. The numerical results for the single quantum dot were compared to analytic results obtained from a quasistatic bath approximation involving homogeneous coupling constants. They found that their numerical data justifies the quasistatic bath approximation for large numbers of bath spins. Furthermore, a transition in the behavior of the magnetization of the central spin was observed in dependence of the strength of the external field.

Recently, Witzel *et al.* [WYD13] introduced a semiclassical description of the spin bath. The autocorrelation function of the bath fluctuations were obtained from a correlated cluster expansion using the secular approximation, see Sect. 1.5.2. Hence, the model only comprises dephasing due to spectral diffusion. The relaxation of the electron spin was not included. The exclusion of back-action effects between central spin and bath is legitimated by their model, which contains an intrinsic dynamics of the bath. However, this is generally not justified for the central spin model where the bath has no intrinsic dynamics.

1.5.5 Other approaches

A perturbative ansatz can be made in the spin-flip terms of the Hamiltonian of the central spin model (1.4). This ansatz is only justified in the limit of strong magnetic fields. Otherwise it cannot be guaranteed that the contribution from the spin-flips is small. Indeed, a comparison with an exact solution lead to the conclusion that the perturbative treatment yields a different behavior in the zero-field limit, see Ref. [SKL03] and the references therein.

Alternatively, it is possible to solve a master equation where the nuclear spin bath is approximated by a Markovian process among other simplifications [SMP02]. In general, the dynamics of the nuclear spins in the central spin model is non-Markovian because the bath has no intrinsic dynamics. The dynamics of the nuclear spins is determined entirely by the interaction with the central spin. Hence, intrinsic dynamics of the bath are essential for the Markovian approximation because it is assumed that the bath is independent from the state of the central spin. Consequently, it is not surprising that the results of this study stand in contradiction to known results. Furthermore, a Markovian approximation was also made in the strong-field limit where the decoherence is governed by spectral diffusion [dSDS03a, dSDS03b]. This approach involves many assumptions and approximations so that the calculated decoherence times exceed the ones measured in experiment.

Other attempts to describe the non-Markovian physics in the central spin model were made on the level of an iterative equation of motion approach for the retarded Green's function of the electron spin in the large-bath limit [DH06, DH08]. Thereby, good results are yield for strong external fields where the contribution of higher orders is negligible.

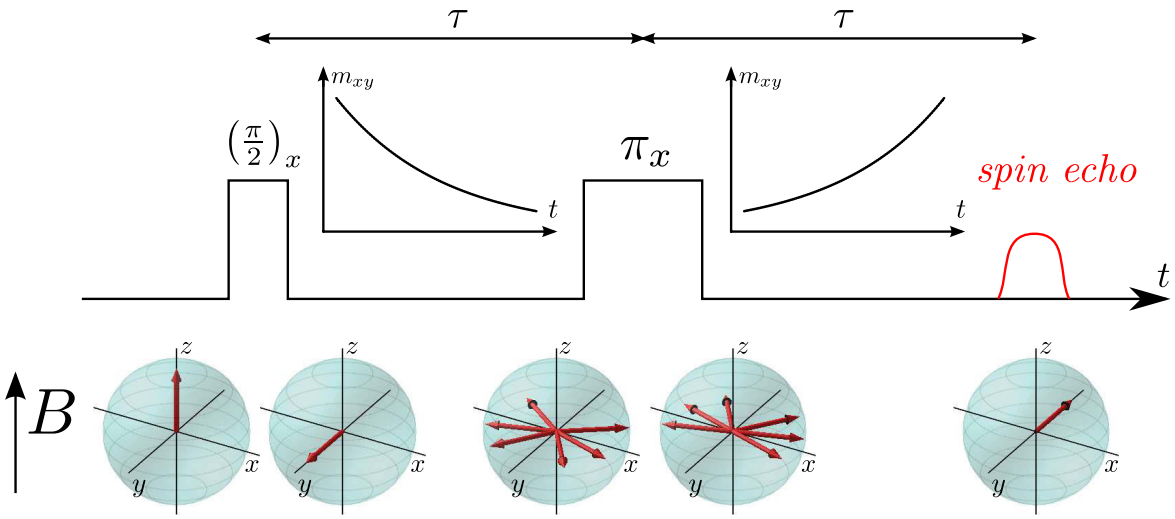

Fig. 1.5: Illustration of the spin echo effect. An exemplary number of six spins is first aligned along the external magnetic field B in z-direction. A $\pi/2$-pulse is applied around the x-axis to rotate the spins into the transverse plane. Then, the spins start to precess around the z-axis. Due to local inhomogeneities in the magnetic field, all spins precess with slightly different frequencies. Hence, the signal of the transverse magnetization decays. A π-pulse is applied around the x-axis after some time τ. The slowly rotating spins are now located ahead of the fast moving spins. Consequently, the transverse magnetization increases again. It obtains its maximum value at the time τ after the π-pulse. In addition, we show the configuration of the spins in the Bloch sphere at selected times.

1.6 Pulses & dynamic decoupling

In the field of QIP, a lot of effort is put in the development of error correction methods [Pre98, Ste96a, Ste96b, SS08, NC10]. The success of quantum error correction is supported by Preskill's *threshold theorem* [Pre98], which was already mentioned in the motivation. According to the theorem, it is sufficient to keep the error rates in a quantum computer below a critical value to enable calculations of arbitrary length. In a classical device, a basic error correction can be achieved by simply copying the information stored in the classical bits. In quantum mechanics, the creation of identical copies of a qubit is forbidden due to the *no-cloning theorem* [SS08, NC10]. But a qubit can be coupled to a larger set of auxiliary qubits so that an imperfect cloning may be achieved. The additional qubits store the type of error and allow a restoration of the faultless state of the qubit.

In addition to quantum error correction, one can try to eliminate the source of decoherence: The interaction between the qubit and its environment. This ansatz is based on the *spin echo effect*, first described by Hahn in NMR experiments in 1950 [Hah50]. In this approach, external electro-magnetic pulses are applied which allow for an effective control

of the rotation of the spins. An illustration of the spin echo effect is shown in Fig. 1.5. An ensemble of spins is initialized in the direction parallel to the external magnetic field. The spins are rotated into the transverse plane by applying a $\pi/2$-pulse around the x- or y-axis. Due to the Larmor precession, the spins start to rotate in the plane perpendicular to the external magnetic field. All spins precess with slightly different frequencies because of inhomogeneities in the local magnetic field. Thus, they dephase with increasing time and the transverse magnetization decays. By applying a π-pulse after some delay τ, the situation is inverted: Spins with lower frequencies are now located ahead of the fast rotating spins. After another delay of length τ, the spins are again in phase and a revival of the transverse magnetization is observed.

Usually, the inhomogeneities of the local magnetic field are dynamic and not static. This implies that the application of a single pulse is not anymore sufficient. Instead, the refocusing of the spins can be achieved by the implementation of pulse sequences which are typically iterated. A famous example is the CPMG sequence (Carr, Purcell, Meiboom and Gill) [CP54, MG58] which consists of two π-pulse cycles. In average, the CPMG sequence suppresses the dephasing interaction between the spins and the environment. The potential power of such sequences is widely known so that the development and optimization of pulse sequences is nowadays a very active field in research. In QIP, pulse sequences have been established under the keyword *dynamic decoupling* (DD) [Ban98, VL98, FTP$^+$05, KL05, CHHC06, WDS07, YLS07]. While simple DD techniques are also based on periodic sequences, a breakthrough was achieved by the invention of sequences with non-equidistant pulses known as Uhrig dynamic decoupling (UDD) [Uhr07]. Thereby, the decoherence time can be improved by multiple orders for any dephasing system [YL08b]. Furthermore, many other types of DD sequences exist, for example, *concatenated dynamic decoupling* [KL05, KL07] or *quadratic dynamic decoupling* [WFL10]. The first one can be extended to UDD sequences [Uhr09], while the latter one consists of a combination of two different UDD sequences. In addition to dephasing, these sequences also suppress the longitudinal relaxation. This requires that the pulses are quicker than the dynamics of the environment.

So far, we assumed that the pulses are ideal, which implies infinitesimal duration and infinite amplitude. In contrast, real pulses always have a finite duration and a finite amplitude. The aim is to design real pulses which are as close to an ideal one as possible. This is achieved by optimizing the time dependence of the pulse amplitudes and of the rotation axis. In NMR, composite pulses are used to reduce the error due to the finite pulse duration. In this way, rotations are decomposed in different partial rotations which are more robust. A theoretical concept for the design of such pulses with piecewise constant amplitudes was first introduced by Tycko [Tyc83]. But the optimization of real pulses

can also be carried out for types of pulses other than composite pulses. For example, pulses with continuous amplitudes or continuous pulses obtained from frequency modulation [SKL+06, PKRU09, FPU12, SFPU12] can be discussed.

A general ansatz for the shaping of pulses is made by a product ansatz for the time-evolution operator $U_{\mathrm{re}}(\tau_{\mathrm{p}})$ during a real pulse of duration τ_{p} [PKRU09]

$$U_{\mathrm{re}}\left(\tau_{\mathrm{p}},0\right)=\widehat{P}_{\tau_{\mathrm{p}}}\cdot U_{\mathrm{c}}\left(\tau_{\mathrm{p}},0\right). \tag{1.11}$$

The operator $\widehat{P}_{\tau_{\mathrm{p}}}$ describes the rotation under the ideal pulse, while $U_{\mathrm{c}}(\tau_{\mathrm{p}},0)$ is a correcting factor which contains the intrinsic dynamics of the bath (if any) and the interaction between the spin and the bath. Both operators obey a Schrödinger equation. To make the real pulse as close as possible to an ideal one, $U_{\mathrm{c}}(\tau_{\mathrm{p}},0)\approx\mathbb{1}$ has to be fulfilled. Theoretically, one way to achieve this is to expand the correcting factor in powers of τ_{p} so that the interaction between the spin and the bath is averaged to zero. Precisely, one obtains

$$U_{\mathrm{c}}\ \left(\tau_{\mathrm{p}}\ ,0\right)=\mathbb{1}+\mathcal{O}\left(\tau_{\mathrm{p}}^{m+1}\right). \tag{1.12}$$

We define a pulse with the property (1.12) to be a pulse of order m. Examples for a first order pulse are the symmetric SCORPSE and the asymmetric CORPSE pulses [CJ00, CLJ03]. In the last years, a variety of π and $\pi/2$ pulses have been proposed which make corrections up to second order vanish [SP05, MdSZW06, PQ08, PS08, PKRU09, FPU12, SFPU12].

In ansatz (1.11), a real pulse is compared with an ideal one of infinitesimal length. An alternative approach is achieved when the dynamics from the pulse and from the system are disentangled. Then, an optimized pulse of order m has to hold [PFKU08, PU08]

$$U_{\mathrm{re}}\left(\tau_{\mathrm{p}}\ ,0\right)=U_{H}\left(\tau_{\mathrm{p}}\ ,\tau_{\mathrm{s}}\ \right)\cdot\widehat{P}_{\tau_{\mathrm{p}}}\cdot U_{H}\Big(\tau_{\mathrm{s}}\ ,0\Big)+\mathcal{O}\left(\tau_{\mathrm{p}}^{m+1}\right), \tag{1.13}$$

where $U_H(\tau_1,\tau_2)$ contains the complete time evolution of the system before and after the pulse and τ_{s} denotes the instance of the instantaneous pulse. The advantage of this ansatz is that both the real as well as the ideal pulse have the same finite duration τ_{p}. However, it was shown that the condition (1.13) can only be fulfilled for a π-pulse in leading order [PFKU08, PU08]. The vanishing of higher order corrections is excluded rigorously.

In summary, the strategy to suppress the decoherence is twofold:

1) Shape pulses which are as close to an ideal one as possible.

2) Design pulse sequences for dynamic decoupling.

A powerful tool for investigating the quality of the analytically derived pulses and pulse sequences are numerical simulations. They enable an exact study of the specific models which is only limited by the properties of the employed method and the CPU limits. Furthermore, the higher-order terms in Eq. (1.12) are captured quantitatively. Hence, a numerical simulation has to be regarded as a complementary method to the analytic calculations. It quantifies the size of the neglected contributions and is essential for the verification of the analytically derived pulses and pulse sequences. The quality of shaped piecewise constant pulses for pure dephasing is discussed on the base of a semiclassical model in Chapter 5.

Chapter 2

Density Matrix Renormalization Group

Contents

In this chapter, we introduce the *density matrix renormalization group* (DMRG) [Whi92, Whi93]. Since its introduction by White in 1992, DMRG has become one if not the leading numerical method for studying the physics of one-dimensional systems. In the present thesis, DMRG serves as the main instrument for the numerical investigation of the central spin model (1.4). After a short motivation and introduction in Sect. 2.1, we demonstrate in Sect. 2.2 how DMRG is adapted for a cluster of spins. This includes a description of the modified infinite and finite size algorithm for the central spin model. The calculation of expectation values at infinite temperature is addressed in Sect. 2.3. Subsequently, we present several methods to extend the method to time-dependent DMRG (tDMRG) in Sect. 2.4. The calculation of the real-time dynamics is essential for an investigation of the decoherence of the central spin. In Sect. 2.5, the most suitable method for calculating the real-time evolution is identified on the basis of a test calculation for a small bath size. An exhaustive study of the occurring errors and the limits of our numerical approach follows in Sect. 2.6. First detailed results for the electron spin dynamics are presented in Sect. 2.7, where the short-time behavior is discussed in the absence and presence of an external magnetic field.

During the past two decades, many extensions to the standard DMRG algorithm have been developed. Besides the real-time evolution, this incorporates many other modifications such as the calculation of the dynamics in frequency domain or the treatment of two-dimensional and quasi two-dimensional models. For an extensive review, the interested reader is referred to Ref. [Sch05a]. A more recent review of DMRG in the framework of matrix product states can be found in Ref. [Sch11]. As a first introduction to DMRG, Ref. [PKWH99] can be recommended.

2.1 Introduction

For a quantum mechanical system, the dimension of the Hilbert space $\mathscr{H}$ grows exponentially with the number of particles. For a system of N spin-1/2, the Hilbert space has the dimension $\dim \mathscr{H} = 2^N$ because each individual spin contributes with two states. Even for a small number of spins, the dimension of the Hilbert space is already very large. Consequently, a complete exact numerical treatment is restricted to small system sizes. As mentioned in Sect. 1.5, numerical techniques based on the exact representation of the Hamiltonian of the central spin model involve a maximum of $N \approx 20$ bath spins [DDR03, CDDS10, HA14].

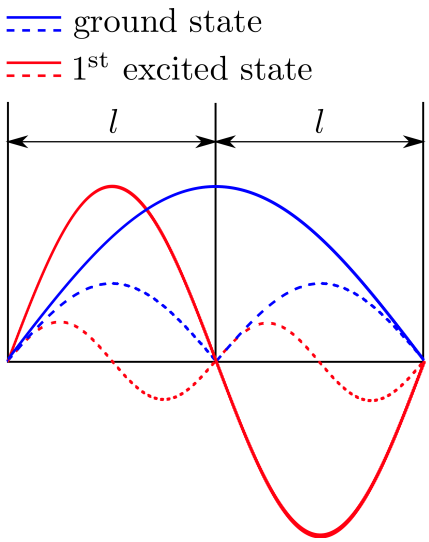

Fig. 2.1: Particle in a box problem: Ground state and first excited state for a system of length $2l$ and for the two sub systems of length l.

The enormous dimension of the Hilbert space suggests that not all basis states are equally important. Furthermore, one is rarely interested in the complete spectra of the Hamiltonian. Often, one focuses on certain properties of the model, for example its ground state or selected excited states. For an effective description, the important states have to be identified according to a well-defined criterion. Thereby, the size of the Hilbert space can be reduced. Such a procedure will be extremely efficient if the number m of contributing states is much smaller than the total dimension of the Hilbert space. The question arises how such an algorithm can be realized with a physically motivated truncation criterion. This is the domain of methods summarized under the keyword *real-space renormalization group*. Starting with a small and exactly tractable system of size l, the system size is increased by the addition of a new site. Therefore, the local operators of the new site as well as the interaction between this site and the existing system have to be added. Then, the basis of the extended system of size $l+1$ is truncated and the total system of size $l+1$ is transformed to the reduced basis. Thereby, one has obtained a "renormalized" Hamiltonian which should contain the effective physical properties of the system. This procedure is repeated successively until the maximum size is reached.

The most famous example is the *numerical renormalization group* (NRG) by Wilson [Wil75] where only the states with the lowest energy are kept. The success of the NRG is based on its original application to the KONDO PROBLEM. In Wilson's ansatz, the impurity problem was first transformed to an energy basis represented by a semi-infinite chain. These "energy sites" are chosen to obey a logarithmic discretization so that their contribution decreases exponentially with increasing distance to the impurity. This allows one to consider even exponentially small energy scales. The NRG has been applied successfully to a large

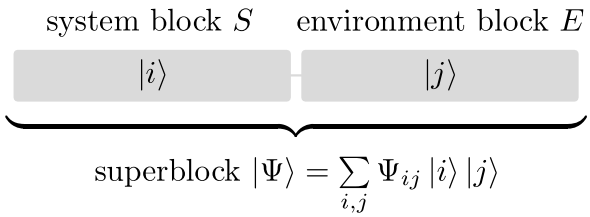

Fig. 2.2: Configuration of the superblock formed by the system block S with basis states $|i\rangle$ and the environment block E with basis states $|j\rangle$.

number of Kondo and Anderson impurity models, see Ref. [BCP08] for a review. However, for other models like the HUBBARD or the HEISENBERG MODEL the truncation scheme of the NRG fails because of the absence of an intrinsic separation of energy levels.

An explanation for the failure of the energy level truncation in the NRG was given by White and Noack [WN92]. For illustration, we consider a simple toy model, the "particle in a box problem". A free particle is confined inside a box of length l by potential walls of infinite height. The setup is sketched in Fig. 2.1 for a block of length $2l$, which can be split into two equal blocks of size l. In addition, the two lowest lying eigenfunctions $\Psi_n(x) \sim \sin(n\pi x/l)$ have been plotted for both block sizes. While the combination of the eigenfunctions of the small blocks always has a node at the center of the large block, the exact eigenfunction in the block of size $2l$ adopts a maximum at the center. Hence, the approximation of the correct ground state by the ground states of the smaller sub-blocks is not suitable because this approach cannot take the correct boundary conditions into account.

This can be remedied by considering a combination of boundary conditions as suggested by White and Noack [WN92]. Each block is diagonalized for different boundary conditions, for example free and fixed boundary conditions. Then, the new basis is chosen by combining the lowest eigenstates of all diagonalized blocks fulfilling different boundary conditions. Alternatively, the block of interest can always be considered to be part of a larger system consisting of $p > 2$ blocks of the same size l [WN92]. The ensemble of all p blocks is called the *superblock*. For the renormalization procedure, the lowest eigenstates of the superblock Hamiltonian are projected onto the two selected blocks. Together, they form the block of size $2l$ for the next step. Consequently, the block size is doubled in each step leading to an exponential growth of the block size. The success of this approach lies in the fact that the fluctuations due to the additional blocks automatically induce the correct boundary conditions for the new blocks of size $2l$. The additional blocks can also be interpreted as environment in which a single block is embedded. By successively increasing the block size, the single block is finally integrated into an environment resembling the thermodynamic limit of the system.

A variation of the superblock method with linearly growing block size is the foundation of DMRG [Whi92, Whi93]. We consider the setup shown in Fig. 2.2. The superblock consists of a system block S with states $\{|i\rangle\}$ and an environment block E with states $\{|j\rangle\}$. The state vector of the superblock

$$|\Psi\rangle = \sum_{i,j}^{d_S,d_E} \Psi_{ij} |i\rangle |j\rangle \tag{2.1}$$

is expressed in the product basis of S and E with coefficients $\{\Psi_{ij}\}$. The number of states in each block is given by the dimension of the corresponding Hilbert space, $d_S := \dim \mathscr{H}_S$ and $d_E := \dim \mathscr{H}_E$, respectively. The goal is to optimize the representation of the system block by truncating the basis $\{|i\rangle\}$ according to a well-defined criterion. Thereby, the dimension d_S of the Hilbert space $\mathscr{H}_S$ of the system block S is reduced. For an ideal representation of the system block, the number of kept states m should be much smaller than its original dimension d_S. But what is an efficient criterion for the truncation? The optimization with respect to the lowest lying energy levels as in NRG does not work well for models extended in real space. Hence, one has to obey a different strategy. Let us specify the requirements which have to be made to the truncation scheme. Ideally, it should

1) minimize the deviation of the optimized wave function from the exact one [Whi92, Whi93],
2) lead to an optimal approximation of the expectation values [Whi98],
3) and preserve a maximum of the entanglement between system and environment block [Gai01, GMD02, ON02, Gai03, LRV04].

2.1.1 Reduced density matrix

Before we present the different derivations leading to the DMRG truncation scheme, we recapitulate the definition and the properties of a density matrix. They are essential for the truncation scheme and can be found in any standard textbook, for example in Ref. [Sch05b]. For a pure state as given in Eq. (2.1), the *reduced density matrix* of the system block reads

$$\rho_S = \mathrm{Tr}_E |\Psi\rangle \langle\Psi| \tag{2.2}$$

where Tr_E denotes the partial trace over the environment block. For simplicity, we omit the index S where this does not lead to confusion. Accordingly, a single element of the

reduced density matrix is given by

$$\rho_{ii'} = \sum_{j}^{d_E} \Psi^*_{ij} \Psi_{i'j}. \tag{2.3}$$

The density matrix (2.2) fulfills the following properties:

$$\operatorname{Tr} \rho = 1 \tag{2.4a}$$

$$\rho^\dagger = \rho \tag{2.4b}$$

$$\rho \geq 0 \Leftrightarrow \langle \nu | \rho | \nu \rangle \geq 0 \; \forall \; |\nu\rangle \in \mathscr{H}_S. \tag{2.4c}$$

Hence, the density matrix is a normalized and diagonalizable operator. Due to its semi-positive definiteness, all eigenvalues w_i are greater than or equal to zero. Consequently, ρ can be expressed in its eigenbasis

$$\rho = \sum_{i}^{d_S} w_i \, |w_i\rangle \, \langle w_i| \tag{2.5}$$

where w_i can be regarded as the probability that ρ is in the eigenstate $|w_i\rangle$. The interpretation of the eigenvalues w_i as probabilities is possible only because of the normalization (2.4a) and the positive semi-definiteness (2.4c) of ρ. If $|\Psi\rangle$ is a pure state, the density matrix is also a projector

$$\rho^2 = \rho, \tag{2.6}$$

which implies that all w_i are either zero or unity. Furthermore, the expectation value of any observable $\widehat{O}$ from the system block can be expressed with the help of the density matrix

$$\begin{aligned} \langle \widehat{O} \rangle &= \operatorname{Tr}_S \rho \widehat{O} \\ &= \sum_{i,i'}^{d_S} \widehat{O}_{i'i} \rho_{ii'}. \end{aligned} \tag{2.7}$$

2.1.2 Truncation of the reduced density matrix

Now, we are able to address our previously made specifications which have to be fulfilled by the DMRG truncation scheme. Each of the following derivations focuses on a different property of the model, but all of them lead to the same criterion for the system block optimization: The states with largest weight in the reduced density matrix of the system block have to be kept.

2.1.2.1 Optimization of the wave function

The derivation of the DMRG truncation from an optimization of the wave function was first discussed by White when he introduced DMRG [Whi92, Whi93]. It relies on a variational optimization of the wave function. In the following, we present a slightly extended derivation which is based on White's original arguments. To this end, we define the truncated wave function

$$|\widetilde{\Psi}\rangle = \sum_{\alpha,j}^{m,d_E} c_{\alpha,j} |u_\alpha\rangle |j\rangle , \tag{2.8}$$

where the basis $\{|i\rangle\}$ of the system block has been reduced to an m-dimensional basis $\{|u_\alpha\rangle\}$ with $|u_\alpha\rangle = \sum_i^{d_S} u_{i,\alpha} |i\rangle$ and $m < d_S$.

For the following steps, it is advisable to rewrite the truncated state (2.8) as

$$|\widetilde{\Psi}\rangle = \sum_{\alpha}^{m} c_\alpha |u_\alpha\rangle |v_\alpha\rangle . \tag{2.9}$$

The components of the vectors $\{|v_\alpha\rangle\}$ are defined by $v_{\alpha,j} := \langle j|v_\alpha\rangle = N_\alpha c_{\alpha,j}$. They are normalized by choosing the constants $\{N_\alpha\}$ so that $\sum_j^{d_E} |v_{\alpha,j}|^2 = 1$.

The truncated state should approximate the exact state (2.1) as well as possible: $|\widetilde{\Psi}\rangle \approx |\Psi\rangle$. Analytically, this is expressed as the minimization of the quadratic distance between the exact and the truncated state

$$\mathcal{S} := \left| |\Psi\rangle - |\widetilde{\Psi}\rangle \right|^2 . \tag{2.10}$$

After inserting (2.1) and (2.9), the quadratic distance is written as

$$\mathcal{S} = \sum_{i,j}^{d_S,d_E} \left(\Psi_{ij} - \sum_{\alpha}^{m} u_{i,\alpha} c_\alpha v_{j,\alpha} \right)^2 . \tag{2.11}$$

This expression has to be minimized by varying over all $\{c_\alpha\}$, $\{u_{i,\alpha}\}$ and $\{v_{j,\alpha}\}$. The $\{u_\alpha\}$ should form an orthonormal basis $\langle u_\alpha|u_{\alpha'}\rangle = \delta_{\alpha,\alpha'}$. By interpreting the coefficients $\{\Psi_{ij}\}$ as elements of a rectangular $d_S \times d_E$ matrix, the minimization of the quadratic distance can be understood as a component-by-component minimization of the individual matrix elements. To solve this problem, we employ a singular value decomposition (SVD) to the matrix $\mathbf{\Psi} = (\Psi_{ij})$ [PTVF07]. Then, the matrix $\mathbf{\Psi}$ is given by

$$\mathbf{\Psi} = \mathbf{U}\mathbf{D}\mathbf{V}^\top . \tag{2.12}$$

For simplicity, real valued matrices are assumed. But the argumentation holds for complex matrices as well. Furthermore, we restrict ourselves to the case $d_S \geq d_E$. The matrix $\mathbf{D}$ is a diagonal $d_E \times d_E$ matrix containing the singular values of $\mathbf{\Psi}$, while $\mathbf{U}$ is a column-orthogonal $d_S \times d_E$ matrix and $\mathbf{V}^\top$ is the transpose of an orthogonal $d_E \times d_E$ matrix $\mathbf{V}$.

According to Eq. (2.11) the matrix elements of the truncated state $\widetilde{\mathbf{\Psi}}$ read

$$\begin{aligned} \widetilde{\Psi}_{ij} &:= \sum_{\alpha}^{m} u_{i,\alpha} c_\alpha v_{j,\alpha} \\ &= \sum_{\alpha}^{d_\mathrm{E}} u_{i,\alpha} c_\alpha v_{j,\alpha}. \end{aligned} \tag{2.13}$$

In the last step, the upper index of the sum has been extended to d_E with $c_\alpha = 0$ for $\alpha > m$. In matrix form, one obtains

$$\widetilde{\mathbf{\Psi}} = \begin{pmatrix} u_{1,1} & \cdots & u_{1,d_\mathrm{E}} \\ u_{2,1} & \cdots & u_{2,d_\mathrm{E}} \\ u_{3,1} & \cdots & u_{3,d_\mathrm{E}} \\ \vdots & \vdots & \vdots \\ u_{d_S,1} & \cdots & u_{d_S,d_\mathrm{E}} \end{pmatrix} \cdot \left(\begin{array}{ccc|c} c_1 & & 0 & \\ & \ddots & & 0 \\ 0 & & c_m & \\ \hline & 0 & & 0 \end{array}\right) \cdot \begin{pmatrix} v_{1,1} & \cdots & v_{1,d_\mathrm{E}} \\ v_{2,1} & \cdots & v_{2,d_\mathrm{E}} \\ v_{3,1} & \cdots & v_{3,d_\mathrm{E}} \\ \vdots & \vdots & \vdots \\ v_{d_E,1} & \cdots & v_{d_E,d_\mathrm{E}} \end{pmatrix}^\top . \tag{2.14}$$

With respect to the minimization of Eq. (2.11), the columns $\{|u_\alpha\rangle\}$ and $\{|v_\alpha\rangle\}$ in the latter expression for $\widetilde{\Psi}$ have to be the corresponding columns of $\mathbf{U}$ and $\mathbf{V}$ obtained from the SVD of $\mathbf{\Psi}$. Then, the truncated superblock state acquires the form

$$\widetilde{\mathbf{\Psi}} = \mathbf{U}\widetilde{\mathbf{D}}\mathbf{V}^\top \tag{2.15}$$

where

$$\widetilde{\mathbf{D}} = \left(\begin{array}{ccc|c} c_1 & & 0 & \\ & \ddots & & 0 \\ 0 & & c_m & \\ \hline & 0 & & 0 \end{array}\right). \tag{2.16}$$

is a diagonal matrix. In general, we could also assume that the matrix $\widetilde{\mathbf{D}}$ is non-diagonal. But the expression (2.13) for $\widetilde{\Psi}$ already implies that the non-diagonal elements have to be zero. Hence, we directly define $\widetilde{\mathbf{D}}$ as a diagonal matrix.

It is easily verified that the distance (2.11) expressed by the matrices $\mathbf{\Psi}$ and $\widetilde{\mathbf{\Psi}}$ acquires the

form

$$\mathcal{S} = \mathrm{Tr}\left(\mathbf{\Psi} - \widetilde{\mathbf{\Psi}}\right)\left(\mathbf{\Psi} - \widetilde{\mathbf{\Psi}}\right)^{\top}. \tag{2.17a}$$

After inserting the expressions for $\mathbf{\Psi}$ (2.12) and $\widetilde{\mathbf{\Psi}}$ (2.15), the latter expression simplifies to

$$\mathcal{S} = \mathrm{Tr}\left(\mathbf{D} - \widetilde{\mathbf{D}}\right)^{2} \tag{2.17b}$$

because of the orthogonality of $\mathbf{U}$ and $\mathbf{V}$. Both, $\mathbf{D}$ and $\widetilde{\mathbf{D}}$, are $d_{\mathrm{E}} \times d_{\mathrm{E}}$ matrices. But $\widetilde{\mathbf{D}}$ only contains m non-zero entries. In order to minimize the quadratic distance in Eq. (2.17b), the diagonal entries $\{c_\alpha\}$ of $\widetilde{\mathbf{D}}$ have to be the largest m singular values of $\mathbf{\Psi}$ stored in the matrix $\mathbf{D}$. Now, we know how the distance $\mathcal{S}$ is minimized. But the SVD of $\mathbf{\Psi}$ still remains to be calculated.

To this end, we consider

$$\begin{aligned}\mathbf{\Psi}\cdot\mathbf{\Psi}^{\top} &= \mathbf{U}\mathbf{D}\underbrace{\mathbf{V}^{\top}\cdot\mathbf{V}}_{=\mathbb{1}}\mathbf{D}^{\top}\mathbf{U}^{\top} \\ &= \mathbf{U}\mathbf{D}^{2}\mathbf{U}^{\top}\end{aligned} \tag{2.18}$$

where the orthogonality of $\mathbf{V}$ has been exploited. The expression (2.18) is nothing else but the reduced density matrix ρ of the system block, see Eq. (2.3). From Eq. (2.18), one can draw two important conclusions. First, the matrix $\mathbf{U}$ diagonalizes the reduced density matrix ρ. Hence, it contains the eigenstates $|w_\alpha\rangle$ of ρ as columns. The corresponding eigenvalues $w_\alpha = c_\alpha^2$ are the elements of the diagonal matrix $\mathbf{D}^2$. Second, the singular values c_α of $\mathbf{\Psi}$ are the square roots of the (positive) eigenvalues of ρ. Thereby, we have shown that the optimal choice for the truncated basis of the system block are the m eigenstates of the reduced density matrix ρ with largest eigenvalues w_α. Ideally, the eigenvalues and the corresponding eigenstates of ρ should be sorted in descending order $w_1 \geq w_2 \geq \ldots \geq w_{d_S}$ so that one can easily pick the m most important eigenstates.

A measure for the accuracy of the truncation is the *discarded weight*

$$\mathrm{err} = 1 - \sum_{\alpha=1}^{m} w_\alpha \tag{2.19}$$

where the sum runs over all weights of the regarded eigenstates. The discarded weight defined in Eq. (2.19) is a measure for the weight of the truncated eigenstates because the reduced density matrix is normalized according to Eq. (2.4a). Thus, a fast decay of the eigenvalues with m is crucial for yielding a good accuracy. The derivation made above is

almost identical for the second case where $m < d_S \leq d_E$. Then, the last $(d_E - d_S)$ columns of $\mathbf{U}$ as well as the last m diagonal elements of $\mathbf{D}$ in (2.12) are zero.

Until now, the derivation of the density matrix criteria was made for a pure state $|\Psi\rangle$, for example the ground state. If the state of the superblock is in a mixed state consisting of several states $\{|\Psi_k\rangle\}$ with corresponding weights $\{W_k\}$, the optimal truncation scheme is still described best by the eigenstates with largest weight in the reduced density matrix [Whi93]. For a mixed state, the reduced density matrix is simply given as superposition

$$\rho = \sum_k W_k \rho_k \tag{2.20}$$

of the individual density matrices of the basis states $|\Psi_k\rangle$. Note that due to normalization $\mathrm{Tr}\,\rho_k = 1$ and $\sum_k W_k = 1$ has to hold. Thus, the density matrix truncation is not restricted to a single state. Several states can be targeted during a truncation. In the present thesis, the use of several target states is exploited for the calculation of autocorrelation functions, see Sect. 2.4.1.

2.1.2.2 Optimization of the expectation values

The density matrix criterion can also be derived from the expectation value of an arbitrary observable $\widehat{O}$, which is contained in the system block [Whi98]. According to Eq. (2.7), the expectation value of $\widehat{O}$ is given by

$$\begin{aligned} \langle \widehat{O} \rangle &= \mathrm{Tr}_S\, \rho \widehat{O} \\ &= \sum_{\alpha=1}^{d_S} w_\alpha \, \langle w_\alpha | \widehat{O} | w_\alpha \rangle \, . \end{aligned} \tag{2.21}$$

In the last step, the representation of the reduced density matrix of the system block in its eigenbasis has been inserted. As introduced in the previous section, we assume that the eigenbasis of ρ is ordered in descending order with respect to its eigenvalues. Then, one can simply truncate the sum in (2.21) after m eigenstates. This corresponds to a projection onto the basis of the m most important eigenstates of ρ

$$\langle \widetilde{O} \rangle = \sum_{\alpha=1}^{m} w_\alpha \, \langle w_\alpha | \widehat{O} | w_\alpha \rangle \, . \tag{2.22}$$

Consequently, the deviation of the approximated expectation value from the exact one reads

$$\begin{aligned}\left|\langle\widehat{O}\rangle - \langle\widetilde{O}\rangle\right| &\leq C_{\widehat{O}} \sum_{\alpha=m+1}^{d_S} w_\alpha \\ &\leq C_{\widehat{O}} \left(1 - \sum_{\alpha=1}^{m} w_\alpha\right) = C_{\widehat{O}} \cdot \mathrm{err}\end{aligned} \tag{2.23}$$

where $C_{\widehat{O}} := \max_{\{\phi\}} |\langle\phi|\widehat{O}|\phi\rangle / \langle\phi|\phi\rangle|$ is the norm of the observable $\widehat{O}$. Again, the error can be estimated by the discarded weight defined in Eq. (2.19).

2.1.2.3 Preservation of the entanglement

Entanglement is a unique feature in quantum mechanics. Entangled states cannot be expressed as a tensor product of two sub states. For example, a spin singlet state or $m_S = 0$ triplet state cannot be written as a simple product state of two spin-1/2 objects. The entanglement of a pure state consisting of two bipartite blocks has been studied in a variety of works [Gai01, GMD02, ON02, Gai03, LRV04] and reveals a close relation between DMRG and quantum information theory.

We start with the representation of the exact state $|\Psi\rangle$ in the basis of the system and environment block (2.1) and recall the singular value decomposition of the matrix $\mathbf{\Psi}$ (2.12). Thereby, one obtains

$$\begin{aligned}|\Psi\rangle &= \sum_{i,j}^{d_S,d_E} \sum_{\alpha}^{d_E} u_{i,\alpha}\sqrt{w_\alpha} v_{j,\alpha} |i\rangle |j\rangle \\ &= \sum_{\alpha=1}^{d_E} \sqrt{w_\alpha} \left(\sum_{i}^{d_S} u_{i,\alpha} |i\rangle\right) \left(\sum_{j}^{d_E} v_{j,\alpha} |j\rangle\right),\end{aligned} \tag{2.24}$$

where $d_S \geq d_E$ has been assumed. The latter expression is equivalent to the Schmidt decomposition [Sch07, NC10]

$$|\Psi\rangle = \sum_{\alpha=1}^{r} \sqrt{w_\alpha} |w_\alpha^S\rangle |w_\alpha^E\rangle \tag{2.25}$$

of $|\Psi\rangle$ where the orthonormal basis states of the system and environment block

$$|w_\alpha^S\rangle = \sum_i^{d_S} u_{i,\alpha} |i\rangle \tag{2.26a}$$

$$|w_\alpha^E\rangle = \sum_j^{d_E} v_{j,\alpha} |j\rangle \tag{2.26b}$$

are obtained from the projection of the orthonormal matrices $\mathbf{U}$ and $\mathbf{V}$. The rank r corresponds to the number of non-zero coefficients $\sqrt{w_\alpha}$. For arbitrary values of d_S and d_E, it is given by

$$r \leq \min\left(d_S, d_E\right). \tag{2.27}$$

The Schmidt decomposition also characterizes the entanglement of a bipartite state. Only if $r > 1$, the two sub states are entangled. The reduced density matrices of the system and the environment block read

$$\rho_S = \sum_{\alpha=1}^{r} w_\alpha |w_\alpha^S\rangle \langle w_\alpha^S| \tag{2.28a}$$

$$\rho_E = \sum_{\alpha=1}^{r} w_\alpha |w_\alpha^E\rangle \langle w_\alpha^E|. \tag{2.28b}$$

The previous expressions are simply obtained from the total density matrix $\rho = |\Psi\rangle \langle\Psi|$ by inserting the Schmidt decomposition (2.25) and tracing out the environment or the system, respectively. The latter result is consistent with the result from the optimization of the wave function, see Sect. 2.1.2.1. The weights $\{\sqrt{w_\alpha}\}$ of the decomposition are given by the square roots of the eigenvalues $\{w_\alpha\}$ of the reduced density matrix. The basis is formed by the eigenstates of the system and environment block, respectively. In addition, the Schmidt decomposition implies that the eigenvalues of the system and the environment block are identical even if both blocks are different. Their number is given by the rank r, which corresponds to the dimension of the smaller block.

The entanglement is measured by the VON NEUMANN ENTROPY

$$\begin{aligned} S_\mathrm{N} &= -\operatorname{Tr} \rho \ln \rho \\ &= -\sum_{\alpha=1}^{r} w_\alpha \ln w_\alpha. \end{aligned} \tag{2.29}$$

As before, we assume that the eigenvalues w_α are ordered with decreasing magnitude $w_1 \geq w_2 \geq \ldots \geq w_r$. The expression $-x \ln x$ in the von Neumann entropy (2.29) is a monotonically growing function for $0 < x \leq 1/\mathrm{e}$, where the upper limit $1/\mathrm{e}$ is much larger than

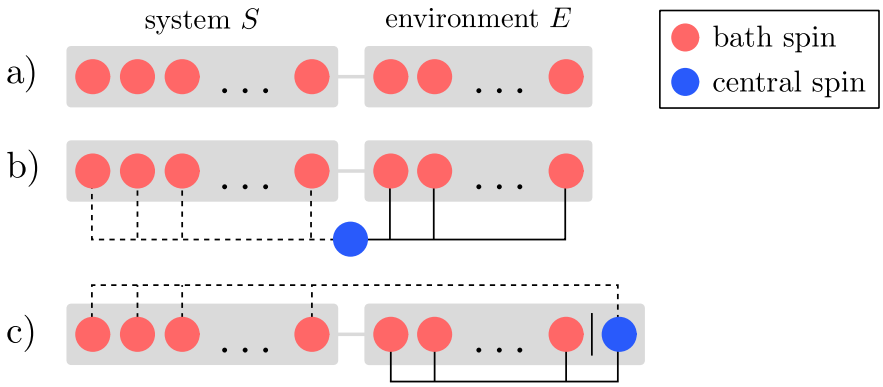

Fig. 2.3: DMRG setup for a cluster of spins linked by a central spin. Panel a): Separation of the bath spins into system and environment block. Panel b): The central site has been added. The dashed and solid lines mark the interaction between the central spin and the system and the environment block, respectively. Panel c): Integration of the central site into the environment block to circumvent a separate bookkeeping of the central site states.

the typically discarded weights. Consequently, a maximum of the entanglement between system and environment block is conserved if the eigenstates with the largest weight in the reduced density matrix of the system block are kept.

Rigorously, the arguments given above are only valid for truncated state vectors which are unnormalized. Due to the truncation, the normalization of the state vector deviates from unity. A renormalization affects the eigenvalues w_α and thus the von Neumann entropy S_N. Hence, the truncated and normalized state might not maximize the entanglement anymore. Luckily, this feature is rather theoretical and usually does not influence the spectra of density matrices occurring in practice: The discarded weight in each step is very small and thus is the effect of the renormalization.

2.2 Adaption of DMRG for the central spin model

Before we introduce the two fundamental DMRG algorithms, namely the infinite and finite size algorithm, we present how DMRG can be adapted for clusters of spins appearing in the central spin model. In contrast to the treatment of one-dimensional structures such as chains, this is no standard application. The implementation of a cluster leads to some slight modifications of the standard DMRG algorithm [Whi92, Whi93]. Precisely, a one-site DMRG [Whi05] is used where only one site is added to the system block in every step of the algorithm. In contrast, the size of both the system and the environment block is

extended by one site in every step of the standard two-site DMRG.

First, we neglect the central spin and only consider the bath spins. They can be viewed as a non-interacting chain of spins, which can be split into the DMRG setup of system and environment block, as described in Sect. 2.1 and sketched in panel a) of Fig. 2.3.

Now, we have to add the central spin to the non-interacting bath spins. The key point for the success of the algorithm lies in the exact treatment of the central spin so that the DMRG only needs to optimize the representation of the bath spins. By keeping the central spin separate from the bath spins, its operators and thus the interaction with the surrounding bath spins is treated exactly. The separated central spin and its interaction with the bath spins is illustrated in panel b) of Fig. 2.3. Hence, the state vector of the superblock (2.1) can now be written as

$$|\Psi\rangle = \sum_{i,j,\sigma_0} \Psi_{ij}^{\sigma_0} |i\rangle |j\rangle |\sigma_0\rangle , \tag{2.30}$$

which corresponds to a representation with three basis sets: System block, environment block, and the central spin. In this notation, the Hamiltonian H_S of the system block as well as the Hamiltonian H_E are both always zero or contain only local contributions, for example from external fields applied to the bath spins. The interaction between central spin and bath is only established when the action of the superblock Hamiltonian onto the superblock state vector is required.

The employment of three basis sets is rather unhandy. To circumvent the bookkeeping for the central site state, it is convenient to integrate the central site into the environment as shown in panel c) of Fig. 2.3. Then, the state of the superblock is given as

$$|\Psi\rangle = \sum_{i,\bar{j}} \Psi_{i\bar{j}} |i\rangle |\bar{j}\rangle \tag{2.31}$$

where $|\bar{j}\rangle = |j\rangle \otimes |\sigma_0\rangle$ is the basis of the environment including the central site and $(\Psi_{i\bar{j}})$ a $d_S \times 2d_E$ matrix containing the coefficients. The new quantum numbers $\bar{j}$ are obtained from the extension of the environment basis with the two basis states $|\uparrow\rangle$ and $|\downarrow\rangle$ of the central site. In this approach, the interactions in H_E are established when the central site is added to the environment block. The system block Hamiltonian is still always zero, despite possible local contributions.

For the buildup of the superblock, one starts with a system and environment block of the same size which contain an exactly tractable number of spins. The number of bath spins in the environment block is fixed, while two sites have to be added to the blocks in each step

of the algorithm: A bath spin to the system block and the central spin to the environment block. For convenience, old system blocks should be reused as environment blocks, for example the exact block from the initial preparation during the buildup of the superblock. These are already the basics of the infinite size algorithm, which is introduced in the next section.

The truncation with respect to the reduced density matrix only affects the basis of the system block. Thus, the basis of the central spin is never truncated and always stored exactly. This particular setup respects the special role of the central spin because it is linked to all other spins in the model. If the basis of the central spin was truncated as well, the complete interaction in the model would only be treated approximately. At this point, it also becomes clear why we choose a one-site algorithm. In each step, one already has to treat two sites exactly, namely one bath site and the central site. In an implementation of the standard two-site DMRG algorithm for clusters, three sites would have to be treated exactly [Fri06]. This would result in an additional doubling of the Hilbert space and consequently to a noticeable increase of the run-time.

In the next two sections, the essential algorithms for the static DMRG are introduced. For an existing DMRG code, the implementation of the algorithms for clusters requires only a small amount of changes. Readers who are familiar with DMRG should be able to adapt an existing code or write a new one without great effort. Compared to a standard DMRG implementation for a one-dimensional system, for example a chain, the changes mainly affect the way how a bath or the central spin is added to a block.

2.2.1 Infinite size algorithm

In this section, we introduce the infinite size algorithm which is used for the buildup of the superblock. The description given below has been adapted for the central spin model. For the original algorithm, we refer to Refs. [Whi92, Whi93].

We assume that the couplings are given in descending order, which is already fulfilled by the distribution presented in Eq. (1.8). The algorithm starts with an exact representation of the system and environment block which both consist of l_0 bath spins so that the initial superblock contains $2l_0$ bath spins in total. Here, the number of kept states is chosen to be $m \equiv 2^{l_0}$ which is in accordance with the number of states of the exact representation of the system block. It is assumed that the system block is initially the left block, while the environment is the right one. Hence, the initial system block contains sites $1, 2, \ldots l_0$

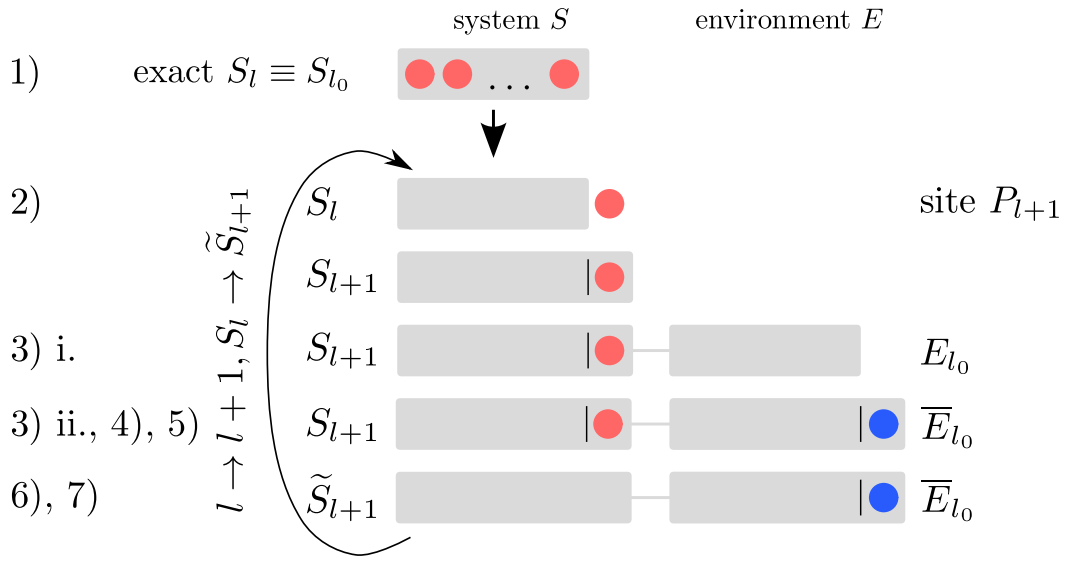

Fig. 2.4: Illustration of the infinite size algorithm as described in the text. Starting from an exact system block S_l, the bath site P_{l+1} is added. The environment block E_{l_0} always contains a fixed number of l_0 bath spins. After the truncation, the system block $\widetilde{S}_{l+1}$ is represented by m basis states. The procedure is repeated until all bath spins have been added.

with the largest coupling constants $J_1, J_2, \ldots, J_{l_0}$, while the environment block contains sites $(l_0+1), \ldots, 2l_0$ with the adjacent coupling constants $J_{l_0+1}, \ldots, J_{2l_0}$. During the buildup process, the system block grows by one site in each step and the size of the environment is kept constant. But the environment block changes in the sense that it always contains the l_0 sites with the l_0 next coupling constants. In practice, decreasing order of the coupling constants has proven to work quite well for our model. Thereby, DMRG optimizes the system block basis for the strongly coupled sites from the beginning on. This is important because the sites with largest couplings to the central site dominate the properties of the model, for example the short-time behavior.

We stick to the following notation. The index l denotes the number of spins in the system block S_l or in the environment block E_l, respectively. An environment block containing the central spin is labeled by $\overline{E}_l$. Where necessary, we use $\widetilde{S}_l$ to explicitly denote a system block with truncated basis. The symbol P_l stands for a single spin with index l. The matrix representation of all observables $\widehat{O}$ in the system block S_l is denoted by $\mathbf{O}_l$. Starting from an exactly represented system block S_{l_0}, the infinite size algorithm reads as follows:

1) Start with an exact representation of the system block $S_l \equiv S_{l_0}$ containing the bath spins with indices 1 to l_0.

2) Add site $l+1$ to the system block S_l. Update its basis and all operators in the block.

3) Representation of the environment block E_{l_0}:

   i. Create an exact environment block E_{l_0} containing the bath spins with indices $(l+2)$ to $(l+l_0+1)$.

   ii. Add central spin to the environment block. Update its basis and all corresponding operators.

4) Calculate all desired target states, for example the ground state.

5) Perform measurements, for example the ground state energy or the magnetization.

6) Basis optimization of the system block:

   i. Use target states to set up the reduced density matrix ρ (2.3) of the system block and diagonalize it.

   ii. Choose the m eigenstates with largest weight in the reduced density matrix. Truncate the basis of the system block and all corresponding operators via

$$\widetilde{\mathbf{\Psi}}_{l+1} = \mathbf{U}\mathbf{\Psi}_{\mathbf{l+1}}\mathbf{U}^{\dagger} \tag{2.32a}$$

$$\widetilde{\mathbf{O}}_{l+1} = \mathbf{U}\mathbf{O}_{\mathbf{l+1}}\mathbf{U}^{\dagger} \tag{2.32b}$$

   where the transformation $\mathbf{U}$ contains the largest m eigenvectors as columns.

7) Continue at step 2) replacing $l \to l+1$ and $S_l \to \widetilde{S}_{l+1}$ until all N bath spins have been added to the superblock.

There are two strategies for the calculation of the target states. First, the target state can be constructed from a tensor product of the local states of all spins. For example, the (random) initial state of every bath site can be parameterized on the Bloch sphere. When the site P_{l+1} is added to the system block, its state has to be added to the state vector by calculating the tensor product between the state of the system block S_l and the state of the single site P_{l+1}.

Second, one can calculate the target state as the ground state of a specific Hamiltonian. This corresponds to the standard application of DMRG for determining the ground state properties of a model. But note that the Hamiltonian for the initialization does not have to be the actual Hamiltonian of the model. For example, one can apply the simple Hamiltonian $H = -\sum_{i=0}^{N} h_i S_i^z$ with $|h_i| \gg 1$ [GKSS05]. In the corresponding ground state, each spin is in a completely polarized state according to the sign of h_i. If possible, we usually employ the first approach based on the tensor product of the local states to avoid the costly calculation of the ground state.

The ground state may be calculated by the well-known Lanczos algorithm [Lan50]. This iterative algorithm requires a repetitive calculation, typically $\mathcal{O}(100)$, of the action of the superblock Hamiltonian H_{SB}

$$H_{\mathrm{SB}} = H_S \otimes \mathbb{1}_{\overline{E}} + \mathbb{1}_S \otimes H_{\overline{E}} + \sum_{i \in S} J_i \vec{S}_{i,S} \otimes \vec{S}_{0,\overline{E}} \tag{2.33}$$

on the state $|\Psi\rangle$, which is the numerically most costly operation. Here, H_S is the Hamiltonian of the system block consisting of only local contributions, while the Hamiltonian $H_{\overline{E}}$ contains already the interaction between central spin and bath spins from the environment block. The sum in Eq. (2.33) involves all links between central spin and bath spins from the system block. In general, the Hamiltonian H_{SB} should never be stored due to its enormous size. Instead, one directly evaluates the action of the superblock Hamiltonian by the relation [PKWH99, Chapter 2]

$$\begin{aligned}(H_{SB}\mathbf{\Psi})_{ij} &= \sum_{i',j'} (H_{SB})_{ij;i'j'}\, \mathbf{\Psi}_{i',j'} \\ &= \sum_{\lambda} \sum_{i'} O^{S,\lambda}_{ii'} \sum_{j'} O^{\overline{E},\lambda}_{jj'} \mathbf{\Psi}_{i',j'}.\end{aligned} \tag{2.34}$$

In the last step, the representation

$$(H_{SB})_{ij;i'j'} = \sum_{\lambda} O^{S,\lambda}_{ii'} O^{\overline{E},\lambda}_{jj'} \tag{2.35}$$

of the superblock Hamiltonian is inserted. The sum runs over all pairs of operators $\mathbf{O}^{S,\lambda}$ and $\mathbf{O}^{\overline{E},\lambda}$ forming the superblock Hamiltonian H_{SB} (2.33). The operator $\mathbf{O}^{S,\lambda}$ denotes the operator from the system block, while $\mathbf{O}^{\overline{E},\lambda}$ stands for the corresponding operator from the environment block. The direct evaluation of the action decreases the numerical effort by one order of magnitude to $\mathcal{O}(m^3)$. A naive application of H_{SB} onto the state vector would imply an effort of $\mathcal{O}(m^4)$ because the dimension of the superblock Hamiltonian is quadratic in the number of states m. In practice, the numerical effort can even be reduced below $\mathcal{O}(m^3)$ if the symmetries of the model under study are exploited.

In the central spin model as defined in Eqs. (1.4) and (1.6), the total magnetization $\sum_{i=0}^{N} S_i^z$ is always conserved. Hence, it is a good quantum number and can be used to index the basis of the blocks. Then, the state vector and all operators take the form of block matrices. Most blocks are empty so they do not have to be stored, while the non-empty blocks are represented by dense matrices. All matrix-matrix and matrix-vector multiplications require an additional loop over the good quantum number. As the good quantum is conserved and many blocks are zero, the multiplication of very large matrices is reduced to multiple multiplications of matrices with a much smaller dimension. This induces a noticeable increase of the performance.

The infinite size algorithm is a tool for the buildup of the superblock. But it suffers from several problems [NM05, Sch05a]. Its original purpose is to obtain the properties of the model in the thermodynamic limit $N \to \infty$. Thus, the obtained quantities yield only an approximation for finite system sizes. Furthermore, the targeted state vector corresponds to a different number of spins in each step which may lead to convergence problems. This effect is crucial when the state vector changes qualitatively with growing superblock size. With respect to the central spin model, the magnetization of the state varies from step to step. In addition, the small environment blocks in the first steps of the algorithm are in general no good representation for the final setup of the superblock. Depending on the actual system under study, additional problems may occur which lead to severe failures of the infinite size algorithm. Thus, we proceed to the finite size algorithm in the next section.

2.2.2 Finite size algorithm

The problems occurring in the infinite size algorithm are repaired by the so-called *finite size algorithm* [Whi93]. After the initialization with the infinite size algorithm, the size of the superblock formed by the system block S_l and by the environment block $E_{l'}$ is kept constant at $N = l + l'$. Then, the border between the system and environment block is moved through the superblock. This procedure is called a *sweep*. A complete sweep consists of two sub procedures: A *forward sweep* and a *backward sweep*. A forward sweep corresponds to a sweep from left to right, where a bath site is successively extracted from the environment block on the right and integrated into the system block on the left until the maximum size of the system block is reached. Then, the role of system and environment are reversed meaning that the former system block of maximal size, the left block, becomes the new environment block of maximal size and vice versa. Now, the system block grows from right to left until it has reached its maximum size. Such a sweep from right to left is called a backward sweep. As before, the roles of system and environment block are interchanged if the system block has reached its maximum size. After that, one continues with a new forward sweep where the system block grows again from left to right. One single sweep is completed after one has arrived at the initial configuration of system and environment block. An illustration of the sweeping procedure is shown in Fig. 2.5. There, a backward sweep is performed in step 2) and a forward sweep is performed in step 3). This concept corresponds to a variational optimization of the wave function for a fixed number of spins in the superblock. The variational concept of DMRG is fully revealed in the framework of matrix product states [Sch11].

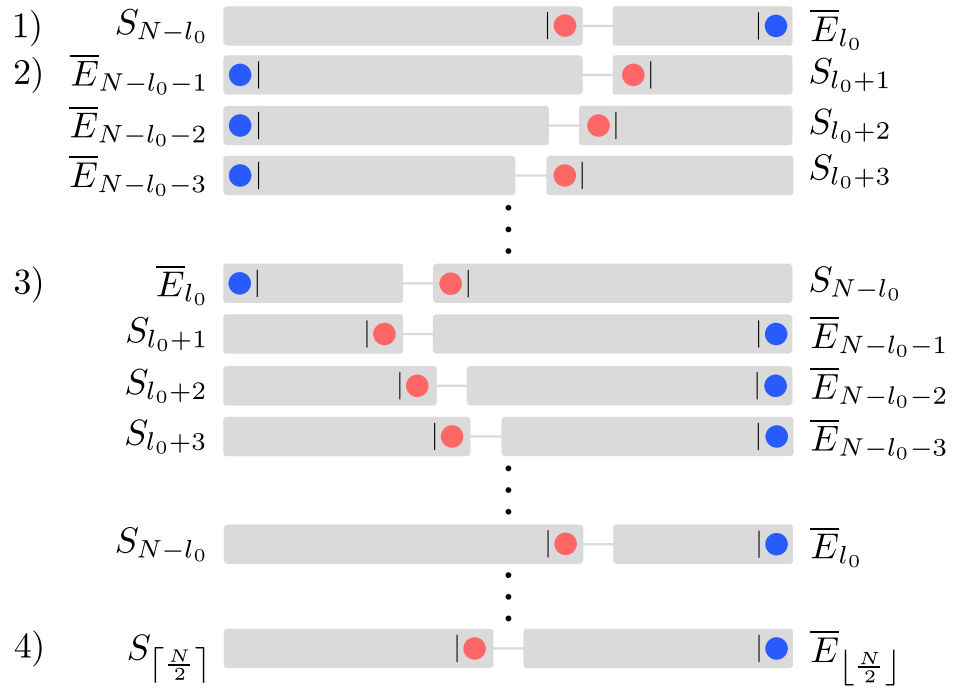

Fig. 2.5: Illustration of forward and backward sweeps in the finite size algorithm. The sweeping procedure starts with a system block S_{N-l_0} of maximum size and an environment block $_{l_0}$ of minimum size, obtained by running the infinite size algorithm, see Fig. 2.4. For clarity, only the configurations of the blocks are shown. This figure does not depict the intermediate steps involving the basis extension, truncation, and so on. After completion, both blocks should contain the same number of bath sites.

In total, the finite size algorithm is carried out as follows:

1) Run the infinite size algorithm (Sect. 2.2.1) to obtain a complete representation of the superblock containing all N bath spins. The system block S_{N-l_0} is left and contains $(N-l_0)$ bath spins, while the environment block $\overline{E}_{l_0}$ is right and consists of l_0 bath spins and the central spin.

2) Backward sweep (half-sweep from right to left):

   i. Swap the roles of system and environment block. The system block S_{l_0} is now the minimal block on the right.

   ii. Add bath site P_{N-l_0} to the system block S_{l_0}.

   iii. Reuse an old system block for the new environment block E_{N-l_0-1} on the left. The size of the superblock $N-l_0-1+1+l_0=N$ is constant.

   iv. Add the central site to the left block E_{N-l_0-1}.

   v. Transform the state $|\Psi\rangle$ to the new basis (see below).

vi. Calculate the desired target states and optimize the basis of the system block via the reduced density matrix by tracing out the left block, as described for the infinite size algorithm.

vii. Unless the system block on the right has reached its maximum size $N - l_0$, replace $l_0 \to l_0 + 1$ and repeat from step 2) ii. Otherwise, proceed to step 3).

3) Forward sweep (half-sweep from left to right):

i. Swap the roles of system and environment block. The system block S_{l_0} is now the minimal block on the left.

ii. Add bath site P_{l_0+1} to the system block S_{l_0}.

iii. Reuse an old system block for the new environment block E_{N-l_0-1} on the right.

iv. Add the central site to the right block E_{N-l_0}.

v. Transform the state $|\Psi\rangle$ to the new basis.

vi. Calculate the desired target states and optimize the basis of the system block.

vii. Unless the system block on the right has reached its maximum size $N - l_0$, replace $l_0 \to l_0 + 1$ and repeat from step 3) ii. Otherwise, proceed with step 4).

4) Repeat from 2) until the desired expectation values have converged. As convergence criterion, one may consider the quantitative change of the observables with respect to the result of the previous sweep. If the absolute distance falls below a predefined threshold ε, the algorithm will be stopped. The last forward sweep is often not completed. Usually, the sweep stops in the middle where system and environment block have the same size and the entanglement of the two blocks acquires its maximum.

Convergence by sweeping through the system is usually reached within a few sweeps. Then, the calculated properties are obtained with very high accuracy. Old system blocks serve as environment blocks during the sweeps. Thus, it is necessary to store the optimized system blocks from the infinite size algorithm. If a block is reused as environment block, only the central site has to be added. Environment blocks are not stored, because we want to have an exact representation of the central site in each step.

For an optimal calculation of the target state, it is recommended to transform the target obtained in the previous step to the new basis [Whi96]. Thereby, the numerical effort is strongly reduced compared to a completely new calculation of the target state. A transformed target vector used as initial state for the Lanczos algorithm reduces the number of iterations to a handful compared to $\mathcal{O}(100)$ for a randomly created initial state. An example for the specific transformation applied during a forward sweep is presented in

N	J_{xy} [J_q]	J_z [J_q]	h_0 [J_q]	E_0 [J_q]	# states m
30	Gaussian		0	-3.537167747803	1024
				-3.537167747803	256
				-3.537167747803	Bethe ansatz (exact)
30	Gaussian		1	-3.990963281904	1024
				-3.990963281904	256
				-3.990963281904	Bethe ansatz (exact)
100	0.25	1	0.5	-25.374689052802	256
				-25.374689052802	exact
100	0.5	1	1	-25.990289431162	256
				-25.990289431162	exact
100	1	1	1	-50.753093964628	256
				-50.753093964628	exact

Tab. 2.1: Ground state energies of the homogeneous and inhomogeneous central spin model (2.36) for selected parameters and coupling constants. The comparison with the exact [Sch08] and Bethe ansatz results [Bor07] reveals a remarkable agreement. Note that the employment of the Bethe ansatz is not required for the ground state energies of the homogeneous model.

Appendix A. Therefrom, the transformations required for the backward sweep and for the commutation of the blocks can easily be deduced. Note that all transformations involve a truncation of the system block basis. Hence, they are only exact up to the discarded weight.

To demonstrate the capability of the finite size algorithm, we calculated the ground state energies E_0 of the anisotropic central spin model

$$H = \sum_{i=1}^{N} \left\{ J_{z,i} S_0^z S_i^z + \frac{J_{xy,i}}{2} \left(S_0^+ S_i^- + \mathrm{h.c.} \right) \right\} - h_0 S_0^z \tag{2.36}$$

for different sets of parameters and coupling constants. For the inhomogeneous model, the isotropic coupling constants have a Gaussian decay [BS07a]

$$J_i = \mathrm{e}^{-\frac{4i^2}{N^2}} J_\mathrm{q}. \tag{2.37}$$

The results shown in Tab. 2.1 are in remarkable agreement with the exact [Sch08] and Bethe ansatz results [Bor07], even for a small number m of kept states. The very high

accuracy of the DMRG results serves as a first verification of our DMRG implementation. It indicates the potential lying in the numerical investigation of the central spin model in the framework of DMRG.

2.3 DMRG at infinite temperature

For studying the decoherence in the central spin model, one has to calculate the real-time evolution of an observable $\widehat{O}$

$$\langle \widehat{O}\,(t)\rangle = \frac{1}{Z}\,\mathrm{Tr}\left(\widehat{O}\,(t)\,\mathrm{e}^{-\beta H}\right) \tag{2.38a}$$

or its autocorrelation function

$$\langle \widehat{O}\,(t)\,\widehat{O}\,(0)\rangle = \frac{1}{Z}\,\mathrm{Tr}\left(\widehat{O}\,(t)\,\widehat{O}\,(0)\,\mathrm{e}^{-\beta H}\right). \tag{2.38b}$$

Here, the canonical ensemble with the partition function Z is used to evaluate the expectation values at a finite temperature $\beta = (k_B T)^{-1}$. In the central spin model, the observable $\widehat{O}$ stands either for the operators S_0^α of the central spin or for the operators A^α (1.5a) of the Overhauser field, where $\alpha \in \{x, y, z\}$. Before we proceed with the calculation of the real-time evolution in the framework of DMRG, we discuss an appropriate choice for the initial state. Without loss of generalization, the time dependence of the observables can be neglected for the discussion presented in this section. Thus, we focus on the expectation values and autocorrelation functions at $t = 0$.

The energy scale of a typical self-assembled quantum dot is usually of the order of 10^{-5} eV [MER02, SKL03]. Experiments are usually performed at temperatures $T = 6$-50 K corresponding to thermal energies $k_\mathrm{B}T \approx 10^{-4}$-$10^{-3}$ eV [HGB$^+$08, GES$^+$09]. Thus, the energy scale of the thermal fluctuations is at least one order of magnitude larger than the intrinsic energy scale of the dot. This implies that the temperatures occurring in experiment are equal to infinite temperature where the spins are completely unpolarized. Thereby, a significant simplification of Eqs. (2.38) is achieved. The partition function reduces to the number of basis states $Z = 2^{N+1}$ which are all equiprobable because $\mathrm{e}^{-\beta H} \to 1$ for $\beta \to 0$. Consequently, the expectation value of an observable reduces to its mean value with respect to all possible basis states $\{|k\rangle\}$

$$\langle \widehat{O}\rangle = \frac{1}{2^{N+1}} \sum_{k=0}^{2^{N+1}} \langle k|\widehat{O}|k\rangle\,. \tag{2.39}$$

As the size of the Hilbert space grows exponentially with the number of spins, a direct evaluation of the corresponding traces is out of question. In the following, a strategy to calculate the trace in Eq. (2.39) as accurately as possible is developed.

2.3.1 Random initial states

A simple approach to this problem is to calculate the expectation values for only a small number $M \ll 2^{N+1}$ of randomly chosen basis states. Then, the result for the trace (2.39) is approximated by the average

$$\langle \widehat{O} \rangle \approx \frac{1}{M} \sum_{k=1}^{M} \langle k|\widehat{O}|k\rangle \,. \tag{2.40}$$

over all M randomly chosen basis states $\{|k\rangle\}$. This method has proven to perform very well in the framework of exact diagonalization and for the Chebychev expansion [SR94, WWAF06]. But for a fast and reliable convergence it is required to use arbitrary superpositions of basis states as initial state. Such states do not have a fixed quantum number such as the total magnetization.

However, for an optimal DMRG calculation it is advisable to use initial states with a well-defined quantum number. Only in this case the conservation of the total magnetization, which is implemented in our code, can be exploited optimally leading to a significant increase of the performance of the algorithm. Thus, we accomplish the sampling for simple product states as initial states. But a few hundred of them will be required to yield reliable results for the trace in Eq. (2.39) because of the $1/\sqrt{M}$-dependence of the standard deviation. For arbitrarily superposed states employed in exact diagonalization, a handful is usually sufficient. In our implementation, a random initial state is a tensor product of single-site spin states generated randomly on the Bloch sphere. This is realized in step 5) of the infinite size algorithm (see Sect. 2.2.1) and replaces other routines normally used for the calculation of the superblock state vector, for example the Lanczos algorithm. No additional changes are required in the other steps of the infinite size or in the finite size algorithm.

In Fig. 2.6, we anticipate some results for the autocorrelation function $\langle S_0^z(t) S_0^z(0)\rangle$ of the central spin for different numbers of bath spins. All curves were obtained by sampling over a finite number M of random initial states, see caption for details. Note that the plot is solely used for demonstrating the disadvantages of random initial states. A detailed discussion of the curves is given in Sect. 2.7.1. All curves feature several crossings and lack of a systematic scaling with the bath size N. This indicates that the number M of sampled

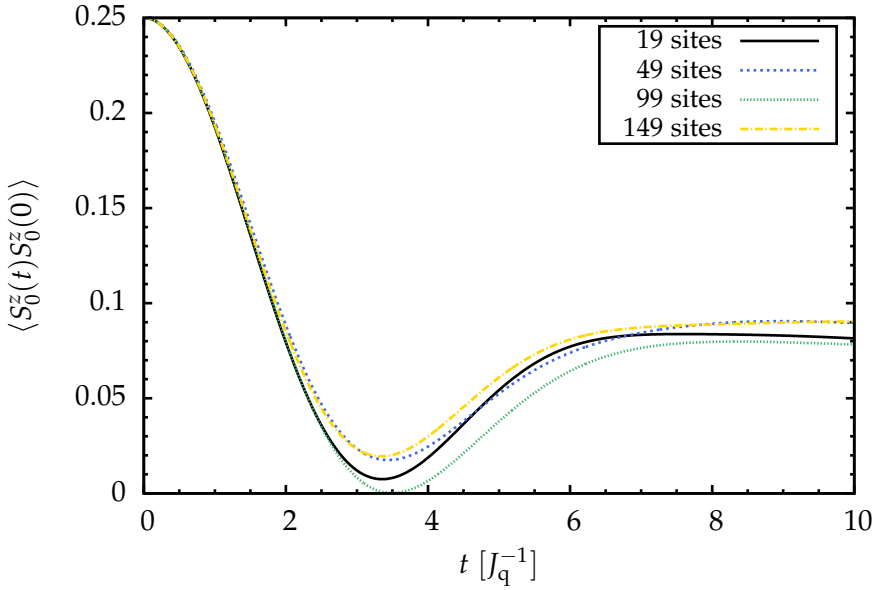

Fig. 2.6: Autocorrelation function $\langle S_0^z(t)S_0^z(0)\rangle$ of the central spin obtained by sampling over random initial states (2.40). In the calculation for $N = 19$ bath spins, $M = 100$ random initial states entered while all other results were obtained from $M = 50$ random initial states. Here, $m = 512$ states were used for the DMRG runs.

random initial states is not sufficient, although a fairly large number of $M = 50$-100 initial states already entered in the calculations. Hence, systematic extrapolations in the system size are hardly possible because of the insufficient precision related to the sampling of a finite number of states. As a consequence, we refrain from discussing random initial states any further and stick to purified states for all future calculations of the trace at infinite temperature.

2.3.2 Purification

Alternatively, we can pursue a route which allows us to calculate the expectation values at $T = \infty$ exactly. This approach is known in the literature under the key word *purification* [BEU00, NC10, KBM12, SRU13]. By introducing an *auxiliary* spin to each *real* spin, the size of the system is artificially doubled.

The DMRG setup for the central spin model with purified bath spins is sketched in the upper panel of Fig. 2.7. The auxiliary spins (circles) are integrated into the bath. The real spins (dots) always have odd indices, while the auxiliary ones are always indexed by even numbers. The setup in the lower panel includes a purified central spin. In general, the purification of the central spin is optional for the model discussed in this thesis, see below. For the following derivation, we assume that only the bath spins have an auxiliary spin.

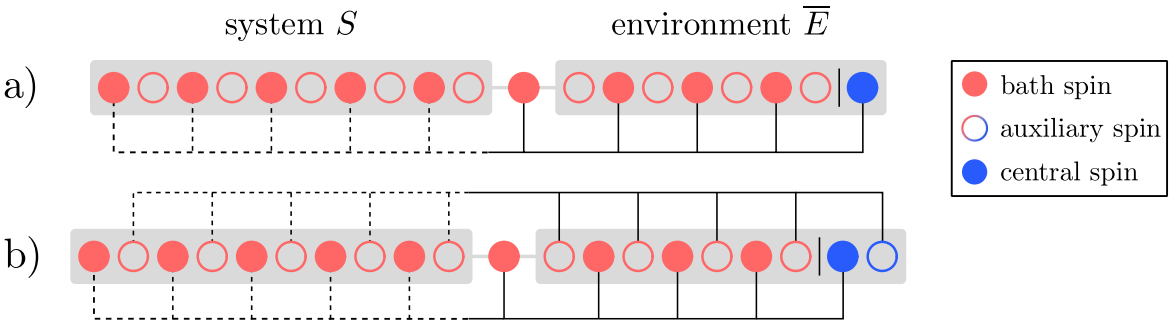

Fig. 2.7: DMRG setup of the central spin model for a purified system. The dashed and solid lines mark the interaction between the central spin and the system and the environment block, respectively. In the lower panel, the central spin is purified as well. Like the real central spin, the auxiliary central spin is integrated into the environment block to avoid an additional loop over its subspace.

At $t = 0$, each real bath spin is prepared in a singlet state with its corresponding auxiliary spin. The initial state $|S\rangle$ of the bath is given by the tensor product

$$|S\rangle := \bigotimes_{i=1}^{N} \frac{1}{\sqrt{2}} \left(|\uparrow_{\mathrm{r}} \downarrow_{\mathrm{a}}\rangle - |\downarrow_{\mathrm{r}} \uparrow_{\mathrm{a}}\rangle \right)_i , \tag{2.41}$$

where r stands for the real spin and a for the auxiliary spin, respectively. The factor $1/\sqrt{2}$ is included for the normalization of each singlet. Then, the total initial state of bath and central spin

$$|\Psi_\alpha(0)\rangle = |S\rangle \otimes |\alpha\rangle_0 , \quad \alpha \in \{\uparrow, \downarrow\} \tag{2.42}$$

is the product state of $|S\rangle$ and the state of the central spin which can be $|\uparrow\rangle$ or $|\downarrow\rangle$. The auxiliary sites serve as a tool to enable a very elegant way of calculating the trace in Eq. (2.39) at infinite temperature. Hence, they must not affect the physics of the model which is achieved by restricting all operators to real spins

$$\widehat{O} \longrightarrow \widehat{O}_{\mathrm{r}} \otimes \mathbb{1}_{\mathrm{a}}. \tag{2.43}$$

The key observation is that the trace of an observable in the space of the real spins is reduced to a simple expectation value in the extended Hilbert space of the real and auxiliary spins [BEU00]

$$\mathrm{Tr}\, \widehat{O}(t)\Big|_{\mathrm{r}} = \frac{\langle \Psi_\uparrow(t)| \widehat{O} |\Psi_\uparrow(t)\rangle + \langle \Psi_\downarrow(t)| \widehat{O} |\Psi_\downarrow(t)\rangle}{2}\Bigg|_{\mathrm{r}\otimes\mathrm{a}} , \tag{2.44}$$

which is taken with respect to the purified initial state from Eq. (2.42). We stress that the

latter expression allows for an exact calculation of the trace with only two independent runs of the DMRG code, one for each state of the central spin. If the central spin would be purified as well, the result would be yield within a single run.

Without any external field, the central spin model in Eq. (1.4) is isotropic and symmetric under a spin flip of the central spin. Thus, a purification of the central spin is not necessary and it is sufficient to consider only one initial state where the central spin at $t = 0$ points either up or down because of the spin-flip symmetry. If the spin-flip symmetry is broken by an external magnetic field, one has to run two independent calculations for both states of the central spin. The total trace is simply given as the mean value of two independent results. Compared to a calculation with a purified central spin, the dimension of the Hilbert space is kept smaller by a factor of two resulting in a decrease of the discarded weight and an overall better performance, see Sect. 2.5.3. However, a purified central spin gives access to conceptual extensions of DMRG. Hence, we come back to this concept for the discussion of the Chebychev polynomials in Sect. 2.4.4.

Although a purified initial state (2.42) implies an additional doubling in the number of bath spins, it should be preferred to the random initial state (2.40) because it enables an exact calculation of the trace. Of course, the purification reduces the number of treatable bath spins by a factor of two. But in the progress of our studies, it turned out that this negative effect is negligible and that the advantages dominate clearly. Furthermore, purification requires at most two independent runs of the DMRG code. For random initial states, the number of runs corresponds to the number of states, which is usually $\mathcal{O}(100)$. With respect to superposed states, the purified initial state (2.42) has a well-defined quantum number. Hence, it is particularly suitable for the DMRG.

Concerning the implementation of a purified initial state, the infinite size algorithm from Sect. 2.2.1 has to be slightly modified. The state vector is constructed as a tensor product of spin singlet states. Since a singlet is a highly entangled state, it cannot be written in the form of product state of two single-spin states. Thus, the system block always grows by two spins during the buildup with the infinite size algorithm. First, the real bath spin is added to the system block, followed directly by the corresponding auxiliary spin. Then, the singlet state is added to the state vector. Before one proceeds with the next pair of spins, the basis of the system block is optimized as usual. No changes have to be made to the finite size algorithm. A special treatment of the auxiliary bath spins is not required during the sweeps because they are integrated into the blocks and alternate with the real sites. If the central site is purified, the transformation of the state vector has to be extended.

The purified initial state (2.42) represents a completely disordered state at infinite temperature. Finite temperatures are reachable by cooling the state which is realized by a time evolution in imaginary time [BSW09]. For the physics under study we do not pursue this option. But this fact underlines the great potential of purified states.

2.4 Real-time evolution with DMRG

In this section, three different extensions of DMRG for the calculation of the real-time evolution are introduced. The first two approaches, based on the Trotter-Suzuki decomposition [WF04] and Krylov vectors [FW05, NM05, MMN05], are applicable to arbitrary initial states. The third ansatz is based on the Chebychev expansion [TEK84], where we exploit explicitly the properties of a purified state.

2.4.1 Autocorrelation functions

As mentioned before, time-dependent observables and autocorrelation functions are the quantities of interest for the investigation of decoherence. Whereas the calculation of single-operator expectation values is straightforward in the framework of DMRG, the calculation of an autocorrelation function is more complex. The capability of DMRG to handle multiple target states (see Sect. 2.1.2.1) has to be exploited [WF04].

By rewriting the autocorrelation function (2.38b) in the Schrödinger picture used for the real-time evolution with DMRG, one obtains

$$\begin{aligned}\langle \widehat{O}(t)\,\widehat{O}(0)\rangle &= \langle\Psi|\,\mathrm{e}^{\mathrm{i}Ht}\,\widehat{O}\,\mathrm{e}^{-\mathrm{i}Ht}\,\widehat{O}|\Psi\rangle \\ &= \langle\Psi|\,\mathrm{e}^{\mathrm{i}Ht}\,\widehat{O}\,\mathrm{e}^{-\mathrm{i}Ht}\,|\Phi\rangle \\ &= \langle\Psi(t)\,|\widehat{O}|\Phi(t)\rangle\,. \end{aligned} \tag{2.45}$$

Hence, the real-time evolution of the state $|\Phi\rangle = \widehat{O}\,|\Psi\rangle$ has to be calculated in addition to the time evolution of the initial state $|\Psi\rangle$. Both state vectors are taken as target states in the reduced density matrix of the system block (2.20) with same weight $W_k = 1/2$.

In practice, one first runs the infinite size algorithm to generate the initial state $|\Psi\rangle$. Before starting the time evolution, the second target state is created by applying the operator $\widehat{O}$ to the initial state $|\Psi\rangle$. For operators acting on the central spin only, this can be done for an

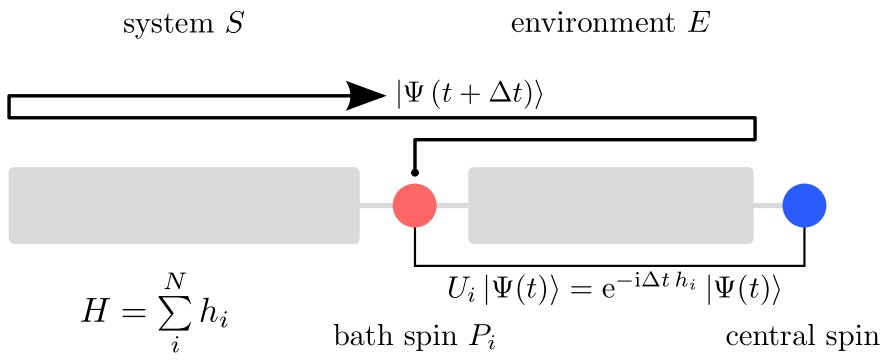

Fig. 2.8: Adaptive time-dependent DMRG involving the Trotter-Suzuki decomposition of the time-evolution operator U. The local time-evolution operators U_i are applied successively during a complete forward and backward sweep.

arbitrary configuration of the superblock because the central spin is always treated exactly. If the operator $\widehat{O}$ acts on a bath spin, it has to be applied when the corresponding site is added to the system block. Then, the operator is represented exactly. Operators acting on multiple sites such as A^α (1.5a) should be applied successively during a complete forward or backward sweep.

2.4.2 Trotter-Suzuki decomposition

The adaptive method based on a Trotter-Suzuki (TS) decomposition of the time-evolution operator was among the first methods for calculating the real-time evolution in the framework of DMRG [DKSV04, WF04]. It is applicable if the Hamiltonian H is decomposable into local parts

$$H = \sum_{i=1}^{N} h_i\,, \tag{2.46}$$

where in our model the local Hamiltonian h_i contains the interaction between bath spin i and the central spin. Then, the TS decomposition is used to split the time-evolution operator

$$U := U\,(t, t+\Delta t) = \mathrm{e}^{-\mathrm{i}H\Delta t} \tag{2.47}$$

into local parts. In second order, one obtains [WF04]

$$U = \mathrm{e}^{-\mathrm{i}h_1\frac{\Delta t}{2}}\,\mathrm{e}^{-\mathrm{i}h_2\frac{\Delta t}{2}}\ldots\mathrm{e}^{-\mathrm{i}h_{N-1}\frac{\Delta t}{2}}\,\mathrm{e}^{-\mathrm{i}h_N\Delta t}\,\mathrm{e}^{-\mathrm{i}h_{N-1}\frac{\Delta t}{2}}\ldots\mathrm{e}^{-\mathrm{i}h_2\frac{\Delta t}{2}}\,\mathrm{e}^{-\mathrm{i}h_1\frac{\Delta t}{2}} + \mathcal{O}\left(\Delta t^3\right). \tag{2.48}$$

Thereby, all local time-evolution operators are applied successively to their corresponding configuration of bath and central spin during the sweeps through the superblock, see Fig. 2.8. During a complete backward and forward sweep, each bath spin is addressed twice and the local time-evolution operator can be applied to the individual configuration of bath and central spin without any additional error beyond the discarded weight. Hence, the real-time time evolution of one or more states is calculated by running the finite size algorithm (Sect. 2.2.2) and successively applying the local time-evolution operators $U_i = \mathrm{e}^{-\mathrm{i}\, h_i \Delta t}$ to update the target states. As usual, the basis is optimized in each step by truncating with respect to the most important eigenstates of the reduced density matrix. After two complete half-sweeps, the time evolution has proceeded by one interval Δt. The desired quantities are measured and one continues to sweep until the maximum time is reached. Changes have to be made only to the transformations of the state vector described in Appendix A. An additional step is introduced after one has arrived at the expression in Eq. (A.5) where both the central spin and the single bath spin are separated from the superblock. This is represented by four different matrices $\mathbf{\Psi}$, each of them corresponding to one of the four configurations $|\sigma_0 \sigma_i\rangle \in \{|\uparrow\uparrow\rangle, |\uparrow\downarrow\rangle, |\downarrow\uparrow\rangle, |\downarrow\downarrow\rangle\}$ of central spin and bath spin. Before one proceeds with the next step (A.6) of the transformation, these four matrices are replaced by

$$\Psi_{\tilde{m}_l, \tilde{m}_{N-l-1}, \sigma_0, \sigma_i} \longrightarrow U_{i;\sigma_0\sigma_i} \Psi_{\tilde{m}_l, \tilde{m}_{N-l-1}, \sigma_0, \sigma_i} \tag{2.49}$$

to calculate the time evolution of the local configuration. Here, the $U_{i;\sigma_0\sigma_i}$ are the matrix elements of the local time-evolution operator U_i. When an auxiliary site is transformed, U_i corresponds to the identity. Otherwise, the local parts U_i in Eq. (2.49) are 4×4 matrices. They are either known exactly or they can be computed with small numerical effort.

The Trotter-Suzuki decomposition (2.48) is not exact and involves an error in addition to the discarded weight. In second order, the Trotter-Suzuki error is $\sim \Delta t^3$. As the decomposition is applied $t_{\max}/\Delta t$ times, the total error accumulates to $\mathcal{O}(\Delta t^2)$.

Higher orders of the Trotter-Suzuki decomposition reduce this error. The fourth order is derived in Appendix B. Thereby, one step in the real-time evolution is performed with three backward and forward sweeps and the Trotter-Suzuki error is of $\mathcal{O}(\Delta t^5)$. Hence, the error due to the decomposition is decreased upon two orders of magnitude by increasing the run-time by a factor of three. However, it is not always necessary to use higher orders of the decomposition. The Trotter-Suzuki error is almost constant so that it usually dominates the total error only for small times. Generically, the discarded weight is the limiting factor because it accumulates with increasing time. A more detailed discussion of the Trotter-Suzuki error is presented in Sect. 2.6. The interested reader is also referred to Ref. [GKSS05].

2.4.3 Krylov vectors

The approach based on the Trotter-Suzuki decomposition takes advantage of the features of the finite size algorithm in a very elegant way. But its application is restricted to Hamiltonians which can be decomposed according to Eq. (2.46). Furthermore, the Trotter-Suzuki error occurs in addition to the discarded weight.

In this section, we follow a different strategy and discuss the direct application of the time-evolution operator U to the state vector so that a decomposition is not required. As the Hamiltonian of the superblock, the time-evolution operator U cannot be applied directly to the superblock state. Thus, U has to be expanded in a well-defined basis. The idea behind this approach is that first the basis is optimized for the time-interval t and $t + \Delta t$. This is done by targeting several states $|\Psi(t_i)\rangle$ for $t_i \in [t, t + \Delta t]$. Usually, this procedure converges fast and a few half sweeps are sufficient to optimize this basis. Afterwards, the time evolution of the superblock state from t to $t + \Delta t$ is calculated. To reduce the integration error, it is possible to use smaller time steps for the evolution than for the calculation of the target states. In a first approach discussed by Feiguin and White [FW05], a Runge-Kutta integration was used to calculate the target states and the real-time evolution. But they also suggested to employ other methods, for example a Lanczos tridiagonalization of the Hamiltonian. In contrast to the Runge-Kutte integration, this approach preserves unitarity. However, we have to keep in mind that unitarity is always violated by the DMRG truncation of the Hilbert space.

Note that an alternative scheme for calculating the time evolution with DMRG based on Krylov vectors was introduced by Schmitteckert [Sch04]. But instead of optimizing the basis and performing the time evolution in the interval t and $t + \Delta t$ successively as suggested later on by Feiguin and White [FW05], Schmitteckert carried out the complete time evolution in each step of the algorithm.

In the following, we employ Krylov vectors [HL97, HL99, MMN05, NM05, Fri06, SRU13] for the calculation of the target states as well as for the real-time evolution and stick to the basis optimization proposed in Ref. [FW05]. Therefore, the state vector at $t + \Delta t$ is expanded in the basis of the Krylov subspace

$$\left\{ |\Psi(t)\rangle, H|\Psi(t)\rangle, H^2|\Psi(t)\rangle, \ldots, H^{k-1}|\Psi(t)\rangle \right\}. \tag{2.50}$$

An orthogonal basis of this subspace is spanned by the so called Krylov vectors $|v_n\rangle$ which are obtained by orthogonalizing the vectors from Eq. (2.50) via the well-known Lanczos tridiagonalization. The recursion relation is given by

$$|v_0\rangle = |\Psi(t)\rangle \tag{2.51a}$$

$$|v_{n+1}\rangle = H|v_n\rangle - \alpha_n |v_n\rangle - \beta_n^2 |v_{n-1}\rangle, \tag{2.51b}$$

where the previous two Krylov vectors and the coefficients

$$\alpha_n = \frac{\langle v_n | H | v_n \rangle}{\langle v_n | v_n \rangle} \tag{2.52a}$$

$$\beta_n^2 = \frac{\langle v_n | v_n \rangle}{\langle v_{n-1} | v_{n-1} \rangle} \tag{2.52b}$$

enter. We consider a k-dimensional Krylov subspace, where k is a very small number $\mathcal{O}(10)$ compared to the dimension of the Hilbert space. In the Krylov subspace, the Hamiltonian

$$\mathbf{T}_k = \mathbf{V}_k^\top H \mathbf{V}_k \tag{2.53}$$

is a tridiagonal matrix and can be diagonalized easily using standard numerical routines. The matrix $\mathbf{V}_k$ contains all k Krylov vectors of the subspace as columns. The time-evolution operator is now approximated in the Krylov subspace

$$|\Psi(t+\Delta t)\rangle \approx \mathbf{V}_k \, \mathrm{e}^{-\mathrm{i}\mathbf{T}_k \Delta t} \, \mathbf{V}_k^\top \, |\Psi(t)\rangle \, . \tag{2.54}$$

Note that $|\Psi(t)\rangle = |v_0\rangle$ is a Krylov vector. Thus, all columns of the matrix $\mathbf{V}_k$ except the first one are orthogonal to $|\Psi(t)\rangle$. The tridiagonal Hamiltonian $\mathbf{T}_k$ is diagonalized by an orthogonal transformation $\mathbf{O}_k$

$$\mathrm{e}^{-\mathrm{i}\mathbf{T}_k \Delta t} = \mathbf{O}_k \; \mathrm{e}^{-\mathrm{i}\mathbf{D}_k \Delta t} \, \mathbf{O}_k^\top , \tag{2.55}$$

where $\mathbf{D}_k$ is a diagonal matrix.

Concerning the implementation of the Krylov vectors within our DMRG code, it is advisable to rewrite $|\Psi(t+\Delta t)\rangle = \mathrm{e}^{-\mathrm{i}\,H\Delta t}\,|\Psi(t)\rangle$ in bra-ket notation. By inserting several basis sets in the latter expression, the real-time evolution from $t \to t + \Delta t$ acquires the form

$$|\Psi(t+\Delta t)\rangle = \sum_{i=0}^{k-1} a_i \, |v_i\rangle \tag{2.56}$$

with the coefficients

$$a_i = \sum_{j=0}^{k-1} \langle v_i | \lambda_j \rangle \, \mathrm{e}^{-\mathrm{i}\lambda_j \Delta t} \, \langle \lambda_j | \Psi(t) \rangle \, . \tag{2.57}$$

The eigenvectors $\{|\lambda_j\rangle\}$ and eigenvalues $\{\lambda_j\}$ result from the diagonalization of $\mathbf{T}_k$, which has to be calculated in addition to the orthogonalized Krylov vectors $\{|v_j\rangle\}$.

The coefficients a_i decay extremely fast with increasing number k. Thus, the dimension k of the Krylov subspace can be kept very small. The modulus of the coefficients can be used

as convergence criterion. In practice, we omit contributions with $|a_k| < 10^{-10}$ and only a handful of Krylov vectors is required.

The appropriate choice for the target states used for the basis optimization was intensively discussed in Ref. [FW05]. In our realization, we stick to the established choice of four states

$$|\Psi_1\rangle = |\Psi(t)\rangle\,,\ |\Psi_2\rangle = |\Psi(t+\Delta t/3)\rangle\,,\ |\Psi_3\rangle = |\Psi(t+2\Delta t/3)\rangle\,,\ |\Psi_4\rangle = |\Psi(t+\Delta t)\rangle\,. \tag{2.58a}$$

The weights of the target states in the reduced density matrix have only a minor influence on the results. An overweight for the target states $|\Psi(t)\rangle$ and $|\Psi(t+\Delta t)\rangle$ has proven to yield a slightly better performance than equal weights. Thus, we adopt the weights

$$W_1 = \frac{1}{3},\ W_2 = \frac{1}{6},\ W_3 = \frac{1}{6},\ W_4 = \frac{1}{3} \tag{2.58b}$$

for the four target states (2.58a) from Feiguin and White [FW05].

Like the TS decomposition, the implementation of the Krylov vector approach is straightforward because the Lanczos algorithm occurs in many standard DMRG codes anyway. The run-times are significantly longer compared to the previously introduced TS decomposition, because the action of the Hamiltonian on the state vector has to be calculated multiple times in each step. But it does not suffer from the error of the TS decomposition. The action of the Hamiltonian on the state vectors is directly evaluated by applying all operators contributing to the Hamiltonian, see Sect. 2.2.1. Thus, special care has to be taken that all operators in a purified system are restricted to real sites only. The accuracy is well controllable by adjusting the cutoff of the expansion coefficients a_k (2.57).

2.4.4 Chebychev expansion

The Chebychev expansion [TEK84] is a widely known approach for calculating the time evolution [DDR03, WWAF06, HA14]. More recently, it has also been implemented in the framework of matrix product states in combination with a variational calculation of the Chebychev polynomials [HWM$^+$11]. In the following, we present how we use the Chebychev expansion to calculate the real-time evolution of autocorrelation functions with a standard DMRG implementation [SRU13].

To this end, we return to the concept of purification as introduced in Sect. 2.3.2 and consider the initial state

$$|0\rangle := \bigotimes_{i=0}^{N} \frac{1}{\sqrt{2}} \left(|\uparrow_\mathrm{r}\downarrow_\mathrm{a}\rangle - |\downarrow_\mathrm{r}\uparrow_\mathrm{a}\rangle\right)_i\,, \tag{2.59}$$

where the central spin is purified as well. This setup is sketched in the lower panel of Fig. 2.7. Since all operators are restricted to real sites, it is possible to apply any unitary operator to the auxiliary sites without affecting the physics of the model. Hence, an artificial time evolution of the auxiliary sites is realizable. We follow the proposal made by Karrasch *et al.* [KBM12]. They studied a purified Heisenberg chain and used the same Hamiltonian for the auxiliary spins but calculated their real-time evolution backwards in time. In the Heisenberg chain, this leads to a slower growth of the entanglement and thus to a slower increase of the discarded weight.

Due to the purified central site in the initial state $|0\rangle$, we are able to adopt this approach for the central spin model. We consider an autocorrelation function of the central spin in the Heisenberg picture, for example in z-direction,

$$S(t) = \langle 0|U^{\dagger}(t)\, S_0^z U(t)\, S_0^z|0\rangle\,, \tag{2.60}$$

where $U(t) = \mathrm{e}^{-\mathrm{i}tH}$ with $H = H_\mathrm{r} - H_\mathrm{a}$ acts on the real *and* the auxiliary spins. The Hamiltonian H_r represents the standard Hamiltonian (1.4) of the central spin model and acts on the real spins only. The auxiliary Hamiltonian H_a involves the same interactions as H_r, but it is solely restricted to the auxiliary spins. As the real spins evolve forward and the auxiliary spins evolve backward in time, the action of $U^{(\dagger)}$ on $|0\rangle$ leaves this state unchanged. This observation is the reason for the reduced growth of entanglement in chain topologies. For a more detailed discussion, see Appendix C. Thus, the autocorrelation function (2.60) acquires the symmetric form

$$S(t) = \langle 0|S_0^z U(t)\, S_0^z|0\rangle\,. \tag{2.61}$$

This is crucial for the Chebychev expansion, which we see below.

Concerning the application of the Chebychev polynomials, the Hamiltonian has to be rescaled with the energy bound $C = 3/4\sum_{i=1}^{N}|J_i|$ to ensure the validity of the expansion. The correct estimate for C is yield from the maximum energy of the Hamiltonian. The energy of a single dimer formed by the bath spin $\vec{S}_i$ and the central spin $\vec{S}_0$ is bounded by $|J_i\vec{S}_i\vec{S}_0| \leq 3|J_i|/4$, which corresponds to the energy of an antiferromagnetic dimer. By summing over all dimers, one obtains the previously mentioned expression for C. An additional factor of two is induced by the auxiliary Hamiltonian H_a, which has the same energy bound. Hence, the eigenvalues of the rescaled Hamiltonian $\widetilde{H} = H/(2C)$ fulfill $-1 \leq \widetilde{E}_n \leq 1$. The time-evolution operator U is now expanded in the basis of the Chebychev polynomials $T_n^{\mathrm{ch}}(\tilde{H})$

$$\mathrm{e}^{-\mathrm{i}\tilde{H}t} = \sum_{n=0}^{\infty} T_n^{\mathrm{ch}}\left(\frac{H_\mathrm{r} - H_\mathrm{a}}{2C}\right) b_n(2Ct)\,. \tag{2.62}$$

Note that the time dependence resides solely in the coefficients $b_n(t)$ which read

$$b_0(t) = J_0(t) \tag{2.63a}$$
$$b_n(t) = 2(-\mathrm{i})^n J_n(t), \tag{2.63b}$$

where $J_n(t)$ is the Bessel function of the first kind of order n. By inserting the coefficients into the expansion, one obtains the expression

$$S(t) = J_0(2Ct)\, m_0 + \sum_{n=1}^{\infty} m_n (-\mathrm{i})^n J_n(2Ct). \tag{2.64}$$

The time-independent coefficients

$$m_n := \langle v_0 | v_n \rangle \tag{2.65}$$

are obtained from the Chebychev polynomials $|v_0\rangle$ and $|v_n\rangle$ calculated via the recursion relation

$$|v_0\rangle = S_0^z |0\rangle \tag{2.66a}$$
$$|v_{n+1}\rangle = \frac{H_\mathrm{r} - H_\mathrm{a}}{C} |v_n\rangle - |v_{n-1}\rangle. \tag{2.66b}$$

Note that the presented form of the Chebychev expansion requires strictly the use of a completely purified initial state (2.59). Only in this case, the autocorrelation function of the central spin acquires a symmetric form (2.61) so that the expansion coefficients can be calculated via Eq. (2.65).

Similar to the Lanczos algorithm, multiple powers of the Hamiltonian have to be calculated which is easily carried out with DMRG. As in the Krylov approach, the basis is optimized first within a few half-sweeps. After the optimization is completed, the coefficient of the next order is calculated and stored. Afterwards, one proceeds to the next order. The required order N_ch depends on the desired time t. The Bessel function $J_n(t)$ contributes noticeable only for $t > n$ so that $N_\mathrm{ch} \geq 2Ct$. Furthermore, a single coupling constant may be approximated by $J \approx 1/\sqrt{N}$ which leads to the bound $C = \sqrt{N}$. Thus, an estimate for the required order N_ch is

$$N_\mathrm{ch} \geq 2t\sqrt{N}, \tag{2.67}$$

where N is the number of bath spins. The time dependence resides separately in the Bessel functions so that the autocorrelation function (2.64) can be evaluated with a separate code or with any computer algebra program, for example Maple.

In the reduced density matrix, at least the four states $|v_0\rangle$, $|v_{n-1}\rangle$, $|v_n\rangle$, and $|v_{n+1}\rangle$ have to be targeted. The targeting of the initial state $|v_0\rangle$ is crucial because it is required for the calculation of the coefficients m_n (2.65). Thereby, one ensures that the basis of $|v_0\rangle$ is always ideally represented. If the target state is missing, errors will occur which lead to false coefficients m_n. However, the state $|0\rangle$ has a very simple structure so that there is no negative effect on the discarded weight when it is targeted in addition to the latest three Chebychev polynomials.

With respect to the special role of $|v_0\rangle$, one also has to be careful about its normalization. If the state $|v_0\rangle$ is transformed over and over again, its normalization will be lost after multiple sweeps, see Sect. 2.5.2.2 for details. To prevent this, we recommend to rebuild the state in each recursion step which can be done during a half-sweep. This strongly reduces the error of the Chebychev polynomials m_n. All others states are only stored for three orders and no recalculation is necessary.

Compared to a Trotter-Suzuki or Krylov calculation, the size of the Hilbert space is doubled due to the purified central site. This leads to an increase of the runtime. But for a fixed value of t, it is much faster than the Krylov vector approach because the required order for the Chebychev expansion involves significantly less applications of the superblock Hamiltonian. An additional speed-up is obtained by outsourcing the calculation of the autocorrelation function (2.64). In total, the required run-time of the Chebychev code is moderate and ranks between the Trotter-Suzuki and Krylov approach, see Sect. 2.5.4 for details.

2.5 Verification of the DMRG implementation

The ground state energies presented in Sect. 2.2.2 already revealed a remarkable agreement between DMRG and the exact results. Before we start with a detailed discussion of the central spin dynamics in the central spin model, the implementation of the real-time evolution based on DMRG has to be verified.

2.5.1 Polarized bath

For the beginning, it is convenient to study a simple initial state where the exact time evolution is known. We discuss a fully polarized bath with all bath spins pointing up and

the central spin pointing down at $t = 0$

$$|\Psi(0)\rangle = |\uparrow, \uparrow, \ldots, \uparrow\rangle \otimes |\downarrow\rangle . \tag{2.68}$$

We choose the coupling constants between the bath and the central spin such to fulfill an unnormalized uniform distribution

$$J_i = \frac{1}{N} (N + 1 - i) J_\mathrm{q}. \tag{2.69}$$

For this simple setup, exact Bethe ansatz results are available [BS07a, Stü08]. The time dependence of the magnetization $\langle S_0^z(t) \rangle$ of the central spin up to $t = 40 J_\mathrm{q}^{-1}$ is shown in Fig. 2.9. In addition, the deviation of the DMRG results from the exact Bethe ansatz result [BS11] is plotted. Note that the discussion of the simple initial state (2.68) is restricted to the TS decomposition and the Krylov vector approach, since the Chebychev expansion has been exclusively introduced for a completely purified state, see Sect. 2.4.4.

The magnetization of the central spin presented in the upper panel of Fig. 2.9 shows fast oscillations at constant frequency. Only a small fraction of the amplitude decays initially so that no complete relaxation is observed. No visible distinction between the DMRG results and the exact Bethe ansatz result can be made in the upper panel. Already in second order TS decomposition, the DMRG data is in excellent agreement with the exact result. The deviation plotted in the lower panel of Fig. 2.9 provides a more detailed comparison of the DMRG and the exact Bethe ansatz result. For the results obtained from the TS decomposition, the deviation corresponds roughly to the TS error which is $\sim 10^{-4}$ in second order. In fourth order, the deviation decreases by approximately three to four orders of magnitude related to the improvement of the TS decomposition by two orders $\Delta t^2 \approx 10^{-4}$. The Krylov approach performs best. Here, the deviation from the exact result rarely exceeds 10^{-10}. This threshold corresponds to the cutoff chosen for the coefficients a_i (2.57). We refrain from showing the accumulated discarded weight because it is always smaller than the deviation shown in Fig. 2.9.

Hence, it can be assumed that the deviation shown in Fig. 2.9 resembles the TS error and the error of the Krylov approach. The number of kept states $m = 256$ exceeds the number of possible basis states which is linear in the total number of spins.

The extremely good agreement between DMRG and the exact Bethe ansatz results persists in the long-time behavior. In the upper panel of Fig. 2.10, the magnetization $\langle S_0^z(t) \rangle$ obtained from the fourth order TS decomposition is plotted up to $t = 1000 J_\mathrm{q}^{-1}$. The precession of the central spin in the Overhauser field continues, while the amplitude shows some short revivals. Even at $t = 1000 J_\mathrm{q}^{-1}$, the deviation from the exact Bethe ansatz result [Stü08, Stü12] does not exceed 10^{-5}.

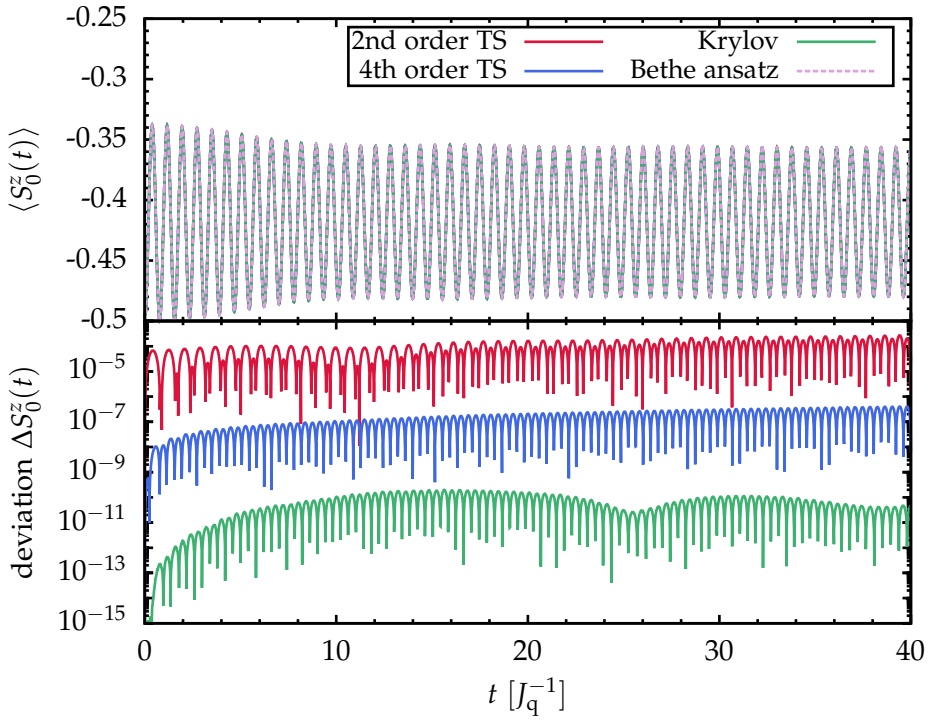

Fig. 2.9: Comparison between DMRG and the exact Bethe ansatz result. At $t = 0$, the bath is fully polarized with all bath spins pointing up, while the central spin points down. The distribution of the couplings is uniform according to Eq. (2.69). All DMRG calculations were done for $N = 30$ bath spins, $m = 256$ states and a time interval of $\Delta t = 0.01\, J_q^{-1}$. In the lower panel, the deviation $\Delta S_0^z(t)$ from the exact Bethe ansatz result is shown. The author is indebted to M. Bortz and J. Stolze for providing the Bethe ansatz data [BS07a, BS11].

In total, the accuracy for the results presented in this section is limited mainly by the special properties of the applied methods, namely the TS error and the finite number of coefficients contributing to the expansion in the Krylov subspace. This behavior is not really surprising because the discussed initial state (2.68) has a very simple structure due to its maximum polarization. Thus, only very sparse matrices and vectors have to be multiplied leading to the minor role of the discarded weight and very fast runtimes. The results for the polarized state serve as a nice first verification of our DMRG implementation. But general conclusions concerning the error and limits of our calculations may not be drawn because of the almost total absence of the discarded weight. For more complicated states, the discarded weight replaces the TS error as the dominating error on the long-time scale because it accumulates with time, see next section.

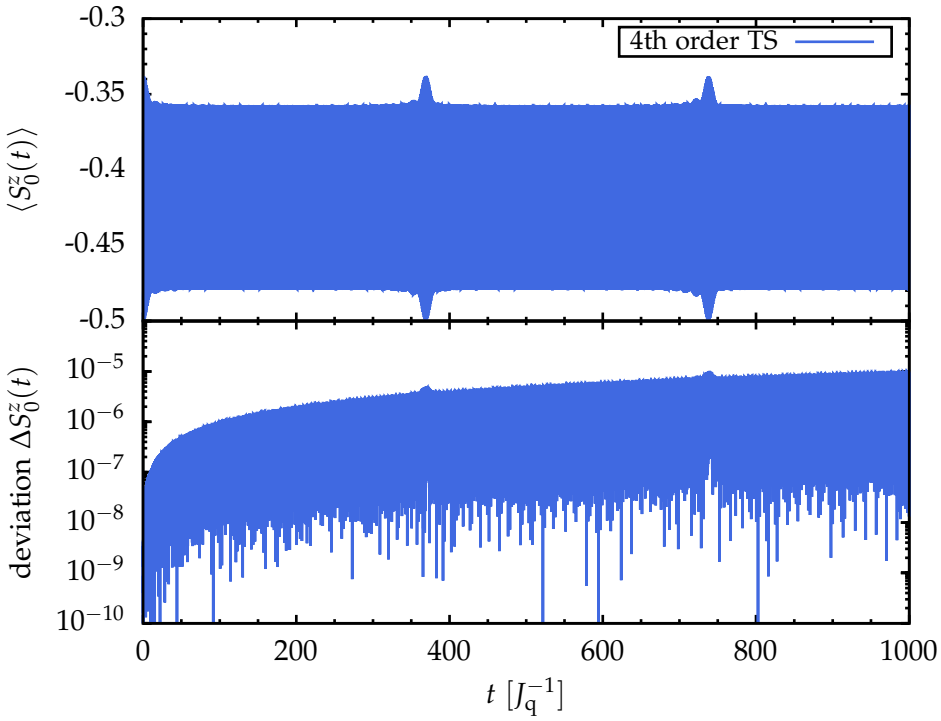

Fig. 2.10: Long-time behavior calculated with the fourth order TS decomposition and deviation from the exact Bethe ansatz result. The parameters and the setting are the same as in Fig. 2.9. The author is indebted to R. Stübner for providing the Bethe ansatz data [Stü08, Stü12].

2.5.2 Purified bath

Now we extend the discussion from the simple polarized bath to a purified bath (2.42) at infinite temperature. This is essential for the study of the decoherence presented in this thesis. From here on, the coupling constants are always chosen according to Eq. (1.8) introduced in Sect. 1.4. The Chebychev expansion is discussed separately from the other methods to explain the peculiarities of this approach.

2.5.2.1 Trotter-Suzuki decomposition & Krylov vectors

We begin with the discussion of the Krylov vector approach and the adaptive method based on the TS decomposition. The bath is now in a completely purified state, while the central spin is prepared as spin-up at $t = 0$. The results for the time dependence of the magnetization $\langle S_0^z(t)\rangle$ for $N = 19$ bath spins are shown in the upper panel of Fig. 2.11. All

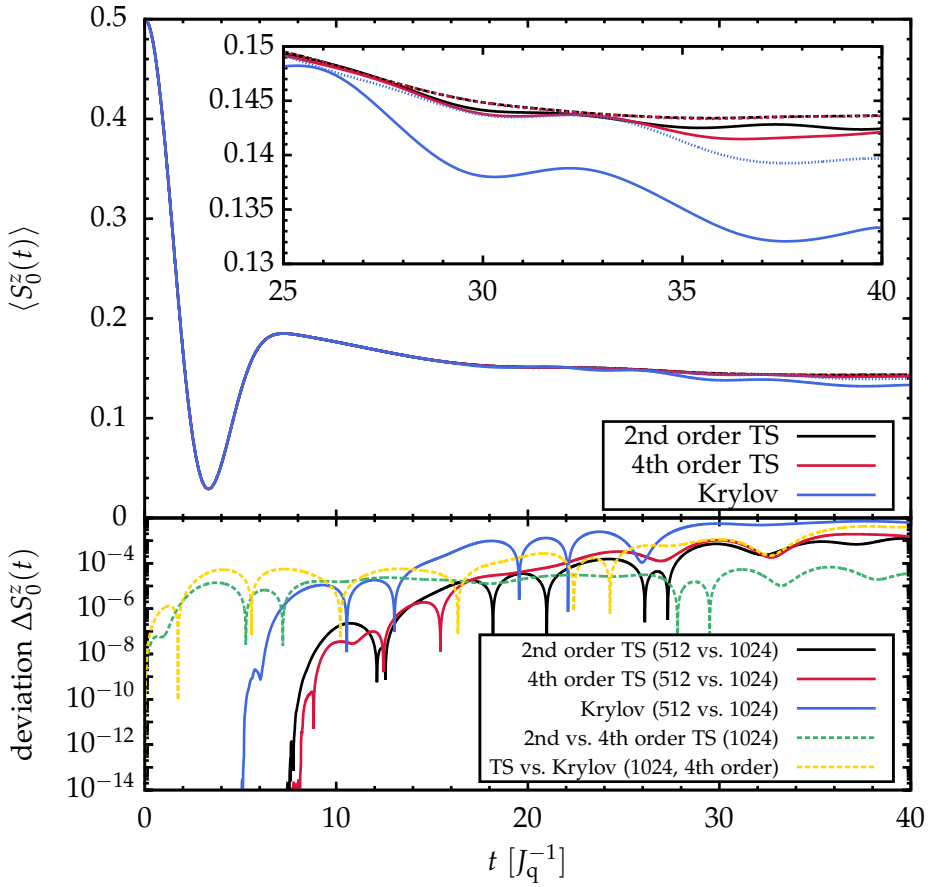

Fig. 2.11: Magnetization $\langle S_0^z(t)\rangle$ of the central spin in a purified bath (upper panel) and the absolute deviation $\Delta S_0^z(t) := |\langle S_0^z(t)\rangle_a - \langle S_0^z(t)\rangle_b|$ for selected pairs of methods a and b as described in the key of the lower panel. At $t = 0$, the central spin points up. All calculations were obtained for $N = 19$ and $\Delta t = 0.01\, J_q^{-1}$. The solid lines in the upper panel refer to calculations with $m = 512$ states, while $m = 1024$ states entered in the calculation of the dashed and dotted curves. A magnification of the magnetization for $t \geq 25\, J_q^{-1}$ is shown in the inset of the upper panel.

results were obtained for a fixed time interval $\Delta t = 0.01\, J_q^{-1}$ and $m = 512$ (solid lines) and $m = 1024$ states (dashed and dotted lines).

The magnetization $\langle S_0^z(t)\rangle$ displays a first minimum at $t \approx 4\, J_q^{-1}$. Afterwards, it arrives at a plateau which decays only marginally. This characteristic behavior is in good agreement with other studies [AHDDH06, FS13b]. Up to $t \approx 15\, J_q^{-1}$, all curves agree very well so that it can be assumed that all calculations yield correct results up to this time scale. Discrepancies between the different approaches are observed for larger times, as is illustrated in the inset of Fig. 2.11. The Krylov results for $m = 512$ and $m = 1024$ states deviate quite early from each as other as well as from the TS results. The deviation between the different curves implies that the Krylov approach fails for intermediate times $t \gtrsim 25\, J_q^{-1}$. As

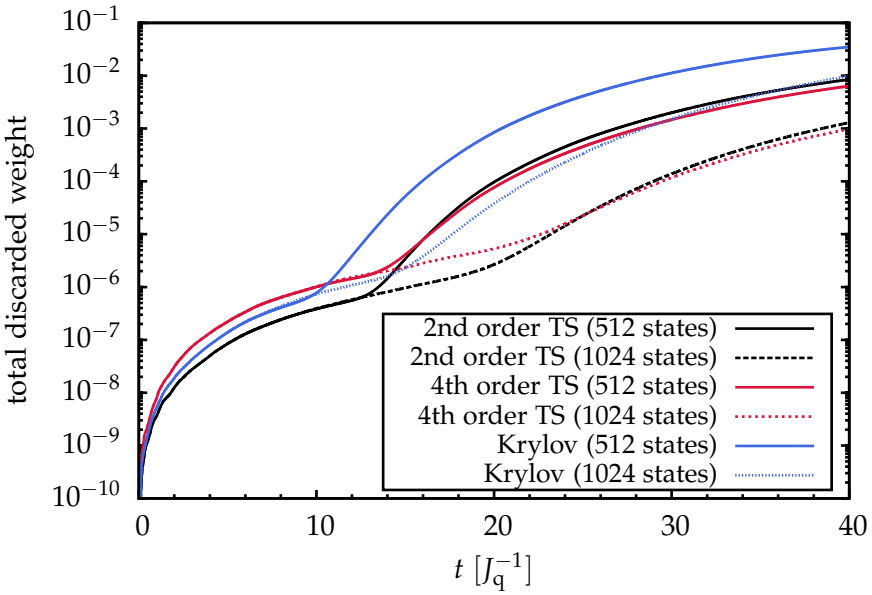

Fig. 2.12: Total discarded weight for the curves shown in Fig 2.11.

long as two different methods agree with each other, they should both render the correct result. Both TS results for $m = 512$ states agree roughly up to $t \approx 25\, J_q^{-1}$ with their counterparts for $m = 1024$ states. Remarkably, no visible distinction between the second order and fourth order result of the TS decomposition for $m = 1024$ states can be made in the complete interval. This is supported by the deviation between the different curves, which is plotted in the lower panel of Fig. 2.11. For $m = 1024$, the deviation between the second and fourth order is nearly constant at $\Delta S_0^z(t) \approx 10^{-5}$-$10^{-4}$. This difference corresponds exactly to the deviation of their TS errors $\sim \Delta t^2$. All other curves reveal a monotonic increase of the deviation up to several orders of magnitude for larger times. The deviation of the Krylov results clearly exceeds the ones of the TS results.

The solid curves in the lower panel of Fig. 2.11 stand for the individual deviation of each method where the result for $m = 1024$ states was used as reference. These curves can be used to define a runaway time t_r at which the result for $m = 512$ states begins to deviate from the reference curve. For $t \geq t_r$, the quantity $\Delta S_0^z(t)$ starts to deviate from zero and acquires a finite positive value. Up to $t = t_r$, both results are in very good agreement and the employment of a larger number of states has no benefit. For $t > t_r$, the quality of the result is improved by a larger number of states because the discarded weight dominates the total error [GKSS05].

The total discarded weights (2.19) corresponding to the curves in the upper panel of Fig. 2.11 are plotted in Fig. 2.12. As the discarded weight accumulates with increasing time, it grows monotonically. By doubling the number of kept states m, it decreases by

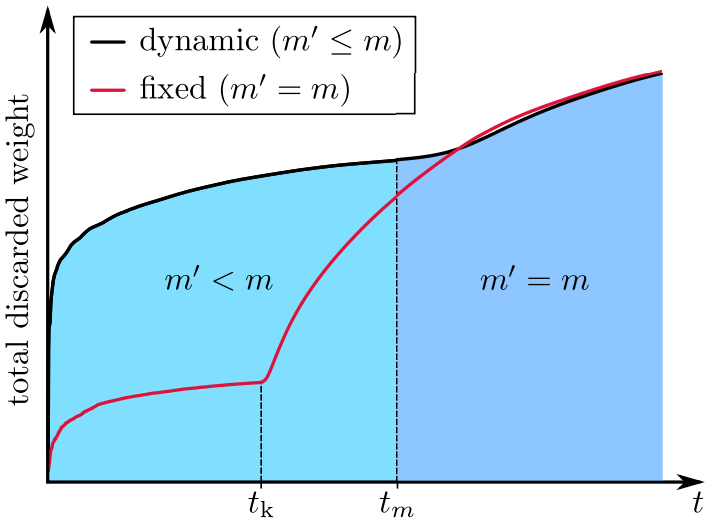

Fig. 2.13: Schematic behavior of the total discarded weight with (black line) and without (red line) dynamic adaption of the number of kept states m'. The maximum number of kept states is denoted by m.

approximately one order of magnitude. Even for $m = 1024$, the total discarded weight of the Krylov vectors at $t = 40\, J_q^{-1}$ ranges in the area of a few percent which explains the deviations observed in the magnetization of the central spin. The total discarded weight of the TS decomposition is always located roughly one order of magnitude lower than the one of the Krylov vectors. Interestingly, only a marginal dependence on the order of the TS decomposition is observed. The fourth order performs slightly better than the second order, although the number of sweeps is larger by a factor of three. Compared to the TS decomposition, the kink in the total discarded weight of the Krylov approach occurs at an earlier time because this approach uses at least four different target states covering a larger part of the Hilbert space.

Our implementation of the DMRG truncation involves a dynamic control of the number of kept states where m denotes their maximum number. Starting from a lower limit (usually $m' = 64$), the number of states m' is successively increased if the discarded weight of a single truncation exceeds a predefined threshold ε_m. In our calculations, the latter is usually set to $\varepsilon_m = 10^{-12}$. If the maximum number $m' = m$ is reached, no further adjustment will be made. The dynamic adjustment of the number of kept states is carried out in every truncation: During the buildup of the initial superblock with the infinite size algorithm as well as during the calculation of the real-time evolution. Thus, the number of kept states m' increases monotonically with t until the maximum number m is reached.

Of course, this procedure has an effect on the total discarded weight which is sketched in Fig. 2.13. On the short-time scale, the dynamic adjustment of m' (black line) induces a

substantial speedup of the algorithm at the cost of a larger total discarded weight compared to the scenario without dynamic adjustment (red line). When the maximum number $m' = m$ is reached at the time $t = t_m$, a kink is observed in the total discarded weight. Then, the increasing discarded weight per truncation cannot be compensated anymore by an adjustment of m' because the maximum number of kept states has been reached. Hence, the total discarded weight increases faster for $t > t_m$.

The total discarded weight of calculations involving a constant number of $m' = m$ states (red line in Fig. 2.13) is much smaller on the short-time scale. But it also exhibits a kink located at the time $t = t_\mathrm{k} < t_m$. Most likely, this kink has to be attributed to the increasing entanglement in the model. Up to t_k, the number of tracked states seems to yield a very good approximation to the exact result because the total discarded weight stays very small. For larger times, m states are not sufficient anymore to capture the increasing entanglement in the model. This likely induces the fast growth of the total discarded weight for $t > t_\mathrm{k}$. For $t \gtrsim t_m$, the total discarded weight coincides roughly with the one obtained from the corresponding calculation including the dynamic adjustment of the number of states. As depicted in Fig. 2.13, the total discarded weight for a fixed number of $m' = m$ kept states is usually slightly larger on the long-time scale. But the main advantage of the dynamic adjustment of m' is the substantial reduction of the runtime. For an exemplary calculation for $N = 19$ bath spins and a maximum of $m = 512$ kept states, the runtime of the code up to $t = 20\, J_\mathrm{q}^{-1}$ is reduced by a factor of three.

Overall, the real-time evolution based on the TS decomposition yields reliable results for a sufficiently large number of tracked states. For $m = 1024$, both orders of the TS decomposition are in remarkable agreement and the results deviate by the magnitude of the difference of their TS errors. Hence, the employment of the second order is usually adequate unless a extremely high accuracy is required. Only then, we recommend to invest the factor of three in the runtime required for the fourth order decomposition. Even for $m = 1024$, the result of the Krylov vectors seems to be unstable for larger times. This is caused by the larger total discarded weight which exceeds the one of the TS decomposition by one order of magnitude. Nevertheless, it is suitable for smaller time scales $t \leq 20\, J_\mathrm{q}^{-1}$. For short times, it should outperform the TS decomposition due to the absence of the TS error, as discussed for the polarized bath. Concerning the number of states, $m = 1024$ appears to be an appropriate choice for the discussed time scale. With respect to the deviation shown in the lower panel of Fig. 2.11 and the total discarded weight in Fig. 2.12, $m = 512$ is sufficient for the time scale $t \approx 0\text{-}15\, J_\mathrm{q}^{-1}$.

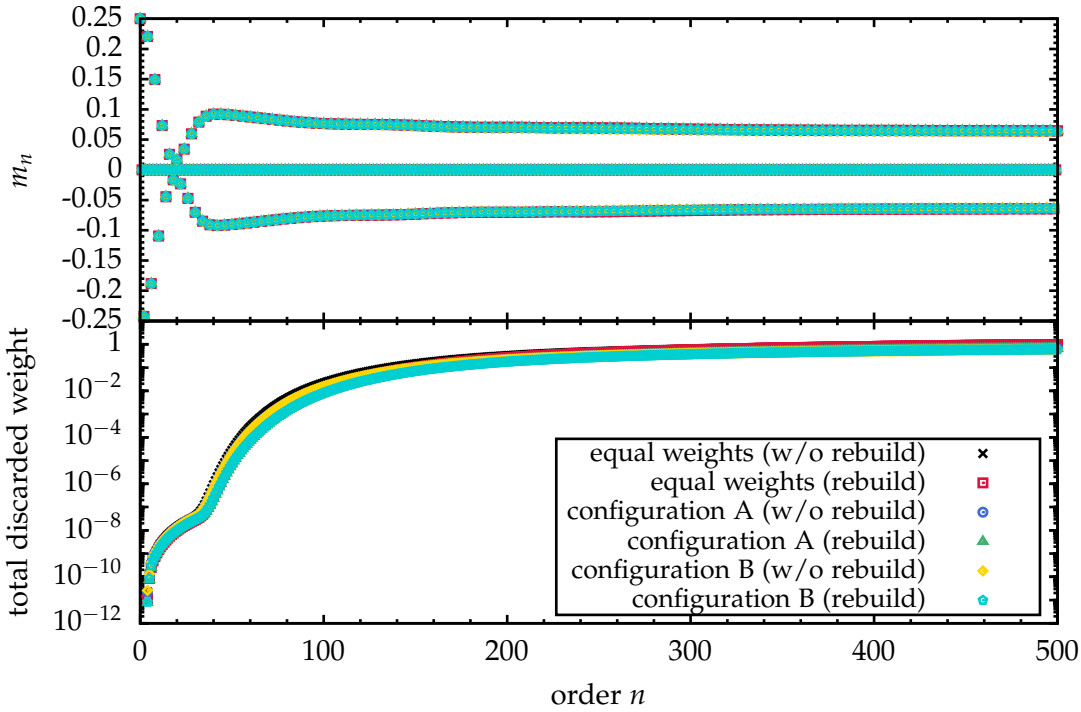

Fig. 2.14: Coefficients m_n (2.65) and total discarded weight of the Chebychev expansion as a function of the order n for $N = 19$ bath spins and $m = 1024$ states. The weights of the different configurations are given in Tab. 2.2.

2.5.2.2 Chebychev expansion

Before we start with the discussion of the autocorrelation function (2.64), we discuss briefly the behavior of the coefficients m_n (2.65) of the Chebychev expansion. They are plotted in the upper panel of Fig. 2.14. Like in the previous section, all calculations were done for $N = 19$ bath spins. We solely show the DMRG data for $m = 1024$ states because the quality of results for $m = 512$ is insufficient. All odd coefficients are zero so that all imaginary contributions to the autocorrelation function vanish. The signs of the non-vanishing coefficients alternate. Thus, the prefactors of the Bessel functions in Eq. (2.64) are always positive. The total discarded weight as a function of the order n is plotted in the lower panel of Fig. 2.14. It exhibits an extremely fast growth. Already at $n \approx 100$, corresponding to $t \approx 10\, J_{\mathrm{q}}^{-1}$, it exceeds 10^{-3}. The weights of the target states have not been addressed so far. We investigated several possible sets of weights which are listed in Tab. 2.2. The numerical data shown in Fig. 2.14 reveal only a minor effect of the different sets of weights. For a final assessment, other quantities have to be considered.

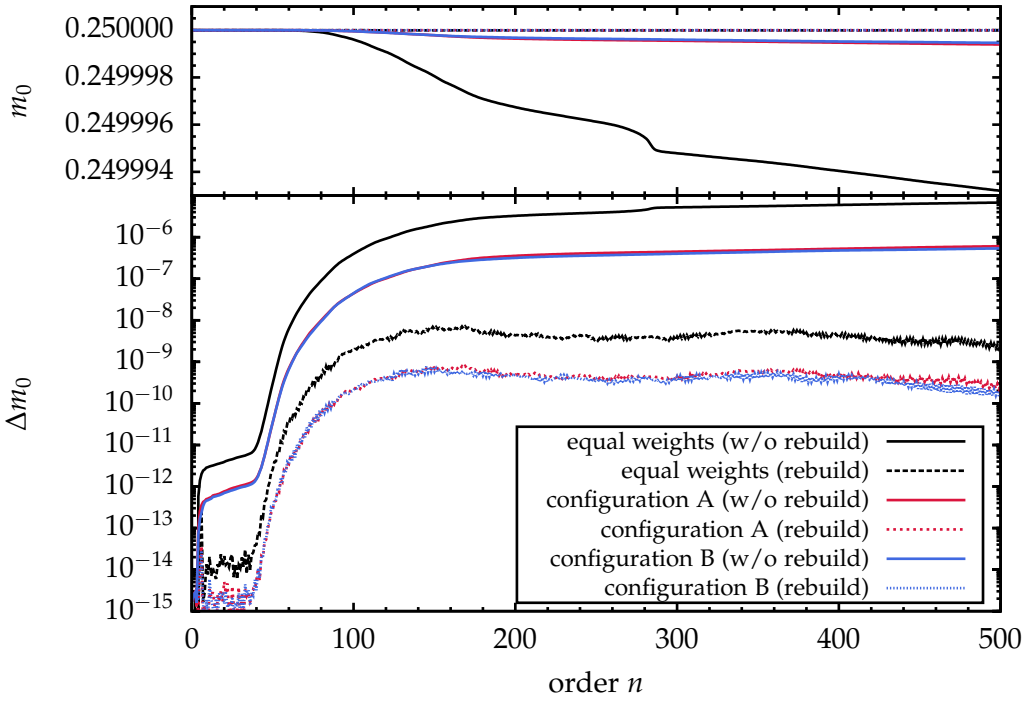

Fig. 2.15: Behavior of the scalar product m_0 of the initial state $|v_0\rangle$ as a function of the order n and deviation from the exact value $m_0 = 1/4$. The weights of the different configurations are given in Tab. 2.2.

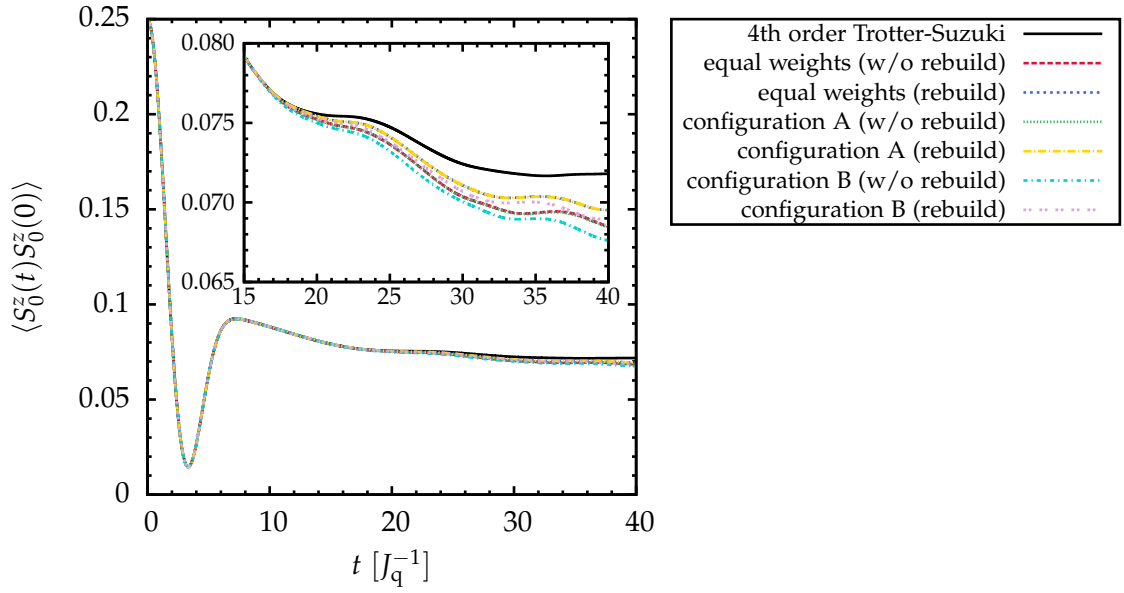

Fig. 2.16: Autocorrelation function $\langle S_0^z(t) S_0^z(0) \rangle$ of the central spin obtained from the Chebychev expansion (2.64). A magnification for $t \geq 15\, J_q^{-1}$ is shown in the inset. The weights of the different configurations are given in Tab. 2.2.

set	W_1	W_2	W_3	W_4
equal weights	1/4	1/4	1/4	1/4
configuration A	1/2	1/6	1/6	1/6
configuration B	1/2	1/8	1/8	1/4

Tab. 2.2: Studied weights for the four target vectors $|\Psi_1\rangle = |v_0\rangle$, $|\Psi_2\rangle = |v_{n-1}\rangle$, $|\Psi_3\rangle = |v_n\rangle$, and $|\Psi_4\rangle = |v_{n+1}\rangle$ required for order $n \geq 4$ of the Chebychev expansion.

A suitable measure for the performance of the different weights is the behavior of the coefficient m_0 as a function of the order n. As mentioned in Sect. 2.4.4, the initial state $|v_0\rangle$ is required in each order to calculate the new coefficient m_n. Hence, one can always calculate the coefficient m_0 and see how it deviates from its exact initial value $m_0 = 1/4$ with increasing order n. The upper panel in Fig. 2.15 demonstrates that a massive gain in accuracy is achieved from the suggested rebuild of $|v_0\rangle$. More details are revealed in the lower panel, where the deviation from the exact value is plotted. If the initial states dominates the reduced density matrix as in configurations A and B (see Tab. 2.2), the rebuild improves the accuracy by another order of magnitude.

For a final conclusion concerning the weights of the target states in the reduced density matrix, we study their influence on the autocorrelation function $\langle S_0^z(t) S_0^z \rangle$ of the central spin. The result shown in Fig. 2.16 was obtained from $N_{\mathrm{ch}} = 400$ coefficients m_n. As soon as the plateau emerges, the various curves quickly start to deviate from each other for $t \gtrsim 15\, J_{\mathrm{q}}^{-1}$. The result from the fourth order TS decomposition is shown as a reference. It agrees with the result from the second order so that we assume that it renders the correct result. Without the rebuild of $|v_0\rangle$, the autocorrelation function shows a strong deviation from the TS result for all tested sets of weights. Improvement is achieved by rebuilding the initial state $|v_0\rangle$ in each order. Then, equal weights and the weights of configuration A yield the best result. An overweight for the most recent Chebychev polynomial tested in configuration B tends to have a negative effect on the autocorrelation function. Thus, we suggest to use either equal weights for the target states or a dominating initial state $|v_0\rangle$ together with equal weights for the three most recent states, as represented by configuration A from Tab. 2.2.

However, a significant discrepancy between the result of the Chebychev expansion and the TS decomposition remains. This is due to the extremely large total discarded weight, which is almost $\mathcal{O}(1)$ for $n = 400$. The fast growth is related to two mechanisms. First, each target state corresponds to a different power of the Hamiltonian so that the overlap of the four target states is rather small compared to the ones entering in the Krylov method. Consequently, it is more difficult to find an optimal basis by a small number of

states. Second, the Chebychev expansion employs a purified central spin which implies an additional doubling of the Hilbert space compared to the other methods.

The question arises whether the performance of the Chebychev expansion can be improved. Higher orders of the expansion do certainly not lead to better results on the discussed time scale, since the Bessel function $J_n(t)$ only contributes for $t > n/J_q$. Besides, the total discarded weight of the coefficients m_n for large n is already close to $\mathcal{O}(1)$ as shown in the lower panel of Fig. 2.14.

The calculation of the Chebychev polynomials may be optimized by a variational ansatz as suggested in Ref. [HWM+11]. This approach was realized with DMRG in the framework of matrix product states [Sch11]. In order to realize this approach, a completely new DMRG implementation has to be written which lies beyond the scope of the present thesis. It also contradicts our intention because we want to keep the realization of the real-time evolution close to a standard DMRG implementation. In particular, the Krylov method and our proposal for the realization of the Chebychev expansion in the framework of DMRG are closely related. Furthermore, the central spin which links all bath spins makes the central spin model a special application. Thus, our proposal for the Chebychev expansion may perform much better without any additional improvements for other models, for instance a one-dimensional Heisenberg chain. But further studies are needed for a firm understanding.

2.5.3 Real-time evolution of the auxiliary spins

The time evolution of the auxiliary sites has already been discussed in the framework of the Chebychev expansion in Sect. 2.4.4 and in Appendix C. But this approach can also implemented for the TS decomposition and the Krylov vectors. In this section, we briefly discuss the realization for the TS decomposition as suggested originally by Karrasch *et al.* [KBM12]. Like for the real spins, the local time-evolution operators acting on the auxiliary bath spins and the auxiliary central spin are applied during a sweep when an auxiliary bath site is shifted from the environment to the system block. The Hamiltonian acting on the auxiliary sites is identical to the one acting on the real sites, but the time evolution is calculated backwards in time by the time interval $-\Delta t$.

For the antiferromagnetic XXZ Heisenberg chain [KBM12], the time evolution of the auxiliary sites leads to a slower growth of the entanglement. Consequently, larger time scales compared to standard DMRG could be reached. For the central spin model, we tried to

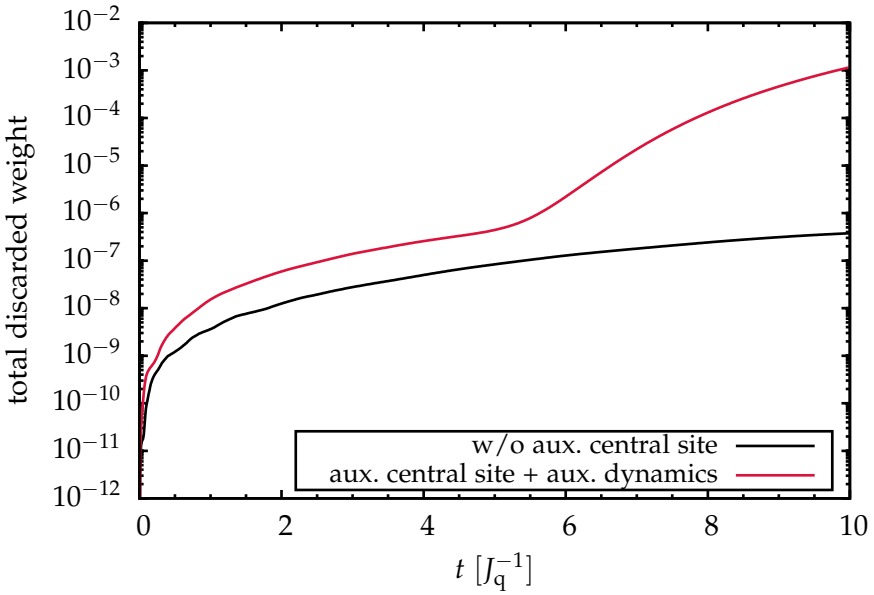

Fig. 2.17: Total discarded weight obtained from the second order TS decomposition with and without time evolution of the auxiliary sites for $m = 512$ states.

verify this behavior for an exemplary system of $N = 19$ bath spins. The obtained total discarded weight is shown in Fig. 2.17. Both results were obtained for $m = 512$ states which is a sufficiently large number for the presented time scale as concluded in Sect. 2.5.2.1. At $t = 10\,J_q^{-1}$, the total discarded weight of the calculation including the dynamics of the auxiliary sites already exceeds the one of the standard implementation by more than three orders of magnitude. One might object that we are comparing two entirely different setups in Fig. 2.17. But we underline that these are the two scenarios competing in practice: Either one includes the dynamics of the auxiliary spins or one leaves it out. But note that the auxiliary central spin is only required for the calculation of the real-time evolution of the auxiliary bath spins. Without such a dynamics, the auxiliary central spin is redundant.

The failure of the proposal made in Ref. [KBM12] is caused by the special structure of the central spin model. First, the introduction of a purified central site implies an additional doubling of the Hilbert space leading to a noticeable increase of the total discarded weight. Second, an entanglement is created by every operator applied to the purified initial state, see Appendix C. During the time evolution, it propagates in the system. Compared to an entanglement created on a local site of a chain, the creation of an entanglement at the central site is crucial. Due to the special topology of the central spin model, the central site plays a dominant role because it is directly linked to all other sites. Thus, an entanglement located at the central site spreads over the complete system by a *single* application of the Hamiltonian. In a chain with nearest-neighbor interaction, the propagation of a local entanglement takes much more time until it is completely spread. For an entanglement

created at site i of a chain, it takes n applications of the Hamiltonian to spread to site $i+n$.

The curves presented in Fig. 2.17 clearly indicate the drawback of this approach for the central spin model. This is also supported by the bad performance of the Chebychev expansion, see previous section. Hence, we do not pursue this approach any further and refrain from using a purified central spin. Instead, the expression in Eq. (2.44) should be used for the calculation of the observables and autocorrelation functions. It requires at most two independent runs of the DMRG code depending on the symmetry of the model and leads to a much smaller total discarded weight.

2.5.4 Discussion

In the previous section, first results for the individual methods for calculating the real-time evolution with DMRG have been presented and discussed. Now, we compare all methods for an exemplary system consisting of $N = 19$ bath spins. The goal of this section is to identify the method which fits our purposes best.

In Fig. 2.18 (upper panel), the autocorrelation function $S(t) = \langle S_0^z(t) S_0^z(0) \rangle$ is presented for the second and fourth order TS decomposition, the Krylov vectors, and the Chebychev expansion. The lower panel shows the deviation $\Delta S(t) := |S_\mathrm{a}(t) - S_\mathrm{b}(t)|$ for selected pairs of methods a and b. All calculations were done with $m = 1024$ states. According to the estimate given in Eq. (2.67), the minimum order of the Chebychev expansion at $t = 40\, J_\mathrm{q}^{-1}$ is roughly $N_\mathrm{ch} = 350$.

In general, all methods agree nicely up to $t \approx$ 15-20 J_q^{-1} with no deviation exceeding 10^{-3}. The Chebychev expansion starts to deviate from the other results for $t \gtrsim 20\, J_\mathrm{q}^{-1}$, followed by the Krylov vector result for $t \gtrsim 25\, J_\mathrm{q}^{-1}$. As mentioned before, no visible distinction can be made between the second and fourth order TS decomposition in the complete interval. The almost constant deviation between the two orders of the TS decomposition plotted in the lower panel of Fig. 2.18 is a strong hint that it is dominated by the TS error. Indeed, the observed deviation of 10^{-5}–10^{-4} is exactly the deviation $\sim \Delta t^2$ of their TS error for $\Delta t = 0.01\, J_\mathrm{q}^{-1}$. All other deviations increase with time and exceed the deviation between the two TS orders by roughly two orders of magnitude.

With respect to the total discarded weight presented in Fig. 2.19, the Chebychev expansion performs worst. Here, it is plotted in dependence of the order n of the expansion. Since

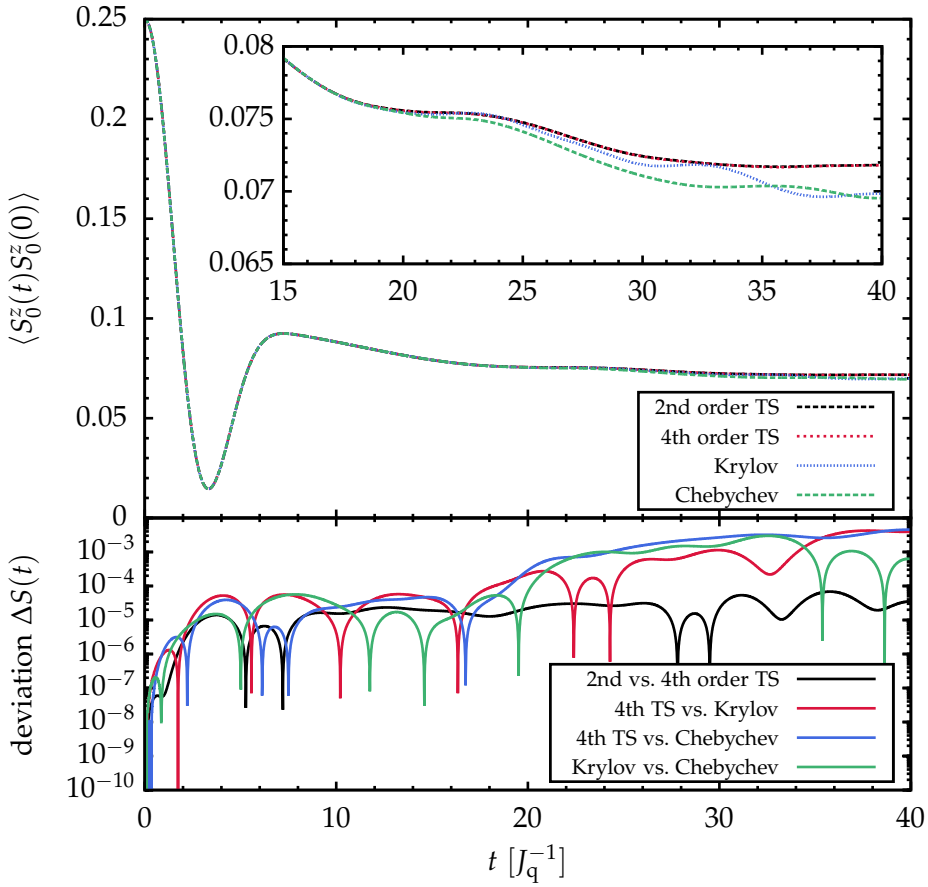

Fig. 2.18: Autocorrelation function $S(t) := \langle S_0^z(t)S_0^z(0)\rangle$ of the central spin (upper panel) and deviation $\Delta S(t) := |S_a(t) - S_b(t)$ for selected pairs of methods a and b (lower panel). All results were obtained for $m = 1024$ states and a time interval $\Delta t = 0.01\, J_q^{-1}$. The inset in the upper panel contains a magnification of the autocorrelation function for $t \geq 15\, J_q^{-1}$.

the required order scales linearly with time, the upper axis depicting the order of the expansion can directly be identified with the lower time axis. The dashed vertical line in Fig. 2.19 indicates the number of polynomials required for the autocorrelation function up to $t \approx 20\, J_q^{-1}$. Already at this intermediate value of t, the total discarded weight lies in the area of double-digit percentage while the total discarded weight of the Krylov vectors lies four orders of magnitude lower. The total discarded weight of the TS decomposition agrees roughly with the one of the Krylov vectors up to $t \gtrsim 20\, J_q^{-1}$. Due to the early kink, the curve for the Krylov vectors is approximately one order of magnitude larger for $t > 20\, J_q^{-1}$. Even at $t = 40\, J_q^{-1}$, the total discarded weight of the TS approach takes only a moderate value.

As a consequence, we refrain from applying the Chebychev expansion for the calculation of the real-time evolution with DMRG in the central spin model. The method suffers from

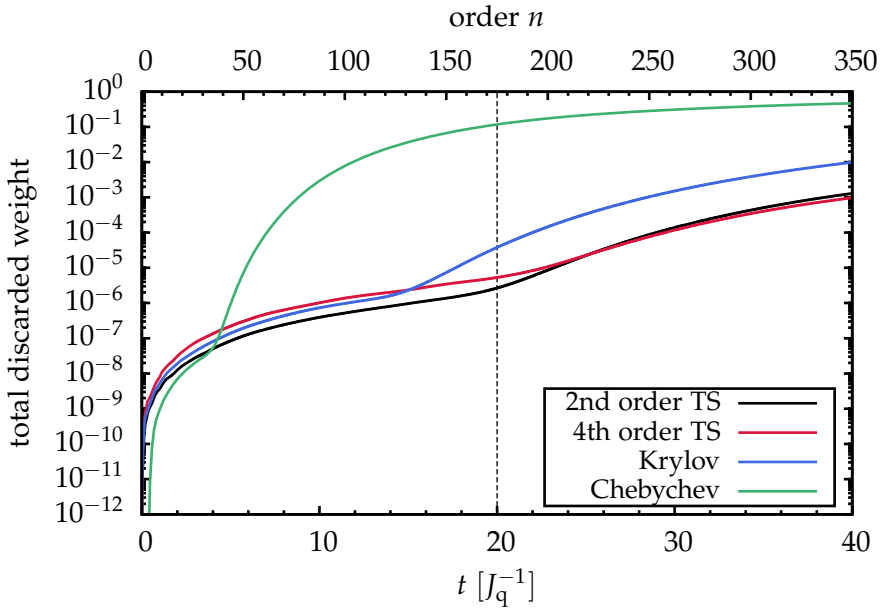

Fig. 2.19: Total discarded weight for all curves shown in the upper panel of Fig. 2.18 as function of time t (Trotter-Suzuki and Krylov; lower x-axis) and as a function of the order n (Chebychev expansion; upper x-axis).

the extremely fast growing total discarded weight and deviates very early from the other results shown in Fig. 2.18. In accordance with the observation from the previous section, the enormous total discarded weight can be attributed to the presence of the auxiliary central site. Together with the issues already addressed in Sect. 2.5.2.2, the Chebychev polynomials do not appear to be very suitable for the study of the electron spin dynamics in the central spin model.

The Krylov vectors yield reliable results up to intermediate time scales where the total discarded weight is still moderate. On the short time scale, it performs even better than the TS decomposition because there is no TS error. However, discrepancies occur for larger times where the Krylov result deviates from both orders of the TS decomposition. As shown in Tab. 2.3, the runtime of the DMRG code for the Krylov vectors is four times larger than the one of the second order TS decomposition. This is too large, especially if one is interested in bath sizes containing $N > 19$ spins. In addition, the Krylov vectors exhibit a larger total discarded weight than the TS approach.

In total, the TS decomposition is the appropriate method for calculating the real-time evolution in the central spin model with DMRG. Even in second order, it has a very good accuracy which is combined with only moderate runtimes (see Tab. 2.3) and a small total discarded weight. The local decomposition of the time-evolution operator U accounts for the fast runtime as well as for the high accuracy. Thereby, the action of the local parts

method	runtime [h]
second order TS	39
fourth order TS	99
Krylov vectors	129
Chebychev expansion	95

Tab. 2.3: Runtime of the DMRG program for the curves shown in the upper panel of Fig. 2.18.

of U on the superblock state vector can be calculated without any additional error. Furthermore, local time-evolution operators are easily accessible so that one can switch to time-dependent Hamiltonians with almost no effort. *This is very handy for future studies, for instance for the examination of pulses and pulse sequences*. The additional TS error does not have a negative effect on the result, because the total discarded weight is the dominating error for larger times. Thus, the employment of the fourth order decomposition is not mandatory. It might be beneficial for short times, but that is not necessarily supported by our observations. Moreover, the minimal gain of accuracy would not be justified by the longer runtime compared to the second order, see Tab. 2.3. Hence, the second order TS decomposition is identified as our standard method for the calculation of the real-time evolution in the central spin model.

Before closing this section, we would like to make a short remark concerning an improvement of our DMRG implementation of the Chebychev expansion. In a revised version of our code, we considered the property [WWAF06, HWM+11]

$$T_{n+m}(x) = 2T_n(x)\,T_m(x) - T_{n-m}(x) \tag{2.70}$$

of the Chebychev polynomials for $n > m$. By applying the initial vector $\langle v_0|$ from the left, one obtains the expression

$$m_{n+m} = 2\langle v_n|v_m\rangle - m_{n-m} \tag{2.71}$$

because $T_n(x)\,|v_0\rangle = |v_n\rangle$. Thereby, the number of coefficients can effectively be doubled without any additional effort so that the runtime is reduced by a factor of two. Nonetheless, one has to keep in mind that there is only a minor difference between the total discarded weight of order N_{ch} and of order $N_{\mathrm{ch}}/2$ if N_{ch} is large, see Fig. 2.19. Another advantage of the relation (2.70) lies in the reduction of the required number of target states: For order $n+1$, it is sufficient to target the last two Chebychev polynomials $|v_n\rangle$ and $|v_{n-1}\rangle$. To this end, we set $m = n$ and $m = n-1$, respectively. Then, we are able to

calculate the odd orders by the relation

$$m_{2n+1} = 2\,\langle v_n | v_{n-1}\rangle - m_1 \tag{2.72a}$$

and the even orders by the relation

$$m_{2n} = 2\,\langle v_n | v_n\rangle - m_0. \tag{2.72b}$$

One might suppose that this procedure may lead to a reduction of the total discarded weight because the targeting of the initial state $|v_0\rangle$ is not required anymore. However, this was not observed indicating that the enormous growth of the total discarded weight has to be attributed to the presence of the purified central spin and not to the permanent targeting of the initial state $|v_0\rangle$.

2.6 Errors & limits

In the following, we discuss the errors and the limits of the real-time evolution with the second order TS decomposition on the basis of the central spin model in the zero-field limit. Furthermore, the scaling of the errors and the performance of the algorithm in dependence of the number of bath spins are addressed. As before, the focus lies on intermediate time scales $t \geq 20\,J_\mathrm{q}^{-1}$. This time scale is particularly important for the plateau emerging at $t \gtrsim 5\,J_\mathrm{q}^{-1}$ which is discussed in more detail later on. Due to the absence of an external field, the central spin model in the zero-field limit corresponds to the most complex case because spin-flips between bath and central spin are not suppressed. In the presence of an external field, the investigation of the model is simplified because the field polarizes the spins. This leads to a simplification of the structure of the superblock state, implying faster runtimes and smaller total discarded weights as less states become important, see Sect. 2.7.2.

In the real-time evolution with DMRG based on the TS decomposition, two parameters can be tuned: The number of tracked states m and the time interval Δt. At first, we keep the number of states $m = 1024$ fixed and examine the influence of the time interval Δt. In Fig. 2.20, the magnetization of the central spin is presented for $N = 19$ (upper panel) and $N = 49$ (lower panel) bath spins for the time intervals $\Delta t = 0.01\,J_\mathrm{q}^{-1}$, $\Delta t = 0.02\,J_\mathrm{q}^{-1}$ and $\Delta t = 0.05\,J_\mathrm{q}^{-1}$. All curves for $N = 19$ bath spins are in good agreement. The magnification shown in the inset of the upper panel reveals some small discrepancies close to $t = 40\,J_\mathrm{q}^{-1}$. But the relative deviation between the curves for the different values of Δt is still less than 10^{-3}. For $N = 49$ bath spins, the deviation increases to the order of roughly 10^{-2}. In total, the agreement between all curves is still excellent in the complete time interval.

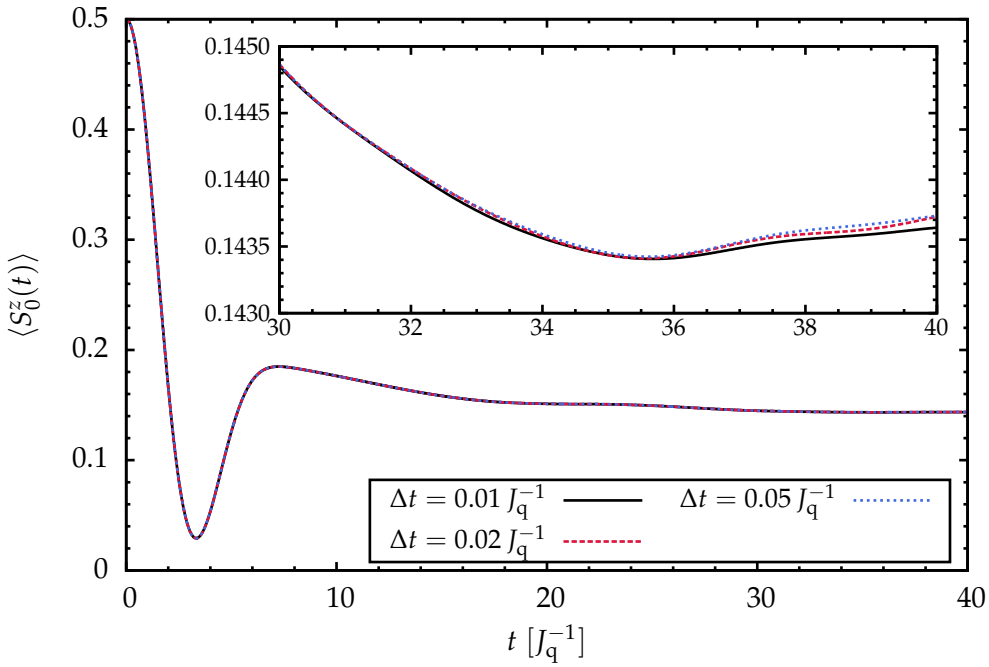

(a) $N = 19$ bath spins

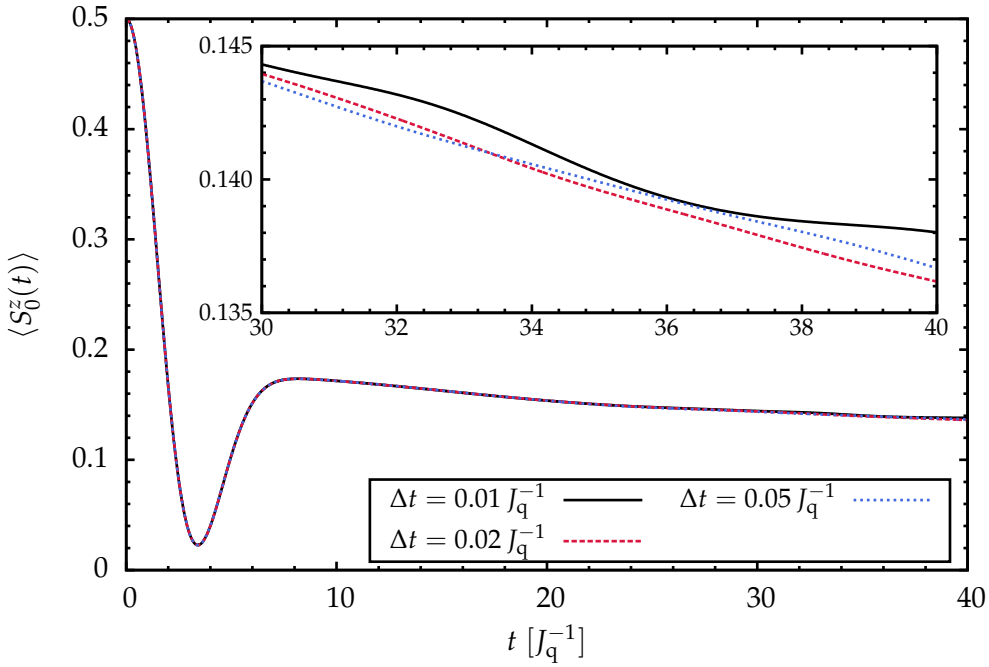

(b) $N = 49$ bath spins

Fig. 2.20: Influence of the time interval Δt on the time evolution of the magnetization $\langle S_0^z(t)\rangle$ of the central spin. All results were obtained for a fixed number of $m = 1024$ states. The bath consisting of N spins is purified, while the central spin points up at $t = 0$. Magnifications of the magnetization for larger values of t are shown in the insets.

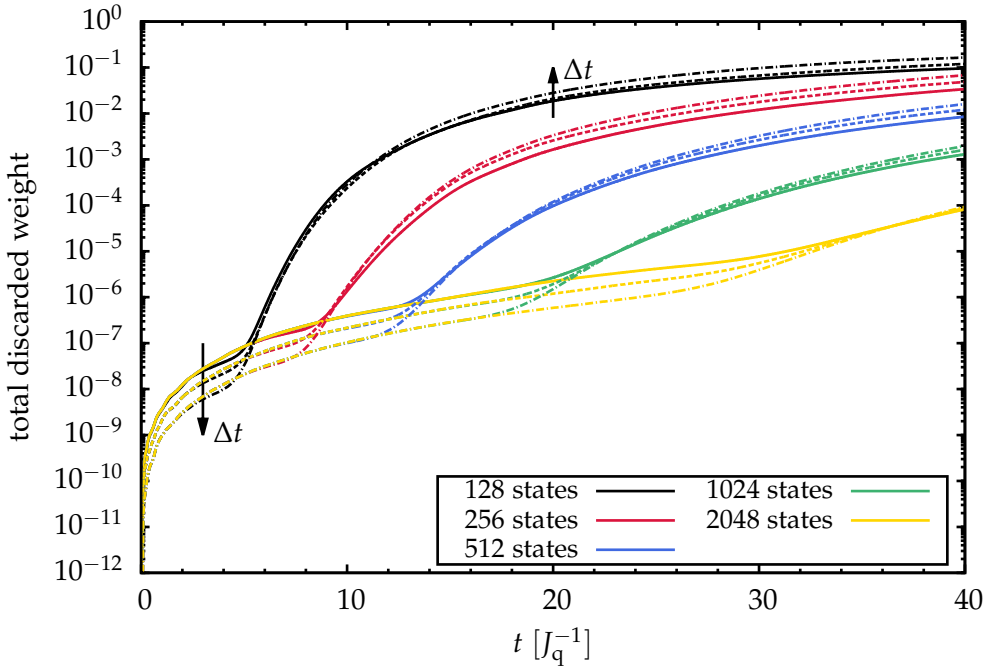

(a) $N = 19$ bath spins

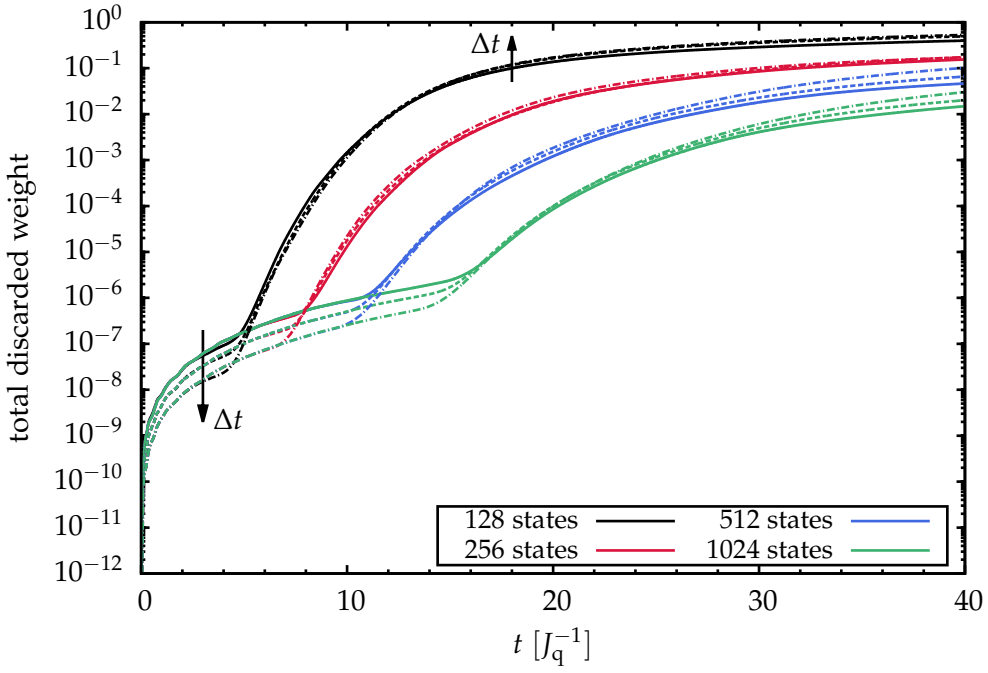

(b) $N = 49$ bath spins

Fig. 2.21: Total discarded weight for the curves shown in Figs. 2.20 and 2.22. Solid lines correspond to the time interval $\Delta t = 0.01\, J_q^{-1}$, dashed lines to $\Delta t = 0.02\, J_q^{-1}$ and dashed-dotted lines to $\Delta t = 0.05\, J_q^{-1}$.

The value of Δt has also an impact on the total discarded weight as it controls the number of performed sweeps and thereby the number of truncations. Hence, increasing Δt should lead to a decrease of the total discarded weight because the number of truncations is reduced. As expected, the total discarded weight plotted in Fig. 2.21 decreases with increasing time interval Δt for small values of t. However, for larger times the situation inverts although a smaller number of truncations is involved. But one has to keep in mind that larger time intervals lead to larger integration errors. By comparing the total discarded weight for $m = 1024$ states and the magnetization in Fig. 2.20, one estimates that the deviations due to finite Δt observed close to $t = 40\, J_{\mathrm{q}}^{-1}$ are of the same order as the total discarded weight. For $N = 19$ bath spins, the TS error $\sim \Delta t^2$ is comparable to the total discarded weight so that it could cause the deviation as well.

In total, all magnetizations calculated for the two bath sizes agree nicely. The observed deviation for larger times does not exceed a few percent. On the discussed time scale, this is an acceptable result for $N = 49$ bath spins. In particular, the relative deviation of the different magnetization curves corresponds roughly to the size of the total discarded weight or TS error. Since the time interval $\Delta t = 0.01\, J_{\mathrm{q}}^{-1}$ has the smallest TS error as well as the smallest total discarded weight, it is employed for all future calculations.

Next, we consider the dependence on the number of tracked states m. The magnetization of the central spin for different values of m and a fixed time interval $\Delta t = 0.01\, J_{\mathrm{q}}^{-1}$ is plotted in Fig. 2.22. The short-time behavior including the minimum and the initial value of the plateau is captured by all calculations for the two presented bath sizes. As soon as the plateau emerges, the calculations employing only a small number of $m = 128$ or $m = 256$ states quickly collapse. Already for $m = 512$ states, acceptable results are obtained. The respective relative deviation is less than a few percent for both bath sizes. The accuracy should even be better for a larger number of states. For $N = 19$ bath spins, no clear distinction between the results for $m = 1024$ and $m = 2048$ states can be made on the scale of the inset shown in Fig. 2.22 a). We refrain from discussing the $m = 2048$ curve for $N = 49$ bath spins because the corresponding calculation would take more than two weeks time. But the improvement for $m = 1024$ states should be similar to the $N = 19$ case. Overall, the accuracy should be of the order of the truncation or TS error as already pointed out in the discussion for different time intervals Δt.

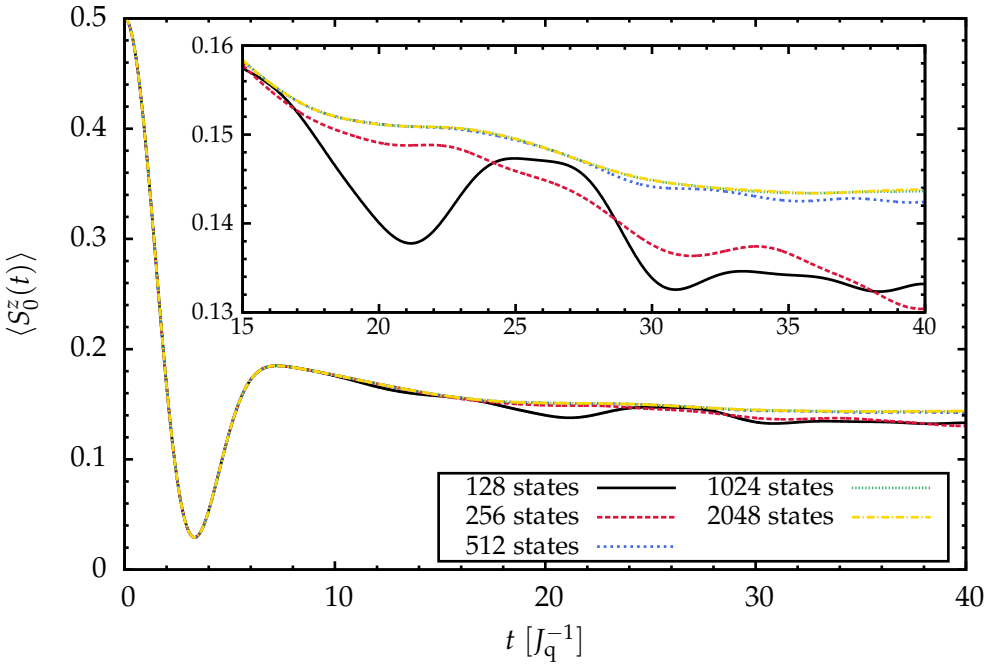

(a) $N = 19$ bath spins

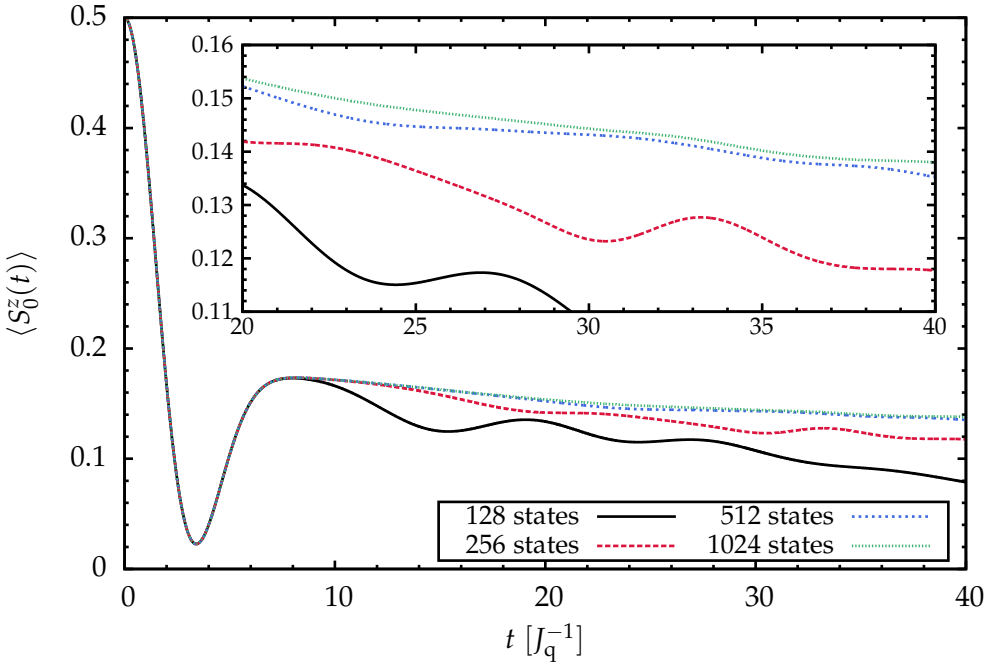

(b) $N = 49$ bath spins

Fig. 2.22: The same as in Fig. 2.20, but now for different values of m and a fixed time interval $\Delta t = 0.01\, J_q^{-1}$.

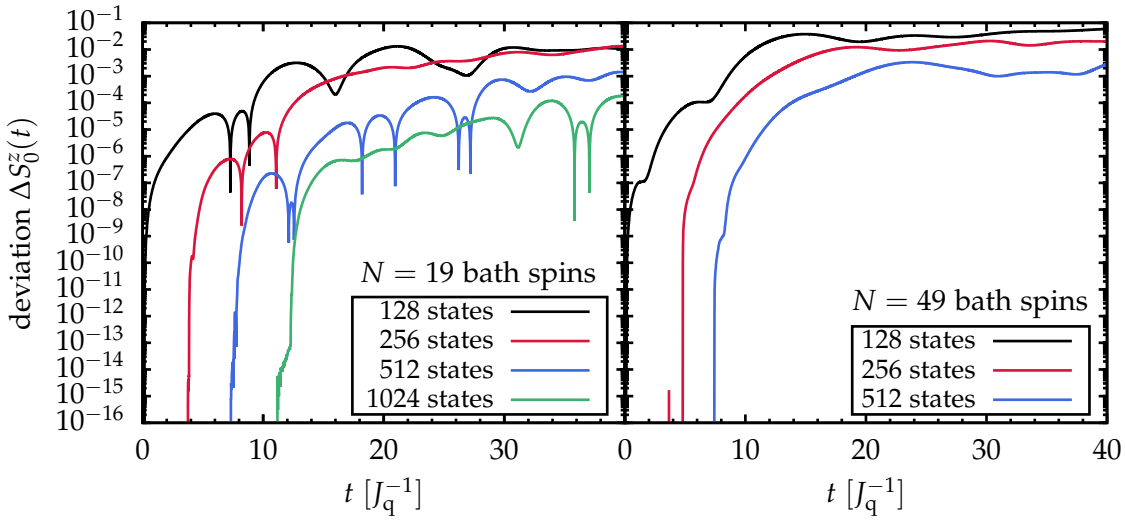

Fig. 2.23: Deviation of the magnetization of the central spin $\Delta S_0^z(t)$ for the data shown in Fig. 2.22. As reference curve, the results obtained for $m = 2048$ states ($N = 19$, left panel) and for $m = 1024$ states ($N = 49$, right panel) were used.

2.6.1 Runaway time

In Sect. 2.5.2.1, we have briefly introduced the runaway time t_r [GKSS05]. For $t < t_r$, the total error is dominated by the error of the TS decomposition, while for $t > t_r$ the total discarded weight dominates the total error. The runaway time t_r can be obtained from the deviation of the DMRG result from the exact result. However, exact results for the purified bath are rarely available. Hence, we follow an alternative route suggested in Ref. [GKSS05]. The deviation $\Delta S_0^z(t)$ plotted in Fig. 2.23 is calculated with respect to a reference curve of $\langle S_0^z(t)\rangle$ corresponding to the calculation using the largest number of states. This curve can be assumed to be exact compared to the results involving smaller values of m. Since the TS error does not depend on m, the deviation $\Delta S_0^z(t)$ is smaller than a predefined threshold $\varepsilon_r = 10^{-15}$ up to $t = t_r$. For $t > t_r$, the total discarded weight begins to dominate and the deviation acquires a finite value which increases with time t.

The runaway time t_r, as indicated by the quick rises in Fig. 2.23, is plotted as a function of m in Fig. 2.24. In addition to $N = 19$ and $N = 49$, it is presented for baths of intermediate sizes containing $N = 29$ and $N = 39$ bath spins. Interestingly, the runaway time t_r does not depend on the bath size. *This very important result implies that there should be no significant decrease of the accuracy for larger bath sizes*. We stress that the t_r is not related to the kink observed in the total discarded weight, see Fig. 2.21. The kink is observed for all discussed methods, while the discussion of the runaway time is solely restricted to the TS decomposition. There, the total error is composed of the truncation and the TS error. The latter is independent of the number of tracked states m. By regarding the absolute deviation $\Delta S_0^z(t)$

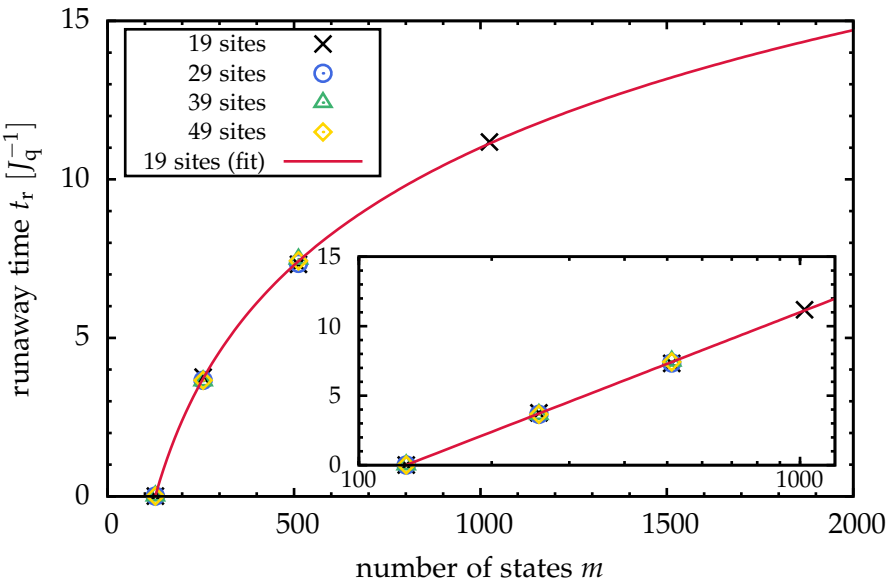

Fig. 2.24: Runaway time t_r extracted from Fig. 2.23 as a function of the number of states m. In addition, the runaway times for $N = 29$ and $N = 39$ bath spins are shown. As illustrated by the inset, the dependence of t_r on m is logarithmic. The solid line represents a logarithmic fit for $N = 19$ bath spins.

between two curves obtained for different values of m but for the same time interval Δt, the TS error is eliminated in $\Delta S_0^z(t)$. Hence, $\Delta S_0^z(t)$ is virtually zero up to the runaway time t_r where the total discarded weight starts to dominate the total error. Consequently, the runaway time does not make any statement about the absolute error, only about the relation between the TS error and the total discarded weight of two different curves.

The inset shown in Fig. 2.24 reveals a logarithmic dependence of t_r on m. Consequently, a substantial increase of the number of tracked states does not make any sense because an exponential growth in m is required for a linear increase of t_r. This observation differs from the one in Ref. [GKSS05] where an approximately linear dependence on m was found for the spin-1/2 XX chain. However, a logarithmic dependence was found as well by Barmettler *et al.* [BPG+10]. In their approach, the time evolution was implemented in the framework of matrix product states for infinite system sizes (iMPS). They also investigated the XX chain but for a different initial state than Ref. [GKSS05]. With respect to our results for the central spin model, no significant influence of Δt on the runaway time t_r is observed because the used values for Δt all lie closely together.

The runaway time can be interpreted as very pessimistic boundary for the reachable time scales in the real-time evolution based on the TS decomposition. From our experience, the method yields reliable results far beyond t_r, see the discussion in the present and the previous section.

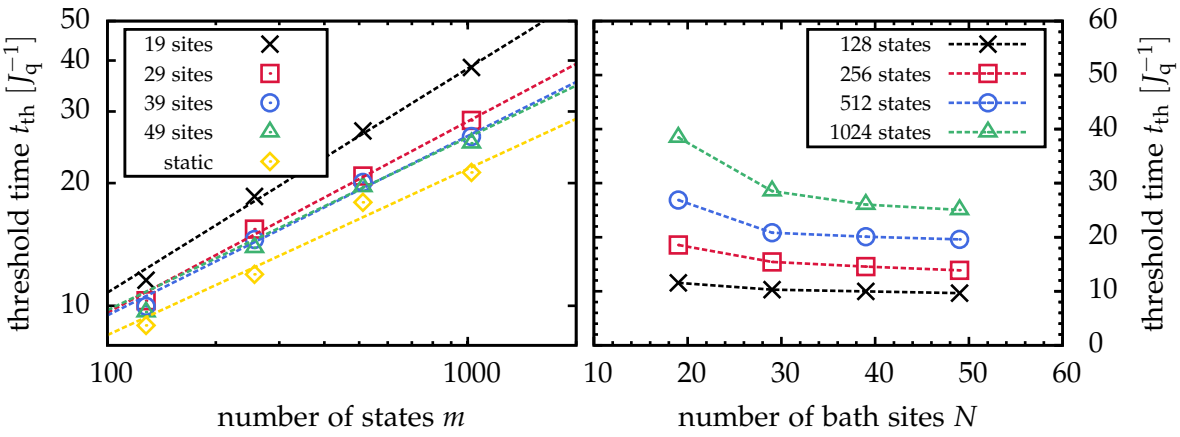

Fig. 2.25: Threshold time $t_{\rm th}$ (2.73) as a function of the number of states m (left panel) and as a function of the number of bath spins (right panel). The dashed lines in the left panel represent the power laws $t_{\rm th}(m) = a_N \cdot m^{\alpha_N}$ obtained by fits to the corresponding data points for N bath spins. The yellow curve in the left panel represents the static limit $N \to \infty$ which was obtained by extrapolating the results from the right panel as a function of $1/N$. The fitted exponents read: $\alpha_{19} = 0.55$; $\alpha_{29} = 0.47$; $\alpha_{39} = 0.44$; $\alpha_{49} = 0.42$; $\alpha_\infty = 0.41$. Aside from $m = 128$ states, $t_{\rm th}$ as a function of m fulfills the power laws really well.

2.6.2 Threshold time

We argued before that the accuracy seems to be limited essentially by the total discarded weight which dominates the total error for $t > t_{\rm r}$. This suggests the introduction of a threshold time

$$t_{\rm th} := t|_{\text{total discarded weight} \leq \varepsilon_{\rm th}} \tag{2.73}$$

determined by the magnitude of the total discarded weight. Considering our previous findings, the value $\varepsilon_{\rm th} = 10^{-3}$ appears to be an appropriate choice for the boundary of the total discarded weight. In Fig. 2.25, the extracted threshold time $t_{\rm th}$ is depicted as a function of the number of tracked states m (left panel) and as a function of the bath size N (right panel). As a function of m, we also plot the result of the static limit $N \to \infty$. The corresponding data points were obtained by an $1/N$-extrapolation of the data points in the right panel. The double logarithmic scaling of the axis in the left panel suggests that the threshold time follows a power law for larger values of m. This is underlined by the fits represented by the dashed lines, which are in nice agreement with the data points for $m \geq 256$. The fitted exponent is approximately $\alpha_{19} = 0.55$ for $N = 19$ and decreases with increasing bath size to $\alpha_{49} = 0.42$, see caption of Fig. 2.25 for details. This is already very close to the static limit where the exponent acquires the value $\alpha_\infty = 0.41$. Thus, the

threshold time as a function of m grows slower than than the square root for large numbers of bath spins. The exponent saturates already for moderately sized baths as indicated by the almost identical dependence on m for $N \geq 39$ bath spins. A saturation for large bath sizes is also stressed by the right panel of Fig. 2.25 where the threshold time is plotted as a function of N for different values of m.

The observed saturation agrees with the behavior of the runaway time t_r, where no dependence of N is observed at all, see Fig. 2.24. Both results, the logarithmic improvement of t_r with m and the growth of t_{th} with approximately the square root of m, discourage us from using a large number of tracked states for the DMRG calculations. Our previous results suggest that $m = 1024$ is a very suitable value for the investigated time scale $t = 0\text{-}40\, J_q^{-1}$. The accuracy is good and should not decrease much further for larger N. Considering the detected logarithm (Fig. 2.24) and the power law (Fig. 2.25, left panel) no significant improvement will be reached for $m > 1024$.

Furthermore, a larger number of tracked states leads to a noticeable increase of the runtime as illustrated in the left panel of Fig. 2.26. As a function of m, the runtime fulfills a power law. The corresponding exponent obtained from a fit to the data points is roughly $1.7 \sim 1.8$. It is independent of N because the runtime is solely determined by the dimension m of the matrices and vectors which have to be multiplied. Of course, the size N of the bath still has an impact on the prefactor of the power law. The non-integer value for the exponent stems from the employment of sparse matrices whose effective dimension is smaller than m. For dense matrices, the runtime of the matrix-vector multiplications inside one block would be of $\mathcal{O}(m^2)$, while the action of the superblock Hamiltonian would be calculated in $\mathcal{O}(m^3)$ steps. However, the latter is not strictly required for the real-time evolution using the TS decomposition unless the energy has to be calculated. The fits shown in the right panel of Fig. 2.26 reveal the expected linear dependence of the runtime on the number of bath spins N. Thus, a further increase of m should be avoided due to the power-law behavior. Larger bath sizes are easy to access, since the amount of CPU times only increases linearly in N.

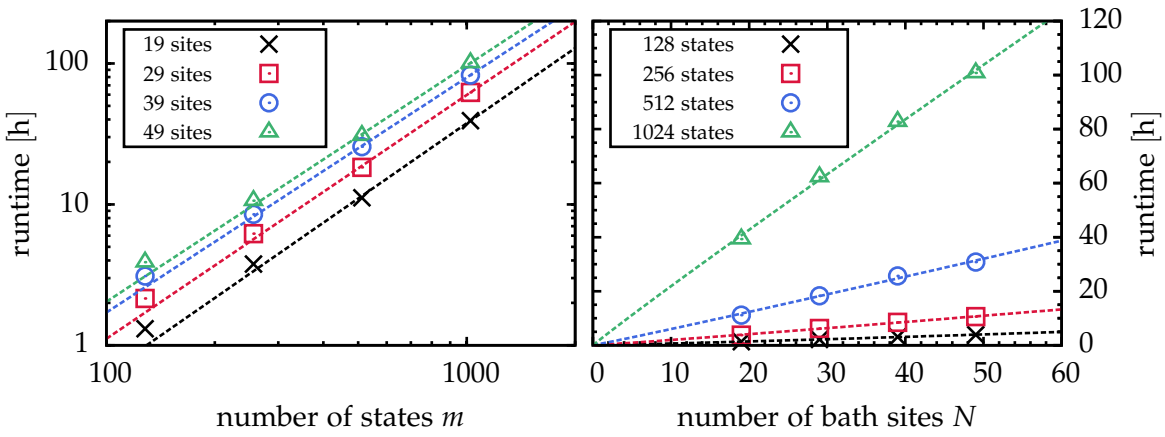

Fig. 2.26: Runtime of the second order TS decomposition up to $t = 40\, J_q^{-1}$ for $\Delta t = 0.01\, J_q^{-1}$ as a function of m (left panel) and as a function of N (right panel). The dashed lines are fits which underline the power law behavior of the runtime in m and the linear behavior in N, respectively.

2.6.3 Entanglement entropy

Before closing this section, we comment briefly on the entanglement entropy

$$S_E(t) = -\sum_i w_i \log_2 w_i, \tag{2.74}$$

where the sum runs over all eigenvalues w_i of the reduced density matrix of the system block. In the left panel of Fig. 2.27, the entanglement entropy $S_E(t)/S_E^{max}$ normalized to its maximum value S_E^{max} is plotted for $N = 19$ and $N = 49$ bath spins. It increases fast for $t > 0$ and obtains a maximum at the position of the minimum of the magnetization of the central spin, see Fig. 2.22. After the plateau has emerged, the normalized entanglement entropy stays almost constant and exhibits only a marginal growth. There is almost no dependence on N which underlines our previous observation that larger baths do not lead to a noticeable worsening of the results. Even for small values of t, the entanglement entropy acquires $\approx 65\,\%$ of its maximum value which is already significant. This is a possible explanation for the fast growing total discarded weight, see Fig. 2.21. However, a tendency towards a further increase for $t > 40\, J_q^{-1}$ can hardly be observed. Furthermore, no distinct features can be detected which could explain the presence of the kink in the total discarded weight.

Note, however, that the entanglement entropy depends not only on t but also on the configuration of the superblock. In the TS approach, the configuration of the superblock before and after the sweep from $t - \Delta t$ to t is determined by the TS decomposition (2.48).

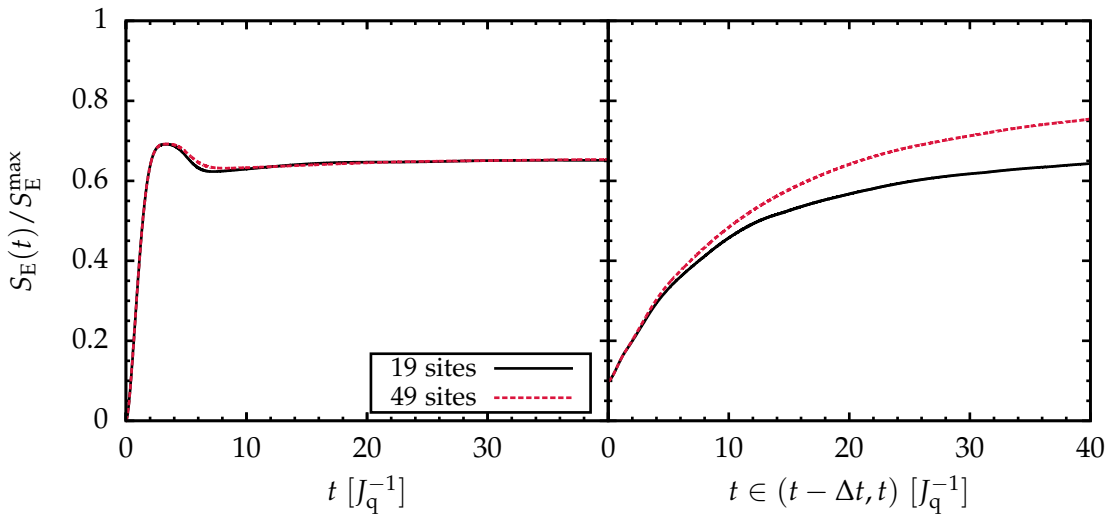

Fig. 2.27: Time dependence of the entanglement entropy $S_e(t)$ (2.74) normalized by its maximum value S_E^{max} for $m = 1024$ states. The left panel depicts the entanglement entropy at time t. In the right panel, the maximum value of the entanglement entropy during the sweep from $t - \Delta t$ to t is plotted.

Thus, measurements at time t are always performed for a system block of either minimum or maximum size. We usually use the latter configuration where the environment block only contains the central site. According to the Schmidt decomposition introduced in Sect. 2.1.2.3, the number of non-zero eigenvalues of the reduced density matrix of the system block is limited by the dimension of the smallest block. Hence, the maximum value for the left panel in Fig. 2.27 is $S_E^{max} = 1$ and not $S_E^{max} = \log_2 m$ because the environment block consists of only two states.

In addition, the maximum value of the normalized entanglement entropy $S_E(t)/S_E^{max}$ during the sweep from $t - \Delta t$ to t is plotted in the right panel of Fig. 2.27. The entanglement entropy acquires its maximum value for symmetric configurations of the system and the environment block. Hence, the corresponding maximum is $S_E^{max} = 10$. Overall, the behavior of the maximum value of the normalized entanglement entropy between $t - \Delta t$ and t agrees roughly with the curve in the left panel. However, the shape is completely different and the monotonic growth is more pronounced for larger times so that the curve explains the increasing worsening of the results with t. In addition, the curve for $N = 49$ bath spins acquires larger values than the one for $N = 19$ bath spins. A more detailed understanding may be achieved from an intensive analysis of the spectrum of the reduced density matrix. But this lies beyond the scope of the present thesis.

2.6.4 Summary

In conclusion, the optimal parameters for the tDMRG calculations in the central spin model are $m = 1024$ states and a time interval of $\Delta t = 0.01\, J_\mathrm{q}^{-1}$. Thereby, the real-time evolution employing the TS decomposition yields a good accuracy up to intermediate time scales $t = 40\, J_\mathrm{q}^{-1}$ where the observed error should not exceed the area of a few percent. The investigation of the runaway time t_r and the threshold time t_th revealed that the accuracy saturates at an acceptable value for larger bath sizes, which are reachable within a linear increase of CPU time. Even for larger times $t > 40\, J_\mathrm{q}^{-1}$ the TS decomposition may yield qualitatively correct results because a direct breakdown cannot be observed in contrast to the other approaches. Results obtained from the Krylov approach or the Chebychev expansion often exhibit a pronounced and unexpected deviation for larger times, so that their failure is usually visible to the naked eye.

2.7 Results for larger bath sizes

In this section, results for larger numbers of bath spins N are presented and discussed. The focus lies on the short-time behavior and its dependence on N. As before, the coupling constants J_i are given by the exemplary uniform distribution introduced in Eq. (1.8), see Sect. 1.4. If not stated otherwise, the parameters for the DMRG calculations are always chosen to be $m = 1024$ and $\Delta t = 0.01\, J_\mathrm{q}^{-1}$ from here on. All results are obtained at infinite temperature using purified states, see Sect. 2.3.2. The long-time behavior is addressed in the following chapters.

2.7.1 Zero-field limit

We continue with the discussion of the central spin in the zero-field limit where all external fields vanish. Due to the absence of a magnetic field, the model and accordingly all observables are completely isotropic.

The results for the autocorrelation function $\langle S_0^z(t) S_0^z(0)\rangle$ of the central spin are plotted in Fig. 2.28. The dependence on N is not very distinctive and fast convergence with increasing N is observed. No distinction can be made between the results for $N = 499$ and $N = 999$ bath spins so that we can assume that the autocorrelation function of the central spin

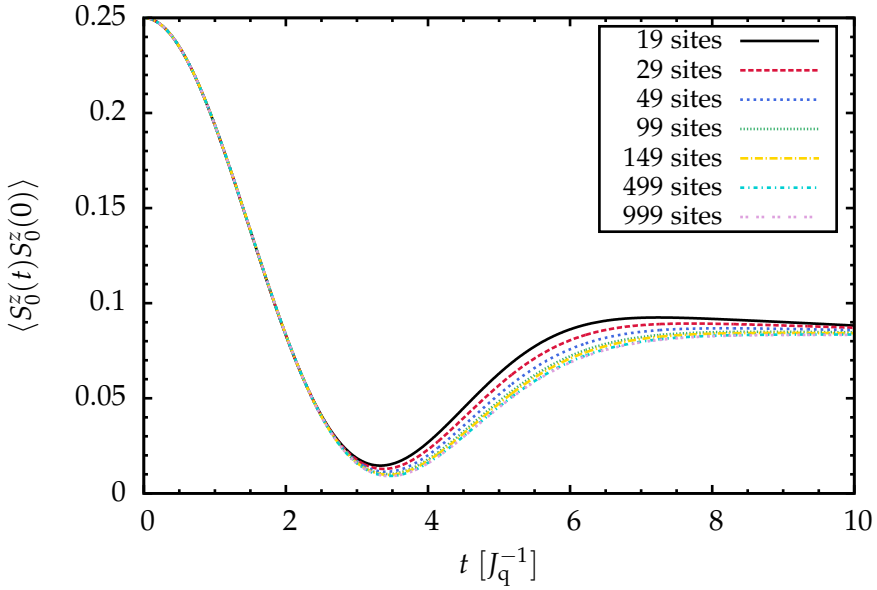

Fig. 2.28: Short-time behavior of the autocorrelation function $\langle S_0^z(t)S_0^z(0)\rangle$ of the central spin in the zero-field limit.

has already converged to the static limit $N \to \infty$. The initial decay of the plateau which is visible for small numbers of bath spins vanishes completely for the shown time scale $t = 0$-$10\,J_q^{-1}$. Thereby, the plateau emerging for $t > 4\,J_q^{-1}$ is stabilized at $\langle S_0^z(t)S_0^z(0)\rangle = 1/12$ for $t \approx 10\,J_q^{-1}$.

Overall, the qualitative behavior our results is in agreement with other findings, see for instance Refs. [AHDDH06, ZDAH+06, FS13b]. Independent from our studies, similar results up to $N = 48$ bath spins were recently obtained from a combination of Bethe ansatz and Monte Carlo sampling [FS13b]. For intermediate time scales $t \gtrsim 5\,J_q^{-1}$, they observed a slight decay of the coherence factor of the central spin which is equivalent to our discussion of the autocorrelation function in the zero-field limit. We return to these findings in Chapters 3 and 4, where the behavior for $t \geq 10\,J_q^{-1}$ is studied. Large nuclear baths containing $N \geq 2000$ spins were addressed in Refs. [AHDDH06, ZDAH+06]. Note, however, that these papers do not discuss the fully quantum model. Moreover, they do not feature a discussion of the convergence with N, which is already achieved for $N \approx 1000$ bath spins according to our results presented in Fig. 2.28.

We stress that the observed plateau $\langle S_0^z(t)S_0^z(0)\rangle = 1/12$ for $t \to \infty$ corresponds indeed to the static limit. In the isotropic model, the initial value $\langle S_0^z(0)\rangle = 1/2$ of the central spin is equally distributed around all three axis for large times. Expressed in terms of the autocorrelation function, one obtains $\langle S_0^z(t)S_0^z(0)\rangle = 1/2 \cdot 1/2 \cdot 1/3 = 1/12$ which is exactly the value observed in the numerical data. Note that the formation of the plateau

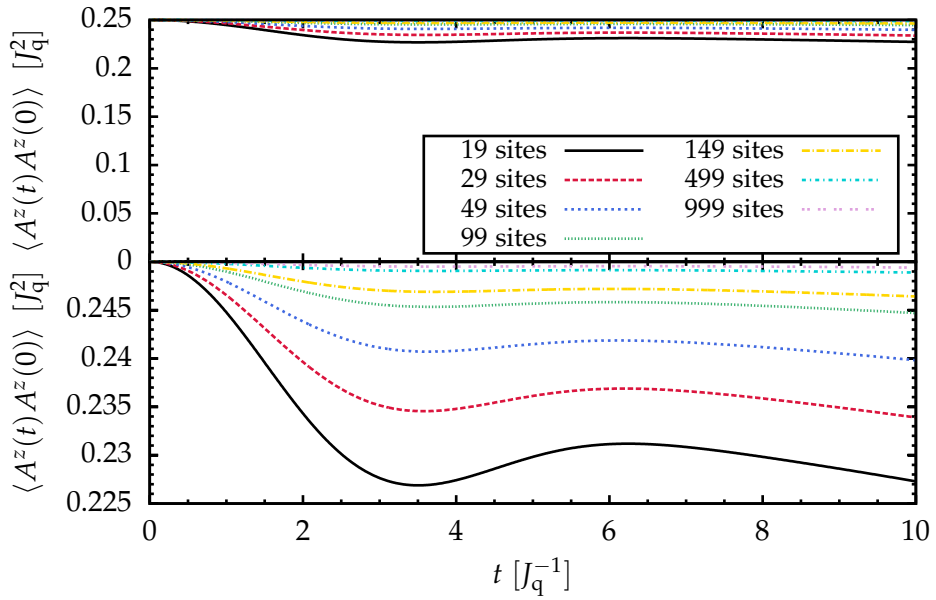

Fig. 2.29: Short-time behavior of the autocorrelation function $\langle A^z(t)A^z(0)\rangle$ of the Overhauser field in the zero-field limit. The lower panel contains the same data as the upper panel, but the y-axis is magnified significantly.

can also be derived from a discussion of the static fluctuations of the bath [MER02] or in the framework of average Hamiltonian theory, see next chapter.

Concerning the autocorrelation function $\langle A^z(t)A^z(0)\rangle$ of the Overhauser field, quantum fluctuations are absent in the static limit $N \to \infty$. As shown in Fig. 2.29, the quantum fluctuations are already almost frozen out for $N = 999$ bath spins. In the limit $N \to \infty$, the autocorrelation function of the Overhauser field takes the constant value $\langle A^z(t)A^z(0)\rangle = J_q^2/4$. The static character of $\langle A^z(t)A^z(0)\rangle$ also explains the minor impact of N on the behavior the central spin related to the quickly decaying influence of quantum fluctuations.

2.7.2 Influence of an external magnetic field

Now, we extend our discussion to the central spin model in the presence of an external field as defined in Eq. (1.6). We distinguish between two different scenarios. In the first one, varying local fields are applied to the bath spins only. This is a simple example for inducing an intrinsic dynamics in the bath. The second scenario, where the external field is solely restricted to the central spin, depicts the situation relevant for experiment. For the latter scenario, the regime of a weak, an intermediate, and a strong external field is considered. In general, an external field induces additional fluctuations in the bath leading to a fast and complete decay of the transverse components of the autocorrelation functions of the central spin and a substantial stabilization of the autocorrelation in the spin direction parallel to the external field.

A magnetic field applied in z-direction breaks the isotropic symmetry of the model. Thus, a zz-autocorrelation function such as $\langle S_0^z(t)S_0^z(0)\rangle$ displays a different behavior than the corresponding xx-autocorrelation function $\langle S_0^x(t)S_0^x(0)\rangle$. Note that the isotropy in the xy-plane is still preserved so that the yy-autocorrelation functions are identical to the xx-autocorrelation functions. In addition, the cross-correlations functions $\langle S_0^x(t)S_0^y(0)\rangle$ and $\langle A^x(t)A^y(0)\rangle$ in the direction perpendicular to the external field are non-zero. They are odd functions. Furthermore, the relation $\langle A^x(t)A^y(0)\rangle \equiv -\langle A^y(t)A^x(0)\rangle$ holds. All other autocorrelation and cross-correlation functions vanish.

2.7.2.1 Fields applied to bath spins

In the following, external magnetic fields

$$h_i = \frac{h_{\mathrm{low}} - h_{\mathrm{up}}}{N-1} i + \frac{N h_{\mathrm{up}} - h_{\mathrm{low}}}{N-1}, \quad i \in \{1, \ldots, N\}, \tag{2.75}$$

are applied to the bath spins. The local fields represented by Eq. (2.75) fulfill an uniform distribution in the interval $h_i \in [h_{\mathrm{low}}, h_{\mathrm{up}}]$ with $h_{\mathrm{low}} < h_{\mathrm{up}}$. They are arranged in descending order so that the strongest field is applied to the bath spin with strongest coupling to the central spin. This scenario does not necessarily depict a situation reflected by experiments. Merely, the external fields are used to induce an artificial dynamics in the bath without introducing dipolar couplings between the bath spins. Here, we choose $h_{\mathrm{low}} = 0.8\, J_{\mathrm{q}}$ and $h_{\mathrm{up}} = 1.2\, J_{\mathrm{q}}$. Then, the external magnetic fields with mean value $\overline{h}_i = J_{\mathrm{q}}$ induce a precession of the bath spins which is much stronger than their precession induced by the field of the central spin because the coupling constants as defined in Eq. (1.8)

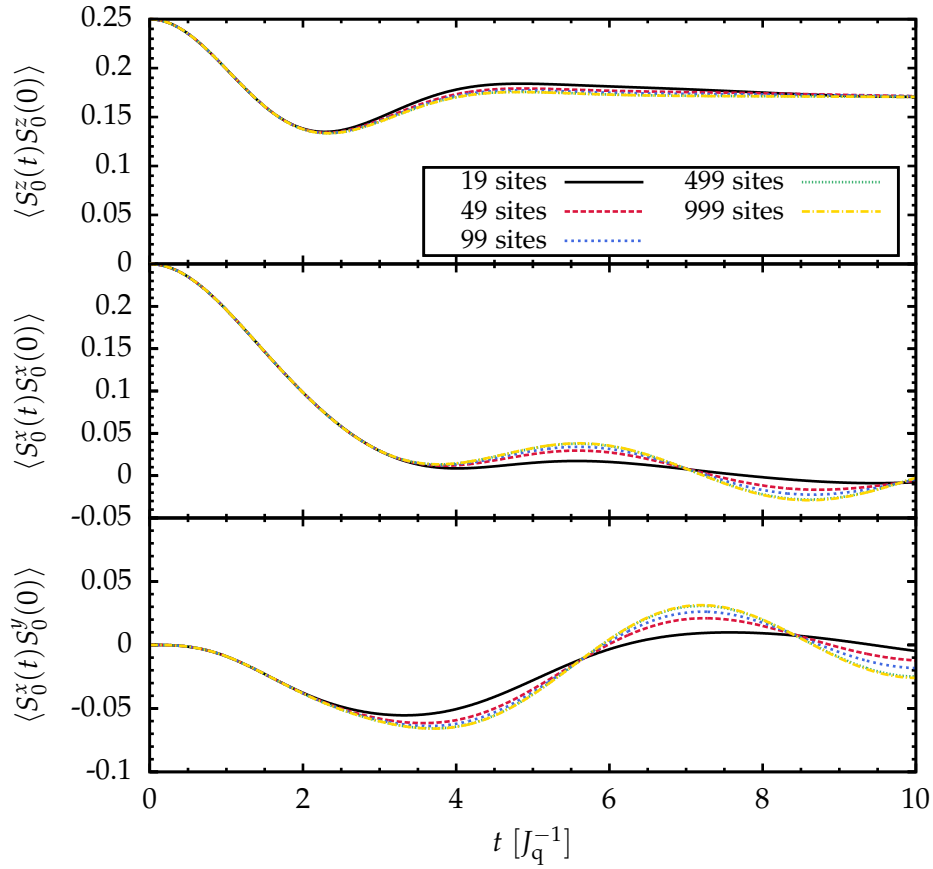

Fig. 2.30: Short-time behavior of the non-vanishing autocorrelation functions $\langle S_0^\alpha(t)S_0^\beta(0)\rangle$ of the central spin with external fields applied to the bath spins according to Eq. (2.75).

are much smaller than the external field.

As shown in Fig. 2.30, the autocorrelation function $\langle S_0^z(t)S_0^z(0)\rangle$ of the central spin is stabilized at a larger value than in the isotropic case by the external magnetic field applied to the bath spins. The same behavior is observed in the corresponding autocorrelation function $\langle A^z(t)A^z(0)\rangle$ of the bath in Fig. 2.31. The dependence on the bath size is similar to the previously discussed zero-field limit. Except the marginal N-dependence of $\langle A^z(t)A^z(0)\rangle$, all correlation functions are already converged for $N = 499$ bath spins.

In the direction perpendicular to the external field, a well-defined oscillation is observed in the fluctuations of the bath. The period of the oscillation is affected by the order of the local fields. Here, the observed oscillation frequency $\omega \approx 1.1\, J_q$ is slightly larger than J_q because the strength of the external fields h_i increases with increasing coupling J_i. On the contrary, a reversed order leads to a lower frequency $\omega = 0.9\, J_q$ as the bath spin with strongest local field has the weakest coupling to the central spin. Since no other differences

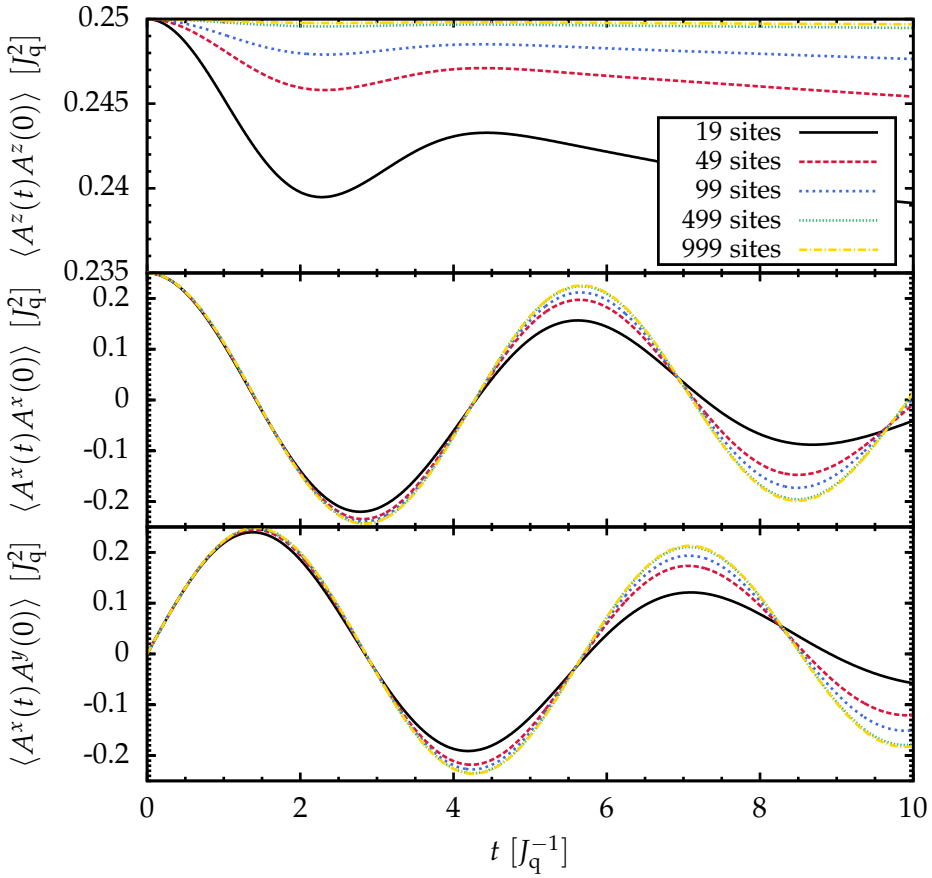

Fig. 2.31: Short-time behavior of the non-vanishing autocorrelation functions $\langle A^\alpha(t)A^\beta(0)\rangle$ of the bath with external fields applied to the bath spins according to Eq. (2.75). Note the deviating scale of the y-axis for $\langle A^z(t)A^z(0)\rangle$.

arise, we refrain from discussing this situation in detail. If the external fields $h_i \in [h_{\text{low}}, h_{\text{up}}]$ were applied in random order, the oscillation frequency would approximately be given by $\omega \approx J_q$. But we refrain from doing so because we want to avoid any kind of randomness in our DMRG calculations.

The amplitude of $\langle A^x(t)A^x(0)\rangle$ decays slowly on the presented time scale $t = 0\text{-}10\, J_q^{-1}$. Concerning the central spin, the fluctuating bath induces a relatively fast dephasing as seen in the middle panel of Fig. 2.30. In addition, the autocorrelation function $\langle S_0^x(t)S_0^x(0)\rangle$ exhibits an oscillation which follows the oscillation of the autocorrelation function of the bath. The same behavior is observed for the cross-correlation functions $\langle S_0^x(t)S_0^y(0)\rangle$ and $\langle A^x(t)A^y(0)\rangle$ as shown in the lower panels of Fig. 2.30 and Fig. 2.31, respectively.

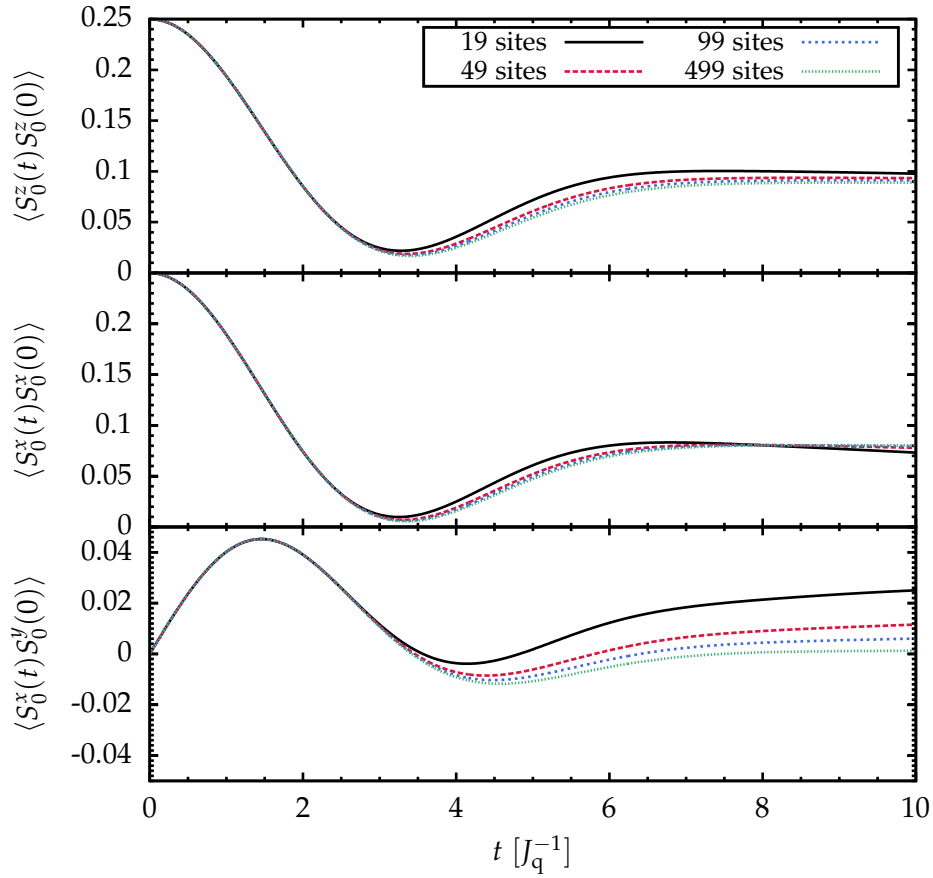

Fig. 2.32: Short-time behavior of the non-vanishing autocorrelation functions $\langle S_0^\alpha(t)S_0^\beta(0)\rangle$ of the central spin for a weak external field $h_0 = 0.2\,J_q$.

2.7.2.2 Field applied to central spin

The previously discussed scenario, where the external magnetic field was applied to the bath spins only, does not reflect a situation occurring in experiment because the magnetic field h_0 acting on the central spin cannot be neglected. Furthermore, the Zeeman splitting is much weaker for a nuclear spin than for an electron spin. Due to the large proton mass m_p, the ratio of the nuclear magneton μ_N and the Bohr magneton μ_B deviates significantly from unity

$$\frac{\mu_N}{\mu_B} \approx \frac{m_e}{m_p} \approx 10^{-3}.$$

Hence, the field acting on the nuclear spins can be neglected while the influence of the field h_0 acting on the electron spin is crucial. In the following, the short-time behavior is discussed for a weak, an intermediate, and a strong value of the field h_0.

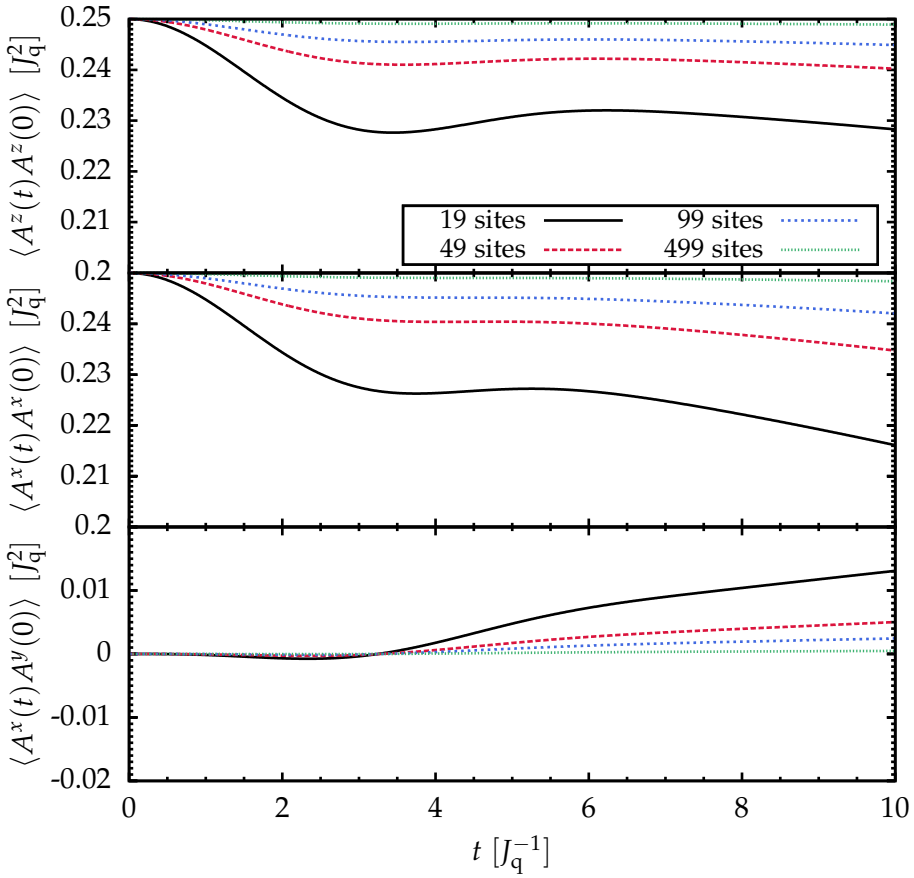

Fig. 2.33: Short-time behavior of the non-vanishing autocorrelation functions $\langle A^\alpha(t)A^\beta(0)\rangle$ of the bath for a weak external field $h_0 = 0.2\,J_q$. Note the different scale of the y-axis in the lowest panel.

Weak-field regime

The results for a weak external magnetic field $h_0 = 0.2\,J_q$ are presented in Figs. 2.32 (autocorrelation of the central spin) and Fig. 2.33 (autocorrelation of the Overhauser field). As $h_0 < J_q$, the influence of the external field is rather weak because the precession of the central spin is dominated by the stronger Overhauser field $\vec{A}$. Compared to the results for the zero-field limit from Sect. 2.7.1, a slight stabilization of the electron spin is observed in z-direction. Perpendicular to the external field, a tendency towards dephasing can be recognized by comparing the isotropic autocorrelation function in the zero-field limit (Fig. 2.28) with the autocorrelation function $\langle S_0^x(t)S_0^x(0)\rangle$ (Fig. 2.32, middle panel). The dephasing is induced by the additional precession of the central spin in the external field. The small amplitude of the cross-correlation function $\langle S_0^x(t)S_0^y(0)\rangle$ underlines the weak effect of h_0 on the dynamics of the central spin. Furthermore, most of the curves for different values of N are still distinguishable. The static limit $N \to \infty$ emerges for

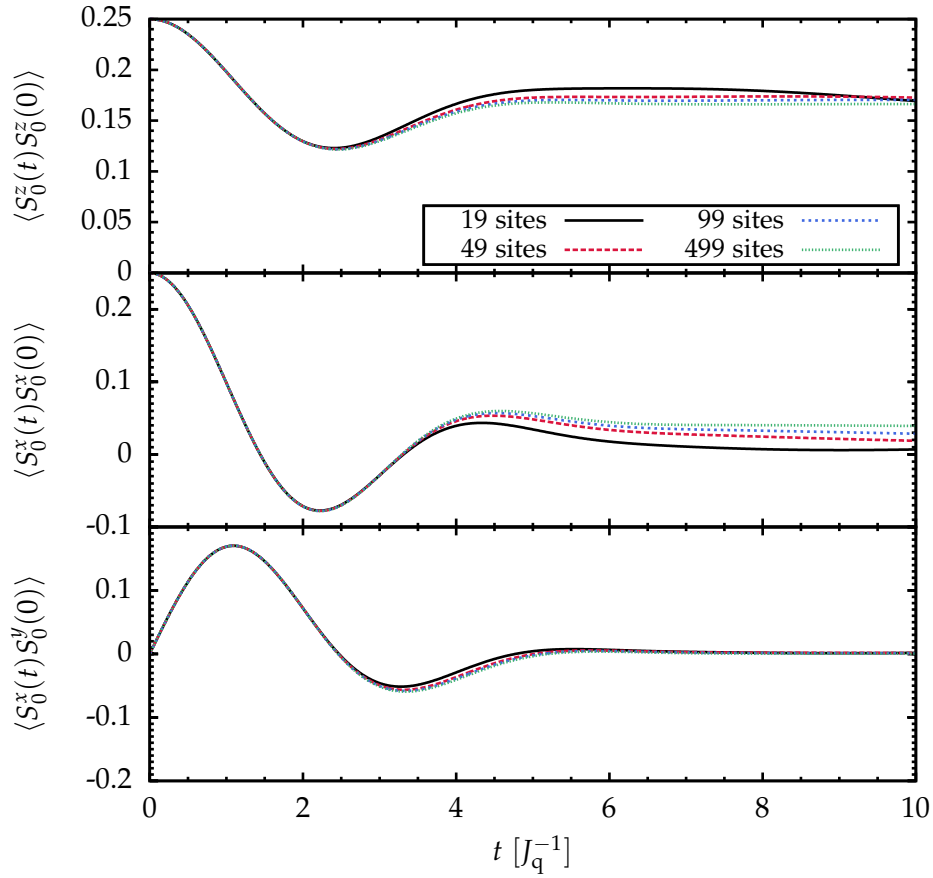

Fig. 2.34: The same as in Fig. 2.32, but now for an intermediate external field $h_0 = J_q$.

$N \approx$ 499-999 bath spins, since the regime of a weak external field $h_0 = 0.2\,J_q$ is closely located to the zero-field limit.

The influence of the weak magnetic field on the dynamics of the Overhauser field is similar, see Fig. 2.33. A stabilization is observed in the spin direction parallel to the external field while a slight damping occurs in the perpendicular directions. The amplitude of the cross-correlation function is even smaller than for the corresponding function of the central spin. The curves for different values of N are clearly distinguishable. For larger bath sizes, the influence of h_0 on the bath is weaker because of the N-dependence $J_i \sim 1/\sqrt{N}$ of the coupling constants. Thus, the bath spins in larger systems are less exposed to the fluctuations of the central spin.

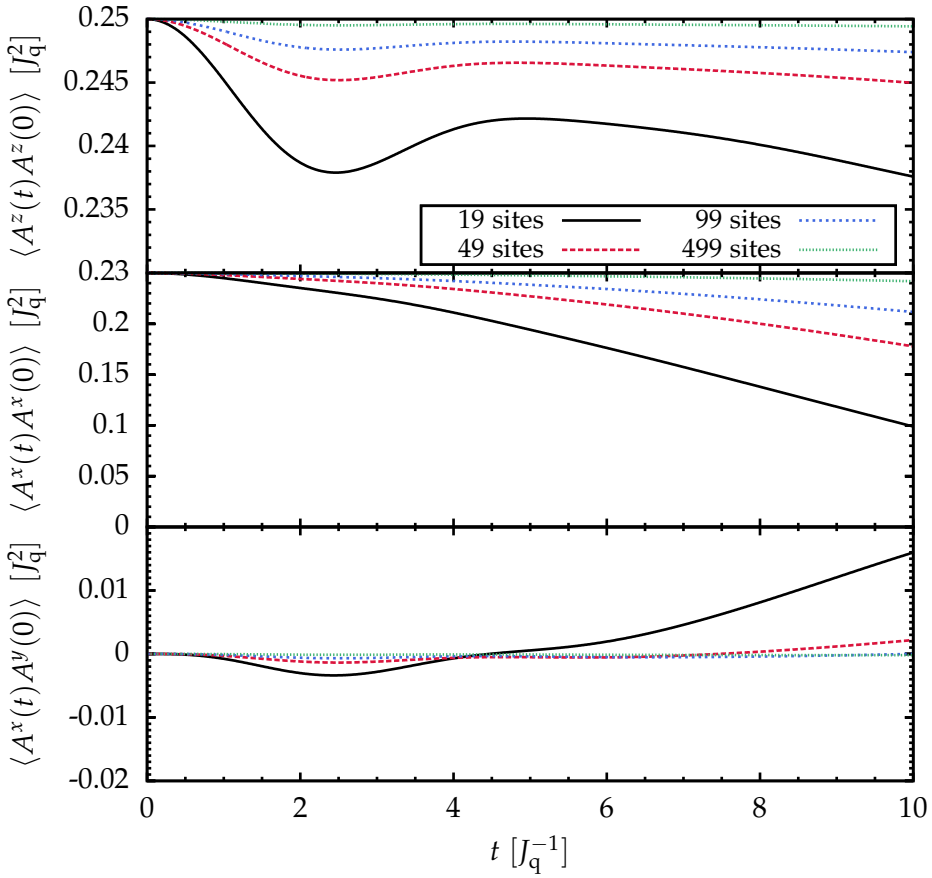

Fig. 2.35: The same as in Fig. 2.33, but now for an intermediate external field $h_0 = J_q$.

Intermediate-field regime

In Fig. 2.34, the central spin dynamics is presented for an intermediate value $h_0 = J_q$ so that the external field has the strength of the energy scale J_q. Thus, the decay of the transverse components of the autocorrelation functions of the central spin takes place on the time scale of the short-time dynamics defined by J_q. Furthermore, the Larmor precision with $\omega_{\text{Larmor}} = J_q$ is expressed by the well-defined oscillation of the transverse correlation functions. The cross-correlation function obtains a significant amplitude which decays after one period of the electron spin precession. As expected, the z-component of the electron spin exhibits a stronger stabilization due to the higher value of h_0.

The autocorrelation functions of the Overhauser field are depicted in Fig. 2.35. A stronger tendency towards dephasing can now be observed compared to the weak-field regime presented in Fig. 2.33. But for a large bath, the intermediate value of h_0 does not induce any significant fluctuations because its influence is still too small. The fluctuations in z-direction are much stronger suppressed than before and almost completely frozen for $N = 499$ bath spins.

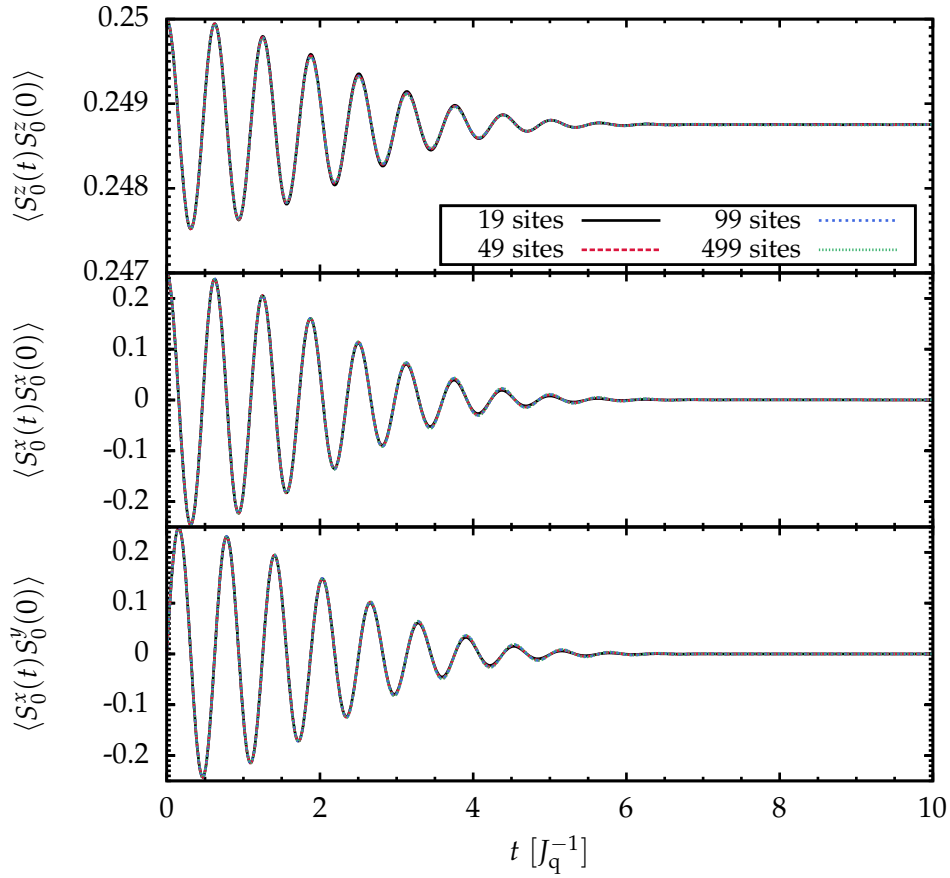

Fig. 2.36: The same as in Fig. 2.32, but now for a strong external field $h_0 = 10\,J_q$.

Strong-field regime

In the strong-field regime presented in Fig. 2.36, the N-dependence of the autocorrelation functions of the central spin is almost completely gone. All curves show a well-defined oscillation with the Larmor frequency $\omega_{\text{Larmor}} = 10\,J_q$ of the central spin. A complete decay of the transverse components is observed on the presented time scale $t = 0\text{-}10\,J_q^{-1}$. The z-component of the central spin is stabilized after some initial oscillations. Further relaxation cannot be estimated on the studied time scale.

The Larmor precision of the central spin is also reflected in the initial oscillations of the autocorrelation function $\langle A^z(t)A^z(0)\rangle$ of the Overhauser field as shown in the upper panel of Fig. 2.37. The oscillation vanishes on the same time scale as the oscillation for the central spin, but a small decay remains. With respect to the scaling of the y-axis in the upper panel, the bath fluctuations in z-direction can be regarded as frozen. No distinct oscillations can be detected for the transverse components. Up to intermediate bath sizes, the autocorre-

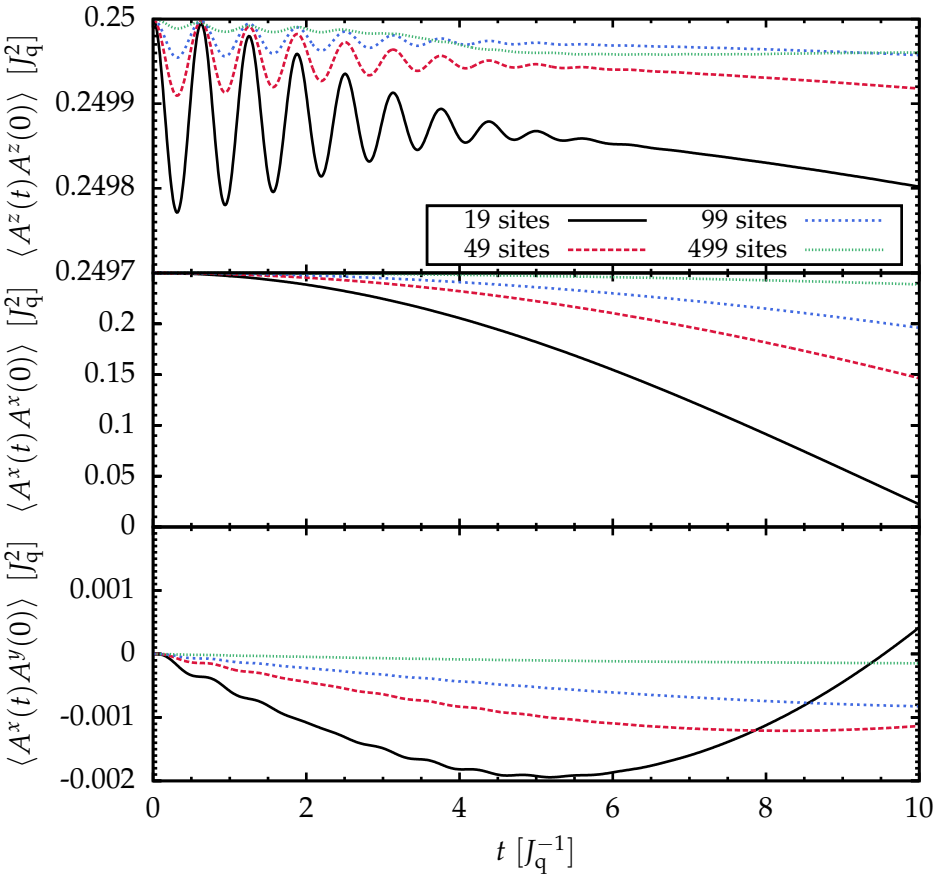

Fig. 2.37: The same as in Fig. 2.33, but now for a strong external field $h_0 = 10\,J_q$.

lation function $\langle A^x(t)A^x(0)\rangle$ decays noticeably. The fluctuations of the cross-correlation function are even stronger suppressed than before.

Before closing the discussion of the strong-field regime, we briefly address the dependence of the dephasing time T_2 on the external magnetic field h_0. The time scale T_2 can be obtained from a fit of the function

$$\langle S_0^x(t)S_0^x(0)\rangle = \frac{1}{4}\cos(\omega t)\,\mathrm{e}^{-\frac{t^2}{2T_2^2}} \tag{2.76}$$

to the DMRG data. In the following, we stick to the static limit and use the DMRG results for $N = 499$ bath spins as input. The extracted dephasing times T_2 are plotted in Fig. 2.38 up to very large values of h_0. The value $h_0 = 2\,J_q$ is the lowest value of the external field for which a fit of the DMRG data to Eq. (2.76) yields a reasonable result. As indicated by the small error bars, the function defined in Eq. (2.76) approximates the autocorrelation function $\langle S_0^x(t)S_0^x(0)\rangle$ for $h_0 > 5\,J_q$ extremely well. The error of the fit increases for smaller values of h_0 where Eq. (2.76) does not fully explain the behavior of the autocorrelation

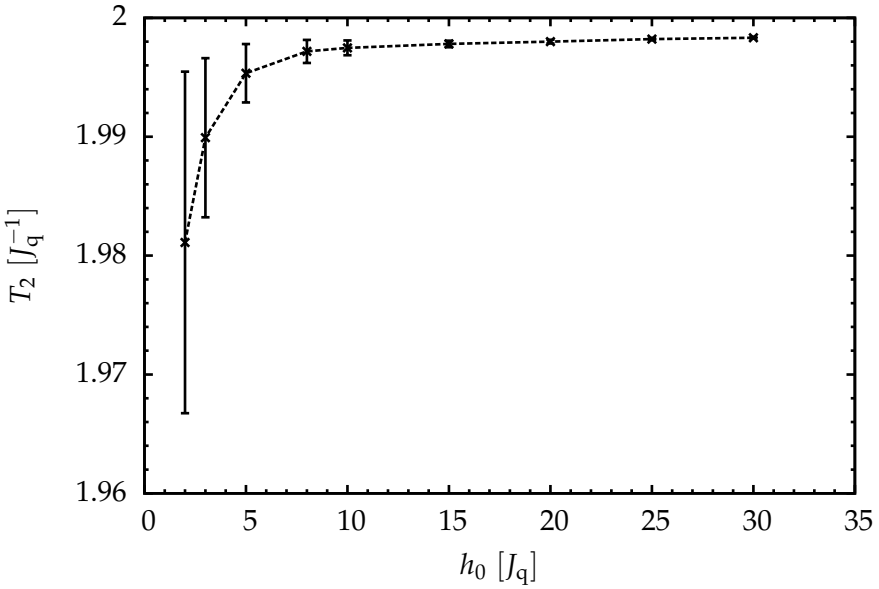

Fig. 2.38: Dependence of the dephasing time T_2 on the external magnetic field h_0. The values for T_2 were obtained by fitting the DMRG autocorrelation function $\langle S_0^x(t)S_0^x(0)\rangle$ for $N = 499$ bath spins to the function defined in Eq. (2.76). The error bars represent the errors of the fitted dephasing times T_2. Note the scale of the y-axis.

function $\langle S_0^x(t)S_0^x(0)\rangle$. But with respect to the scale of the y-axis in Fig. 2.38, almost no dependence of T_2 on h_0 can be observed. Thus, we may establish that the dephasing time T_2 is solely determined by the intrinsic time scale J_q^{-1} of the hyperfine interaction. The external field h_0 does not have any influence on the dephasing time T_2, it just defines the Larmor frequency of the central spin.

Summary

From the weak-field to the strong-field regime, the relaxation of the Overhauser field and the central spin is stronger and stronger suppressed. The additional Larmor precession of the central spin in the external field induces dephasing for all transverse autocorrelation functions. For weak magnetic fields, the transverse autocorrelation function exhibits a smooth decay, while damped oscillations at the Larmor frequency of the central spin are observed for stronger magnetic fields. A similar transition emerges for the autocorrelation functions in parallel to the magnetic field. Instead of decaying to zero, the corresponding autocorrelation function acquires a finite value depending on the strength of the external field. In Ref. [ZDAH$^+$06], this crossover was also described for the magnetization of the central spin. However, they did not make any statement on the dephasing because the central spin was initially prepared as a fully polarized spin. In the strong-field limit, the

static limit $N \to \infty$ already emerges in the autocorrelation functions of the central spin for a small number of bath spins. As initially explained, the fluctuations of the Overhauser field exhibit a N-dependence due to $J_i \sim 1/\sqrt{N}$.

A finite external field simplifies the DMRG calculations significantly. Due to the suppression of the relaxation in the spin direction parallel to external field, less states become important so that the total discarded weight is reduced. Compared to the zero-field limit, the total discarded weight at $t = 10\, J_\mathrm{q}^{-1}$ is at least one order of magnitude lower in the regime of a strong external field. Moreover, a significant growth for larger times does not occur. But there is also a substantial impact of the external field on the runtime of the DMRG code. For strong external fields, a DMRG run for $N = 499$ bath spins up to $t = 10\, J_\mathrm{q}^{-1}$ is completed within a few hours compared to one to two days in the zero-field limit. The enormous speedup has to be attributed to the dynamic adjustment of the number of kept states.

Chapter 3

Classical Gaussian Fluctuations in the Zero-Field Limit

Contents

In the previous chapter, the numerical treatment of the central spin model (1.4) in the framework of DMRG was presented. Thereby, we gained access to relatively large spin baths consisting of up to $N \approx 1000$ spins. But reachable times are limited to $t \approx 30$-$50\, J_{\mathrm{q}}^{-1}$ because of the accumulating discarded weight and the growing entanglement in the system.

Now, we take one step back from the heavy numerical treatment with DMRG and consult an effective semiclassical picture for the dynamics of the central spin. To this end, we first motivate the approximation of the bath by a classical random field in Sect. 3.1. The semiclassical model is studied by numerical simulation and on the basis of average Hamiltonian theory (AHT). The latter is derived in leading order in Sect. 3.2. In Sect. 3.3, we demonstrate that the dynamics of the central spin is indeed captured well by the semiclassical model for a large number of bath spins up to intermediate times. But the comparison with DMRG and AHT reveals that there is still room for improving the numerical simulation of the semiclassical model. Hence, the separate treatment of the conserved total spin as well as the classical treatment of the central spin is addressed in Sect. 3.4. The present discussion of the semiclassical model is solely restricted to the zero-field limit. In Sect. 3.5, a short remark concerning the semiclassical model in finite external fields is made.

3.1 Motivation & introduction

For the zero-field limit discussed in Sect. 2.7.1, the DMRG results revealed a fast convergence of the autocorrelation functions and an almost static bath already for moderate numbers of bath spins. This is a strong hint that quantum fluctuations play only a minor role in the bath. The classical character of the bath achieves further backup by the following simple analytic argument. We regard the square of an operator norm

$$\mathrm{Tr}\left(A^{\alpha}\right)^{2} = \frac{1}{4}\sum_{i=1}^{N} J_i^2 = \frac{J_{\mathrm{q}}^2}{4} \tag{3.1a}$$

where the operator A^{α} represents the component α of the Overhauser field as defined in Eq. (1.5a). Obviously, one concludes that $A^{\alpha} = \mathcal{O}(1)$ if the coupling constants are scaled as motivated in Sect. 1.4. But for the commutator we find

$$\mathrm{Tr}\left(\left[A^{\alpha}, A^{\beta}\right]\right)^{2} = \frac{1}{4}\sum_{i=1}^{N} J_i^4 \propto \frac{1}{4}\sum_{i=1}^{N}\left(\frac{J_{\mathrm{q}}^2}{N}\right)^{2} = \frac{1}{4}\frac{J_{\mathrm{q}}^4}{N}. \tag{3.1b}$$

This implies that the norm of the commutator vanishes in the limit $N \to \infty$ because $[A^{\alpha}, A^{\beta}] = \mathcal{O}(J_{\mathrm{q}}^2/\sqrt{N})$. Hence, the bath can be regarded as a classical variable for a large number of bath spins. This is well described by the Hamiltonian

$$H_{\mathrm{sc}} = \vec{\eta}\,(t)\cdot\vec{S}_0, \tag{3.2}$$

where an electron spin-1/2 interacts with a classical random field $\vec{\eta}(t)$.

The semiclassical model in Eq. (3.2) is derived from the central spin model (1.5) by replacing the quantum bath $\vec{A}$ by a classical fluctuating field $\vec{\eta}(t)$. Thereby, back-action effects of the central spin on the fluctuations of the Overhauser field are neglected. According to the central limit theorem, the bath obeys Gaussian statistics because it consists of a large number of independent two-level fluctuations. Thus, the fluctuations are fully defined by their autocorrelation function

$$g_{\alpha\beta}\left(t_1 - t_2\right) = \overline{\eta_{\alpha}\left(t_1\right)\eta_{\beta}\left(t_2\right)} \tag{3.3a}$$

and their mean value

$$\overline{\eta\left(t\right)} = 0. \tag{3.3b}$$

Without loss of generality, it is set to zero because a finite mean value only creates a constant offset.

When comparing the semiclassical model to the quantum model, the correlation function $g_{\alpha\beta}(t)$ of the gaussian noise is identified with the autocorrelation $\langle A^\alpha(t)A^\beta(0)\rangle$ of the Overhauser field. In the present chapter, we focus on the zero-field limit where all non-diagonal correlations vanish and all diagonal correlations are isotropic: $g(t) \equiv g_{\alpha\alpha}(t)$, see Sect. 2.7.1 for comparison.

The investigation of a semiclassical model for the central spin problem, where the bath is replaced by an effective field, was already addressed before [MER02, EN04]. In a recent preprint by Witzel *et al.* [WYD13], a semiclassical approximation was applied to the spin bath in the strong-field limit. The correlation function of the bath was obtained from a correlated cluster expansion [YL08a, YL09, WCCDS12]. Due to the strong external field, spin flips between central spin and bath were neglected. The decoherence was induced by spectral diffusion, which is typical for cluster expansions, see Sect. 1.5.2 for details. Hence, their semiclassical ansatz only comprised dephasing, the relaxation of the central spin was excluded.

3.2 Average Hamiltonian theory

We begin with an analytical investigation of the semiclassical model in the zero-field limit on the level of average Hamiltonian theory. For a time-dependent Hamiltonian, the analytical evaluation of the time-evolution operator

$$U(t) = \mathcal{T}\exp\left[-\mathrm{i}\int_0^t \mathrm{d}t'\, H(t')\right], \tag{3.4}$$

in a closed form is usually impossible due to the time-ordering expressed by the operator $\mathcal{T}$. To simplify the time-evolution operator, we apply the Magnus expansion [Mag54, BCOR09] which enables a systematic analytical treatment of Eq. (3.4). In leading order, the time-ordering in Eq. (3.4) is simply neglected. The approximation

$$U(t) \approx \exp\left[-\mathrm{i}\int_0^t \mathrm{d}t'\, H(t')\right] \tag{3.5}$$

is certainly justified if the Hamiltonian is almost static or if it fluctuates very quickly. For the semiclassical picture, a static Hamiltonian corresponds to a constant correlation function of the noise. This is well supported by the DMRG results for the zero-field limit

discussed in Sect. 2.7.1. The operator A^{α} (1.5a) representing the Overhauser field contains all local operators of the bath and the corresponding autocorrelation function is nearly constant, see Fig. 2.29 for details.

By exploiting the properties of the Pauli matrices and the spherical symmetry of the fluctuations in the zero-field limit, the time-evolution operator (3.5) is rewritten in the form

$$U(t) = \cos\frac{v}{2}\cdot\mathbb{1} - \mathrm{i}\sin\frac{v}{2}\cdot\sigma^{\vec{v}} \tag{3.6}$$

where the vector

$$\vec{v} := \int_0^t \mathrm{d}t'\,\vec{\eta}(t') \tag{3.7}$$

stands for the leading order of the Magnus expansion. It contains the complete time dependence. The operator

$$\begin{aligned}\sigma^{\vec{v}} &= \frac{\vec{\sigma}\cdot\vec{v}}{|\vec{v}|}\\ &= \sin\theta\cos\varphi\,\sigma^x + \sin\theta\sin\varphi\,\sigma^y + \cos\theta\,\sigma^z\end{aligned} \tag{3.8}$$

is the projection of the Pauli matrices along the direction of $\vec{v}$. Here, the angles φ and θ originate from the representation of $\vec{v}$ in spherical coordinates. The simplified form of the time-evolution operator (3.6) is used to calculate the autocorrelation function

$$\langle S_0^z(t)S_0^z(0)\rangle = \frac{1}{8}\,\mathrm{Tr}\left[U^{\dagger}(t)\,\sigma^z U(t)\,\sigma^z\right] \tag{3.9}$$

of the central spin. After some straightforward simplifications, it takes the form

$$\langle S_0^z(t)\,S_0^z(0)\rangle = \frac{1}{4}\left[\cos^2\frac{v}{2} + \sin^2\frac{v}{2}\left(2\cos^2\theta - 1\right)\right] \tag{3.10}$$

prior to averaging over v. Next, the average with respect to θ and v has to be carried out. Because of the spin rotational symmetry, the average over the angle θ simply yields $\overline{\cos^2\theta} = 1/3$. The remaining contribution

$$\overline{\langle S_0^z(t)\,S_0^z(0)\rangle} = \frac{1}{4}\overline{\left(\frac{1}{3} + \frac{2}{3}\cos v\right)} \tag{3.11}$$

is averaged with respect to the Gaussian distribution

$$p(v) = \frac{1}{\sqrt{2\pi\,\mathrm{Var}\;v(t)}}\,\mathrm{e}^{-\frac{v^2}{2\,\mathrm{Var}\;v(t)}} \tag{3.12}$$

of the fluctuations. After all integrations have been carried out analytically, the final result for the autocorrelation function of the central spin is given as

$$\overline{\langle S_0^z(t)\, S_0^z(0)\rangle} = \frac{1}{6}\left[\left(1 - \mathrm{Var}\; v(t)\right) \mathrm{e}^{-\frac{\mathrm{Var}\; v(t)}{2}} + \frac{1}{2}\right], \tag{3.13}$$

where the time dependence resides in the variance $\mathrm{Var}\; v(t) = \overline{(\int_0^t \mathrm{d}t'\, \eta(t'))^2}$. It is related to the autocorrelation function of the random noise

$$\mathrm{Var}\; v(t) = 2\int_0^t \mathrm{d}t_1 \int_0^{t_1} \mathrm{d}t_2\, g(t_1 - t_2)\,. \tag{3.14}$$

For the beginning, we discuss a constant autocorrelation function $g(t) = J_\mathrm{q}^2/4$ valid in the limit $N \to \infty$, see Fig. 2.29. Then, the variance $\mathrm{Var}\; v(t) = t^2 J_\mathrm{q}^2/4$ increases quadratically in time and the autocorrelation function of the central spin in leading order of our AHT reads

$$\overline{\langle S_0^z(t)\, S_0^z(0)\rangle} = \frac{1}{6}\left[\mathrm{e}^{-\frac{t^2 J_\mathrm{q}^2}{8}}\left(1 - \frac{t^2 J_\mathrm{q}^2}{4}\right) + \frac{1}{2}\right]. \tag{3.15}$$

This result is identical to the one obtained by Merkulov *et al.* [MER02] which was derived from a classical discussion of the static spin bath. Our AHT for the semiclassical model (3.2) has the merit to be based on the Magnus expansion and can be extended systematically to higher orders in nested commutators [BCOR09]. But note that there are no corrections in higher order for a static autocorrelation function. Furthermore, the correlation function $g(t)$ of the fluctuations enters in the general expression for $\langle S_0^z(t) S_0^z(0)\rangle$ from Eq. (3.13) via the variance $\mathrm{Var}\; v(t)$. Hence, the results can easily be adapted to arbitrary correlation functions $g(t)$. They do not necessarily have to be given by an analytic expression, numerical results for $g(t)$ are also legitimate. For example, this may comprise autocorrelation functions obtained from DMRG or experimental results. There, one usually measures the spectrum of the bath which is linked to the real-time correlation function by Fourier transform. We highlight that independently of the actual time dependence of $\mathrm{Var}\; v(t)$, the autocorrelation function in Eq. 3.13 always converges to a plateau of $1/12$ as long as $\mathrm{Var}\; v(t)$ diverges monotonically in time.

Finally, we verify our AHT result by a numerical simulation of the semiclassical model. As we are dealing with a two-level system, the integration is carried out easily. A reduction of the integration error for time-dependent Hamiltonians is achieved by commutator-free exponential time propagators (CFETs) as introduced by Alvermann *et al.* [AF11, AFL12]. The additional numerical effort is negligible because an exact analytical representation of the time-evolution operator of a two-level system is available. Hence, no additional

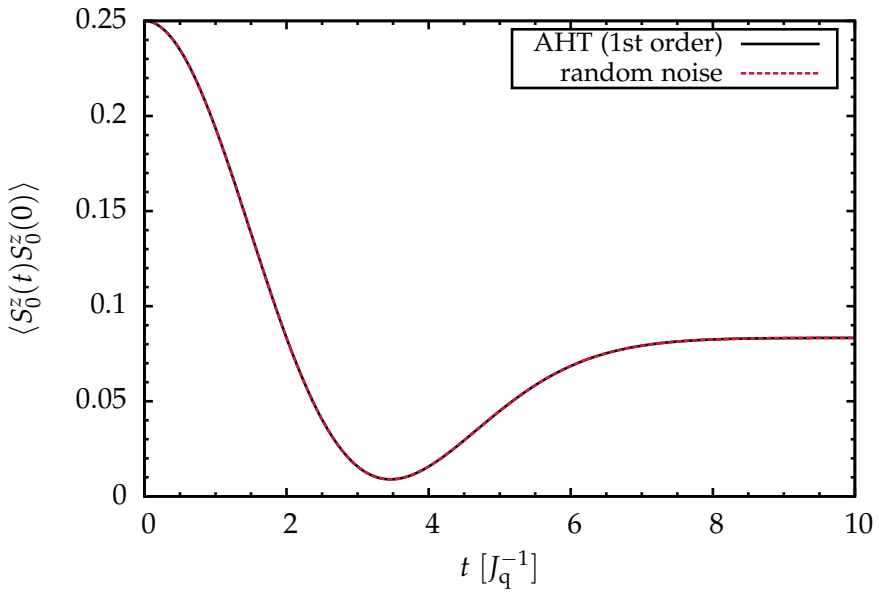

Fig. 3.1: First order AHT result from Eq. (3.15) and result of the numerical simulation involving $M = 100,000$ random fluctuations. Here, the random noise obeys a constant correlation function $g(t) = J_q^2/4$.

diagonalizations are induced by the CFETs. The most costly operation is the sampling of the Gaussian fluctuations $\vec{\eta}(t)$ obeying the predefined autocorrelation function $g(t)$. For this purpose, we developed two algorithms which are introduced in Appendix E. The results for the autocorrelation function $\langle S^z_0(t)S^z_0(0)\rangle$ are plotted in Fig. 3.1. The random noise simulation involved the sampling of $M = 100.000$ random fluctuations $\vec{\eta}(t)$. For each fluctuation $\vec{\eta}(t)$, the time evolution was carried out individually. Finally, the resulting autocorrelation function $\langle S^z_0(t)S^z_0(0)\rangle$ was obtained by averaging over the results for all M random fluctuations. As to be expected, both curves are in perfect agreement so that the AHT resembles the correct physics if the correlation function of the noise is a constant.

3.3 Comparison with DMRG

So far, the AHT result for a constant correlation function of the bath was investigated. But the discussion can be extended to arbitrary types of Gaussian noise. In this section, we identify the correlation function of the Gaussian fluctuations with the correlation function of the Overhauser field in the fully quantum central spin model [SRU13]. Thus, we set

$$g_{\alpha\beta}(t) \equiv \langle A^\alpha(t)\, A^\beta(0)\rangle, \tag{3.16}$$

where the autocorrelation function $\langle A^\alpha(t)\, A^\beta(0)\rangle$ of the Overhauser field is given by the DMRG results presented in Fig. 2.29.

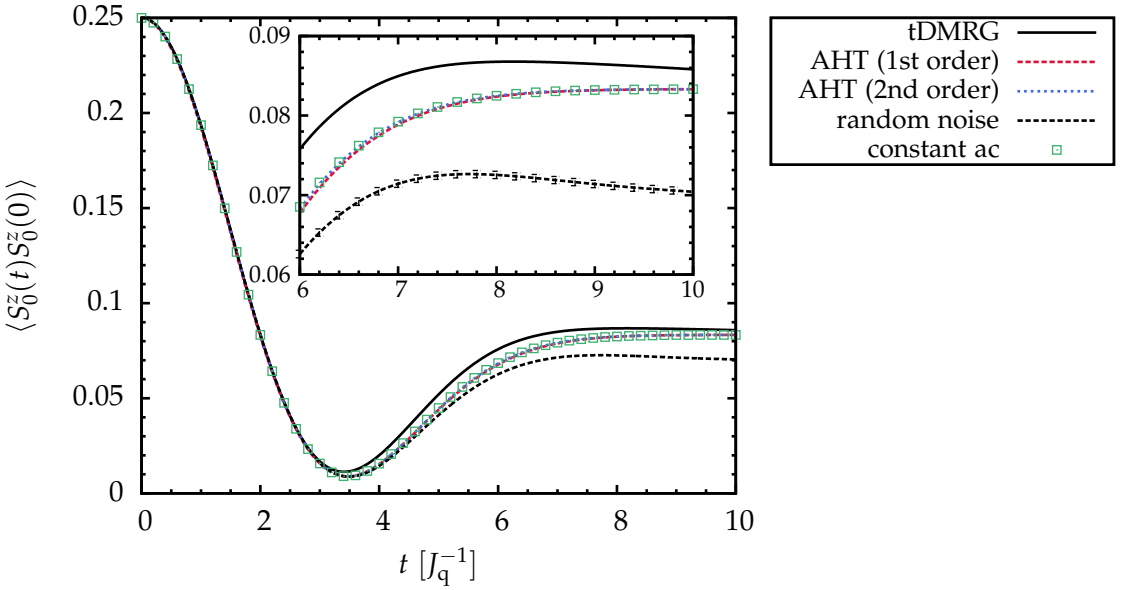

Fig. 3.2: Comparison between the DMRG, the random noise simulation, and the AHT result in first and second order for $N = 49$ bath spins. The AHT and the random noise results have both been calculated with the DMRG autocorrelation function (red and blue lines) and a constant autocorrelation function (constant ac, squares) as input. A magnification for $t \geq 6\,J_q^{-1}$ is shown in the inset. The error bars indicate the error of the random noise simulation caused by averaging over a finite number of $M = 100,000$ fluctuations.

At first, we discuss the behavior for an exemplary system of $N = 49$ bath spins and compare the results of the different methods, namely DMRG, AHT, and the numerical simulation of the semiclassical Hamiltonian. In addition to leading order AHT, the second order involving the second order correction of the Magnus expansion is shown in Fig. 3.2. The second order AHT renormalizes the Gaussian probability distribution, see Appendix D for a detailed derivation. All results in Fig. 3.2 hold for $N = 49$ bath spins. In general, the AHT results are very stable towards small fluctuations of the correlation function. Hence, no quantitative change occurs in the AHT when the slightly time-dependent DMRG autocorrelation is replaced by a completely constant one. Moreover, the second order correction does not lead to any recognizable improvement compared to the first order AHT. For the present scenario, the first order AHT is already close to optimum because the bath is nearly static. In particular, the plateau of the central spin autocorrelation function is not altered in second order. It only depends on the variance for $t \to \infty$ and always emerges as long as Var $v(t) \to \infty$ for $t \to \infty$. Once reached, it persists for all times. A further decay of the plateau as observed in DMRG cannot be explained on the level of the Magnus expansion.

Compared to the other results shown in Fig. 3.2, the AHT results are located between the

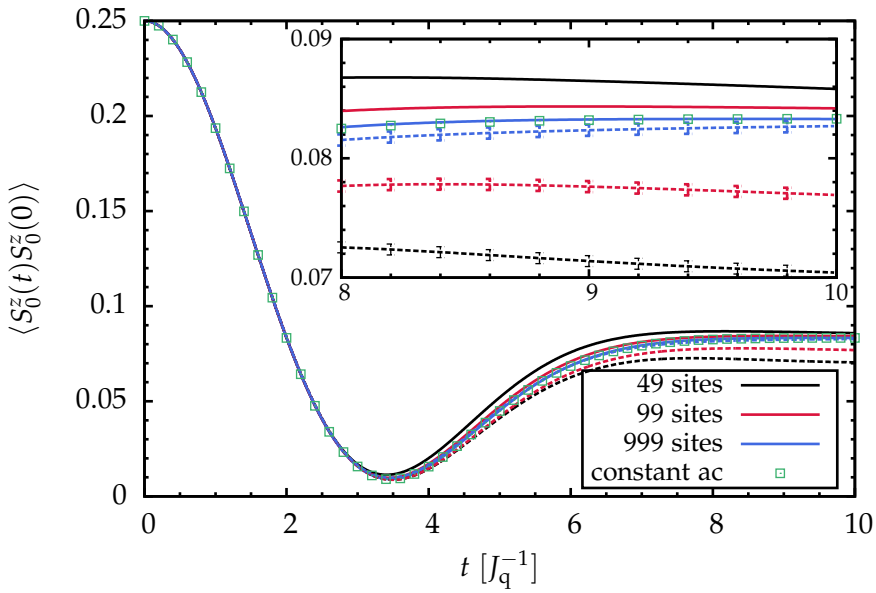

Fig. 3.3: Convergence of DMRG (solid lines) and random noise simulation (dashed lines) towards the AHT result (squares) for the static bath limit. In the random noise simulation, the autocorrelation functions obtained by DMRG are used to sample the fluctuations. The inset contains a magnification of the plateau for $t \geq 8\,J_q^{-1}$. The error bars indicate the error of the random noise simulation caused by averaging over a finite number of $M = 100,000$ fluctuations.

DMRG and the random noise results. The plateau in the DMRG result is located above the AHT result. After it has reached its maximum value, the autocorrelation function again displays a slight decay. Most likely, the decay will sustain for longer times because we are dealing with a finite system. In contrast, the random noise simulation does not reach the plateau of the AHT. After the local minimum close to $t \approx 4\,J_q^{-1}$, the autocorrelation function of the central spin increases slightly but starts to exhibit a decay shortly afterwards. The decay is still slow but much more pronounced than the one observed in the DMRG result.

Now, we proceed to the results in Fig. 3.3 which are obtained for up to $N = 999$ bath spins. In the limit $N \to \infty$, both the DMRG and the random noise result converge to the AHT result which is identical to the random noise simulation for a constant autocorrelation function. The DMRG curves converge from above towards the AHT result, while the random noise curves converge from below. The DMRG result for $N = 999$ bath spins almost lies on top of the AHT result. At first glance, the random noise simulation converges a little bit slower than the DMRG results. However, one has to keep in mind that the sampling in the simulation is always done for a finite number of M random fluctuations. Thus, an error of order $1/\sqrt{M}$ is always present. For a typical number of $M = 100,000$ fluctuations, the error is visible on the scale of the inset in Fig. 3.3 as indicated by the error bars.

The convergence towards the AHT result is expected because the bath becomes more and more static with increasing number of bath spins. To our knowledge, it is the first time that the systematic convergence has been demonstrated. This has to be attributed to DMRG which is capable of treating fairly large system sizes where the convergence sets in. Along with the analytical argument presented Sect. 3.1, our results prove that the bath behaves classically already for a moderate number of bath spins. The convergence in the short-time behavior is observed for $\mathcal{O}(1000)$ bath spins, which is roughly one to two orders of magnitudes smaller than the typical number of nuclear spins interacting with a single electron spin confined in a quantum dot, see Sect. 1.3.

So far, our discussion is restricted to the short time behavior. Recent comparisons between the static bath approximation [MER02] and a combination of Bethe ansatz and Monte Carlo techniques [FS13b] revealed a stronger influence of quantum fluctuations on longer time scales expressed by a fractional decay of the plateau. But the numerical investigation of the central spin model was limited to $N = 48$ bath spins at most so that a conclusion for large baths cannot be drawn. According to Ref. [MER02], the reduction of the plateau by a certain fraction is due to fluctuations in the nuclear spin bath. However, the complete impact of these back-actions effects occurs on a time scale which is not fully captured by DMRG and consequently not by our semiclassical approach which uses the DMRG output for the fluctuations of the Overhauser field as input.

3.4 Optimization of the numerical simulation

The curves from Fig. 3.3 revealed that the plateau $\langle S_0^z(t) S_0^z(0) \rangle = 1/12$ arises in the random noise simulation only when the bath fluctuations are completely frozen. As long as the correlation function of the noise exhibits a marginal decay, the exact value of this plateau is not reached. Moreover, the autocorrelation function of the central spin in the semiclassical picture always displays a decay, even if the correlations decay on very long time scales. The neglect of conservation laws of the full quantum model in the semiclassical treatment is one reason for this behavior.

A well-known example for a conserved quantity in the central spin model is the total spin

$$\vec{I} = \sum_{i=0}^{N} \vec{S}_i. \tag{3.17}$$

The DMRG captures the conservation of the total spin as well as all other conservation laws in the central spin model numerically exact. However, this statement does not hold for the semiclassical model as defined in Eq. (3.2).

3.4.1 Conservation of the total spin

In this section, we present how the conservation of the total spin $\vec{I}$ can be incorporated into the semiclassical model. Therefore, we study the slightly modified Hamiltonian

$$H' = \vec{S}_0 \sum_{i=0}^{N} J_i \vec{S}_i \tag{3.18}$$

for the quantum central spin model. The central spin $\vec{S}_0$ has been included in the sum which was restricted to the bath spins originally. The new contribution induces a constant shift $= 3J_0/4$ in the Hamiltonian for $S = 1/2$. Thus, it has no influence on the relevant physics of the model. The mean value of all couplings is assigned to the coupling constant of the central spin

$$J_0 := \frac{1}{N} \sum_{i=1}^{N} J_i. \tag{3.19}$$

Consequently, the fluctuating field

$$\vec{A} = \sum_{i=0}^{N} J_i \vec{S}_i \tag{3.20a}$$

now comprises the central spin $\vec{S}_0$ in addition to the bath spins. To take the conservation of the total spin into account, we rewrite it in the form

$$\vec{A} = \vec{A}_0 + \Delta\vec{A}. \tag{3.20b}$$

The part

$$\vec{A}_0 = J_0 \vec{I} \tag{3.21a}$$

is constant and conserved, while the contribution

$$\Delta\vec{A} = \sum_{i=1}^{N} (J_i - J_0)\, \vec{S}_i \tag{3.21b}$$

contains the fluctuating part. The separation into two contributions respects the conserved total momentum because the fluctuating part $\Delta\vec{A}$ is always perpendicular to the constant part $\vec{A}_0$, see below. Additionally, the separation is well supported by the results for the quantum model: The correlation function of the bath (see Fig. 2.29) is nearly a constant only modulated by some weak fluctuations on top.

With $\vec{A}_0(t) = \vec{A}_0(0)$, one deduces immediately that the correlation function of the conserved part is given by the constant expression

$$\langle A_0^\alpha(t)\, A_0^\beta(0)\rangle = J_0^2 \frac{N+1}{4}\delta_{\alpha\beta}. \tag{3.22a}$$

We still stick to the isotropic model, but use a general notation so that the present discussion can easily be extended to other symmetries. Moreover, the conserved and the fluctuating part are independent at all times

$$\begin{aligned}\langle A_0^\alpha(t)\,\Delta A_0^\beta(0)\rangle &= \langle A_0^\alpha(0)\,\Delta A_0^\beta(0)\rangle \\ &= \frac{J_0}{4}\delta_{\alpha\beta}\sum_{i=0}^{N}(J_i - J_0) = 0.\end{aligned} \tag{3.22b}$$

Thus, the autocorrelation function of the field $\vec{A}$ acquires the form

$$g_{\alpha\beta}(t) = J_0^2\frac{N+1}{4}\delta_{\alpha\beta} + \Delta g_{\alpha\beta}(t) \tag{3.23}$$

with

$$\Delta g_{\alpha\beta}(t) := \langle \Delta A^\alpha(t)\,\Delta A^\beta(0)\rangle. \tag{3.24}$$

Next, we address the central spin $\vec{S}_0$ which is treated similarly to the field $\vec{A}$

$$\vec{S}_0 = \frac{1}{N+1}\vec{I} + \Delta\vec{S}_0, \tag{3.25}$$

where the fluctuating part reads

$$\Delta\vec{S}_0 = \frac{N}{N+1}\vec{S}_0 - \frac{1}{N+1}\sum_{i=1}^{N}\vec{S}_i \tag{3.26}$$

and the fraction $\vec{I}/(N+1)$ of the total spin $\vec{I}$ (3.17) is the constant contribution. Like for $\vec{A}$, there is no correlation between the constant and the fluctuating part

$$\begin{aligned}\langle I^\alpha(t)\,\Delta S_0^\beta(0)\rangle &= \langle I^\alpha(0)\,\Delta S_0^\beta(0)\rangle \\ &= \frac{1}{4}\frac{N}{N+1} - N\frac{1}{4}\frac{1}{N+1} = 0.\end{aligned} \tag{3.27}$$

Consequently, the autocorrelation function of the central spin $\vec{S}_0$ is given by

$$\langle S_0^\alpha(t)\, S_0^\beta(0)\rangle = \delta_{\alpha\beta}\frac{1}{4}\frac{1}{N+1} + \Delta c_{\alpha\beta}(t) \tag{3.28}$$

with

$$\Delta c_{\alpha\beta}(t) := \langle \Delta S_0^\alpha(t)\, \Delta S_0^\beta(0)\rangle\,. \tag{3.29}$$

In this way, the conserved part has been separated from the fluctuating part for both the central spin and the operator $\vec{A}$. We incorporate this concept into the semiclassical model by regarding the Hamiltonian

$$H'_{\mathrm{sc}} = \vec{\eta}(t)\cdot\Delta\vec{S}_0 \tag{3.30a}$$

which only treats the fluctuating part of the central spin. Since the conserved part is a constant, it does not enter in the latter Hamiltonian. As before, the fluctuating field $\vec{\eta}(t)$ is a random Gaussian variable. But its correlation function is defined by $g_{\alpha\beta}(t)$ from Eq. (3.23) involving the separate treatment of the fluctuating and the conserved part of $\vec{A}$ from Eq. (3.20b). By inserting the expression for $\Delta\vec{S}_0$ in Eq. (3.30a), the semiclassical Hamiltonian may be written as

$$H'_{\mathrm{sc}} = \sum_{i=0}^{N} h_i \tag{3.30b}$$

where

$$h_0 := \frac{N}{N+1}\vec{\eta}(t)\cdot\vec{S}_0 \tag{3.31a}$$

$$h_i := -\frac{1}{N+1}\vec{\eta}(t)\cdot\vec{S}_i, \quad i\in\{1,2,\ldots,N\}\,. \tag{3.31b}$$

Hence, the time evolution of the bath spins $\vec{S}_i$ is completely independent and the fluctuating part $\Delta c_{\alpha\beta}(t)$ of the autocorrelation function of the central spin can be calculated by

$$\Delta c_{\alpha\beta}(t) = \left(\frac{N}{N+1}\right)^2 \Delta c_{\alpha\beta}^{(0)}(t) + \frac{N}{(N+1)^2}\Delta c_{\alpha\beta}^{(i)}(t) \tag{3.32}$$

with the two independent contributions

$$\Delta c_{\alpha\beta}^{(0)}(t) := \langle S_0^\alpha(t)\, S_0^\beta(0)\rangle \quad \text{with } h_0 \text{ from Eq. (3.31a)} \tag{3.33a}$$

$$\Delta c_{\alpha\beta}^{(i)}(t) := \langle S_i^\alpha(t)\, S_i^\beta(0)\rangle \quad \text{with } h_i \text{ from Eq. (3.31b).} \tag{3.33b}$$

In total, two independent runs of the code are required for simulating the semiclassical model including the conservation of the total spin. The run with the Hamiltonian h_0 involves the strong coupling $N/(N+1)$ between central spin and bath. Thus, the contribution $\Delta c^{(0)}_{\alpha\beta}(t)$ dominates the dynamics of the autocorrelation function $\langle S^{\alpha}_0(t)\, S^{\beta}_0(0)\rangle$. In contrast, the coupling $-1/(N+1)$ between a single bath spin $\vec{S}_i$ and $\vec{\eta}(t)$ is very small. Consequently, the Hamiltonian h_i induces only a very weak dynamics which hardly has an impact on the discussed time scales.

The separate treatment of the conserved total spin leads to a stabilization of the plateau observed for intermediate time scales. The stabilization depends on the number of bath spins N. In Sect. 3.4.3, we present the numerical results up to intermediate time scales and discuss the improvement compared to the plain numerical simulation of the semiclassical model.

3.4.2 Classical treatment of the central spin

In the above introduced modification of the random noise simulation, the central spin is still treated on the quantum level while the bath is a classical variable. However, the precession of a quantum spin-1/2 is identical to the one of a classical vector in $\mathbb{R}^3$, see for instance Ref. [MER02]. This is due to the local isomorphism between the rotation group $\mathrm{SO}(3)$ of all rotations in a three-dimensional real vector space and the group $\mathrm{SU}(2)$ of complex rotations, see below. Furthermore, the equations of motion of a spin in a field are linear so that it does not matter whether one follows the operators or the expectation values. Thus, the question arises how the classical treatment of the central spin affects the numerical simulation of the semiclassical model. Outgoing from the optimized simulation including the conservation of the total spin, we now address the central spin on the classical level.

We recall the semiclassical Hamiltonian of Eq. (3.30a) and insert the expression for the fluctuating part $\Delta\vec{S}_0$ of the central spin defined by Eq. (3.25)

$$H_{\mathrm{sc}} = \vec{\eta}(t)\left(\vec{S}_0 - \frac{1}{N+1}\vec{I}\right). \tag{3.34}$$

According to Eq. (3.20b), the Gaussian fluctuation $\vec{\eta}(t)$ can be written as

$$\vec{\eta}(t) = J_0\vec{I} + \Delta\vec{\eta}(t). \tag{3.35}$$

From the latter Hamiltonian, one easily deduces the two classical equations of motion

$$\frac{\mathrm{d}}{\mathrm{d}t}\vec{S}_0 = \vec{\eta}\,(t) \times \vec{S}_0 \tag{3.36a}$$

$$\frac{\mathrm{d}}{\mathrm{d}t}\vec{I} \;= -\frac{1}{N+1}\vec{\eta}\,(t) \times \vec{I}. \tag{3.36b}$$

Here, all spins are classical vectors in $\mathbb{R}^3$. We can also adopt the former expression for the autocorrelation function

$$\overline{S_0^\alpha\,(t)\,S_0^\beta\,(0)} = \frac{1}{4}\frac{1}{N+1}\delta_{\alpha\beta} + \Delta c_{\alpha\beta}\,(t) \tag{3.37}$$

with

$$\Delta c_{\alpha\beta}\,(t) := \overline{\left(\vec{S}_0 - \frac{1}{N+1}\vec{I}\right)^\alpha\left(t\right)\left(\vec{S}_0 - \frac{1}{N+1}\vec{I}\right)^\beta\left(0\right)}. \tag{3.38}$$

To distinguish the latter expressions from the quantum description, the expectation values are denoted by an overbar and not by brackets $\langle . \rangle$.

The equations of motion (3.36) may be integrated using standard methods, for example Runge-Kutta integration. But we choose an alternative strategy and exploit the local isomorphism between the groups SO(3) and SU(2). Thereby, we are able to reuse the code for the semiclassical model and avoid the development of an entirely new one. The local isomorphism encodes the classical vectors $\vec{S}_0$ and $\vec{I}$ in the basis of the Pauli matrices

$$\widehat{S}\,(t) := S^x(t)\sigma^x + S^y(t)\sigma^y + S^z(t)\sigma^z \tag{3.39a}$$

$$\widehat{I}\,(t) := I^x(t)\sigma^x + I^y(t)\sigma^y + I^z(t)\sigma^z, \tag{3.39b}$$

where the coefficients $S^\alpha(t)$ and $I^\alpha(t)$ are the entries of the corresponding classical vectors. Here, we label the representation in the basis of the group SU(2) explicitly with a hat to distinguish the quantum spins from the classical ones. The time evolution of the encoded classical spins $\widehat{S}_0(t)$ and $\widehat{I}(t)$ is determined by the Hamiltonians

$$H_{\widehat{S}_0} = -\frac{1}{2}\left(J_0\vec{I} + \Delta\vec{\eta}\,(t)\right)\cdot\vec{\sigma} \tag{3.40a}$$

$$H_{\widehat{I}} = -\frac{1}{2}\frac{1}{N+1}\left(J_0\vec{I} + \Delta\vec{\eta}\,(t)\right)\cdot\vec{\sigma}, \tag{3.40b}$$

which are derived by comparing the classical equations of motion (3.36) with the Heisenberg equations of motion. As before, two independent runs of the integration are required: One for a strong coupling (3.40a) and one for a weak coupling to the random field $\vec{\eta}(t)$ (3.40b). Thereby, the integration can be carried out with the same code as before.

In addition to sampling the Gaussian fluctuations $\Delta\vec{\eta}(t)$ obeying the autocorrelation function $\Delta g_{\alpha\beta}(t)$ defined in Eq. (3.24), the initial values of I^α and $\Delta S_0^\alpha(0)$ have to be chosen randomly from a Gaussian distribution with vanishing mean value. According to Eq. (3.22a), the variance of a single component of the total spin reads

$$\left\langle \left(I^\alpha(0)\right)^2 \right\rangle = \frac{N+1}{4}. \tag{3.41a}$$

For a single component of the fluctuating part $\Delta S_0^\alpha(t)$, the initial variance at $t = 0$ is given by the expression

$$\left\langle \left(\Delta S_0^\alpha(t)\right)^2 \right\rangle = \frac{1}{4}\frac{N}{N+1}. \tag{3.41b}$$

The initial values enter in the Hamiltonians (3.40) as well as in the autocorrelation function $\overline{S_0^z(t)S^z(0)}$ of the central spin. Now, we have all ingredients for calculating the time evolution of the operators $\widehat{I}$ and $\widehat{S}_0$ containing the components of the classical spins $\vec{I}$ and $\vec{S}_0$. For each value of t, one extracts the values of the components $I^\alpha(t)$ and $S_0^\alpha(t)$ from the matrix elements of $\widehat{I}(t)$ and $\widehat{S}_0(t)$. They enter in the autocorrelation function of the central spin defined in Eqs. (3.37) and (3.38).

3.4.3 Discussion

Before we discuss the impact of the conservation of the total spin on the semiclassical model, we briefly address the autocorrelation function of the operator $\vec{A}$ as defined in Eq. (3.20b). In Fig. 3.4, the DMRG results for the autocorrelation function including the constant part (upper panel) and for the fluctuating part $\Delta\vec{A}$ only (lower panel) are plotted up to intermediate time scales. The lower panel demonstrates that the fluctuating part is indeed small compared to the constant one. For large times, one can expect that the fluctuating part vanishes completely and only the sizeable constant part remains. The inclusion of the central spin in $\vec{A}$ induces a stronger correlation between the fluctuations which should stabilize the autocorrelation function of the central spin on the same time scale. As before, the autocorrelation function converges towards $\langle A^z(t)A^z(0)\rangle = J_\mathrm{q}^2/4$ for $N \to \infty$. In this case, the result for the central spin coincides with the previous result from Sect. 3.3. Note that there is no direct physical interpretation of the redefined operator $\vec{A}$. It serves mainly as a tool which incorporates the total spin conservation in the semiclassical picture.

In Fig. 3.5, the time dependence of the autocorrelation function $\langle S_0^z(t)S_0^z(0)\rangle$ of the central spin is presented. For each bath size, we compare the DMRG result with the results

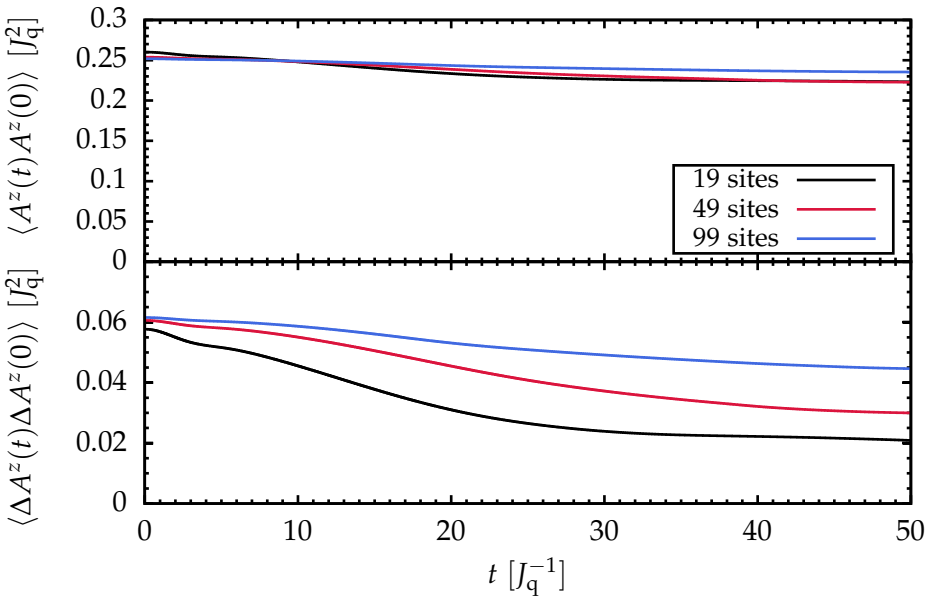

Fig. 3.4: Autocorrelation function $\langle A^z(t)A^z(0)\rangle$ as defined in Eq. (3.20b) (upper panel) and the separate fluctuating part $\langle \Delta A^z(t)\Delta A^z(0)\rangle$ (lower panel) obtained by DMRG up to intermediate time scales. For all curves, the total discarded weight does not exceed 10 %. We believe that the accuracy of the autocorrelation functions is of the same order of magnitude.

obtained for the semiclassical model. If the conservation of the total spin is included, the central spin is treated on the operator level as well as on the classical level. Like in Sect. 3.3, the DMRG autocorrelation functions serve as input for the correlation function of the random noise.

The results clearly point out the importance of a separate treatment of the conserved quantities because the conservation of the total spin leads to a substantial improvement of the results. Compared to the quantum level, no significant differences occur when the central spin is treated classically. Some oscillations are more pronounced, but this is only a minor effect. In general, the classical description matches the minimum in the short-time behavior better than the quantum description. The agreement between the semiclassical and the quantum model improves quickly for larger bath sizes. While a significant mismatch is observed for $N = 19$, a very good agreement is already achieved for $N = 49$ bath spins. The semiclassical results for $N = 99$ even overshoot the DMRG results for larger times. But this might also be accounted to inaccurate DMRG results because the total discarded weight is of the order of a few percent for long times.

In total, we achieved a significant improvement in the semiclassical description of the central spin model by incorporating the conservation of the total spin explicitly. However, two essential disadvantages of the semiclassical approach remain. First, it relies on an

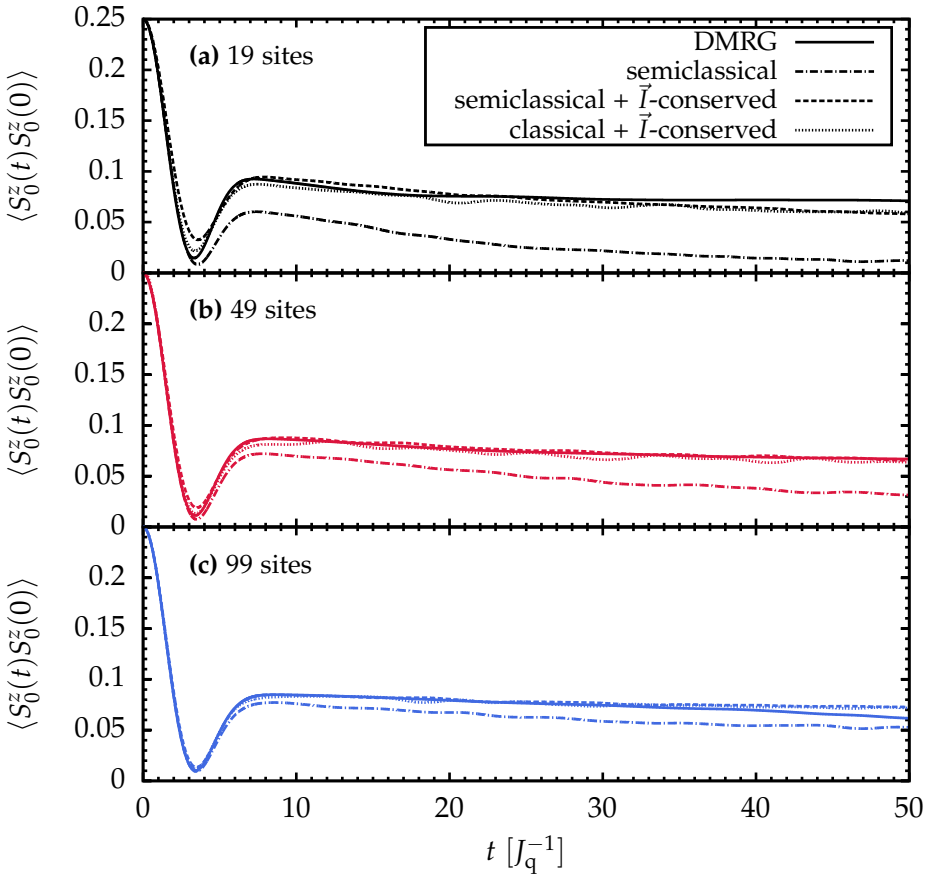

Fig. 3.5: Autocorrelation function of the central spin up to intermediate time scales. In each panel, the results for the semiclassical model are compared with the corresponding DMRG result. All curves involving random noise have been obtained for $M = 50,000$ fluctuations.

external method providing the correlation function of the random noise. Hence, accessible time scales are limited by the external method and almost no resources are saved. Second, it does not respect the energy conservation

$$0 \stackrel{!}{=} \frac{\mathrm{d}}{\mathrm{d}t} H_{\mathrm{sc}} = \frac{\mathrm{d}\vec{\eta}\,(t)}{\mathrm{d}t} \cdot \vec{S}_0 \neq 0. \tag{3.42}$$

Of course, the energy is conserved in the fully quantum model where the state of the bath depends on the state of the central spin. The corresponding back-actions effects are not included in the semiclassical picture so that the energy conservation is lost. This may be repaired by the introduction of a correction term in Eq. (3.42) which compensates the energy changes. But the derivation of such a sophisticated correction is complex. A much better approach involves the self-consistent calculation of the bath fluctuations. Naturally, self-consistency is achieved when treating the central spin model on a thoroughly classical level which we will deal with in the next chapter.

3.5 Remarks on finite external magnetic fields

The discussion of the semiclassical model in the present chapter was restricted to the zero-field limit where the model is completely isotropic. But the investigation may of course be extended to finite external magnetic fields. For example, one can investigate the scenarios discussed in Sect. 2.7.2 where the external magnetic field is applied either to the bath spins or to the central spin.

In extension of the derivation of the AHT in the zero-field limit, we addressed the first scenario where the field is applied to the bath spins. Then, the semiclassical Hamiltonian remains unchanged but the random fluctuations $\vec{\eta}(t)$ obey a cylindric symmetry. We derived the corresponding AHT up to second order. It requires the introduction of a cylindric probability distribution which is renormalized similar to the second order in the zero-field limit, see Appendix D. However, it turned out that the results only yield an insufficient approximation of the DMRG results. Hence, we refrain from presenting this treatment in the present thesis because the unsatisfactory quality of the results does not justify the lengthy derivation of the corresponding AHT. At first sight, the poor performance for the cylindric symmetry might be surprising because the AHT worked well in the zero-field limit. Its failure for finite external fields likely has to be attributed to the more complex correlations of the random noise inducing anisotropic fluctuations as well as to cross-correlations. Furthermore, the static character of the random fluctuations is much less pronounced because the external fields induce a precession of the spins which is also reflected in the correlation functions $g_{\alpha\beta}(t)$.

We also addressed finite external magnetic fields within the random noise simulation. While the behavior in the spin directions perpendicular to the external field resembles the behavior of the quantum model nicely, the plateau in the direction parallel to the external field is not completely captured. Like in the zero-field limit, a significant decay is found in the random noise simulation in contrast to the DMRG results. The optimized version of the random noise simulation introduced in Sect. 3.4 may also be adapted to finite external fields. Similarly to the zero-field limit, we suppose that the results should be significantly improved. But the lack of energy conservation and the other disadvantages remain so that we do not pursue this option further.

Chapter 4

Classical Equations of Motion

Contents

The semiclassical model, which was introduced for an effective description of the central spin dynamics in the last chapter, has proven to work quite well in the zero-field limit as long as the bath size is not too small. However, the sampling of the random noise relies on the correlation function of the Overhauser field which has to be known from an external and independent source. Furthermore, the replacement of the quantum bath by a classical random field does not respect the energy conservation. In this chapter, we circumvent these problems by solving the complete set of classical equations of motion for the central spin model. This approach implies a consistent calculation of the bath fluctuations. Hence, no external method is required and a closed description of the classical spin dynamics for both the central spin as well as for the bath spins is obtained.

After the brief introduction of the classical equations of motion in Sect. 4.1, their solutions in presence and in absence of an external magnetic field are presented up to intermediate time scales. The zero-field limit is addressed in Sect. 4.2, while the results for finite external fields are discussed in Sect. 4.3. For the latter scenario, the external field is restricted to the central spin for brevity and for experimental relevance. Precisely, we adopt the scenarios from Sect. 2.7.2.2 where the weak, the intermediate, and the strong-field regime was investigated by DMRG on short-time scales.

4.1 Introduction

Classically, the spin dynamics in the central spin model is determined by the $3(N+1)$ equations of motion (EOMs)

$$\frac{\mathrm{d}}{\mathrm{d}t}\vec{S}_0 = \vec{A} \times \vec{S}_0 - \vec{h}_0 \times \vec{S}_0 \tag{4.1a}$$

$$\frac{\mathrm{d}}{\mathrm{d}t}\vec{S}_i = J_i \vec{S}_0 \times \vec{S}_i, \tag{4.1b}$$

where $i \in \{1, 2, \ldots, N\}$ and $\vec{h}_0$ is the external field applied to the central spin. As for the quantum model, the classical Overhauser field is defined by

$$\vec{A} := \sum_{i=1}^{N} J_i \vec{S}_i. \tag{4.2}$$

Note, however, that the Overhauser field is now a simple vector in $\mathbb{R}^3$ and not an operator anymore as in the quantum model. It is easily verified that the total energy

$$\begin{aligned} E &= \vec{A} \cdot \vec{S}_0 \\ \Rightarrow \frac{\mathrm{d}E}{\mathrm{d}t} &= \dot{\vec{A}} \cdot \vec{S}_0 + \vec{A} \cdot \dot{\vec{S}}_0 = 0 \end{aligned} \tag{4.3}$$

is conserved because of the properties of the outer product.

The set (4.1) of coupled EOMs is solved best using standard numerical routines such as Runge-Kutta integration. Here, we stick to the adaptive Runge-Kutta-Fehlberg method which is part of the GNU Scientific Library (GSL) [GDT+09]. The initial values for all spins $\vec{S}_i(t)$ at $t = 0$ are chosen from a random distribution with vanishing mean value and variance

$$\overline{S_i^\alpha(0) S_i^\alpha(0)} = \frac{1}{4}. \tag{4.4}$$

By carrying out the numerical integration, one obtains all spins $\vec{S}_i$ as function of time. Thereby, the desired autocorrelation functions are calculated by averaging over a large number M of random initial configurations. This corresponds to the investigation of a completely unpolarized system. The conservation of the energy and of the total spin has explicitly been checked to verify the correctness of the implementation. The energy in the regarded time interval $t \in [0, 1000\, J_\mathrm{q}^{-1}]$ is conserved up to order 10^{-6} which also corresponds to the step-size of the Runge-Kutta integration. On the same time scale, the total momentum is conserved up to order 10^{-12}. Decreasing the step-size of the Runge-Kutta method did not lead to a significant improvement so that we use 10^{-6} as standard value.

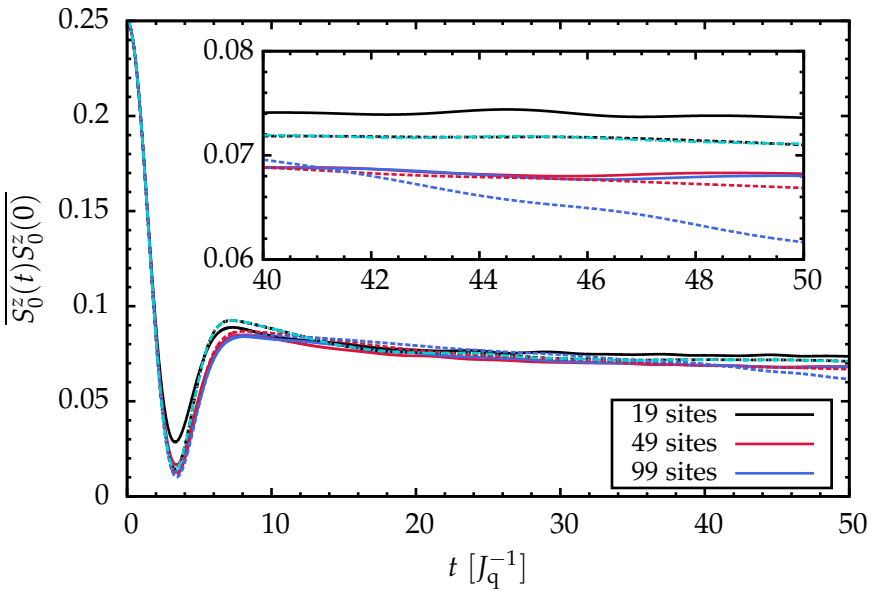

Fig. 4.1: Autocorrelation function of the central spin in the zero-field limit up to intermediate time scales. In addition to the solution obtained from the classical EOMs (solid lines), the corresponding DMRG results of the quantum model are plotted (dashed lines). The inset contains a magnification for $t \geq 40\, J_q^{-1}$. On the time scale of the inset, the DMRG result for $N = 99$ seems to be inaccurate. The turquoise curve was obtained from the Chebychev expansion for $N = 19$ bath spins involving an exact representation of the Hamiltonian. The results for the classical EOMs are averaged over $M = 1,000,000$ random initial configurations. The author is indebted to J. Hackmann for providing the Chebychev expansion result [Hac13].

The central spin model was already studied on the classical level before [EN04, CBB07]. Besides our motivation of the classical treatment, an alternative motivation was discussed in Ref. [CBB07]. There, the classical EOMs were derived from the quantum model in the limit of large spin baths $N \to \infty$ by the saddle point approximation for the spin coherent path integral. Thereby, it was shown that the classical limit is well justified if the number of spins is large. But none of the cited references features a full solution of the complete set of EOMs (4.1). Rather, additional simplifications were made to draw conclusions on the asymptotic long-time behavior of the central spin, see Sect. 1.5.4 for details.

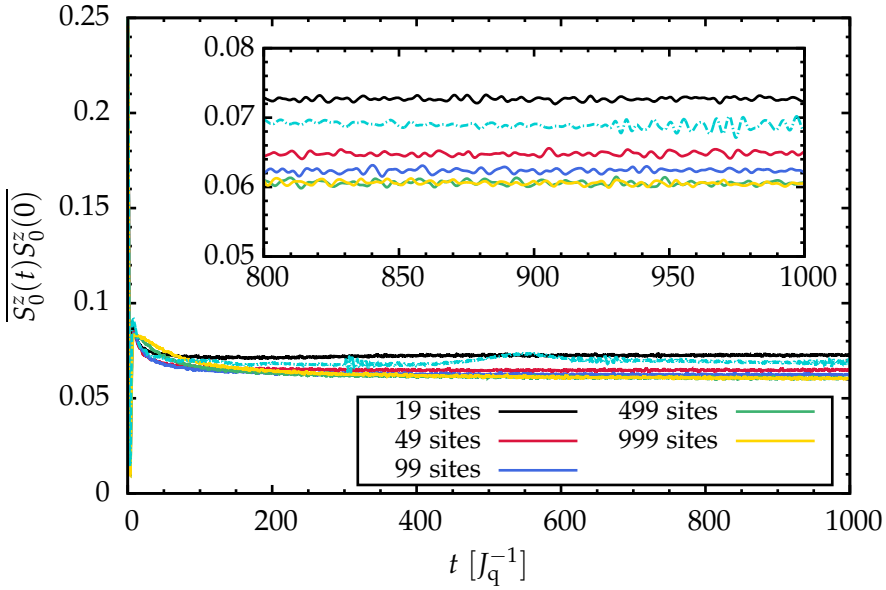

Fig. 4.2: Long-time behavior of the autocorrelation function of the central spin obtained from the solution of the classical EOMs for up to $N = 999$ bath spins. The inset contains a magnification for larger times $t \geq 800\, J_q^{-1}$ where the curves fluctuate around a constant non-zero value. The turquoise curve was obtained from the Chebychev expansion for $N = 19$ bath spins involving an exact representation of the Hamiltonian [Hac13]. The results for the classical EOMs are averaged over $M = 1,000,000$ random initial configurations.

4.2 Zero-field limit

At first, we study the zero-field limit where no external field is present at all. The results for the autocorrelation function of the central spin are plotted in Fig. 4.1. Overall, there is a very nice agreement between the classical solution (solid lines) and the DMRG results (dashed lines) up to intermediate times $t = 50\, J_q^{-1}$. The minimum close to $t \approx 4\, J_q^{-1}$ is not correctly captured by the classical solution if the bath size is small. However, fast convergence with N is observed so that only a marginal difference between the classical and the quantum result remains for a moderate number of $N = 99$ bath spins. After the plateau has emerged, a qualitative agreement between classical and quantum results still persists. Of course, a complete quantitative agreement is not achieved. But this is not surprising, since classical physics and quantum mechanics are two distinct descriptions. Hence, the observed agreement between the two approaches is already remarkable and not obvious. The drop in the DMRG result for $N = 99$ bath spins close to $t \geq 40\, J_q^{-1}$ has to be attributed to numerical inaccuracies because the total discarded weight is close to ten percent on the respective time scale.

In general, a first tendency can be estimated from the results up to intermediate times that the quantum autocorrelation function of the central spin is slightly stronger suppressed

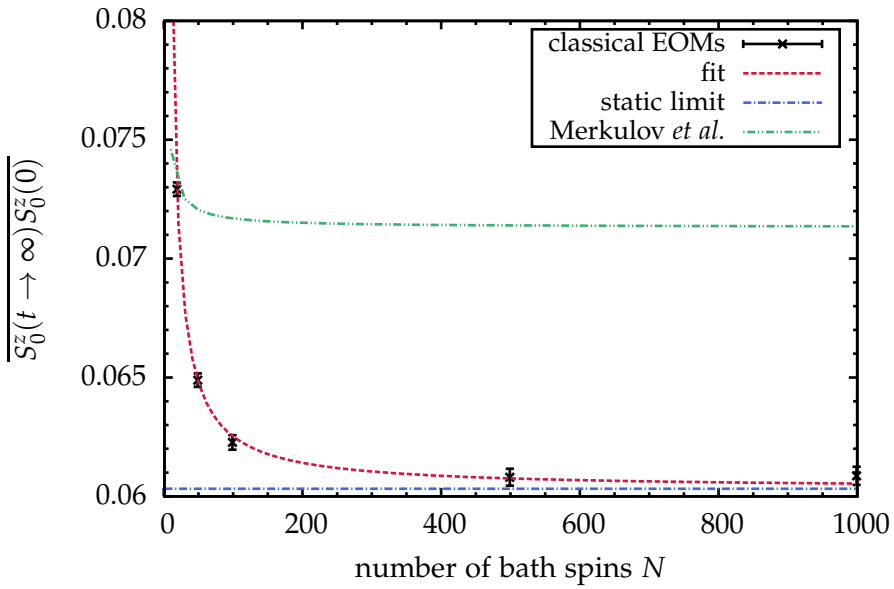

Fig. 4.3: Non-decaying fraction of the autocorrelation function of the central spin (symbols) versus the number of bath spins N. As the long-time results of the classical EOMs fluctuate around a constant value (see inset in Fig. 4.2), the mean values for $t = 500$-$1000\, J_q^{-1}$ are plotted. The error bars depict the standard deviation. The red curve represents the fitted function $f(N) = 3a(N/b+1)/(N/b-1)$ with $a = 0.0201$ and $b = 1.79$. In addition, we plot the static limit $f(N) \xrightarrow{N\to\infty} 3a$ as determined by the fit (blue curve). The green curve is a theoretical curve deduced from Ref. [MER02] for our set of coupling constants.

than the classical one. This is stronger pronounced in the long-time behavior, which is shown in Fig. 4.2. For large values of t, all curves acquire a plateau value depending on the actual bath size. For the quantum model, a result for the long-time behavior is only available for $N = 19$ bath spins (turquoise line). It was obtained from the Chebychev expansion involving an exact representation of the Hamiltonian [HA14]. Compared to the corresponding classical solution, one observes that the plateau in the autocorrelation of the central spin is slightly suppressed due to influence of quantum fluctuations. The non-decaying fraction of the autocorrelation function for the classical system decreases with increasing number of bath spins. This is related to the increasing number of only weakly coupled spins because the tail of small coupling constants grows with N.

Similar to the short-time behavior of the quantum model discussed in Sect. 2.7.1, a saturation is observed for $N \approx 1000$ bath spins. As a function of N, the non-decaying fraction of the autocorrelation function does neither obey a power law nor a logarithm. The function

$$\overline{S_0^z(t\to\infty)S_0^z(0)} \propto \frac{\overline{J_i}^2}{\overline{J_i^2} - \overline{J_i}^2} = 3\frac{N+1}{N-1} \tag{4.5}$$

provides a good fit to the numerical data if the prefactor and the bath size N are appropriately renormalized, see Fig. 4.3. Thereby, one deduces that the autocorrelation function of the central spin never exhibits a complete decay. A certain fraction always persists even in the asymptotic limit $N \to \infty$. From the fit to our numerical data for the classical set of EOMs, one deduces that $\overline{S_0^z(\infty) S_0^z(0)} \approx 0.06$ for $N \to \infty$, see caption of Fig. 4.3. However, we cannot provide an analytical argument for the observed behavior as a function of N. In Ref. [MER02], an estimate for the non-decaying fraction was derived by including the fluctuations of the nuclear bath. Compared to the full solution of the classical EOMs, the integrals derived by Merkulov *et al.* overestimate the non-decaying fraction. Overall, the asymptotic value deduced from their theory for our parameters is roughly 20 % larger than the numerical solution of the classical EOMs, see Fig. 4.3. Note, however, that the quantity $\overline{J_i}^2 / (\overline{J_i^2} - \overline{J_i}^2)$ enters in their calculations.

In total, the dynamics of the electron spin in the zero-field limit is essentially classical up to intermediate time scales. On the long-time scale, the influence of quantum fluctuations increases which is expressed by a reduced non-decaying fraction of the autocorrelation function of the quantum model. Although the reduction in the inset in Fig. 4.2 is rather small and almost of the order of the error due to averaging over a finite number of random initial configurations, it has to be regarded as significant. But the results for $t \leq 50\, J_\mathrm{q}^{-1}$ suggest that the differences between the classical and the quantum description will dissolve if N is large. In essence, our observations agree with results by Coish *et al.* [CLYA07]. They compared the quantum solution with the corresponding classical solution for a single initial state and found that the dynamics is essentially classical up to a certain time. Beyond that time, quantum fluctuations have to be taken into account. However, they did not study the average over all initial conditions as we do. Furthermore, all couplings in their study were homogeneous $J_i = J$ and the expectation values of the observables were calculated on the mean-field level. A numerical solution of the full set of EOMs was not considered. Furthermore, our result for the isotropic model seems to resemble the one presented in Ref. [AHDDH06], despite the different distribution of the coupling constants. The method in Ref. [AHDDH06] also involves a classical treatment of the central spin dynamics in the unpolarized model. It is derived from the P-representation of the central spin density matrix. The authors claim to reproduce the exact EOMs for the part describing the central spin, while the behavior of the bath seems not to be captured correctly. The derivation of the EOMs in Ref. [AHDDH06] is kept very short and remains rather elusive so that a classification of the approach compared the classical EOMs given in Eq. (4.1) is difficult.

It is a very interesting feature that, even for large times $t > 100\, J_\mathrm{q}^{-1}$, the results converge already for $N \approx 1000$ bath spins. In a real quantum dot, the number of bath spins is roughly one to two orders of magnitude larger, see Sect. 1.3. Hence, one may assume that

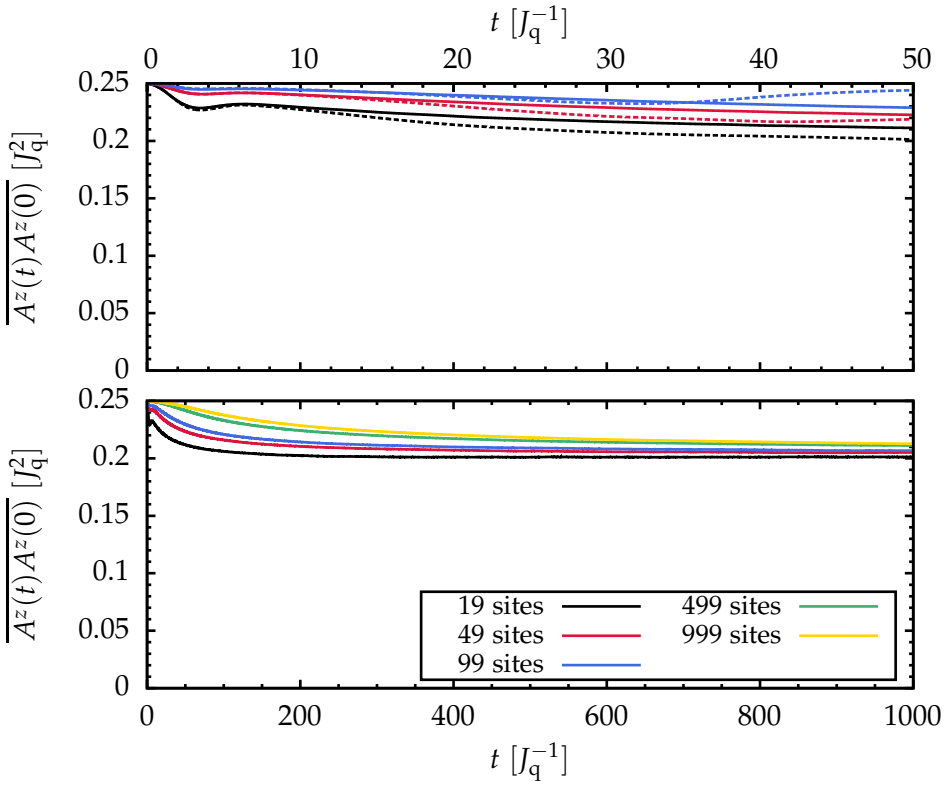

Fig. 4.4: Autocorrelation function of the Overhauser field in the zero-field limit up to intermediate (upper panel) and long times (lower panel). The solid lines represent the solutions obtained from the classical EOMs. In addition, the DMRG results are plotted as reference in the upper panel (dashed lines). The results for the classic EOMs are averaged over $M = 1,000,000$ random initial configurations.

the dynamics of a single electron spin confined in a quantum dot is essentially classical. Accordingly, a comparison between the quantum and classical solution for a fairly large bath size containing roughly the realistic number of bath spins coupled to a single electron spin is a promising route for future research. It is highly unlikely that a method providing the full quantum solution for a system of $\mathcal{O}(10^4\text{-}10^5)$ spins will be available in the near future, especially for investigations on long-time scales.

Before passing to a finite external magnetic field, we briefly discuss the behavior of the autocorrelation function of the Overhauser field which is presented in Fig. 4.4. Deviations between the classical and the quantum solution already occur on intermediate time scales (upper panel) for $t \geq 10\, J_q^{-1}$ and they are more pronounced than for the central spin. As before, this has to be attributed to quantum fluctuations which suppress the autocorrelation of the Overhauser field. Again, DMRG seems to fail for $N = 99$ bath spins for $t \geq 40\, J_q^{-1}$. Thus, we do not believe the increase in the DMRG result for $N = 99$ bath spins for $t \gtrsim 40\, J_q^{-1}$. On the long-time scale (lower panel), the autocorrelation function decays faster for small bath sizes. The non-decaying fraction increases with N opposed

to the non-decaying fraction observed for the central spin. Furthermore, no convergence with N can be observed on the long-time scale because the non-decaying fraction of the autocorrelation function still exhibits a clear, though small, N-dependence.

In conclusion, the classical treatment of the EOMs in the zero-field limit works well as long as one focuses on the behavior of the central spin. This is similar to the previously mentioned method based on the P-representation of the central spin density matrix introduced by Al-Hassanieh *et al.* [AHDDH06]. Their EOMs coincide with the exact ones only for the part describing the central spin. For small bath sizes, the non-decaying fraction of the autocorrelation function of the central spin obtained from the classical EOMs is larger than the non-decaying fraction in the quantum case due to the absence of quantum fluctuations. However, the convergence of the quantum solution with N remains an open question. For $N \to \infty$, it is possible that both the classical as well as the quantum solution converge towards the same asymptotic value.

4.3 Finite external magnetic field

In this section, we turn on a finite external magnetic field $\vec{h}_0 = (0\ 0\ h_0)^\top$ in z-direction. According to the EOMs in Eq. (4.1), the external field is solely applied to the central spin. In the framework of DMRG, the short-time behavior for this scenario was already addressed in detail in Sect. 2.7.2.2. As before, the case of a weak, an intermediate, and a strong-field is investigated. The following results comprise the behavior up to intermediate times. In addition, the long-time behavior determined from the classical EOMs is discussed.

4.3.1 Weak-field regime

In Fig. 4.5, the solutions of the classical EOMs (solid lines) for a weak external magnetic field $h_0 = 0.2\, J_\mathrm{q}$ are compared with the corresponding DMRG results for the quantum model (dashed lines of the same color) up to intermediate times. The autocorrelation functions of the central spin obtained from the classical solution agree nicely with the quantum autocorrelation functions. As in the zero-field limit, the minimum observed in the short-time behavior is captured only if the bath size is not too small. The external magnetic field applied in z-direction stabilizes the autocorrelation function in that direction so that a larger non-decaying fraction remains compared to the scenario without any external field. This effect is slightly stronger for the classical solution due to the absence of quantum

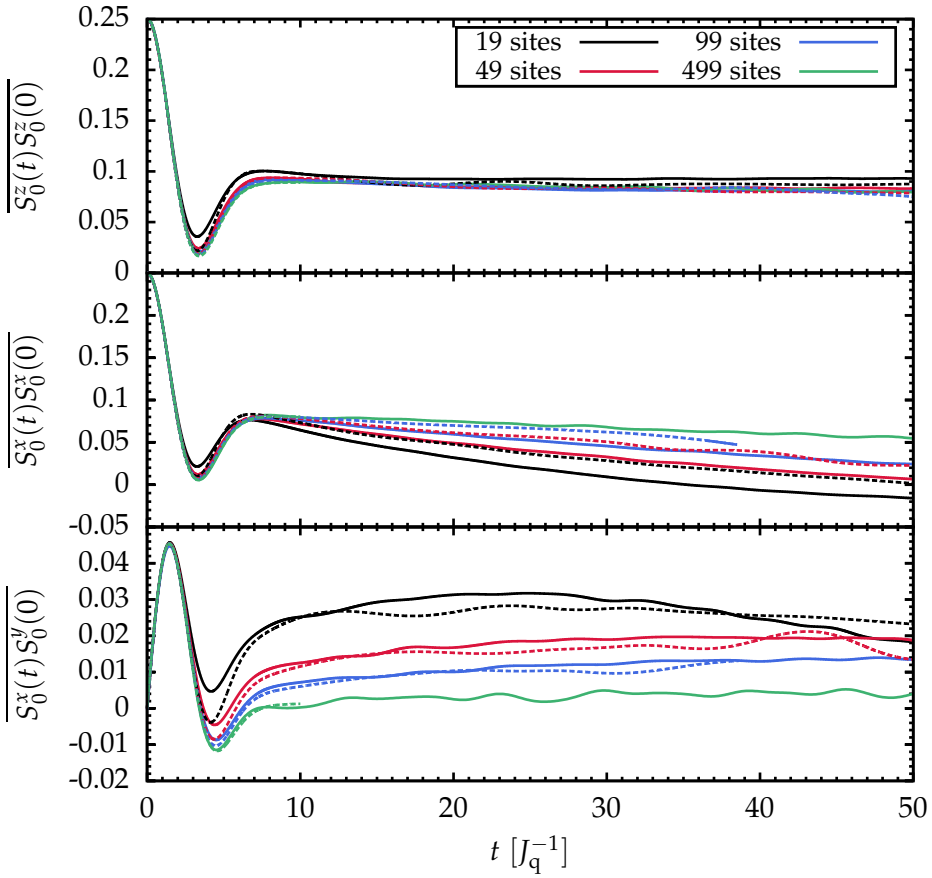

Fig. 4.5: Non-vanishing autocorrelation functions $\overline{S_0^\alpha(t)S_0^\beta(0)}$ of the central spin for a weak external field $h_0 = 0.2\,J_q$. The solid lines represent the solution of the classical EOMs, while the dashed lines are the quantum results calculated with DMRG. The latter are shown up to the time where the total discarded weight exceeds 10 %. Here, the DMRG results for $N = 499$ bath spins are only available up to $t = 10\,J_q^{-1}$. All classical curves are obtained by averaging over $M = 1,000,000$ random initial configurations. Note the differing scalings of the y-axes in the different panels.

fluctuations. In the direction perpendicular to the external field, the situation is vice versa. There, the quantum solutions exhibit a slower decay than the classical ones. A convergence with N cannot be observed, which is in agreement with the observations in the weak-field regime in Sect. 2.7.2.2.

Due to the weak strength $h_0 = 0.2\,J_q$ of the external magnetic field, the autocorrelation functions plotted in Fig. 4.5 have not yet reached their asymptotic value for $t \to \infty$. Thus, the long-time behavior determined by the classical EOMs is plotted in Fig. 4.6 up to $t = 1000\,J_q^{-1}$. In the direction parallel to the external field, a non-decaying fraction of the autocorrelation function is preserved. Because of the finite external field, its asymptotic value is larger than in the zero-field limit, see Fig. 4.2 for comparison. Furthermore, some

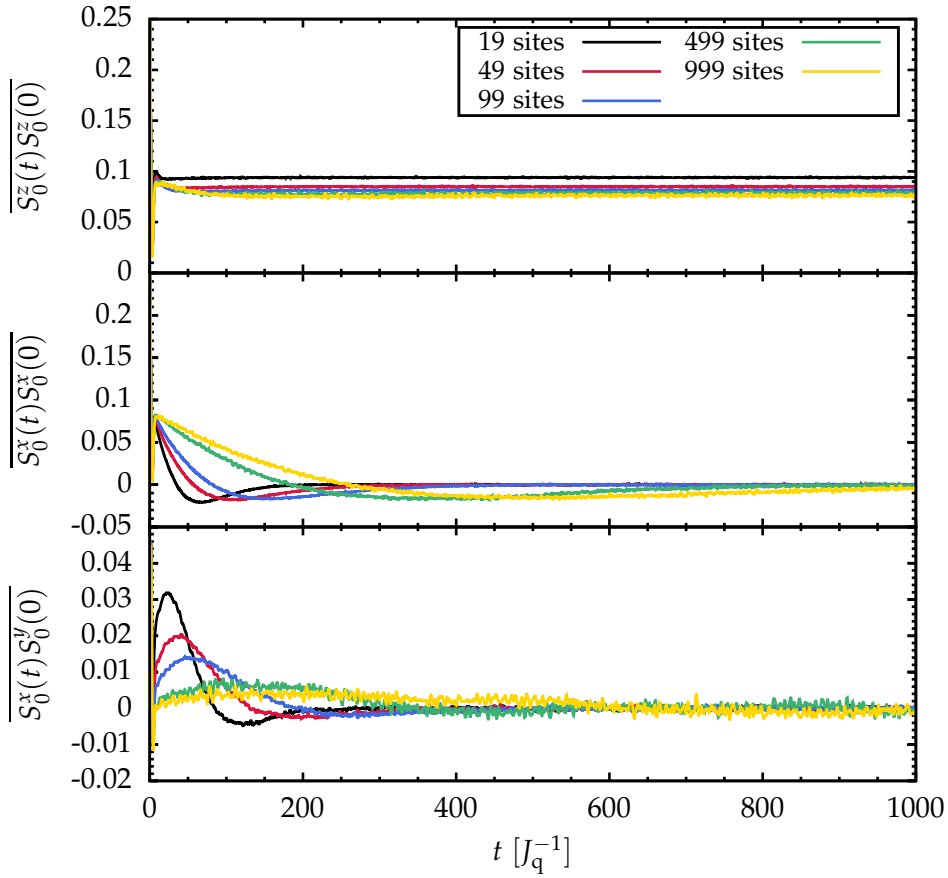

Fig. 4.6: Long-time behavior of the non-vanishing autocorrelation functions $\overline{S_0^\alpha(t)S_0^\beta(0)}$ of the central spin for a weak external field $h_0 = 0.2\,J_q$ obtained from the solution of the classical EOMs. All curves are averaged over $M = 100,000$ ($N = 499$ and $N = 999$ bath spins) or $M = 1,000,000$ (other bath sizes) random initial configurations .

dependence on N is still visible. But the results for large bath sizes suggest a saturation if the number of bath spins is increased further. In contrast, a slow but complete decay of the autocorrelation functions in spin directions perpendicular is induced by the precession of the central spin in the external field.

The results for the autocorrelation functions of the Overhauser field are presented in Fig. 4.7. They reveal a good agreement between the classical and the quantum description on short times up to $t = 10\,J_q^{-1}$. Similar to the zero-field limit (see Fig. 4.4), the deviation increases for larger times. In general, the fast decay of the quantum solutions suggests a noticeable influence of quantum fluctuations in the bath. The value of t where the classical solution begins to deviate from the quantum one increases with N. Thus, one may expect that for $N \to \infty$ both solutions coincide. However, the corresponding convergence sets in very slowly because the quantum and classical result always deviate quite early

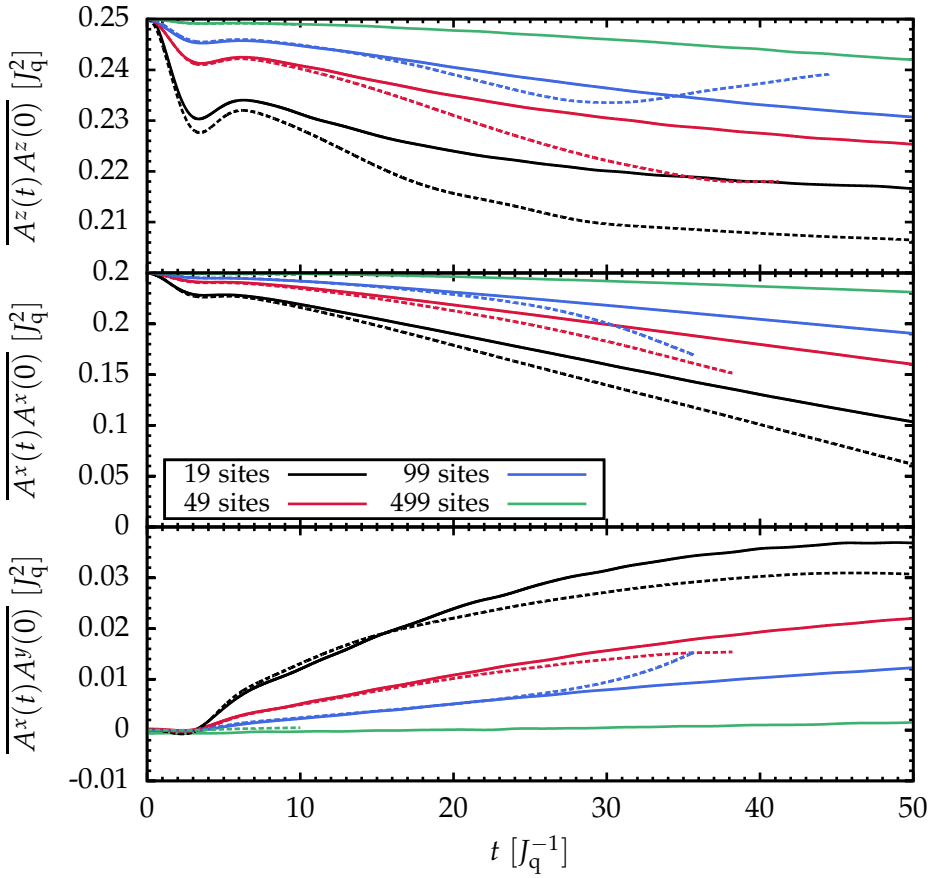

Fig. 4.7: Non-vanishing autocorrelation functions $\overline{A^\alpha(t)A_0^\beta(0)}$ of the Overhauser field for a weak external field $h_0 = 0.2\,J_q$. The solid lines represent the solution of the classical EOMs, while the dashed lines are the quantum results obtained from DMRG. The latter are shown up to the time where the total discarded weight exceeds 10 %. The DMRG results for $N = 499$ bath spins are only available up to $t = 10\,J_q^{-1}$. All classical curves are obtained by averaging over $M = 1,000,000$ random initial configurations. Note the different scalings of the y-axes in the different panels.

from each other. As already mentioned in Sect. 2.7.2.2, all curves are clearly distinguishable because of the N-dependence $J_i \sim 1/\sqrt{N}$ of the coupling constants. Note that the DMRG calculations, especially the one of $\langle A^z(t)A^z(0)\rangle$ for $N = 99$ bath spins, exhibit a large total discarded weight. Hence, their correctness for larger times $t \gtrsim 30\,J_q^{-1}$ cannot be guaranteed.

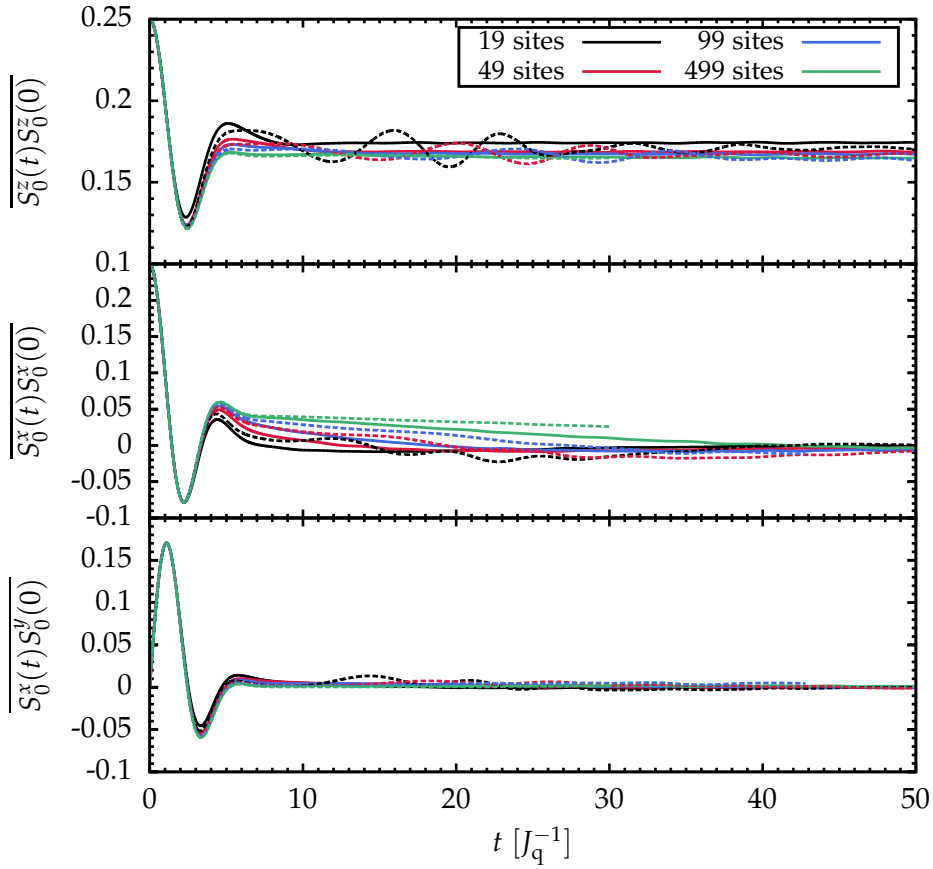

Fig. 4.8: The same as in Fig. 4.5, but now for an intermediate external magnetic field $h_0 = J_q$. Here, the DMRG results for $N = 499$ bath spins are also available for times $t > 10\, J_q^{-1}$.

4.3.2 Intermediate-field regime

The autocorrelation functions of the central spin for an intermediate external magnetic field $h_0 = J_q$ are plotted in Fig. 4.8. Overall, the performance is similar to the weak-field regime. For small bath sizes, the DMRG results exhibit a pronounced oscillation with the Larmor frequency $\omega_{\text{Larmor}} = J_q$ which is not present in the corresponding classical solutions. With increasing N, the oscillations are more and more suppressed. Like in the weak-field regime, the classical autocorrelation functions in the spin directions perpendicular to the external field decay slightly faster. In parallel to the external field, the non-decaying fraction of the autocorrelation function has increased because a stronger external field implies a more pronounced stabilization of the central spin along this field.

For $h_0 = J_q$, the central spin precesses quite fast so that the asymptotic behavior of the autocorrelation functions already emerges on the time scale presented in Fig. 4.8. Thus,

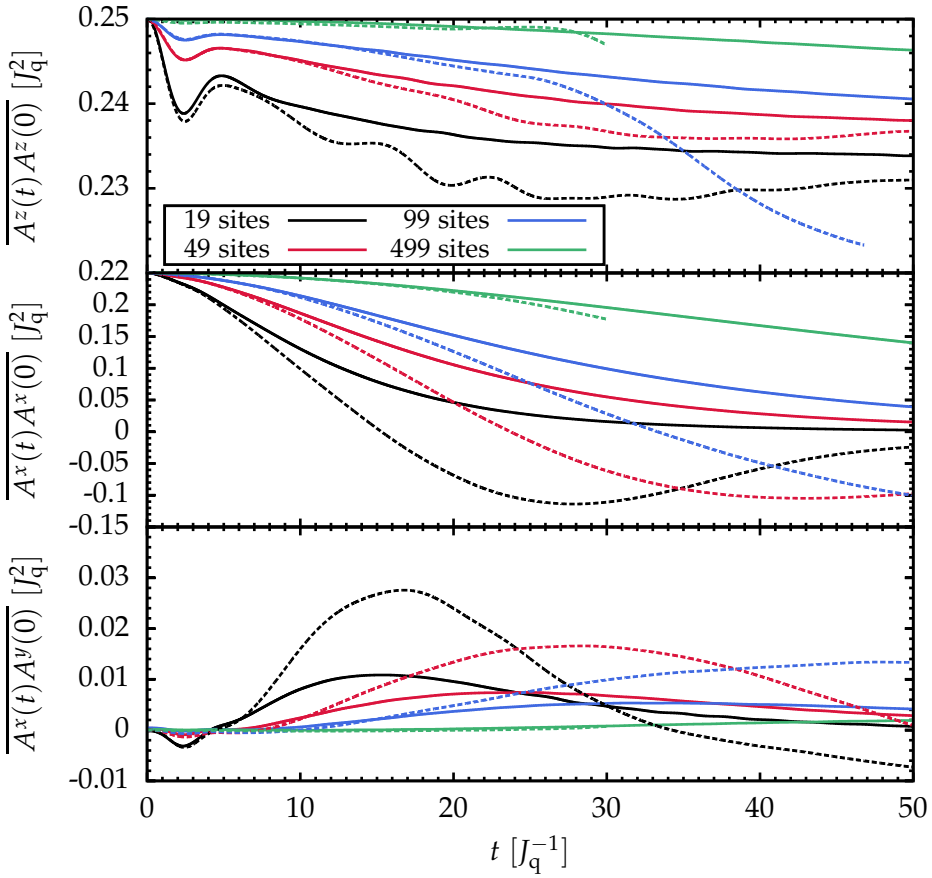

Fig. 4.9: The same as in Fig. 4.7, but now for an intermediate external magnetic field $h_0 = J_q$. Here, the DMRG results for $N = 499$ bath spins are also available for times $t > 10\, J_q^{-1}$.

we do not show an additional plot for the long-time behavior because is does not contain any substantially new information

Concerning the Overhauser field, the discrepancy between the classical and the quantum solution is more pronounced than in the weak-field regime, see Fig. 4.9. Even for a very large bath consisting of $N = 499$ spins, the solution of the classical EOMs deviates from the quantum solution for $t \geq$ 20-30 J_q^{-1}. But this observation may also be attributed to inaccuracies in the DMRG results.

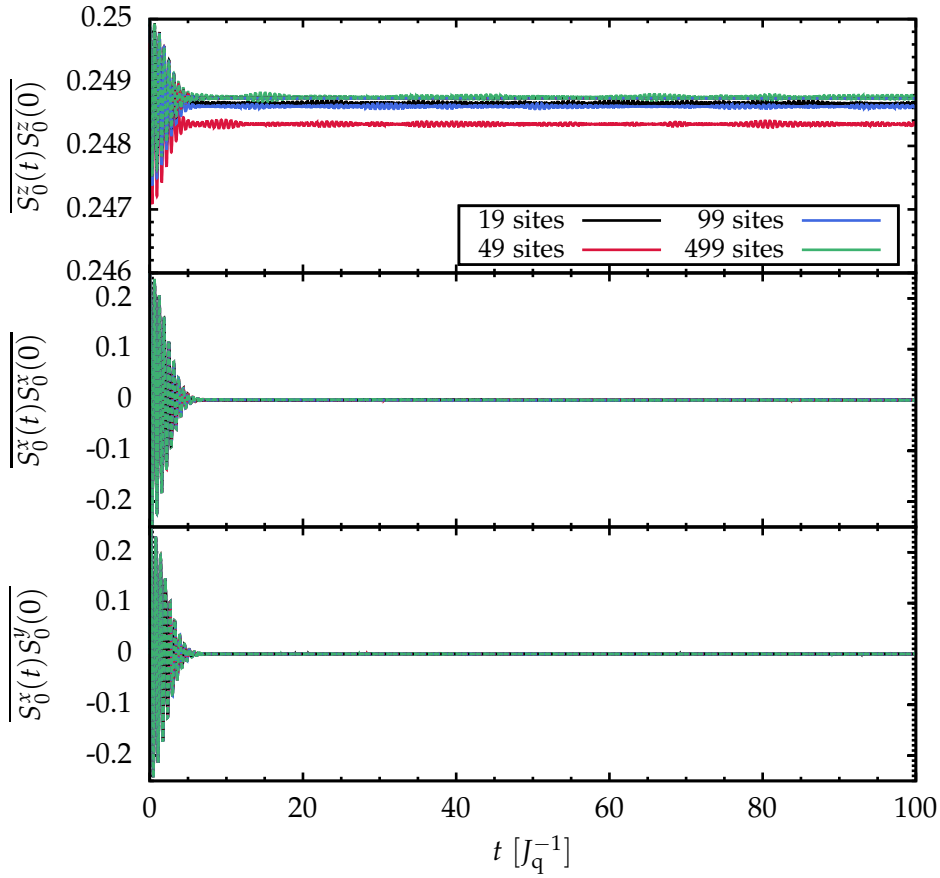

Fig. 4.10: The same as in Fig. 4.5, but now for a strong external magnetic field $h_0 = 10\,J_q$. We highlight that the total discarded weight of all DMRG results does not exceed $\mathcal{O}(10^{-4})$. In the lower two panels, the DMRG results lie directly on top of the classical results so that they are hard to distinguish. More details are revealed in the plots containing the short-time behavior, see Fig. 4.11.

4.3.3 Strong-field regime

Finally, we discuss the strong-field regime where $h_0 = 10\,J_q$. The autocorrelation functions of the central spin are presented in Fig. 4.10. Note that the different curves are hardly distinguishable because they lie directly on top of each other. Additional plots containing only the short-time behavior are presented in Fig. 4.11. Like in Sect. 2.7.2.2, an N-dependence cannot be observed because the physics is dominated by the fast precession of the central spin. The classical solutions are in perfect agreement with the DMRG results. Thus, quantum fluctuations are negligible in the strong-field regime and the central spin behaves classically. The strong external field implies a suppression of the relaxation in the spin direction parallel to the external field and a very fast dephasing in the spin directions perpendicular to the external field. The long-time solutions of the classical EOMs

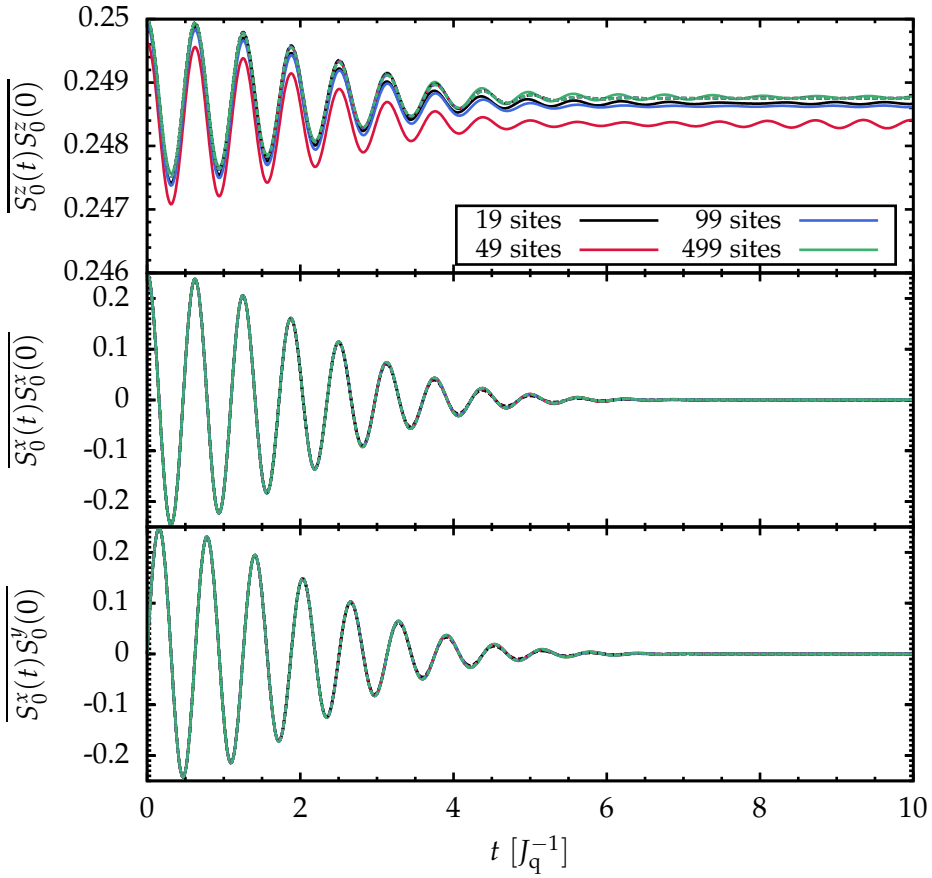

Fig. 4.11: The same as in Fig. 4.10, but now limited to the short-time behavior.

do not reveal any additional features. Thus, the autocorrelation functions of the central already reach their asymptotic values on the short-time scale $t \lesssim 10\, J_q^{-1}$. The dephasing times T_2 can easily be extracted from the middle panel of Fig. 4.11. As the classical and quantum solutions coincide, we do not repeat the analysis of T_2 in the present section and refer to previous discussion presented in Sect. 2.7.2.2. The unsystematic behavior of $\overline{S_0^z(t)S_0^z(0)}$ with N is due to averaging over a limited number of random initial conditions. For $M = 1,000,000$, the corresponding error $\sim 1/\sqrt{M}$ is visible on the scale of the y-axis.

In contrast, there are strong discrepancies between the classical and quantum autocorrelation function of the Overhauser field in the spin directions perpendicular to the external field. All classical autocorrelation functions plotted in Fig. 4.12 exhibit a smooth decay with approximately Gaussian shape. The decay rate depends on the bath size because $J_i \sim 1/\sqrt{N}$. In contrast, the DMRG autocorrelation functions oscillate with an N-dependent frequency and decay on a larger time scale than their classical counterparts. However, the results in Fig. 4.12 suggest that the classical and the quantum solution will coincide in the static limit $N \to \infty$.

On the long-time scale, the classical autocorrelation functions of the Overhauser field in spin directions perpendicular to the external field remain zero once they have decayed. In the spin direction parallel to the external field, the classical and the quantum autocorrelation functions agree nicely, see two upper panels of Fig. 4.12. The minute discrepancies observed in the magnification of $\overline{A^z(t)A^z(0)}$ originate from the sampling of a finite number of random initial configurations for the classical EOMs.

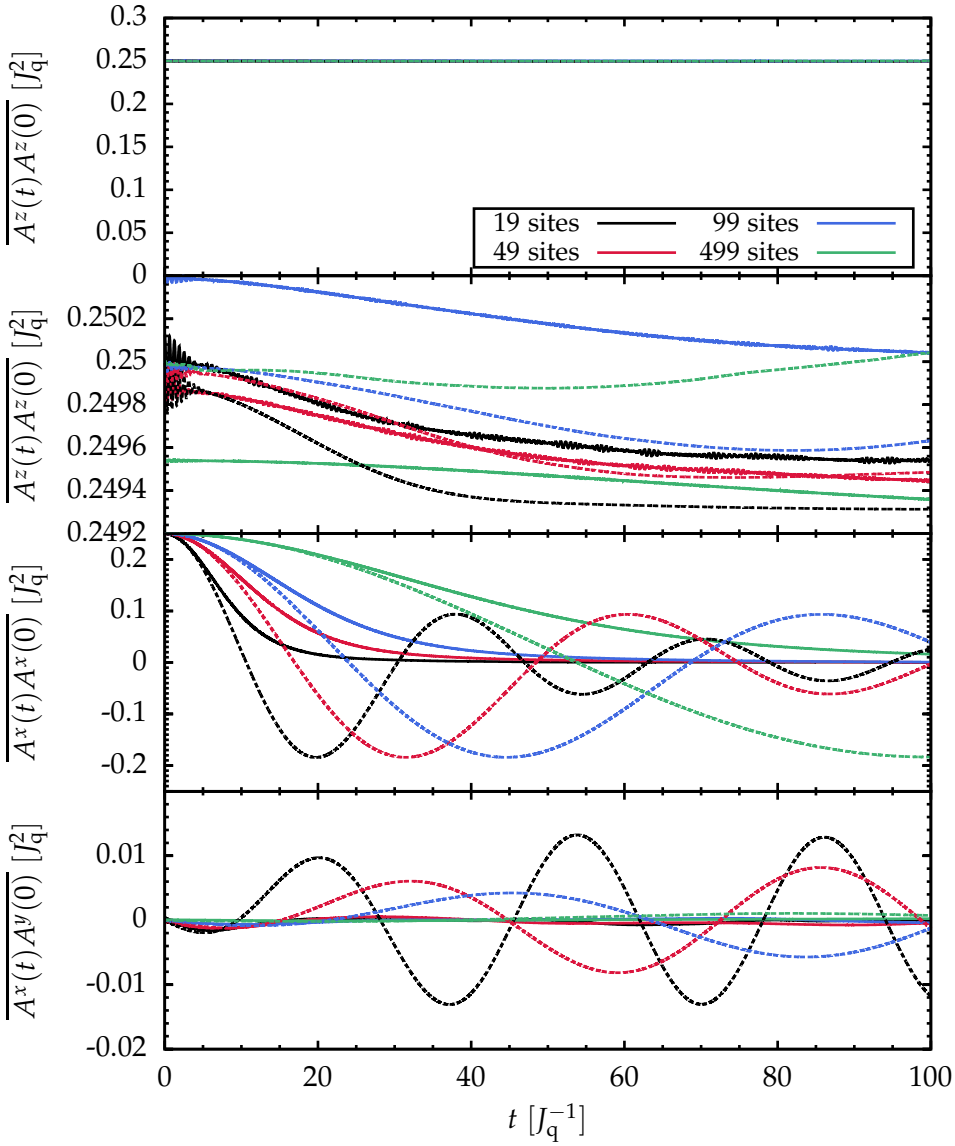

Fig. 4.12: The same as in Fig. 4.7, but now for a strong external magnetic field $h_0 = 10\,J_q$. The second panel contains a magnification of the autocorrelation function $\overline{A^z(t)A^z(0)}$ shown in the first panel. We stress that the total discarded weight of all DMRG calculations does not exceed $\mathcal{O}(10^{-3})$.

4.3.4 Summary

In total, the performance of the classical spin dynamics in a finite external magnetic field h_0 is similar to the zero-field limit. The essential dynamics of the central spin is well captured by the classical EOMs. For weak and intermediate values of h_0, a noticeable influence of quantum fluctuations still persists on intermediate time scales leading to a quantitative deviation between the classical and the DMRG result. Still, for large baths one observes qualitatively the same behavior. In the spin direction parallel to the external field, quantum fluctuations induce a marginal reduction of the autocorrelation function. Perpendicular to h_0, the classical autocorrelation functions decay slightly faster than their quantum counterparts. For a very strong external field, the quantum and classical solutions cannot be distinguished. In this regime, the dependence on the number N of bath spins is also gone. Generally, the classical EOMs capture the crossover from the weak to the strong-field regime as described in Sect. 2.7.2.2 and in Ref. [ZDAH$^+$06]. Note that DMRG also exhibits a very good performance in the strong-field regime, see Sect. 2.7.2.2. The external field suppresses the relaxation of the central spin. Hence, the number of important states increases significantly slower with t implying a reduction of the total discarded weight. In consequence, the code runs faster and much larger times can be reached. This fact is also expressed by the small total discarded weight. Even on long time scales, it does not exceed $\mathcal{O}(10^{-4}\text{-}10^{-3})$ in all DMRG calculations.

However, the classical treatment of the Overhauser field is not very successful. This effect is more pronounced for a strong external field than for a weak field. Due to the fast precession of the central spin in the external field, the classical bath spins feel only an effective average field of the central spin. This induces the smooth decay of the corresponding autocorrelation functions and suppresses the oscillations in the Overhauser field. As long as the field is rather weak and the bath contains a sufficiently large number of spins, the classical solution yields a relatively good approximation to the quantum solution up to limited values of t. For larger times, the behavior of a finite-size quantum bath will always differ from the corresponding classical bath.

Chapter 5

Pulses for Pure Dephasing

Contents

In this chapter, we discuss a semiclassical model to study the fidelity of shaped π-pulses. The semiclassical approach to the central spin problem is well-known from Chapter 3. As already mentioned in Sect. 1.6 of the Introduction, real pulses with finite amplitude and duration can be optimized by shaping their amplitudes and switching instances. This makes them closer to an ideal pulse leading to a substantial increase of their performance compared to an unshaped pulse of finite length.

At first, a semiclassical model for simulating optimized pulses suppressing the dephasing of an electron spin is introduced in Sect. 5.1. For the numerical investigation of shaped pulses, it is essential to quantify their fidelity. An appropriate measure for the deviation of a shaped pulse from an ideal one is introduced in Sect. 5.2. The numerical results presented in Sect. 5.3 reveal an unexpected behavior of the pulses when the autocorrelation function has a cusp at $t = 0$. This can be explained on the level of average Hamiltonian theory, which is derived and verified in Sect. 5.4. Furthermore, we specify the supplemental condition which may be incorporated in the design of optimized pulses in addition to the well-known standard conditions for a first order pulse. In Appendix G, it is proven

that a simultaneous fulfillment of all conditions is excluded rigorously. Hence, only a minimization of the supplemental condition can be achieved when the standard first order conditions are fulfilled.

5.1 Semiclassical model for pure dephasing

The upcoming discussion is restricted to pulses comprising solely the dephasing of the electron spin. Dephasing is the primary contribution to the decoherence of an electron spin in a quantum dot because experiments revealed that the longitudinal relaxation takes place on a much larger time scale $T_1 \gg T_2$, see Sect. 1.3. Thus, we may study a simplified semiclassical model

$$\begin{aligned} H_{\mathrm{tot}}(t) &= H(t) + H_{\mathrm{p}}(t) \\ &= \eta\,(t)\,\sigma^z + v\,(t)\,\sigma^x, \end{aligned} \tag{5.1}$$

where σ^α are the Pauli matrices. For simplicity, the factor $1/2$ of the spin operators has been neglected. The control Hamiltonian

$$H_{\mathrm{p}}\,(t) = v\,(t)\,\sigma^x \tag{5.2a}$$

describes a pulse of amplitude $v(t)$ rotating the electron spin around the x-axis. The bath is represented by a single random field $\eta(t)$ obeying Gaussian statistics. It couples to the electron spin in z-direction

$$H\,(t) = \eta\,(t)\,\sigma^z. \tag{5.2b}$$

As introduced in Chapter 3, the Gaussian fluctuations are fully described by their autocorrelation function $g(t) = \overline{\eta(t)\eta(0)}$ and their mean value $\overline{\eta(t)} = 0$. As before, the latter is again set to zero. In the semiclassical model (5.1), the energy scale is determined by the parameter g_0. It enters in the initial value $g(0) = g_0^2$ of the correlation function of the random noise and characterizes the amplitude of the fluctuations $\eta(t)$.

A semiclassical model such as (5.1) has already been frequently used for the simulation of pulses and pulse sequences with different backgrounds and for various types of Gaussian and non-Gaussian noise [MdSZW06, CLNDS08, KMB$^+$08, dLWR$^+$10, BB11]. Compared to a purely quantum mechanical model, only a moderate amount of CPU time is required for the numerical investigation. Furthermore, pulses optimized specifically for a classical bath [SFPU12, Sti12] can be simulated. Pulses shaped for a quantum bath may be studied as well because they have to fulfill additional conditions compared to pulses derived for a classical bath.

5.2 Frobenius norm

Before the numerical analysis of shaped pulses is carried out, an appropriate measure for the fidelity of a shaped pulse should be defined. It has to capture the deviation of the time evolution $U_{\mathrm{re}}(\tau_{\mathrm{p}},0)$ under the real pulse from the propagation $U_{\mathrm{id}}(\tau_{\mathrm{p}},0)$ under the ideal pulse. As already mentioned in Sect. 1.6, an ideal pulse of infinitesimal length and infinite amplitude corresponds to an instantaneous rotation $U_{\mathrm{id}}(\tau_{\mathrm{p}},0)=\widehat{P}_{\tau_{\mathrm{p}}}$ of the spin. Here, we are only dealing with π-pulses applied around the x-axis of the spin.

In the following, we stick to the choice of Ref. [PKU11] and discuss the Frobenius norm

$$\Delta_{\mathrm{F}}^2 := \frac{1}{3}\sum_{\alpha=x,y,z}\mathrm{Tr}\left(\rho^{\alpha}\right)^2. \tag{5.3}$$

The density matrix

$$\rho^{\alpha} := \rho_{\mathrm{id}}^{\alpha}-\rho_{\mathrm{re}}^{\alpha} \tag{5.4}$$

contains the deviation between the ideal π-pulse

$$\rho_{\mathrm{id}}^{\alpha} := \widehat{P}_{\tau_{\mathrm{p}}}\rho_0^{\alpha}\widehat{P}_{\tau_{\mathrm{p}}}^{\dagger} \tag{5.5a}$$

and the real π-pulse

$$\rho_{\mathrm{re}}^{\alpha} := U_{\mathrm{re}}(\tau_{\mathrm{p}},0)\rho_0^{\alpha}U_{\mathrm{re}}^{\dagger}(\tau_{\mathrm{p}},0). \tag{5.5b}$$

Each initial density matrix ρ_0^{α} represents a totally polarized state of the central spin in direction of the α-axis. They are related to the Pauli matrices σ^{α} via the relation

$$\rho_0^{\alpha}=\frac{1}{2}\left[\mathbb{1}+\sigma^{\alpha}\right]. \tag{5.6}$$

By carrying out the square in Eq. (5.3) and exploiting the properties of the time-evolution and the rotation operator, the expression for the Frobenius norm is simplified to

$$\Delta_{\mathrm{F}}^2=2\left[1-\frac{1}{3}\sum_{\alpha=x,y,z}\mathrm{Tr}\left(\rho_{\mathrm{id}}^{\alpha}\rho_{\mathrm{re}}^{\alpha}\right)\right]. \tag{5.7}$$

5.3 Simulation of pulses

As for the semiclassical model studied in Chapter 3, the most demanding part in the numerics is the sampling of the random fluctuations $\eta(t)$. This is again realized as described in Appendix E. In the numerical simulation, the time evolution under a specific pulse is carried out for every fluctuation $\eta(t)$. Thereby, one obtains the corresponding value of the squared Frobenius norm Δ_F^2 which is averaged over all fluctuations at last. As for the central spin model, the numerical simulations are carried out for the energy scale $g_0 = 1$.

In the present thesis, we discuss results for two exemplary types of autocorrelation functions $g(t)$ of the noise: One with exponential decay and a Gaussian. While the latter one is smoothly differentiable at $t = 0$, an exponentially decaying autocorrelation function $g(t) = g_0^2 \, \mathrm{e}^{-\gamma|t|}$ features a cusp at $t = 0$. This shape of $g(t)$ is not supported by our DMRG results for the central spin model. For short times, the smooth autocorrelation function $\langle A^\alpha(t) A^\alpha(0) \rangle$ of the Overhauser field is well represented by a fit to a Gaussian, see Sect. 2.7 for details. However, an exponentially decaying autocorrelation function is characteristic for an Ornstein-Uhlenbeck process [UO30]. This is a valid approximation for other types of baths, see Ref. [dLWR+10] and the references therein. An Ornstein-Uhlenbeck process can be identified with baths containing highly energetic fluctuations. They dominate the short-time behavior and induce a very fast initial decay leading to the cusp in $g(t)$. The origin of highly energetic fluctuations may be the intrinsic dynamics of the bath or mechanisms such as spin-orbit coupling. In the frequency spectrum of the noise, an Ornstein-Uhlenbeck process is related to an asymptotic $1/\omega^2$-decay. This is characteristic for a Lorentzian frequency spectrum which is linked to the exponentially decaying autocorrelation function $g(t)$ via Fourier transform.

For both types of noise, we investigate the behavior of the Frobenius norm Δ_F as a function of $1/v$ where v denotes the maximum amplitude of the pulse. This choice respects the scenario relevant for experiment where one would always stick to the maximally realizable pulse amplitude to keep the pulses as short as possible. Note that by considering a fixed value of v one compares pulses of different duration τ_p. Besides an unshaped rectangular pulse of order zero, our selection of piecewise constant π-pulses comprises the first order SCORPSE and CORPSE pulses [CJ00, CLJ03]. In second order, a pulse optimized for classical bath [SFPU12, Sti12] and the SYM2ND and ASYM2ND pulses [PKRU09] optimized for a quantum bath are studied. More information on the pulses, their amplitudes and their switching instances can be found in Appendix F.

The results for the Gaussian autocorrelation function are shown in Fig. 5.1 for two dif-

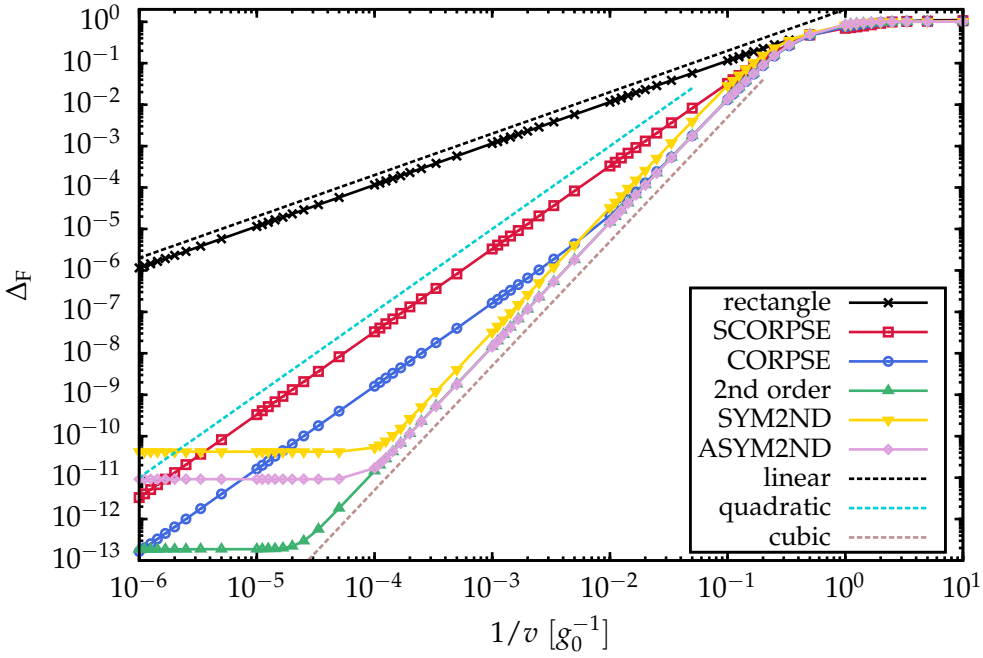

(a) $\gamma = 0.1\, g_0$

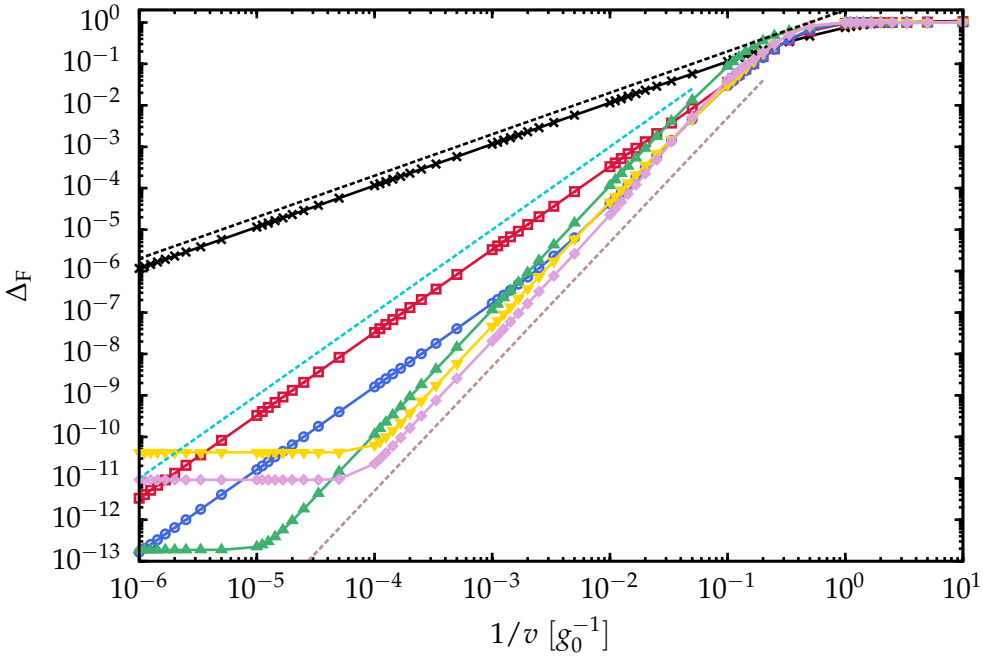

(b) $\gamma = g_0$

Fig. 5.1: Frobenius norm Δ_F versus the inverse pulse amplitude $1/v$. The autocorrelation function of the noise is a Gaussian $g(t) = g_0^2\, e^{-\gamma^2 t^2}$. The plotted data for Δ_F is the average of five independent runs of the simulation. In each run, the integration was carried out for 100,000 random fluctuations $\eta(t)$.

ferent values $\gamma = 0.1\,g_0$ (upper panel) and $\gamma = g_0$ (lower panel) of the decay rate γ. For large values of $1/v$, a saturation of the Frobenius norm Δ_F is observed because there is almost no overlap between an ideal pulse and a real pulse when the pulse amplitude is small. This corresponds to the limit $v \to 0$, where the trace in Eq. (5.7) vanishes and the Frobenius norm acquires its maximum value $\Delta_F = \sqrt{2}$. By decreasing $1/v$, a characteristic power law $\Delta_F \sim 1/v^{m+1}$ is revealed where m is the order of the pulse, see Eq. (1.12) in Sect. 1.6. This is accomplished by all pulses, except the CORPSE pulse. It represents a positive exception and behaves like a second order pulse for intermediate values of $1/v$. This behavior is rather incidental and implies that the CORPSE pulse makes second order corrections vanish for a limited range of the parameter v. For small values of $1/v$, it performs like a first order pulse as to be expected. But it still outperforms the SCORPSE pulse significantly. Thus, the CORPSE pulse has to be preferred over the SCORPSE pulse in first order. The qualitative differences between the two studied decay rates $\gamma = 0.01\,g_0$ and $\gamma = g_0$ are negligible.

In second order, the influence of the decay rate is more distinctive. For a slowly decaying Gaussian $g(t)$, the second order pulse optimized for a classical bath is comparable to the ASYM2ND pulse optimized for a quantum bath. With increasing decay rate γ, the ASYM2ND pulse clearly outperforms all other second order pulses. The failure of the pulse optimized for a classical bath can be explained by recalling its derivation. It involves the two leading orders of the Magnus expansion [SFPU12, Sti12] which is only a good approximation as long as $g(t)$ decays slowly. For a fast decaying autocorrelation function, the leading orders of the Magnus expansion do not capture all the relevant physics. The plateaus observed for very small values of $1/v$ are induced by the limited accuracy of the pulse amplitudes and switching instances, see Tab. F.1 in Appendix F. More precisely, the minimum acquired by the Frobenius norm for small values of $1/v$ scales roughly linearly with the precision of the pulse. In Fig. 5.1, this behavior is depicted by the second order pulse optimized for a classical bath. The quantum SYM2ND and ASYM2ND pulses perform slightly worse because of their more complex structure.

The numerical results for an exponentially decaying autocorrelation function are presented in Fig. 5.2. Only the unshaped rectangle behaves linearly as expected. All pulses of first and second order reveal a rather surprising behavior expressed by the power law $\Delta_F \sim 1/v^{3/2}$ involving an unexpected half-integer value $3/2$ for the exponent. In the upper panel of Fig. 5.2, power-laws with exponents $> 3/2$ can still be estimated for a very limited interval of $1/v$. If the autocorrelation function of the noise decays faster (lower panel), these regions vanish completely and $\Delta_F \sim 1/v^{3/2}$ is the only identifiable power law. From our point of view, the occurrence of half-integer exponents is a unique feature which has not been mentioned in the literature so far. Most likely, this untypical behavior has to be accounted

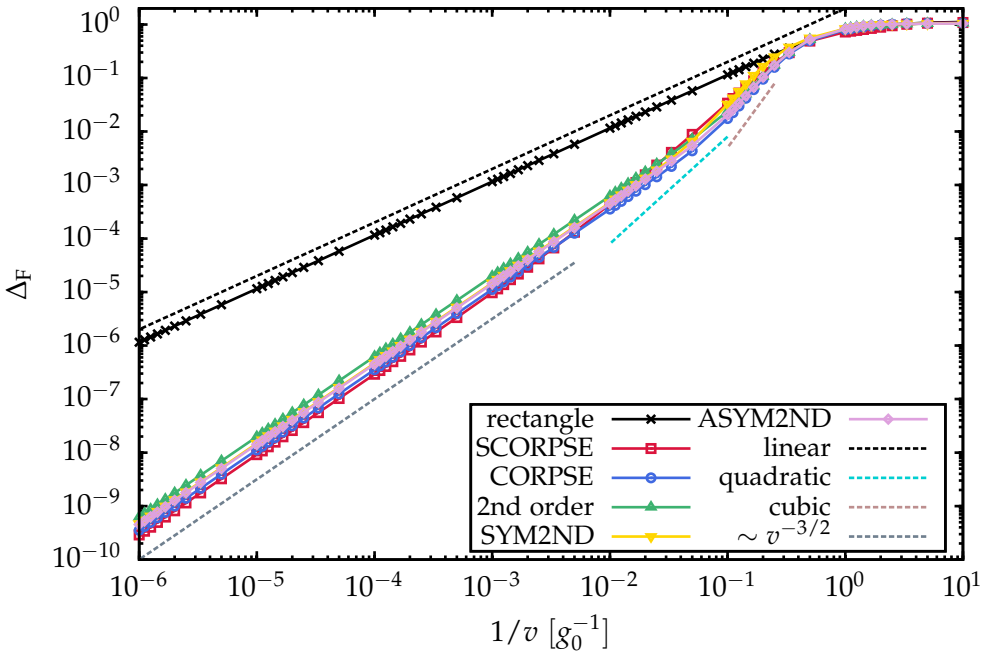

(a) $\gamma = 0.01\, g_0$

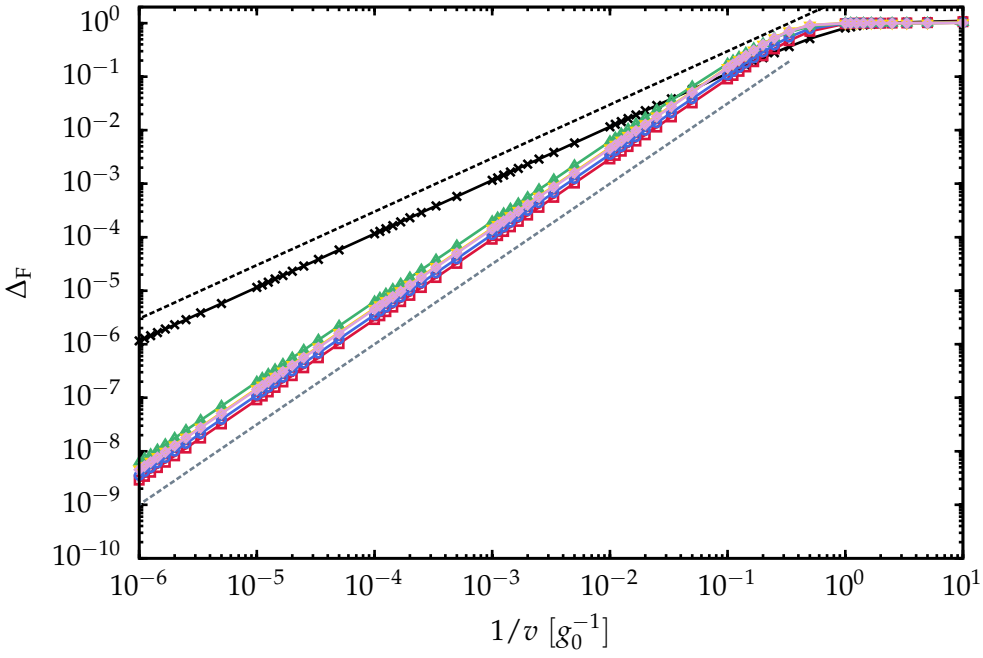

(b) $\gamma = g_0$

Fig. 5.2: The same as in Fig. 5.1, but now for an exponentially decaying autocorrelation function $g(t) = g_0^2\, \mathrm{e}^{-\gamma|t|}$.

to the cusp in $g(t)$. We come back to this issue in the next section, where we present an analysis of Δ_F based on AHT.

We close this section with some short remarks on the numerics. During our studies it turned out that the influence of the discretization of the t-axis is crucial. The switching instances as well as the amplitudes of the pulses have to be represented as exactly as possible. Otherwise, unexpected plateaus emerge in the Frobenius norm. Then, the expected power laws cannot be detected because Δ_F already saturates for fairly large values of $1/v$. The observed limitations correspond roughly to the accuracy of the implementation of the pulses. This is prevented by employing a special discretization scheme of the t-axis. For each constant segment of the pulse, the t-axis is split into a fixed number of intervals leading to a segment-depending value of Δt. Thereby, the switching instances of the pulses can be represented exactly. Compared to the pulse amplitude $v(t)$, the supporting points of the fluctuations $\eta(t)$ are shifted by half a time interval Δt. To reduce the integration error further, all time-evolution operators are represented by fourth order commutator-free exponential time propagators (CFETs) as introduced by Alvermann *et al.* [AF11, AFL12].

The observations made in our numerics also have a considerable impact on the experiment implying that the pulses have to be implemented with high precision. Only then, a reliable performance can be expected. This knowledge may also be used for the design of new pulses. For example, one could establish an additional constraint so that the switching instances would be a multiple integer of each other. Then, a fixed value of Δt could be used for all segments of the pulse. Furthermore, rational numbers as switching instances would be helpful.

5.4 Average Hamiltonian theory

In the following, we derive an analytic expression for the Frobenius norm Δ_F. Thereby, we are able to analyze the influence of the shape of $g(t)$ on Δ_F. The theory is based on the Magnus expansion of the time-evolution operator [Mag54, BCOR09, AF11] which was already employed for the AHT introduced in Chapter 3.

5.4.1 Analytical expression for the Frobenius norm

We start by further simplifying the Frobenius norm (5.7). For the time evolution under the real pulse we recall the ansatz $U_\mathrm{re}(\tau_\mathrm{p},0) = \widehat{P}_{\tau_\mathrm{p}} \cdot U_\mathrm{c}(\tau_\mathrm{p},0)$ from Eq. (1.11). This product ansatz decomposes $U_\mathrm{re}(\tau_\mathrm{p},0)$ into an ideal rotation $\widehat{P}_{\tau_\mathrm{p}}$ times a correcting factor $U_\mathrm{c}(\tau_\mathrm{p},0)$ induced by the coupling between spin and bath. This ansatz is well justified because it was used to design the pulses investigated in the present thesis [PKRU09, SFPU12, Sti12]. The ideal rotation $\widehat{P}_{\tau_\mathrm{p}}$ as well as the correction $U_\mathrm{c}(\tau_\mathrm{p},0)$ fulfill a Schrödinger equation. For the latter, the formal solution is given by

$$U_\mathrm{c}(\tau_\mathrm{p},0) = \mathcal{T}\left[\mathrm{e}^{-\mathrm{i}\int_0^{\tau_\mathrm{p}} \mathrm{d}t\, \widetilde{H}(t)}\right] \tag{5.8}$$

with the transformed Hamiltonian

$$\widetilde{H}(t) := \widehat{P}_t^\dagger H(t) \widehat{P}_t\,. \tag{5.9}$$

Thus, the correction $U_\mathrm{c}(\tau_\mathrm{p},0)$ depends solely on the coupling between spin and bath. The operator $\widehat{P}_t$ with $t \leq \tau_\mathrm{p}$ represents an ideal rotation of the central spin, see next section. For $t = \tau_\mathrm{p}$, the operator $\widehat{P}_t$ corresponds to an ideal π-pulse around the x-axis. By exploiting the unitarity of $\widehat{P}_{\tau_\mathrm{p}}$ and the properties of the trace, all ideal rotations in Δ_F cancel and the Frobenius norm reduces to

$$\Delta_\mathrm{F}^2 = 2\left[1 - \frac{1}{3}\sum_{\alpha=x,y,z} \mathrm{Tr}\left(\rho_0^\alpha U_\mathrm{c}(\tau_\mathrm{p},0)\rho_0^\alpha U_\mathrm{c}^\dagger(\tau_\mathrm{p},0)\right)\right]. \tag{5.10}$$

The correcting factor $U_\mathrm{c}(\tau_\mathrm{p}) := U_\mathrm{c}(\tau_\mathrm{p},0)$ is evaluated within the Magnus expansion. Without loss of generality, one may write

$$U_\mathrm{c}(\tau_\mathrm{p}) = \mathrm{e}^{-\mathrm{i}\,\vec{\mu}\cdot\vec{\sigma}} \tag{5.11a}$$

because the Magnus expansion $\vec{\mu}$ is always linear in the Pauli matrices σ^α for a two-level system, see Sect. 3.2 for comparison. At this point, no further assumptions have to be made for $\vec{\mu}$. By exploiting the properties of the Pauli matrices explicitly, one obtains a non-exponential representation of Eq. (5.11a)

$$U_\mathrm{c}(\tau_\mathrm{p}) = \mathbb{1} \cdot \cos|\vec{\mu}| - \mathrm{i}\sin|\vec{\mu}| \cdot \frac{\vec{\mu}\,\vec{\sigma}}{|\vec{\mu}|}. \tag{5.11b}$$

For a single value of α, the trace in Eq. (5.10) is given as

$$\mathrm{Tr}\left(\rho_0^\alpha U_\mathrm{c}(\tau_\mathrm{p})\rho_0^\alpha U_\mathrm{c}^\dagger(\tau_\mathrm{p})\right) = \cos^2|\vec{\mu}| + \frac{\sin^2|\vec{\mu}|}{|\vec{\mu}|^2} \cdot \mu_\alpha^2, \tag{5.12}$$

with μ_α^2 denoting the component α of $\vec{\mu}$. After carrying out the sum over all components α, the squared Frobenius norm acquires the simple form

$$\Delta_\mathrm{F}^2 = \frac{4}{3}\left[1 - \cos^2|\vec{\mu}|\right]. \tag{5.13}$$

5.4.2 Magnus expansion

In the previous section, the formal notation $\vec{\mu}$ was introduced as place holder for the Magnus expansion. Now, we have to derive the expansion for the semiclassical Hamiltonian $H(t)$ containing the coupling between spin and bath (5.2b). To keep this section short, the following derivation is restricted to the Hamiltonian H_tot as defined in Eq. (5.1). A more general derivation is given in Refs. [PKRU09, SFPU12, Sti12].

For an ideal rotation around the x-axis, the rotation operator is given as

$$\begin{aligned}\widehat{P}_t &= \mathrm{e}^{-\mathrm{i}\sigma^x \frac{\psi(t)}{2}} \\ &= \mathbb{1} \cdot \cos\frac{\psi(t)}{2} - \mathrm{i}\,\sigma^x \cdot \sin\frac{\psi(t)}{2}\end{aligned} \tag{5.14}$$

where

$$\psi(t) := 2\int_0^t \mathrm{d}t'\, v(t'). \tag{5.15}$$

Consequently, the expression for the transformed Hamiltonian (5.9) reads

$$\widetilde{H} = \eta(t)\sin\psi(t) \cdot \sigma^y + \eta(t)\cos\psi(t) \cdot \sigma^z. \tag{5.16}$$

Now, we address the Magnus expansion of $U_\mathrm{c}(\tau_\mathrm{p})$ which is encoded in the vector

$$\vec{\mu} = \sum_k \vec{\mu}^{(k)}. \tag{5.17}$$

Here, the sum runs over all required orders $\vec{\mu}^{(k)}$ of the expansion. This corresponds to an expansion in the pulse duration τ_p because the k-th order of the Magnus expansion induces contributions $\vec{\mu}^{(k)} \sim \tau_\mathrm{p}^k$. As explained in Chapter 3, the time ordering in Eq. 5.8 is simply neglected in leading order of the Magnus expansion. By comparing Eqs. (5.8) and (5.11a), one obtains two non-zero contributions

$$\mu_y^{(1)} = \int_0^{\tau_\mathrm{p}} \mathrm{d}t\, \eta\,(t) \sin \psi\,(t) \tag{5.18a}$$

$$\mu_z^{(1)} = \int_0^{\tau_\mathrm{p}} \mathrm{d}t\, \eta\,(t) \cos \psi\,(t)\,. \tag{5.18b}$$

In second order, one has to evaluate the commutator $[\widetilde{H}(t_1), \widetilde{H}(t_2)]$, see Appendix D. The only non-vanishing contribution is given by

$$\mu_x^{(2)} = \int_0^{\tau_\mathrm{p}} \mathrm{d}t_1 \int_0^{\tau_\mathrm{p}} \mathrm{d}t_2\, \eta\,(t_1)\, \eta\,(t_2) \sin\left[\psi\,(t_1) - \psi\,(t_2)\right]. \tag{5.19}$$

Finally, the average of the squared Frobenius norm Δ_F^2 with respect to all fluctuations $\eta(t)$ has to be calculated. This is also carried out in our numerical simulation, see Sect. 5.3. Analytically, the calculation of the average with respect to $\eta(t)$ corresponds to

$$\overline{\left|\vec{\mu}\right|^2} \equiv \overline{\mathrm{Tr}\left[U_\mathrm{c}(\tau_\mathrm{p})\rho_0^\alpha U_\mathrm{c}^\dagger(\tau_\mathrm{p})\right]}. \tag{5.20}$$

Thereby, the averaged expression obtained from the first order contributions of the Magnus expansion (5.18) reads

$$\overline{\left(\mu_y^{(1)}\right)^2 + \left(\mu_z^{(1)}\right)^2} = \int_0^{\tau_\mathrm{p}} \mathrm{d}t_1 \int_0^{\tau_\mathrm{p}} \mathrm{d}t_2\, g\,(t_1 - t_2) \cos\left[\psi\,(t_1) - \psi\,(t_2)\right]. \tag{5.21}$$

This expression induces contributions $\Delta_\mathrm{F}^2 \sim 1/v^2$ and higher due to the presence of the autocorrelation function $g(t)$. Consecutively, the average $\overline{(\vec{\mu}^{(2)})^2}$ of the second order of the Magnus expansion (5.19) induces terms which are of order $1/v^4$ and higher. Since we are searching for a contribution $\Delta_\mathrm{F}^2 \sim 1/v^3$, we do not have to take the second order of the Magnus expansion into account.

From a first guess, one might suppose that odd powers of $1/v$ in Δ_{F}^2 could be induced by contributions $\sim \mu_\alpha^{(1)} \mu_\beta^{(2)}$ origination from a combination of the first and the second order of the Magnus expansion. In fact, such terms arise during the analytical evaluation of $U_{\mathrm{c}}(\tau_{\mathrm{p}}) \rho_0^\alpha U_{\mathrm{c}}^\dagger(\tau_{\mathrm{p}})$. But they do not contribute under the trace because they are linear in the Pauli matrices. This fact is also embedded in our final expression for the Frobenius norm (5.13). The first order of the Magnus expansion is proportional to σ^y and σ^z, while the second order only features a single contribution proportional to σ^x. Hence, a combination of the first and second order cannot emerge from $|\vec{\mu}|$.

Alternatively to Eq. (5.20), one might pursue a different strategy by averaging the Magnus expansion of the correction $U_{\mathrm{c}}(\tau_{\mathrm{p}}, 0)$

$$\overline{\vec{\mu}} \equiv \overline{\mathrm{Tr}\; U_{\mathrm{c}}(\tau_{\mathrm{p}})}. \tag{5.22}$$

Compared to Eq. (5.20), the average would be carried out at an earlier stage of our analytical derivation. Thus, the simple average $\overline{\vec{\mu}}$ of the Magnus expansion $\vec{\mu}$ does not capture all occurring contributions. For example, only contributions linear in the mean value $\overline{\eta(t)}$ would be induced by the leading order of the Magnus expansion. The correlation function $g(t)$ of the noise would not appear.

5.4.3 Unexpected contributions for autocorrelation functions displaying a cusp at $t = 0$

In the following, we evaluate the averaged expression from Eq. (5.21) for an exponential autocorrelation function $g(t) = g_0^2 \mathrm{e}^{-\gamma|t|}$ or - more general - an autocorrelation function whose leading-order expansion at $t = 0$ is given by

$$g(t) = g_0^2 \left(1 - \gamma |t|\right) + \mathcal{O}(t^2). \tag{5.23}$$

The second term characterizes the cusp at $t = 0$ and will induce the $\Delta_{\mathrm{F}}^2 \sim 1/v^3$-power law as we show below.

In leading order of $g(t)$, one obtains the contribution

$$I_1 = g_0^2 \int_0^{\tau_{\mathrm{p}}} \mathrm{d}t_1 \int_0^{\tau_{\mathrm{p}}} \mathrm{d}t_2 \, \cos\left[\psi(t_1) - \psi(t_2)\right] \sim \left(\frac{1}{v}\right)^2 \tag{5.24}$$

which is only non-zero for an unshaped pulse of finite length. By applying the addition

theorem to $\cos(a+b)$, Eq. 5.24 reduces to two one-dimensional integrals

$$I_1 = g_0^2 \left[\int_0^{\tau_\mathrm{p}} \mathrm{d}t \, \cos\psi(t) \right]^2 + g_0^2 \left[\int_0^{\tau_\mathrm{p}} \mathrm{d}t \, \sin\psi(t) \right]^2 \tag{5.25}$$

which vanish for pulses of first order and higher by definition [SFPU12, Sti12]. Consequently, we have to claim that

$$0 \equiv \int_0^{\tau_\mathrm{p}} \mathrm{d}t \, \sin\psi(t) \tag{5.26a}$$

$$0 \equiv \int_0^{\tau_\mathrm{p}} \mathrm{d}t \, \cos\psi(t) \tag{5.26b}$$

when shaping pulses of first order. Next, we consider the linear order of $g(t)$ implying

$$I_{3/2} = -g_0^2 \gamma \int_0^{\tau_\mathrm{p}} \mathrm{d}t_1 \int_0^{\tau_\mathrm{p}} \mathrm{d}t_2 \, |t_1 - t_2| \cos\left[\psi(t_1) - \psi(t_2)\right] \sim \left(\frac{1}{v}\right)^3. \tag{5.27}$$

Thereby, the candidate leading to a contribution $\Delta_\mathrm{F}^2 \sim 1/v^3$ has been identified. In the next section, the Frobenius norm is evaluated for the CORPSE and SCORPSE pulse. This serves as a final verification of our AHT. We underline that the extinction of the latter expression is in general not proposed in the derivation of shaped pulses. Hence, one has to demand that the supplemental condition

$$0 \equiv \int_0^{\tau_\mathrm{p}} \mathrm{d}t_1 \int_0^{\tau_\mathrm{p}} \mathrm{d}t_2 \, |t_1 - t_2| \cos\left[\psi(t_1) - \psi(t_2)\right] \tag{5.28}$$

has to be accomplished in addition to Eqs. (5.26) to improve pulses of first order or higher. The occurrence of this new condition has to be attributed to the cusp in the autocorrelation function $g(t)$ at $t = 0$ which induces the odd orders in the expansion (5.23). Furthermore, one has to employ the correct strategy when calculating the average over all random fluctuations. If the correction $U_\mathrm{c}(\tau_\mathrm{p})$ is averaged alone, the expression in Eq. (5.21) will only depend on the squared mean value of the fluctuations and not on $g(t)$. Since the mean value is set to zero, the AHT for Δ_F^2 does not contain odd powers of $1/v$ in this case.

To our knowledge, the additional condition (5.28) as well as the observation of contributions $\Delta_\mathrm{F} \sim 1/v^{3/2}$ has not been described in the literature so far. This unique feature occurs as soon as the autocorrelation function of the noise exhibits a cusp at $t = 0$, for example in Ornstein-Uhlenbeck processes. In this case, the strategy for shaping pulses has to be

revised. In the framework of dynamic decoupling, a similar behavior was recently found by Wang and Liu [WL13]. They showed that a sequence of pulses can only suppress the decoherence up to a limited order depending on the high-frequency cutoff of the noise. For an Ornstein-Uhlenbeck-type noise, their results are in agreement with our findings for the Frobenius norm under a single pulse.

Only when the conditions in Eqs. (5.26) and (5.28) are simultaneously fulfilled, a shaped first order pulse displays the expected behavior. However, it has been proven that both conditions cannot be accomplished at the same time, see Appendix G. Hence, one should stick to first order pulses and try to minimize Eq. (5.28) in addition to the extinction of Eqs. (5.26). Thereby, the prefactor of the power law is minimized. To our present knowledge, the optimal solution is given by the well-known SCORPSE pulse [Fau13]. Better pulses have not been identified so far. If there is no linear order in $g(t)$, one can of course proceed as usual.

By considering higher orders of $g(t)$ and the Magnus expansion, subsequent orders of Δ_{F}^2 can easily be deduced. Contributions $\Delta_{\mathrm{F}}^2 \sim 1/v^4$ are obtained from the averaged first order of the Magnus expansion (5.21) in combination with the quadratic order of $g(t)$ and from the averaged second order of the Magnus expansion in combination with the constant order of $g(t)$. The systematic expansion may be pushed further to reveal odd contributions of higher orders. For example, Eq. (5.21) induces terms $\Delta_{\mathrm{F}}^2 \sim 1/v^5$ in combination with the cubic order of $g(t)$. Thus, more and more so far unknown conditions arise with increasing order of the pulse. This is already a sophisticated task in first order so that one should refrain from deriving pulses of second order and higher when odd terms are present in the expansion of the autocorrelation function.

Our analytical results for the Frobenius norm may also be used to draw conclusions from a measurement of the pulse fidelity on the type of noise of the bath. For example, an experimental investigation of pulses could reveal an unusual behavior in dependence of the inverse pulse amplitude $1/v$ or the pulse duration τ_{p}. In the measured quantity, this may be expressed by contributions proportional to odd or half-integer powers of $1/v$ or τ_{p}. Consequently, the autocorrelation function $g(t)$ should likely feature a cusp at $t = 0$ according to our results. This would imply the presence of highly energetic processes in the bath which dominate the short-time behavior of the noise. Vice versa, the presence of a soft high-energy cutoff $\sim 1/\omega^2$ in the measured noise spectrum of the bath would indicate that the efficiency of pulses is limited. In particular, this would imply that second order pulses do not lead to a significant improvement compared to first order pulses.

5.4.4 Verification for the CORPSE and SCORPSE pulse

In the previous section, an analytic expression for the Frobenius norm explaining the unexpected $\Delta_F^2 \sim 1/v^{3/2}$ contribution has been derived in the framework of AHT. But we still owe the reader a verification of this result. Therefore, we employ our theory and deduce analytic expressions for the $1/v^{3/2}$-power laws observed in Fig. 5.2. The following discussion is restricted to the first order CORPSE and SCORPSE pulse, but the extension to other pulses is straightforward.

First, the expression for the Frobenius norm (5.13) is expanded in leading order

$$\Delta_F^2 = \frac{4}{3}\overline{|\vec{\mu}|^2} + \mathcal{O}\left(\overline{|\vec{\mu}|^4}\right). \tag{5.29}$$

Second, we have to carry out the integrals in Eq. (5.27). As long as one is only interested in the leading order, it is sufficient to consider the latter one. The evaluation for the individual pulses is straightforward, but rather lengthy. Hence, we only give a short description of the procedure and present the results. At first, one has to evaluate $\psi(t)$ (5.15) for each pulse under study. After the piecewise constant expressions for $\psi(t)$ have been inserted in Eq. (5.27), the two-dimensional integration can be carried out. By inserting the results for $\overline{|\vec{\mu}|^2} = I_{3/2}$ from Eq. (5.27) in Eq. (5.29), one obtains the power laws

$$\Delta_F^2\big|_{\text{CORPSE}} = 4\pi g_0^2 \gamma \left(\frac{1}{v}\right)^3 \tag{5.30a}$$

$$\Delta_F^2\big|_{\text{SCORPSE}} = \frac{8\pi}{3} g_0^2 \gamma \left(\frac{1}{v}\right)^3 \tag{5.30b}$$

for the leading order of the Frobenius norm Δ_F.

In Fig. 5.3, the power laws (dashed lines) are plotted together with the results obtained from the numerical simulation (symbols, see Fig. 5.2 for details). For both pulses and all values of γ, our AHT results are in perfect agreement with the numerics. Hence, the occurrence of unexpected terms $\Delta_F \sim 1/v^{3/2}$ is indeed attributed to the contribution resulting from Eq. (5.27).

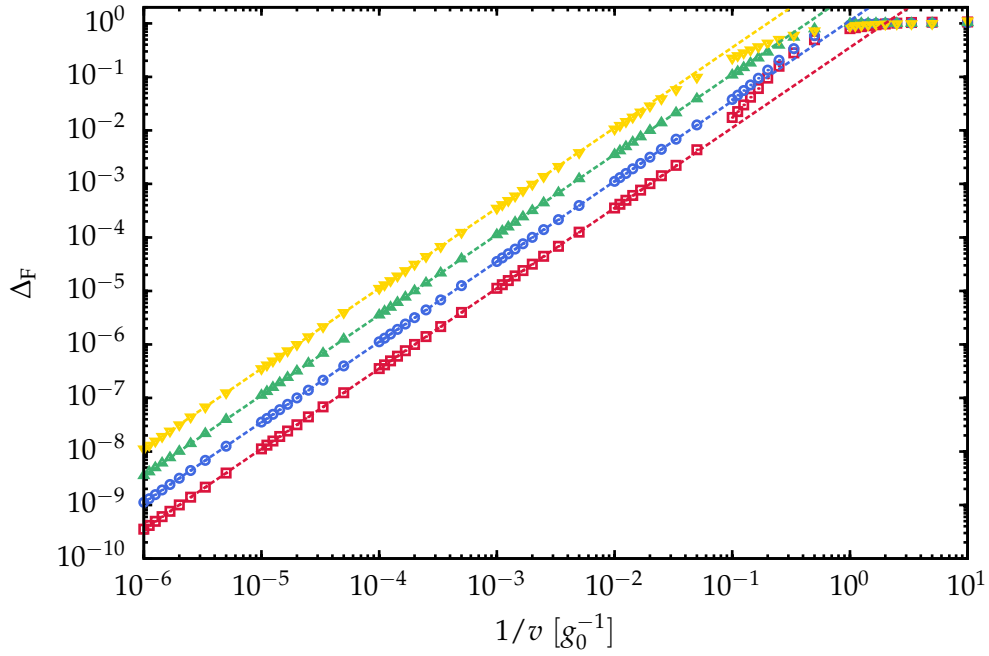

(a) CORPSE pulse

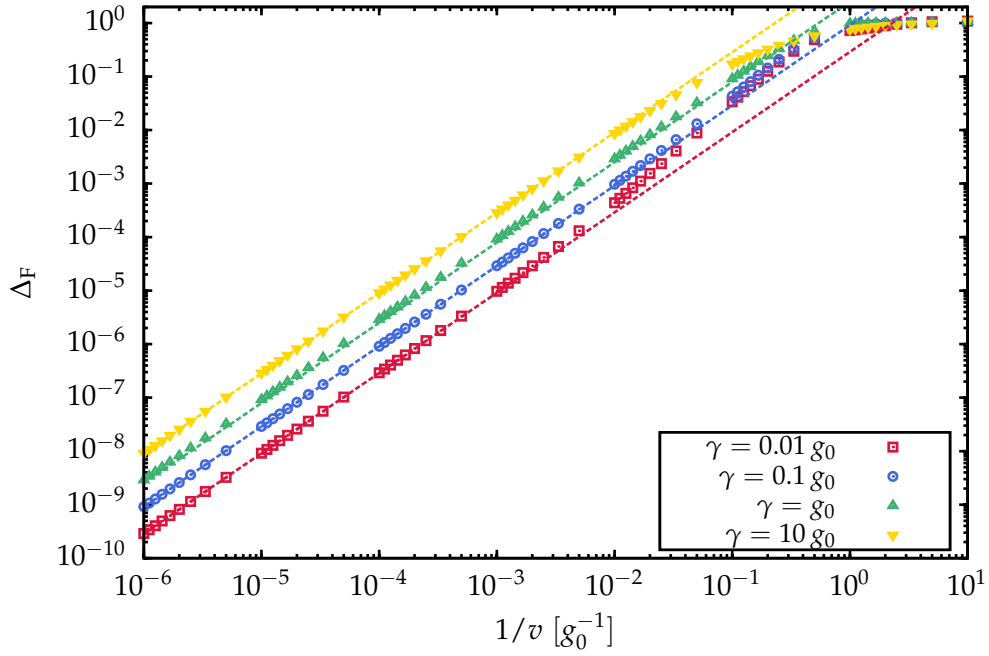

(b) SCORPSE pulse

Fig. 5.3: Frobenius norm Δ_F versus the inverse pulse amplitude $1/v$ for an exponentially decaying autocorrelation function $g(t) = g_0^2\, e^{-\gamma|t|}$ of the noise. The AHT (dashed lines) thoroughly explains the unexpected $\Delta_F \sim 1/v^{3/2}$ behavior observed in the numerical results for the Frobenius norm Δ_F (symbols). We highlight that the AHT is a purely analytical theory, it does not involve a fit to the numerical data.

Conclusion

In this thesis, we investigated the spin dynamics in the central spin model with and without external magnetic field. Experimentally, the central spin model describes the decoherence of a single electron spin confined in a quantum dot which is dominated by the hyperfine interaction between the electron spin and the surrounding nuclear spins in the dot. We tackled the problem on three different levels: A full treatment of the quantum model in the framework of DMRG, a semiclassical model involving a replacement of the bath by a classical random field, and by solving the classical equations of motion.

The numerical treatment on the level of DMRG captures the full hyperfine interaction in the central spin model. Compared to exact diagonalization and Bethe ansatz techniques, the number of accessible bath spins is at least one order of magnitude larger. Therefore, we demonstrated how DMRG can be efficiently adapted for a starlike cluster of spins as defined by the topology of the central spin model. The exact calculation of the trace of the observables at infinite temperature is enabled by purifying the initial state at the cost of doubling the size of the bath. For calculating the real-time evolution in the framework of DMRG, three different approaches were introduced and tested. Thereby, the adaptive method based on the Trotter-Suzuki decomposition of the time-evolution operator was identified to work best for our purposes. Even in second order, the Trotter-Suzuki decomposition has proven to yield good results up to intermediate times $t \approx$ 30-50 J_{q}^{-1}. In general, it is not required to employ the fourth order decomposition. Due to the moderately growing total discarded weight and acceptable run times, up to $N \approx 1000$ bath spins can be treated on intermediate time scales.

In contrast, Krylov vectors do not suffer from the Trotter-Suzuki error so that they exceed the accuracy of the Trotter-Suzuki decomposition on the short-time scale. But they fail for larger times because of the fast growing total discarded weight and the strongly increasing amount of CPU time. In addition, we implemented the real-time evolution on the basis of Chebychev polynomials. However, this approach cannot be recommended due to extremely fast growing total discarded weight. The comparison with the two other approaches revealed that it already fails for small numbers of bath spins. This has to be accounted to the special symmetry of the central spin model: Due to the starlike structure,

a perturbation created at the site of the central spin spreads immediately over the whole cluster of spins. But the performance of the Chebychev expansion might be improved by including the doubling of the number of coefficients as suggested in Sect. 2.5.4. Thereby, one could also avoid the permanent targeting of the initial state.

Subsequently, we presented a detailed analysis of the performance of the real-time evolution with DMRG based on the Trotter-Suzuki decomposition. As a first application, the influence of the number of bath spins on the short-time dynamics in the central spin model was investigated. Without any external field, the autocorrelation function of the central spin never exhibits a complete decay and the autocorrelation function of the Overhauser field is almost static. An external field induces an additional precession of the central spin and the bath spins. This causes the dephasing of the central spin in the spin directions perpendicular to the external field. In contrast, a finite external field suppresses the relaxation in the spin direction parallel to the external field. By increasing the external field, a crossover from a smooth to an oscillating decay of the transverse autocorrelation functions occurs.

Compared to other approaches applicable for large bath sizes, our ansatz based on the DMRG fully captures the dynamics in the quantum central spin model for arbitrary external fields while cluster expansions and solutions of non-Markovian master equations always require a finite external field. Moreover, cluster expansions usually involve the secular approximation where spin flips between the central spin and the bath spins are neglected. Furthermore, an intrinsic dynamics of the bath is induced by dipolar couplings between the bath spins which are usually distributed randomly. A well-defined distribution of the couplings is not used. Thus, the employed model cannot be compared directly to the central spin model studied in the present thesis.

In contrast, master equations are employed to study the central spin dynamics in the central spin model. With respect to our distribution of the coupling constants, the latest non-perturbative master equation solution by Barnes *et al.* [BCDS12] requires a finite external field which has to be at least of the order of the energy scale J_q for $N \approx 1000$ bath spins. In addition, the accessible time scale is limited by the largest coupling constant. We stress that there is no such restriction in our DMRG calculations. For $N \approx 1000$ bath spins, DMRG yields good results up to $t \approx 25\text{-}30\, J_\mathrm{q}^{-1}$ while the non-perturbative solution of the master equation is restricted to $t \approx 18\, J_\mathrm{q}^{-1}$ which is significantly smaller. Hence, the DMRG outperforms the non-perturbative solution of the master equation also with respect to the accessible time scales, see Appendix H for more details. Older master equation solutions, for example the one presented in Ref. [FBN$^+$08], require an even larger external field so that the strength has to be a multiple of the energy scale J_q. The same restriction holds for

the perturbative approach presented in Ref. [CL04]. Consequently, these approaches deliver solutions valid only in the strong-field regime, where DMRG works extremely well and the dynamics is essentially classical, see below.

Motivated by the results for the zero-field limit and by a simple analytic argument, we introduced an effective semiclassical picture for the central spin problem. In the semiclassical model, the bath is replaced by a classical Gaussian variable, while the central spin is still treated on the quantum level. First, we introduced an average Hamiltonian theory for the central spin based on the systematic Magnus expansion of the time-evolution operator. Second, a numerical simulation of the central spin in the semiclassical model involving a sampling of the random fluctuations was carried out. Together with DMRG, we were able to show that - depending on the exact value of t - both the semiclassical as well as the quantum result converge towards the static bath approximation for already a moderate number of $N \gtrsim 100$ bath spins. But the comparison with the DMRG results up to intermediate times revealed that a separate treatment of the conserved quantities in the numerical simulation of the semiclassical model is crucial. When the conserved total spin is treated separately, a nice agreement between the semiclassical and the quantum picture is achieved in the zero-field limit up to intermediate times. However, this approach requires the correlation function of the bath to be known from an external source. Moreover, it does not fulfill the conservation of the total energy.

The latter was achieved by regarding the fully classical equations of motion. The numerical solution of the classical equations of motion also comprises a consistent calculation of the autocorrelation functions of the bath. In the zero-field limit, it turned out that the dynamics of the central spin on the short-time scale is essentially classical as long as the size of the bath is not too small ($N \gtrsim 100$ bath spins). For larger times, the influence of quantum fluctuations increases. Compared to the classical description, they slightly reduce the non-decaying fraction of the autocorrelation function of the central spin. In a finite external field, the accuracy of the classical approximation depends on the strength of the external field. A qualitative description of the central spin dynamics is achieved always. The agreement between the classical and the quantum description increases upon growing external field. In the strong-field limit, both qualitative and quantitative agreement is acquired. With respect to the Overhauser field, the differences between the classical and the quantum picture are more pronounced. As long as the external field is weak or not present at all, the classical description of the Overhauser field is still fairly good. However, discrepancies arise in the spin directions perpendicular to the external field when the strength of the field is increased. For large fields, the classical bath spins only feel an effective field of the central spin due to its very fast precession. Hence, the autocorrelation functions of the classical Overhauser field in spin directions perpendicular to the external field do not

display any oscillations as their quantum counterparts. Instead, they decay smoothly to zero. But concerning the static limit, our observations suggest that the classical as well as the quantum description of the Overhauser field will coincide if the number of bath spins is sufficiently large.

Finally, we considered an application of the semiclassical model and investigated optimized pulses suppressing the dephasing of the central spin. Thereby, an unexpected $\Delta_F \sim 1/v^{3/2}$ behavior of the Frobenius norm was revealed for pulses of first order and higher if the autocorrelation function of the noise displays a cusp at $t = 0$, for instance due to an Ornstein-Uhlenbeck process. On the level of average Hamiltonian theory, we verified that this unusual behavior has to be attributed to the cusp in the autocorrelation function of the noise. To diminish the effect of the half-integer contribution, we derived an additional condition to be fulfilled by pulses of first order and higher. But the contribution of the half-integer order can only be minimized, it cannot be eliminated. This could be established rigorously.

Outlook

With the DMRG code for the quantum model and the corresponding codes for the semiclassical and classical model, we have developed a wide selection of powerful tools for investigating the spin dynamics in the central spin model. In the following, we suggest several applications of the existing tools and some possible future extensions.

So far, a generic uniform distribution of the coupling constants was used for the proof-of-principle investigation presented in this thesis. Without any additional effort, the existing codes can be employed to study the influence of various types of distributions on the spin dynamics. Thereby, one can account for more realistic shapes of the central spin wave function and parameters extracted from experiment, see for instance Ref. [SKL03, HA14]. Moreover, one may also investigate the spin dynamics for anisotropic coupling constants as discussed in Ref. [HA14].

Additional pulses can be implemented easily in the random noise simulation of the semiclassical model. In particular, the simulation may serve as a nice benchmark for pulses optimized specifically for an Ornstein-Uhlenbeck type noise. Future work could also comprise the numerical simulation of pulse sequences from dynamic decoupling or pulses and pulse sequences in the framework of the classical equations of motion or in the framework of DMRG, see below.

With respect to the real-time evolution based on the Chebychev expansion, one should definitely implement the doubling of the coefficients as described in Sect. 2.5.4. Additionally, other orthogonal polynomials such as HERMITE POLYNOMIALS may be employed for the calculation of the real-time evolution. A comparison of the advantages and disadvantages of different orthogonal polynomials would certainly be worthwhile.

Several other extensions of the DMRG code are feasible. Starting from a purified initial state, finite temperatures may be reached by cooling the system via a time evolution in imaginary time. The implementation is straightforward, since the required routines may be taken over from the time evolution based on the Trotter-Suzuki decomposition. However, the central site has to be purified as well which may imply a certain caveat. Furthermore, one could study the influence of an intrinsic dynamics in the bath induced by a dipolar interaction between the bath spins. To avoid dipolar couplings going beyond nearest neighbor interaction, one should consider an exemplary dipolar interaction where the bath spins form a linear chain. A non-interacting linear alignment of the bath spins has already been assumed in the DMRG setup of system and environment block. Hence, just the corresponding interaction terms would have to be added to the Hamiltonian.

Another worthwhile - but ambitious - extension is the simulation of pulses or even pulse sequences in the framework of time-dependent DMRG. While ideal pulses may be realized without great effort in the existing code, some severe changes would be required for the implementation of real pulses of finite length. Due to the Trotter-Suzuki decomposition, the implementation of time-dependent Hamiltonians is straightforward because only the local time-evolution operators must be modified. But a real pulse implies a continuous change of the magnetization of the superblock state. Consequently, the magnetization is not a conserved quantity anymore and the corresponding good quantum number cannot be used to label the basis of the blocks. This would result in a significant decrease of the performance of the algorithm because the block structure of the matrices would be gone. Consequently, the accessible number of bath spins and maximum time scales would have to be reduced to compensate the loss of performance.

Appendix

Appendix A

Transformation of the DMRG Superblock State

In this appendix, an example for the transformation of the state vector in DMRG is presented. The implementation of such transformations was first suggested by White [Whi96]. Applied during the finite size algorithm introduced in Sect. 2.2.2, they speed up the calculation of the target state by improving the initial guess for iterative procedures. The target state of the previous block configuration is transformed approximately to the basis of the next DMRG step and can thus be used as starting point of, for example, the Lanczos algorithm to calculate the ground state. Furthermore, they are essential for the sweeps occurring in all methods for the real-time evolution, see Sect. 2.4. In the adaptive approach based on the TS decomposition, the local time-evolution operators are applied during the transformation of the superblock state, see Sect. 2.4.2.

In the following, we depict the scenario where the system block is left and the environment block is right. The transformation extracts the bath site P_{l+1} from the environment block $\overline{E}_{N-l}$ and integrates it into the system block S_l. This corresponds to a single step in the half-sweep from left to right. Before the transformation, the state of the superblock has the form

$$|\Psi\rangle = \sum_{m_l, \overline{m}_{N-l}} \Psi_{m_l, \overline{m}_{N-l}} \, |m_l\rangle_{\mathrm{L}} \, |\overline{m}_{N-l}\rangle_{\mathrm{R}} \,, \tag{A.1}$$

where m_l and $\overline{m}_{N-l}$ are the quantum numbers of the left and right block, as denoted by the indices of the basis vectors. The indices of the quantum numbers denote the number of bath spins in the respective block. As before, the bar indicates that the basis of the right block incorporates the central spin.

At first, we insert the truncated basis $\sum_{\widetilde{m}_l} |\widetilde{m}_l\rangle \langle \widetilde{m}_l| \approx \mathbb{1}$ to reduce the basis of the system

block. Then, the superblock state is given as

$$|\Psi\rangle = \sum_{\widetilde{m}_l, \overline{m}_{N-l}} \Psi_{\widetilde{m}_l, \overline{m}_{N-l}} \, |\widetilde{m}_l\rangle_{\mathrm{L}} \, |\overline{m}_{N-l}\rangle_{\mathrm{R}} \tag{A.2a}$$

with the new coefficients

$$\Psi_{\widetilde{m}_l, \overline{m}_{N-l}} = \sum_{m_l} \Psi_{m_l, \overline{m}_{N-l}} \, {}_{\mathrm{L}}\langle \widetilde{m}_l | m_l \rangle_{\mathrm{L}} \quad . \tag{A.2b}$$

The matrix elements ${}_{\mathrm{L}}\langle \widetilde{m}_l | m_l \rangle_{\mathrm{L}}$ are obtained from the basis truncation of the previous step. Note that this step is only approximative because $|\widetilde{m}_l\rangle$ is not a complete representation of the system basis.

In our adaption of the DMRG algorithm, the central spin is always the last spin added in each step. Thus, it has to be separated from the environment block before the bath site can be transformed. Thereby, one obtains an additional loop over the state $|\sigma_0\rangle$ of the central site

$$|\Psi\rangle = \sum_{\widetilde{m}_l, \widetilde{m}_{N-l}, \sigma_0} \Psi_{\widetilde{m}_l, \widetilde{m}_{N-l}, \sigma_0} \, |\widetilde{m}_l\rangle_{\mathrm{L}} \, |\widetilde{m}_{N-l}\rangle_{\mathrm{R}} \, |\sigma_0\rangle \tag{A.3a}$$

where

$$\Psi_{\widetilde{m}_l, \widetilde{m}_{N-l}, \sigma_0} = \sum_{\overline{m}_{N-l}} \Psi_{\widetilde{m}_l, \overline{m}_{N-l}} \, {}_{\mathrm{R}}\langle \widetilde{m}_{N-l}, \sigma_0 | \overline{m}_{N-l} \rangle_{\mathrm{R}} \quad . \tag{A.3b}$$

The transformation ${}_{\mathrm{R}}\langle \widetilde{m}_{l+1}, \sigma_0 | \overline{m}_{l+1} \rangle_{\mathrm{R}}$ stores how the state $|\sigma_0\rangle$ of the central site is added to the truncated basis $|\widetilde{m}_{l+1}\rangle_{\mathrm{R}}$ of the environment block.

Subsequently, the basis of the environment block is extended via

$$|\Psi\rangle = \sum_{\widetilde{m}_l, m_{N-l}, \sigma_0} \Psi_{\widetilde{m}_l, m_{N-l}, \sigma_0} \, |\widetilde{m}_l\rangle_{\mathrm{L}} \, |m_{N-l}\rangle_{\mathrm{R}} \, |\sigma_0\rangle \tag{A.4a}$$

where

$$\Psi_{\widetilde{m}_l, m_{N-l}, \sigma_0} = \sum_{\widetilde{m}_{N-l}} \Psi_{\widetilde{m}_l, \widetilde{m}_{N-l}} \, {}_{\mathrm{R}}\langle m_{N-l} | \widetilde{m}_{N-l} \rangle_{\mathrm{R}} \quad . \tag{A.4b}$$

The is achieved by the inverse transformation ${}_{\mathrm{R}}\langle m_{N-l} | \widetilde{m}_{N-l} \rangle_{\mathrm{R}}$ obtained in a former step where the system block was on the right-hand side.

Now, we can address the rightmost site P_{l+1} in the environment block. After its separation, one obtains an additional loop over the state $|\sigma_{l+1}\rangle$ of the single bath spin and the

superblock state reads

$$|\Psi\rangle = \sum_{\widetilde{m}_l,\widetilde{m}_{N-l-1},\sigma_0,\sigma_{l+1}} \Psi_{\widetilde{m}_l,\widetilde{m}_{N-l-1},\sigma_0,\sigma_{l+1}} \, |\widetilde{m}_l\rangle_{\mathrm{L}} \, |\widetilde{m}_{N-l-1}\rangle_{\mathrm{R}} \, |\sigma_0\rangle \, |\sigma_{l+1}\rangle \tag{A.5a}$$

where

$$\Psi_{\widetilde{m}_l,\widetilde{m}_{N-l-1},\sigma_0,\sigma_{l+1}} = \sum_{m_{N-l}} \Psi_{\widetilde{m}_l,m_{N-l},\sigma_0} \, {}_{\mathrm{R}}\langle\sigma_{l+1},\widetilde{m}_{N-l-1}|m_{N-l}\rangle_{\mathrm{R}} \quad . \tag{A.5b}$$

The transformation ${}_{\mathrm{R}}\langle\sigma_{l+1},\widetilde{m}_{N-l-1}|m_{N-l}\rangle_{\mathrm{R}}$ stores how the bath site P_{l+1} was integrated into the environment block during the former half-sweep from right to left. Now, all exact sites of the current configuration of the superblock are separated. At this step, they can be addressed individually which is a key aspect for the calculation of the real-time evolution introduced in Sect. 2.4.2.

Next, the bath spin P_{l+1} is moved to the system block by the transformation

$$|\Psi\rangle = \sum_{m_{l+1},\widetilde{m}_{N-l-1},\sigma_0} \Psi_{m_{l+1},\widetilde{m}_{N-l-1},\sigma_0} \, |m_{l+1}\rangle_{\mathrm{L}} \, |\widetilde{m}_{N-l-1}\rangle_{\mathrm{R}} \, |\sigma_0\rangle \quad . \tag{A.6a}$$

The loop in the coefficients

$$\Psi_{m_{l+1},\widetilde{m}_{N-l-1},\sigma_0} = \sum_{\widetilde{m}_l,\sigma_{l+1}} \Psi_{\widetilde{m}_l,\widetilde{m}_{N-l-1},\sigma_0,\sigma_{l+1}} \, {}_{\mathrm{L}}\langle m_{l+1}|\widetilde{m}_l,\sigma_{l+1}\rangle_{\mathrm{L}} \tag{A.6b}$$

runs additionally over the state $|\sigma_{l+1}\rangle$ of the freshly added bath spin. The matrix elements ${}_{\mathrm{L}}\langle m_{l+1}|\widetilde{m}_l,\sigma_{l+1}\rangle_{\mathrm{L}}$ describe the extension of the system block basis due to the bath site P_{l+1}. They are obtained from the basis extension of the system block which is performed before the call of the wave function transformation.

Finally, the central site is integrated back into the environment block by

$$|\Psi\rangle = \sum_{m_{l+1},\overline{m}_{N-l-1}} \Psi_{m_{l+1},\overline{m}_{N-l-1}} \, |m_{l+1}\rangle_{\mathrm{L}} \, |\overline{m}_{N-l-1}\rangle_{\mathrm{R}} \tag{A.7a}$$

where

$$\Psi_{m_{l+1},\overline{m}_{N-l-1}} = \sum_{\widetilde{m}_{N-l-1},\sigma_0} \Psi_{m_{l+1},\widetilde{m}_{N-l-1},\sigma_0} \, {}_{\mathrm{R}}\langle\overline{m}_{N-l-1}|\widetilde{m}_{N-l-1},\sigma_0\rangle_{\mathrm{R}} \quad . \tag{A.7b}$$

The transformation ${}_{\mathrm{R}}\langle\overline{m}_{N-l-1}|\widetilde{m}_{N-l-1},\sigma_0\rangle_{\mathrm{R}}$ contains all the information concerning the extension of the environment related to the integration of the central site.

Thereby, the transformation of the superblock state to the new basis is complete. It is not

exact due to the involved basis truncation. But the DMRG truncation with respect to the reduced density matrix keeps all important states so that the error should be of the order of the discarded weight. Concerning the implementation, all required transformations described above have to be stored during the runtime of the algorithm. This applies to all basis truncations as well as to all basis extensions. The transformations for the half-sweep from right to left and for the interchange of the left and the right block are closely related to the presented example and can be adapted easily.

Appendix B

Fourth Order Trotter-Suzuki Decomposition

The second order as well as the fourth order of the Trotter-Suzuki (TS) decomposition are derived from the Magnus expansion [Mag54, BCOR09, AF11] of the time-evolution operator. In this appendix, we present our derivation of the fourth order decomposition [SRU13].

For abbreviation, we denote the unitary time evolution realized in a forward sweep, i.e. a half-sweep from left to right, through the superblock by

$$P_{1N}(x) = \mathrm{e}^{-\mathrm{i}xh_1}\,\mathrm{e}^{-\mathrm{i}xh_2}\ldots\mathrm{e}^{-\mathrm{i}xh_N}, \tag{B.1}$$

where N is the number of bath spins. The local Hamiltonian h_i represents the complete interaction between bath spin i and the central spin. The corresponding backward sweep to (B.1) is denoted by $P_{N1}(x)$ and is simply obtained by reversing the order of the local time-evolution operators in (B.1). Thereby, the second order of the TS decomposition acquires the form

$$\begin{aligned}\mathrm{e}^{-\mathrm{i}2xH} &= P_{1N}(x)\,P_{N1}(x) + \mathcal{O}\left(\Delta t^3\right)\\ &= \mathrm{e}^{-\mathrm{i}xh_1}\,\mathrm{e}^{-\mathrm{i}xh_2}\ldots\mathrm{e}^{-\mathrm{i}xh_{N-1}}\,\mathrm{e}^{-\mathrm{i}xh_N}\,\mathrm{e}^{-\mathrm{i}xh_N}\,\mathrm{e}^{-\mathrm{i}xh_{N-1}}\ldots\mathrm{e}^{-\mathrm{i}xh_2}\,\mathrm{e}^{-\mathrm{i}xh_1} + \mathcal{O}\left(\Delta t^3\right)\end{aligned} \tag{B.2}$$

with $x = \Delta t/2$.

As the second order, the fourth order of the TS decomposition is derived as the average Hamiltonian expression for a half-sweep P_{1N} or P_{N1} (B.1), respectively. By the successive application of six half-sweeps which are chosen to be symmetric with respect to time-reversal, one obtains

$$P_{1N}(\mu)\,P_{N1}(\lambda)\,P_{1N}(1)\,P_{N1}(1)\,P_{1N}(\lambda)\,P_{N1}(\mu) = \mathrm{e}^{c_1+c_2+c_3+\mathcal{O}\left(\Delta t^5\right)}, \tag{B.3}$$

where the right-hand side results from the Magnus expansion. The operators c_i in the exponential read

$$c_1 = 2\Omega_1 \left(1 + \lambda + \mu\right) \tag{B.4a}$$

$$c_2 = \Omega_2 \left(\lambda^2 - \lambda^2 + \mu^2 - \mu^2\right) = 0 \tag{B.4b}$$

$$c_3 = 2\Omega_3 \left(\lambda^3 + \mu^3 + 1\right) + [\Omega_1, \Omega_2] \left(1 + \mu^3 + 2\lambda\mu^2 + 2\mu^2 - \lambda^3 - 2\lambda^2\right), \tag{B.4c}$$

where Ω_n denotes the n-th order contribution of the Magnus expansion [AF11]. The first order is given by the local decomposition of the Hamiltonian H

$$\Omega_1 = \sum_{i=1}^{N} h_i \,. \tag{B.5}$$

The brackets in Eq. (B.4b) vanish by construction due to the time-reversal symmetry of the sequence. For the same reason we know without calculation that there is no contribution $c_4 \sim \Delta t^4$ [Hae76]. The brackets in Eq. (B.4c) vanish for $\mu = -1/\sqrt[3]{2} = \lambda$ so that Eq. (B.3) corresponds to the desired time-evolution operator up to $\mathcal{O}(\Delta t^5)$.

Now, we define

$$\begin{aligned} \mathrm{e}^{-\mathrm{i}H\Delta t} = {} & P_{1N}\left(\alpha\frac{\Delta t}{2}\right) \cdot P_{N1}\left(\beta\frac{\Delta t}{2}\right) \cdot P_{1N}\left(\gamma\frac{\Delta t}{2}\right) \cdot P_{N1}\left(\gamma\frac{\Delta t}{2}\right) \\ & \cdot P_{1N}\left(\beta\frac{\Delta t}{2}\right) \cdot P_{N1}\left(\alpha\frac{\Delta t}{2}\right) + \mathcal{O}\left(\Delta t^5\right). \end{aligned} \tag{B.6}$$

for the fourth order of the TS decomposition. The coefficients

$$\alpha = \frac{1}{2 - 2^{1/3}} = \beta \tag{B.7a}$$

$$\gamma = -\frac{1}{2^{2/3} - 1} \tag{B.7b}$$

are obtained by rescaling the solutions for λ and μ from Eqs. (B.4).

If the fourth order decomposition is used to calculate the real-time evolution with the adaptive method, three back and forth sweeps are required to proceed one step Δt in time. After $t/\Delta t$ applications, the TS error in fourth order accumulates to $\mathcal{O}(\Delta t^4)$.

Appendix C

Purified States

In this appendix, we present an analytic argument that the time-evolution operator

$$U = \mathrm{e}^{-\mathrm{i}(H_\mathrm{r} - H_\mathrm{a})\Delta t} \tag{C.1}$$

leaves a completely purified initial state $|0\rangle$ as defined in Eq. (2.59) unchanged. The Hamiltonian of the real spins is denoted by H_r, while H_a denotes the Hamiltonian for the auxiliary spins. They are both identical, but the auxiliary spins propagate backwards in time. The following line of argument is taken from Ref. [SRU13] where we argued on the basis of a simple toy model.

We consider a singlet state

$$|S_1, S_2\rangle = \frac{1}{\sqrt{2S+1}} \sum_i^{2S} (-1)^i \, |S-i, -(S-i)\rangle \tag{C.2}$$

of two half-integer spins, for example two nearest neighbors taken from a chain. The operators acting on site 1 and 2 are denoted by $\vec{S}_{i,\mathrm{r}}$. A generic Hamiltonian for the two spins is $H_\mathrm{r} = \vec{S}_{1,\mathrm{r}} \cdot \vec{S}_{2,\mathrm{r}}$. In addition, an auxiliary spin with operator $\vec{S}_{i,\mathrm{a}}$ is introduced for each real spin.

The action of H_r on the initial state $|S_1, S_2\rangle$ is given as

$$H_\mathrm{r} \, |S_1, S_2\rangle = \vec{S}_{1,\mathrm{r}} \cdot \vec{S}_{2,\mathrm{r}} \, |S_1, S_2\rangle \tag{C.3a}$$

$$= -\vec{S}_{1,\mathrm{a}} \cdot \vec{S}_{2,\mathrm{r}} \, |S_1, S_2\rangle \,, \tag{C.3b}$$

where the spin S_1 has been swapped with its auxiliary antiparallel spin sitting on the same site, see Eq. (2.59). Swapping the second spin with its auxiliary one cancels the minus sign

again so that the action of H_r on the initial state is given as

$$H_\mathrm{r} \left|S_1, S_2\right\rangle = \vec{S}_{1,\mathrm{a}} \cdot \vec{S}_{2,\mathrm{a}} \left|S_1, S_2\right\rangle . \tag{C.3c}$$

The latter expression implies

$$H_\mathrm{r} \left|S_1, S_2\right\rangle = H_\mathrm{a} \left|S_1, S_2\right\rangle , \tag{C.4}$$

where the Hamiltonian $H_\mathrm{a} = \vec{S}_{1,\mathrm{a}} \cdot \vec{S}_{2,\mathrm{a}}$ acts on the auxiliary sites only. Hence, the action of both Hamiltonians on the initial state $\left|S_1, S_2\right\rangle$ is the same.

Consequently, the action of the Hamiltonian

$$H = H_\mathrm{r} - H_\mathrm{a} \tag{C.5}$$

on a purified initial state $\left|0\right\rangle$ is always zero because all contributions compensate each other. For the application of the time-evolution operator $U = \mathrm{e}^{-\mathrm{i}Ht}$, this implies

$$\mathrm{e}^{-\mathrm{i}(H_\mathrm{r} - H_\mathrm{a})} \left|0\right\rangle = \left|0\right\rangle , \tag{C.6}$$

which is valid as long as all real sites are prepared as singlets (or $m = 0$ triplets for $S = 1/2$) with their corresponding auxiliary sites. The property (C.6) is destroyed if any operator is applied to the real sites so that $\left|0\right\rangle$ is changed to a state different from a product of singlets.

Note, however, that the advantage of using $H = H_\mathrm{r} - H_\mathrm{a}$ depends on the topology. In a chain with nearest-neighbor interactions, the benefit is largest because a local perturbation at site j will be felt at site $j + n$ only at the n-th application of H. In the star topology of the central spin model the situation is different. Applying an operator to the central spin and subsequently H destroys the singlet character already at every bath site.

Appendix D

Second Order Average Hamiltonian Theory

In Chapter 3, the first order of the average Hamiltonian theory for the semiclassical model $H_{\mathrm{sc}} = \vec{\eta}(t) \cdot \vec{S}_0$ has been derived. It is based on the leading order of the Magnus expansion of the time-evolution operator. In the following, we include the subsequent order of the Magnus expansion and derive the second order corrections of our average Hamiltonian theory, see also Ref. [SRU13].

To this end, we recall the expression for the autocorrelation function $\langle S_0^z(t) S_0^z(0) \rangle$ prior to averaging as given in Eq. (3.11). It is rewritten in the form

$$\langle S_0^z(t) S_0^z(0) \rangle = \frac{1}{12} + \frac{1}{6} X(1) \tag{D.1}$$

with

$$X(a) = 4\pi \int_0^\infty \mathrm{d}v \, v^2 \cos(va) \, P(v) \,. \tag{D.2}$$

Here, $P(v)$ is a spherical probability distribution obeying the spin rotational symmetry of the model. Hence, it depends on the modulus $v = |\vec{v}|$ only. The previous expression for X is generalized by replacing $P(v)$ with the probability distribution of a single component of $\vec{v}$, for example the z-component

$$\begin{aligned} p(v_z) &= \iiint \mathrm{d}^3 v \, P(v) \, \delta(v_z - v\cos\theta) \\ &= 2\pi \int_{|v_z|}^\infty \mathrm{d}v \, v P(v) \,. \end{aligned} \tag{D.3}$$

This equation is differentiated with respect to v_z and inserted into Eq. (D.2). Hence, one

obtains

$$X(a) = -2\int_0^\infty \mathrm{d}v\, v \cos(va)\, p'(v)\,. \tag{D.4}$$

By partially integrating this expression with respect to a, it is reduced to

$$X(a) = \tilde{p}(a) + a\tilde{p}'(a) \tag{D.5}$$

where the Fourier transform $\tilde{p}(a) = \int_{-\infty}^{\infty} \mathrm{d}v\, p(v)\, \mathrm{e}^{\mathrm{i}va}$ of $p(v)$ has been introduced. The expression in Eq. (D.5) is a general representation of the non-constant part of the autocorrelation function of the central spin (D.1). Just the Fourier transform $\tilde{p}(a)$ remains to be calculated, which is nothing else but the mean value of the exponential factor $\mathrm{e}^{\mathrm{i}av}$.

In the following, we present how this expression is calculated and evaluated. The Magnus expansion [Mag54, BCOR09] up to second order reads

$$U(t) = \exp\left\{-\mathrm{i}\int_0^t \mathrm{d}t'\, H(t') + \frac{1}{2}\int_0^t \mathrm{d}t_1 \int_0^{t_1} \mathrm{d}t_2\, \left[H(t_1), H(t_2)\right]\right\}. \tag{D.6}$$

For a single spin-1/2, the Magnus expansion is always linear in the spin operators. Thus, it can be written in the form

$$U(t) = \mathrm{e}^{-\mathrm{i}\frac{\vec{v}\cdot\vec{\sigma}}{2}} \tag{D.7}$$

with

$$v_x = \int_0^t \mathrm{d}t'\, \eta_x(t') + \frac{1}{2}\int_0^t \mathrm{d}t_1 \int_0^t \mathrm{d}t_2\, \eta_y(t_1)\, \eta_z(t_2)\, \mathrm{sgn}(t_1 - t_2) \tag{D.8}$$

and cyclic in the components x, y and z. This expression is the desired argument of the exponential in $\tilde{p}(a)$, just the average

$$\tilde{p}(a) = \overline{\mathrm{e}^{\mathrm{i}av_x}} \tag{D.9}$$

with respect to all three components η_x, η_y, and η_z has yet to be calculated. By applying the general identity

$$\overline{\exp\left[\int_{t_1}^{t_2} \mathrm{d}\tau\, a(\tau)\, \eta(\tau)\right]} = \exp\left[\frac{1}{2}\int_{t_1}^{t_2} \mathrm{d}t \int_{t_1}^{t_2} \mathrm{d}\tau\, a(t)\, g(t-\tau)\, a(\tau)\right]. \tag{D.10}$$

valid for Gaussian fluctuations, the mean value can be evaluated analytically. In the contribution resulting from the first order of the Magnus expansion, only the mean value for η_x has to be calculated. Therefore, one obtains

$$\overline{\exp\left[\mathrm{i}a\int_0^t \mathrm{d}t'\,\eta_x\left(t'\right)\right]}^{x} = \exp\left[-a^2 G\left(t\right)\right] \tag{D.11}$$

where

$$G\left(t\right) = \int_0^t \mathrm{d}t_1 \int_0^{t_1} \mathrm{d}t_2\, g\left(t_1 - t_2\right) \tag{D.12}$$

is an even function as is $g(t)$. For the contribution from the second order of the Magnus expansion, the average with respect to η_y is carried out analytically

$$\begin{aligned}\overline{\exp\left[\frac{\mathrm{i}a}{2}\int_0^t \mathrm{d}t_1 \int_0^t \mathrm{d}t_2\,\eta_y\left(t_1\right)\eta_z\left(t_2\right)\operatorname{sgn}\left(t_1 - t_2\right)\right]}^{y} \\ = \exp\left[-\frac{a^2}{8}\int_0^t \mathrm{d}t_1 \int_0^t \mathrm{d}t_1'\,\alpha(t_1) g(t_1 - t_1')\alpha(t_1')\right]\end{aligned} \tag{D.13}$$

where

$$\alpha\left(t_1\right) := \int_0^t \mathrm{d}t_2 \operatorname{sgn}\left(t_1 - t_2\right)\eta_z\left(t_2\right) \tag{D.14}$$

still depends on η_z. After rearranging the integrals in the latter expression, the intermediate result for $\tilde{p}(a)$ from Eq. (D.9) can be written as

$$\tilde{p}\left(a\right) = \mathrm{e}^{-a^2 G(t)} \cdot \overline{\mathrm{e}^{-\frac{a^2}{8}\int_0^t \mathrm{d}t_2 \int_0^t \mathrm{d}t_2'\,\eta_z(t_2')A(t_2', t_2)\eta_z(t_2)}}^{z}. \tag{D.15a}$$

The two integrations with respect to t_1 and t_1' in $A(t_2', t_2)$ are carried out analytically and one obtains

$$\begin{aligned}A(t_2', t_2) &:= \int_0^t \mathrm{d}t_1 \int_0^t \mathrm{d}t_1' \operatorname{sgn}(t_1' - t_2')g(t_1' - t_1)\operatorname{sgn}(t_1 - t_2) \\ &= 2\left[G(t_2 - t) + G(t_2' - t) - 2G(t_2 - t_2') + G(t_2) + G(t_2') - G(t)\right].\end{aligned} \tag{D.15b}$$

The average with respect to η_z still remains and cannot be calculated in a closed form analytically, even though it is a Gaussian average. Thus, we introduce a simple numerical approach based on the discretization of time t in D intervals of width $\Delta t = t/D$. Then, the average of $\vec{\eta}_z = (\eta_z(t_1) \dots \eta_z(t_N))^\top$ is carried out with respect to an D-dimensional Gaussian probability distribution and the integrals in the exponential are replaced by sums. Consequently, the Fourier transform (D.15a) reads

$$\tilde{p}\,(a) = \frac{\mathrm{e}^{-a^2 G(t)}}{\sqrt{\det \mathbf{M}}} \int\limits_{-\infty}^{\infty} \frac{\mathrm{d}^D \eta_z}{(2\pi)^{D/2}}\, \mathrm{e}^{-\frac{1}{2}\vec{\eta}_z^{\top} \mathbf{M}^{-1} \vec{\eta}_z}\, \mathrm{e}^{-\frac{1}{2}\vec{\eta}_z^{\top} \mathbf{P} \vec{\eta}_z}\ . \tag{D.16}$$

The matrix $\mathbf{M} = (M_{ij})$ is the covariance matrix defined by

$$M_{ij} := g(t_i - t_j), \tag{D.17a}$$

while

$$P_{ij} := \frac{a^2}{4} A(t_i, t_j) \Delta t^2 \tag{D.17b}$$

contains the correction of the second order. The discretized time steps of width $\Delta t = t/D$ are given as

$$t_i = \left(i - \frac{1}{2}\right) \frac{t}{D}, \quad i \in \{1, \dots, D\}. \tag{D.17c}$$

Note that the structure of the correction in Eq. (D.16) is also bilinear in η_z. Hence, the D-dimensional integration is carried out easily and the final result for the Fourier transform is given by

$$\tilde{p}\,(a) = \frac{1}{\sqrt{\det\left(\mathbb{1} + \mathbf{PM}\right)}}\, \mathrm{e}^{-a^2 G(t)}\,. \tag{D.18}$$

In total, the second order of the AHT leads to a renormalization of the probability distribution by a factor $1/\sqrt{\det\left(\mathbb{1} + \mathbf{PM}\right)}$. With the Fourier transform and Eqs. (D.1) and (D.5), we have obtained the final expression for the autocorrelation function $\langle S_0^z(t) S_0^z(0) \rangle$ in second order AHT.

Concerning the numerical evaluation, only a rough discretization of t is sufficient. In practice, it turned out that $D = 20$-30 is an adequate number for evaluating Eq. (D.1) up to $t = 10$. As an example, the effect of the second order AHT is illustrated for the exemplary correlation function $g(t) = 1/4\ \mathrm{e}^{-|t|/(8\tau)}$ in Fig. D.1. The renormalization of the probability distribution induces a faster stabilization of the plateau in the autocorrelation function of the central spin. We stress that the plateau does not exist in the numerical simulation.

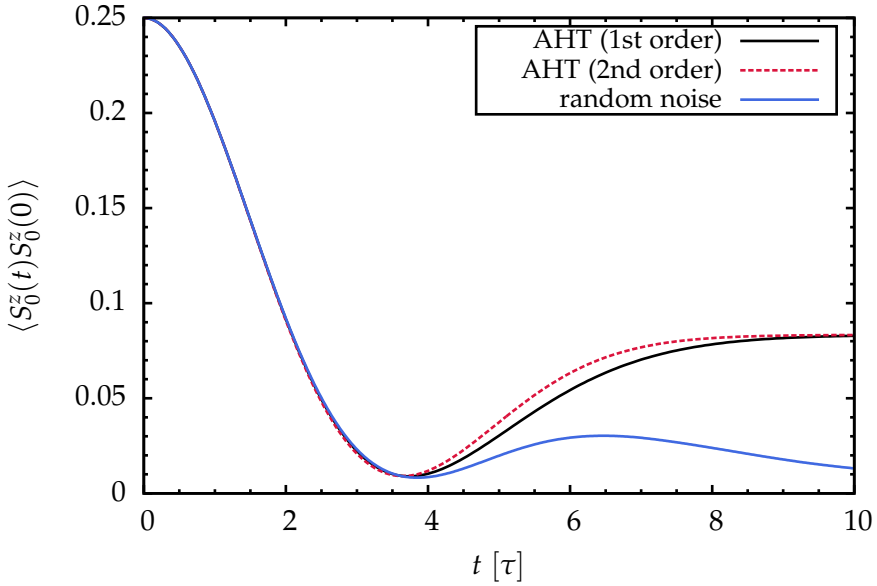

Fig. D.1: AHT in first and second order for the exemplary autocorrelation function $g(t) = 1/4\ \mathrm{e}^{-|t|/(8\tau)}$ of the bath. The random noise result was averaged over $M = 100,000$ random fluctuations.

There, the autocorrelation function of the central spin decays completely for $t \gg 0$. This must be attributed to effects beyond the Magnus expansion because the plateau is not altered by the contribution resulting from the second order of the Magnus expansion.

Appendix E

Sampling of Random Gaussian Fluctuations

The ability to sample random Gaussian noise $\eta(t)$ obeying a pre-defined autocorrelation function

$$\begin{aligned} g\left(t_1 - t_2\right) &= \overline{\eta\left(t_1\right)\eta\left(t_2\right)} \\ &= \overline{\eta\left(t_1 - t_2\right))\eta\left(0\right)} \end{aligned} \tag{E.1a}$$

is required for the numerical investigation of the semiclassical models in Chapters 3 and 5. We assume that the mean value

$$\overline{\eta\left(t\right)} = 0 \tag{E.1b}$$

vanishes since it would only induce a constant offset.

In this appendix, we explain how the noise can be generated for arbitrary autocorrelation functions $g(t)$. The only requirement is the capability of sampling white Gaussian noise $h(t)$ with properties

$$\overline{h\left(t_1\right)h\left(t_2\right)} = h_0\delta\left(t_1 - t_2\right) \tag{E.2a}$$

$$\overline{h\left(t\right)} = 0. \tag{E.2b}$$

The underlying white noise $h(t)$ has to be Gaussian because we want that the sampled fluctuations $\eta(t)$ are Gaussian as well. They are both linked via linear transformations so that the Gaussian character of the noise is conserved. As we are dealing with a very large number of fluctuations, the employed random number generator must have a very large period. A well-established and reliable generator is the Mersenne Twister generator which passes many statistical tests [MN98]. Its implementation is part of several numerical libraries such as the GNU Scientific Library (GSL) [GDT+09]. The library also includes the Box-Muller transformation which generates random numbers obeying a Gaussian distribution from the output of the random number generator.

E.1 Exponentially decaying autocorrelation functions

For the beginning, we restrict ourselves to Gaussian noise $\eta(t)$ with exponentially decaying autocorrelation function

$$g\left(t\right) = g_0^2\, \mathrm{e}^{-\gamma|t|} \tag{E.3a}$$

$$\overline{\eta\left(t\right)} = 0. \tag{E.3b}$$

The exponential shape of the autocorrelation function resembles the one of processes summarized under the name Ornstein-Uhlenbeck process [UO30].

The noise $\eta(t)$ can be viewed as fulfilling the inhomogeneous linear differential equation

$$\dot{\eta} = -\gamma\eta + h\left(t\right), \tag{E.4}$$

where $h(t)$ represents the white noise. The general solution to Eq. (E.4) is given by

$$\eta\left(t\right) = \left[\int_0^t \mathrm{d}t'\, h(t')\, \mathrm{e}^{\gamma t'} + \eta_0\right] \mathrm{e}^{-\gamma t}, \tag{E.5}$$

with $\eta_0 := \eta(0)$. It is derived from the solution of the homogeneous differential equation involving a variation of parameters. For determining the appropriate values of h_0 and η_0, we calculate the autocorrelation function

$$\begin{aligned}\overline{\eta\left(t_1\right)\eta\left(t_2\right)}^h = \mathrm{e}^{-\gamma(t_1+t_2)} \Bigg\{ &\overline{\eta_0^2 + \eta_0\left[\int_0^{t_1} \mathrm{d}t_1'\, h(t_1')\, \mathrm{e}^{\gamma t_1'} + \int_0^{t_2} \mathrm{d}t_2'\, h(t_2')\, \mathrm{e}^{\gamma t_2'}\right]} \\ &\overline{+ \int_0^{t_1} \mathrm{d}t_1' \int_0^{t_2} \mathrm{d}t_2'\, h(t_1')h(t_2')\, \mathrm{e}^{\gamma\left(t_1'+t_2'\right)}}^h \Bigg\},\end{aligned} \tag{E.6a}$$

where the average is carried out with respect to the white Gaussian noise $h(t)$. By exploiting its properties (E.2a), the latter expression simplifies to

$$g(t_1,t_2) = \mathrm{e}^{-\gamma(t_1+t_2)} \left[\eta_0^2 + h_0 \int_0^{t_1} \mathrm{d}t_1' \int_0^{t_2} \mathrm{d}t_2'\, \delta\left(t_1 - t_2\right) \mathrm{e}^{\gamma\left(t_1'+t_2'\right)}\right]. \tag{E.6b}$$

Without loss of generality, we may assume $0 < t_2 < t_1$ and obtain

$$g(t_1,t_2) = \eta_0^2\, \mathrm{e}^{-\gamma(t_1+t_2)} + \frac{h_0}{2\gamma}\left(\mathrm{e}^{-\gamma(t_1-t_2)} - \mathrm{e}^{-\gamma(t_1+t_2)}\right) \tag{E.6c}$$

for the preliminary result of the autocorrelation function. The latter expression does not solely depend on the relative time $t_1 - t_2$ which is unphysical. It acquires the desired form (E.3a) if the intrinsic parameter h_0 corresponding to the variance of the white Gaussian noise is chosen to be

$$h_0 = 2\gamma g_0^2 \tag{E.7}$$

with $g_0^2 \equiv \eta_0^2$. Thereby, we have shown that the Gaussian fluctuations sampled via the differential equation (E.4) indeed have an exponentially decaying autocorrelation function.

In the numerics, one deals with a discretized time axis $t \to t_i = i\Delta t$ with Δt being an appropriate small time interval. The continuous fluctuation $\eta(t)$ is then approximated by a series $\eta(t) \to \eta(t_i)$ which is sampled from a series of white Gaussian noise $h(t_i)$. Its variance Var h is given as

$$\text{Var } h = \frac{h_0}{\Delta t}, \tag{E.8}$$

because $\delta(\Delta t(i-j)) = \delta(i-j)/\Delta t$. After inserting the differential quotient, one obtains the discretized form of the differential equation (E.4)

$$\eta(t_{i+1}) = \Delta t \left(-\gamma\eta(t_i) + h(t_i)\right) + \eta(t_i). \tag{E.9}$$

The initial value η_0 of the fluctuations is chosen randomly from white Gaussian noise with vanishing mean value $\overline{\eta_0} = 0$ and variance Var $\eta_0 = g_0^2$.

As an example, the autocorrelation function $g(t)$ and the mean value $\overline{\eta(t)}$ is plotted in Fig. E.1 for $\gamma = g_0$. For the numerical evaluation, the energy scale is again set to $g_0 = 1$. Already for a moderate number M of sampled fluctuations, the autocorrelation function $g(t)$ is in very nice agreement with the exact one. The mean value fluctuates within in the error bars which are $\sim 1/\sqrt{M}$.

E.2 Arbitrary autocorrelation functions

In the following, we present a simple approach for sampling fluctuations obeying an arbitrary autocorrelation function $g(t)$. The autocorrelation function may be represented by an analytical function or by numerical data, for example from a DMRG calculation.

We assume a t-axis which is discretized into D intervals. The fluctuations $\{\eta(t_i)\}$ have

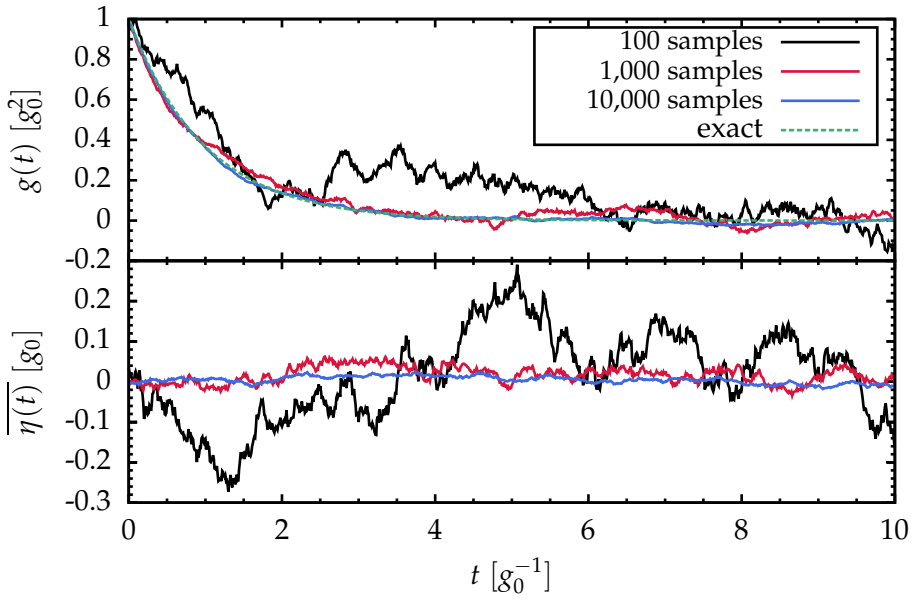

Fig. E.1: Autocorrelation function $g(t)$ and mean value $\overline{\eta(t)}$ for different numbers of sampled fluctuations with exponentially decaying autocorrelation function. The dashed line in the upper panel is the exact autocorrelation function $g(t) = g_0^2\,\mathrm{e}^{-t}$ obtained for $\gamma = g_0$.

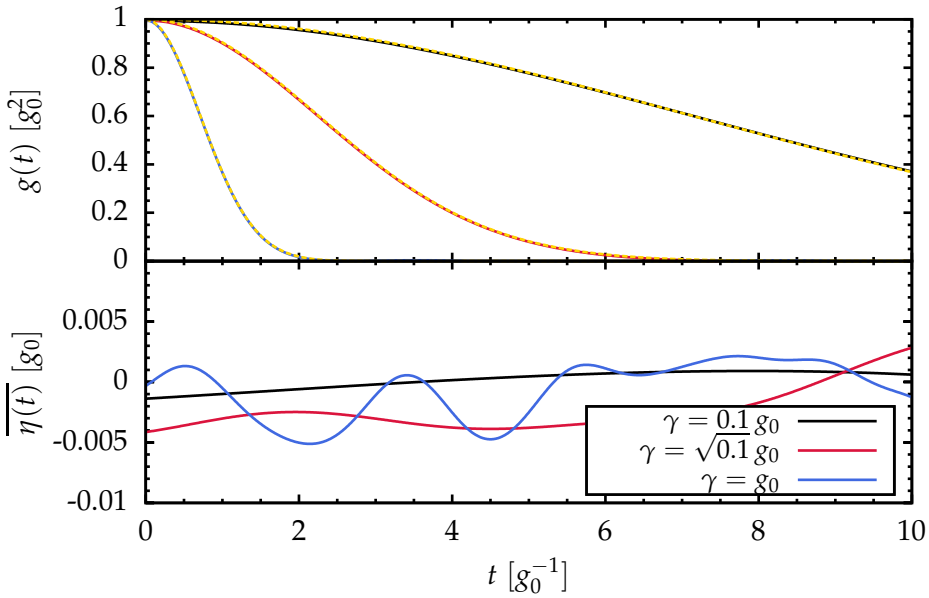

Fig. E.2: Gaussian autocorrelation function $g(t) = g_0^2\,\mathrm{e}^{-\gamma^2 t^2}$ and mean value $\overline{\eta(t)}$ for different values of γ. All curves are averaged over $M = 100,000$ fluctuations sampled via the covariance matrix $\mathbf{M}$. The dashed yellow lines in the upper panel represent the exact autocorrelation functions. Note that the energy scale is set to $g_0 = 1$.

to fulfill a Gaussian distribution at every discrete time step t_i. This can be interpreted as D-dimensional Gaussian distribution

$$p\left(\vec{\eta}\right) = \frac{1}{\left(2\pi\right)^{D/2}\sqrt{\det \mathbf{M}}}\, \mathrm{e}^{-\frac{1}{2}\vec{\eta}^{\top}\mathbf{M}^{-1}\vec{\eta}} \tag{E.10}$$

where the D-dimensional vector $\vec{\eta} = \left(\eta(t_1) \ \ldots \ \eta(t_D)\right)^{\top}$ contains the discretized fluctuations, see Appendix D for comparison. In multiple dimensions, the covariance matrix $\mathbf{M}$ replaces the variance. Hence, it holds the values of the autocorrelation function as entries

$$M_{ij} := g(t_i - t_j). \tag{E.11}$$

It follows directly from the properties of the autocorrelation function that $\mathbf{M}$ is a symmetric matrix. Thus, it is diagonalizable

$$\mathbf{D} = \mathbf{O}^{\top}\mathbf{M}\mathbf{O} \tag{E.12}$$

via an orthogonal transformation $\mathbf{O}$ containing the eigenvectors $\vec{\lambda}_i$ of $\mathbf{M}$ as columns. The relation

$$\vec{\eta}' = \mathbf{O}^{\top}\vec{\eta} \tag{E.13}$$

transforms the vector $\vec{\eta}$ to the vector $\vec{\eta}'$ in the diagonal basis. Due to this linear transformation, the vector $\vec{\eta}'$ fulfills a Gaussian probability distribution characterized by the diagonal covariance matrix $\mathbf{D}$. It contains the eigenvalues $\lambda_i \geq 0$ of $\mathbf{M}$ on its main diagonal. By definition, all eigenvalues λ_i have to be positive because they correspond to the variance of the fluctuations in the diagonal basis. Consequently, the non-diagonal matrix $\mathbf{M}$ is positive semi-definite. But in practice this property may be violated due to rounding errors, see below.

Thereby, we have all ingredients for sampling the fluctuations $\vec{\eta}$. The procedure reads as follows:

1) Construct the covariance matrix $\mathbf{M}$ according to Eq. (E.11).

2) Diagonalize $\mathbf{M}$ to obtain all eigenvalues λ_i and -vectors $\vec{\lambda}_i$ forming the columns of the transformation $\mathbf{O}$.

3) Sample the fluctuations $\vec{\eta}' = \left(\eta'(t_1) \ \ldots \ \eta'(t_D)\right)^{\top}$ in the diagonal basis according to a Gaussian probability distribution with variance

$$\mathrm{Var}\, \eta'(t_i) = \lambda_i \tag{E.14}$$

and vanishing mean value.

4) Transform the fluctuations back to the non-diagonal basis via

$$\vec{\eta} = \mathbf{O}\vec{\eta}'. \tag{E.15}$$

The fluctuations sampled via this algorithm satisfy the autocorrelation function $g(t)$ which entered in the construction of the covariance matrix $\mathbf{M}$. This principle can easily be extended to autocorrelation functions spanning all spatial dimensions x, y, and z. Then, the covariance matrix is a 3×3 block matrix

$$\mathbf{M} = \begin{pmatrix} \mathbf{M}^{xx} & \mathbf{M}^{xy} & \mathbf{M}^{xz} \\ \mathbf{M}^{yx} & \mathbf{M}^{yy} & \mathbf{M}^{yz} \\ \mathbf{M}^{zx} & \mathbf{M}^{zy} & \mathbf{M}^{zz} \end{pmatrix} \tag{E.16a}$$

formed by the individual $D \times D$ covariance matrices $\mathbf{M}^{\alpha\beta} = (M_{ij}^{\alpha\beta})$ with entries

$$M_{ij}^{\alpha\beta} = g_{\alpha\beta}(t_i - t_j), \quad \alpha, \beta \in \{x, y, z\}. \tag{E.16b}$$

If an external field is applied in one direction, the covariance matrix has block diagonal form because there is no correlation between the spin directions parallel and perpendicular to the external field.

Problems may arise in step 3) of the algorithm where the square root of the eigenvalues λ_i has to be calculated. By definition, a covariance matrix is positive semi-definite. But in practice negative eigenvalues may occur due to the discretization and numerical inaccuracies. This is a widely known problem in fields where covariance matrices are constructed from empirical data, for example in finance. Mathematical algorithms have been developed to find the nearest positive semi-definite covariance matrix to a given matrix [Hig02].

In our applications, only very small negative eigenvalues occur stemming from rounding errors and a numerical correction of the covariance matrix is not necessary. For the sampled fluctuations with Gaussian autocorrelation function shown in Fig. E.2, the largest negative eigenvalues still lie below -10^{-12}. They may simply be set to zero without any negative effect on the results. From our practical experience, this procedure can be carried out even for larger negative eigenvalues as long as $|\lambda_i| \lesssim 10^{-6}$-$10^{-5}$.

Appendix F

Piecewise Constant Pulses

In this appendix, the details of the π-pulses studied in Chapter 5 are summarized. All pulses consist of piecewise constant amplitudes and rotate the spin either around the x- or around the y-axis. Hence, they only prevent the dephasing of the electron spin. The investigated pulses comprise the well-known symmetric SCORPSE and the asymmetric CORPSE pulse [CJ00, CLJ03] which are both first order pulses. Furthermore, a second order pulse derived for a classical bath [Sti12, SFPU12] is studied. In addition, we discuss the second order symmetric SYM2ND and the asymmetric ASYM2ND pulses from Ref. [PKRU09] where the bath was treated on the quantum level.

The time dependence of the pulse amplitudes $v(t)$ is plotted in Fig. F.1, while the corresponding switching instances τ_i and amplitudes v_{τ_i} are listed in Tab. F.1.

The parameters of the second order pulses in Tab. F.1 are given in the same high precision as used in our numerical simulation. Thereby, a substantial increase of the accuracy is gained compared to the low-precision parameters published in Refs. [PKRU09, SFPU12]. The author is indebted to S. Pasini for providing the high-precision parameters of the SYM2ND and ASYM2ND pulse [Pas13] and to C. Stihl for providing the high-precision parameters of the second order pulse optimized for a classical bath [Sti13].

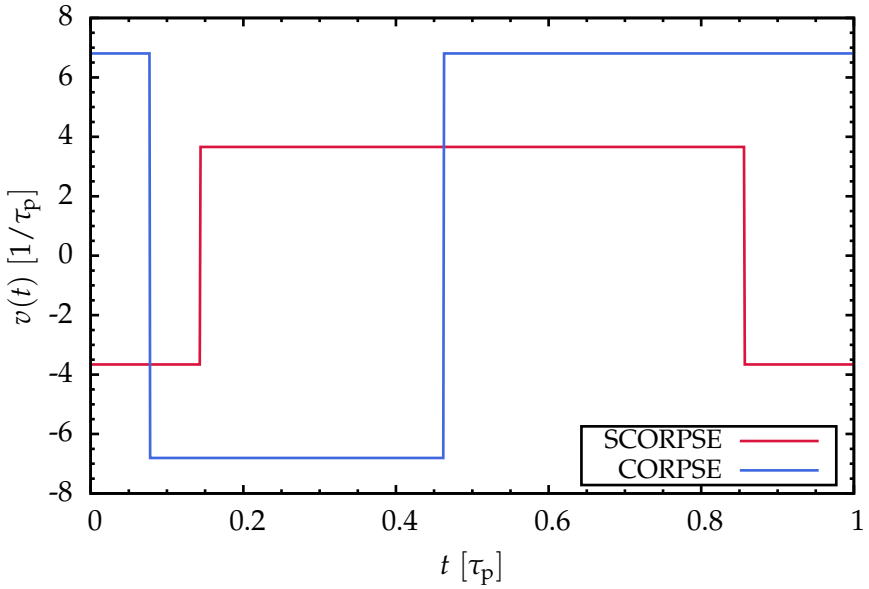

(a) First order π-pulses.

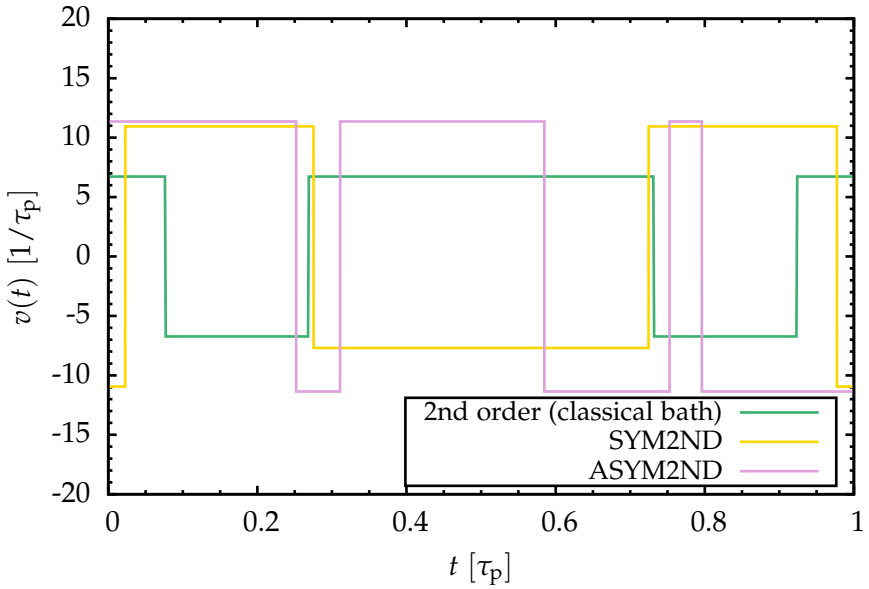

(b) Second order π-pulses.

Fig. F.1: Pulse amplitudes $v(t)$ as a function of time t. The first order π-pulses are the symmetric SCORPSE and asymmetric CORPSE pulse [CJ00, CLJ03]. In second order, a π-pulse derived for a classical bath [Sti12, SFPU12] and the quantum mechanical symmetric SYM2ND and asymmetric ASYM2ND π-pulses [PKRU09] are presented.

Amplitude(s) v_{τ_i} $[1/\tau_\mathrm{p}]$	Switching instances τ_i $[\tau_\mathrm{p}]$
SCORPSE	
$\pm\frac{7\pi}{6}$	$\frac{1}{7}$
	$\frac{6}{7}$
CORPSE	
$\pm\frac{13\pi}{6}$	$\frac{1}{13}$
	$\frac{6}{13}$
Second order (classical bath)	
$\pm$6.72572865242397	0.07623077665509
	0.26784318744464
	0.73215681255536
	0.92376922334491
SYM2ND	
$\pm$10.95012043866828575	0.0228054551625108
$-$7.69537638364247465	0.2752692173069500
	0.7247307826930500
	0.9771945448374892
ASYM2ND	
$\pm$11.36443379447147705	0.2520112376736856
	0.3108959015038718
	0.5847810746672190
	0.7528254671237393
	0.7960392449336322

Tab. F.1: Amplitudes v_{τ_i} and switching instances τ_i of the first and second order π-pulses as plotted in Fig. F.1.

Appendix G

No-Go Theorem for Pulses under Cusp-Like Autocorrelation Functions

If the correlation function of the random noise exhibits a cusp at $t = 0$, unexpected half-integer contributions $\Delta_F \sim 1/v^{3/2}$ arise in the Frobenius norm Δ_F. This has to be accounted to an additional condition emerging for shaped pulses under an Ornstein-Uhlenbeck type noise of the bath. The supplemental integral is not fulfilled by standard and new pulses respecting the extended set of conditions have to be derived. However, it can be shown that both the two standard first order conditions from Eqs. (5.26) as well the supplemental condition from Eq. (5.28) cannot be fulfilled simultaneously. In the following, we depict an analytic argument by G. Uhrig which proofs this situation [Uhr13].

We recall the supplemental condition from Eq. (5.28). After the application of an additional theorem, it can be rewritten in the form

$$I_{3/2} = I^a_{3/2} + I^b_{3/2} \tag{G.1}$$

with

$$I^a_{3/2} = \int_0^{\tau_P} \mathrm{d}t_1 \int_0^{\tau_P} \mathrm{d}t_2 \, \cos\psi_1 \, |t_1 - t_2| \cos\psi_2 \tag{G.2a}$$

$$I^b_{3/2} = \int_0^{\tau_P} \mathrm{d}t_1 \int_0^{\tau_P} \mathrm{d}t_2 \, \sin\psi_1 \, |t_1 - t_2| \sin\psi_2. \tag{G.2b}$$

For simplicity, we abbreviate $\psi_i := \psi(t_i)$. In the Hilbert space $\mathscr{H}$ of integrable functions, both integrals may be interpreted as an expectation value

$$I^a_{3/2} = \langle \cos\psi | A | \cos\psi \rangle \tag{G.3a}$$

$$I^b_{3/2} = \langle \sin\psi | A | \sin\psi \rangle \tag{G.3b}$$

of the linear operator

$$A\left(t_1, t_2\right) = \left|t_1 - t_2\right|. \tag{G.4}$$

It maps the function $\varphi(t) \in \mathscr{H}$ onto the function $\psi(t)$ by

$$A: \quad \varphi\left(t\right) \longmapsto \psi\left(t\right) = \int_0^{\tau_\mathrm{p}} \mathrm{d}t'\, A(t,t')\varphi(t'). \tag{G.5}$$

The expectation value of the operator A should have a well-defined sign. Hence, we attempt to find a relation $A \sim BB^\dagger$ where the operator B is proportional to the square root of A. An adequate ansatz for B is given by

$$B: \quad \varphi\left(t\right) \longmapsto \psi\left(t\right) = \int_0^{\tau_\mathrm{p}} \mathrm{d}t'\, \mathrm{sgn}(t-t')\varphi(t'). \tag{G.6}$$

Consequently, the mapping for B^2 reads

$$B^2: \quad \varphi\left(t\right) \longmapsto \chi\left(t\right) = \int_0^{\tau_\mathrm{p}} \mathrm{d}t_1 \int_0^{\tau_\mathrm{p}} \mathrm{d}t_2\, \mathrm{sgn}(t-t_1)\,\mathrm{sgn}(t_1-t_2)\varphi(t_2). \tag{G.7}$$

The integration with respect to t_1 can be carried out analytically. Then, the latter expressions acquires the form

$$B^2: \quad \varphi\left(t\right) \longmapsto \chi\left(t\right) = \int_0^{\tau_\mathrm{p}} \mathrm{d}t_2\, \left(2\left|t-t_2\right| - 1\right) \varphi(t_2). \tag{G.8}$$

Thereby, we have found the desired relation between the operators A and B. It is given by

$$A = \frac{1}{2}\left(C - B^\dagger B\right) \tag{G.9}$$

where we have exploited the antisymmetry $B = -B^\dagger$ of the operator B. Furthermore, the operator

$$C: \quad \varphi\left(t\right) \longmapsto \psi\left(t\right) = \int_0^{\tau_\mathrm{p}} \mathrm{d}t'\, \varphi(t') \tag{G.10}$$

has been introduced. Compared to the operators A and B, the mapping of C simply corresponds to the identity.

Now, we restrict ourselves to integrable functions $f(t)$ from a subspace $\mathscr{H}_\mathrm{s} \subseteq \mathscr{H}$ of the Hilbert space of integrable functions. We assume that every $f(t) \in \mathscr{H}_\mathrm{s}$ accomplishes

$$0 \equiv \int_0^{\tau_\mathrm{p}} \mathrm{d}t\, f\,(t)\,. \tag{G.11}$$

Hence, $f(t)$ represents all pulses which fulfill the standard conditions of a first order pulse (5.26). The latter expression implies $\langle f|C|f\rangle \equiv 0$. Together with the relation from Eq. (G.9), we obtain the expression

$$\langle f|A|f\rangle = -\frac{1}{2}\,\langle Bf|Bf\rangle \leq 0 \tag{G.12}$$

for the expectation value of the operator A. It is valid for all $f(t) \in \mathscr{H}_\mathrm{s}$ and explains why the supplemental integral $I_{3/2}$ from Eq. (5.27) never changes its sign.

However, we still have to verify whether $f(t)$ can make Eq. (G.12) in addition to Eq. (G.11) vanish. This implies

$$\begin{aligned} & 0 \equiv B\,|f\rangle \\ \Leftrightarrow\; & 0 \equiv \psi\,(t) = \int_0^{\tau_\mathrm{p}} \mathrm{d}t'\ \mathrm{sgn}(t-t')f(t') \end{aligned} \tag{G.13}$$

for all values of t. The latter expression is differentiated with respect to t, which yields

$$\begin{aligned} \partial_t\,\psi\,(t) &= 2\int_0^{\tau_\mathrm{p}} \mathrm{d}t'\,\delta(t-t')f(t') \\ &= 2f(t) \neq 0. \end{aligned} \tag{G.14}$$

This expression stands in contradiction to Eq. (G.13) because the derivative $\partial_t\,\psi(t)$ should be equivalent to zero when $\psi(t) \equiv 0$. Hence, the strict inequality in Eq. (G.12) always holds for all $f(t) \in \mathscr{H}_\mathrm{s}$. Thereby, we have proven rigorously that a shaped pulse cannot accomplish the standard conditions from Eqs. (5.26) and the supplemental condition from Eq. (5.28) simultaneously. As a consequence, pulses designed for an Ornstein-Uhlenbeck type noise should be optimized in a way that the standard integrals (5.26) vanish under the constraint that the supplemental integral (5.28) is minimized. Then, the influence of the half-integer contribution $\Delta_\mathrm{F} \sim 1/v^{3/2}$ is diminished.

Appendix H

DMRG versus a Non-Perturbative Master Equation Solution

In the following, we compare the maximum time accessible within our numerical ansatz based on the DMRG with the limitations of the non-perturbative master equation solution for the central spin model by Barnes *et al.* [BCDS12]. To this end, we calculate the limiting parameters of the latter approach, namely the largest coupling constant and the value of the finite external magnetic field, for our uniform distribution of couplings defined in Eq. (1.8) and the parameters given in Ref. [BCDS12].

In contrast to the DMRG, the solution of the master equation always requires a finite external magnetic field. Moreover, its validity is limited to the time scale set by the largest coupling constant

$$t_{\max} = \frac{1}{J_{\max}}. \tag{H.1}$$

The results in Ref. [BCDS12] are characterized by the quantity

$$\Lambda := \frac{J_{\text{tot}}}{h_0}, \tag{H.2}$$

where

$$J_{\text{tot}} = \sum_{i=1}^{N} J_i \tag{H.3a}$$

is the total interaction energy and

$$h_0 = g\mu_{\text{B}} B \tag{H.3b}$$

is the Zeeman energy. Here, $g = 2$ is the g-factor of the electron spin and $\mu_B = 57.88\,\mu\text{eV/T}$ is the Bohr magneton. For the specified external magnetic field of strength $B = 100\,\text{mT}$ and $\Lambda = 30$ [BCDS12], the quantities in Eqs. (H.3) acquire the values $J_{\text{tot}} = 347.28\,\mu\text{eV}$ and $h_0 = 11.58\,\mu\text{eV}$, respectively.

With $J_{\text{max}} \equiv J_1$ and our distribution for the J_i defined in Eq. (1.8), the maximum time t_{max} in units of J_{q}^{-1} can directly be deduced from Eq. (H.1) in dependence of the bath size N.

Furthermore, the absolute value of J_{q} in μeV has to be calculated. For this, we evaluate the quantity

$$\frac{J_{\text{tot}}}{J_{\text{q}}} = \sqrt{\frac{6N}{2N^2+3N+1}}\frac{N+1}{2}. \tag{H.4}$$

for a fixed N. Subsequently, one obtains the corresponding value of J_{q} in μeV by dividing the absolute value $J_{\text{tot}} = 347.28\,\mu\text{eV}$ through the result of Eq. (H.4). Finally, we are able to express the parameter h_0 in units of J_{q} to determine the regime of the magnetic field in which the non-perturbative master equation solution is valid.

All extracted parameters are summarized in Tab. H.1 for exemplary numbers of N. The limiting time t_{max} of the non-perturbative master equation solution has to be compared with the maximum time $t_{\text{max}}^{\text{DMRG}}$ of the DMRG calculation for the corresponding values of N and h_0. Note, however, that there is no well-defined $t_{\text{max}}^{\text{DMRG}}$. Hence, the values in Tab. H.1 are based on our experience.

For all values of N, our ansatz based on the DMRG outperforms the non-perturbative master equation solution. We stress that the parameter h_0/J_{q} increases with N because $J_{\text{tot}} \sim \sqrt{N}$. This observation is crucial because the solution of the master equation was obtained in the large-bath limit [BCDS12]. For large baths, the quantity h_0/J_{q} has to take a substantial value to compensate the decreasing energy scale J_{q}. Consequently, one arrives quickly in the strong-field regime where the DMRG works extremely well and the dynamics is essentially classical. In addition, we highlight once more that the investigation of the zero-field limited on the basis of the non-perturbative master equation solution is excluded rigorously.

N	J_{tot} $[J_{\mathrm{q}}]$	J_{q} $[\mu\mathrm{eV}]$	h_0 $[J_{\mathrm{q}}]$	J_{max} $[J_{\mathrm{q}}]$	t_{max} $[J_{\mathrm{q}}^{-1}]$	$t_{\mathrm{max}}^{\mathrm{DMRG}}$ $[J_{\mathrm{q}}^{-1}]$
10	2.80	123.89	0.09	0.51	1.96	50-100
100	8.68	40.00	0.29	0.17	5.82	40-50
1,000	27.39	12.68	0.91	0.05	18.27	25-30
10,000	86.60	4.01	2.89	0.02	57.74	-

Tab. H.1: Parameters limiting the validity of the non-perturbative master equation solution derived by Barnes *et al.* [BCDS12]. For different bath sizes N, the quantities were calculated for our uniform distribution of the coupling constants as defined in Eq. (1.8) and the parameters given in Ref. [BCDS12], see text for details. In addition, the estimated maximum time $t_{\mathrm{max}}^{\mathrm{DMRG}}$ of our DMRG calculations is given for the corresponding values of N and h_0.

Bibliography

[AF11] Alvermann, A. and Fehske, H. High-order commutator-free exponential time-propagation of driven quantum systems. *J. Comput. Phys.* **230** (15), 5930 (2011).

[AFL12] Alvermann, A., Fehske, H., and Littlewood, P. B. Numerical time propagation of quantum systems in radiation fields. *New J. Phys.* **14** (10), 105008 (2012).

[AHDDH06] Al-Hassanieh, K., Dobrovitski, V., Dagotto, E., and Harmon, B. N. Numerical modeling of the central spin problem using the spin-coherent-state *P* representation. *Phys. Rev. Lett.* **97** (3), 037204 (2006).

[Ban98] Ban, M. Photon-echo technique for reducing the decoherence of a quantum bit. *J. Mod. Opt.* **45** (11), 2315 (1998).

[BB11] Biercuk, M. J. and Bluhm, H. Phenomenological study of decoherence in solid-state spin qubits due to nuclear spin diffusion. *Phys. Rev. B* **83** (23), 235316 (2011).

[BBP04] Breuer, H.-P., Burgarth, D., and Petruccione, F. Non-markovian dynamics in a spin star system: Exact solution and approximation techniques. *Phys. Rev. B* **70** (4), 045323 (2004).

[BCDS12] Barnes, E., Cywiński, L., and Das Sarma, S. Nonperturbative master equation solution of central spin dephasing dynamics. *Phys. Rev. Lett.* **109** (14), 140403 (2012).

[BCOR09] Blanes, S., Casas, F., Oteo, J., and Ros, J. The magnus expansion and some of its applications. *Phys. Rep.* **470** (5-6), 151 (2009).

[BCP08] Bulla, R., Costi, T. A., and Pruschke, T. Numerical renormalization group method for quantum impurity systems. *Rev. Mod. Phys.* **80** (2), 395 (2008).

[BES+10a] Bortz, M., Eggert, S., Schneider, C., Stübner, R., and Stolze, J. Dynamics and decoherence in the central spin model using exact methods. *Phys. Rev. B* **82** (16), 161308 (2010).

[BES10b] Bortz, M., Eggert, S., and Stolze, J. Spectrum and screening cloud in the central spin model. *Phys. Rev. B* **81** (3), 035315 (2010).

[BEU00] Bühler, A., Elstner, N., and Uhrig, G. High temperature expansion for frustrated and unfrustrated $S = 1/2$ spin chains. *Eur. Phys. J. B* **16** (3), 475 (2000).

[BHH+01] Bayer, M., Hawrylak, P., Hinzer, K., Fafard, S., Korkusinski, M., Wasilewski, Z. R., Stern, O., and Forchel, A. Coupling and entangling of quantum states in quantum dot molecules. *Science* **291** (5503), 451 (2001).

[Bor07] Bortz, M. Private communication (2007).

[BP07] Breuer, H.-P. and Petruccione, F. *The Theory of Open Quantum Systems*. Oxford University Press, Oxford, paperback edition (2007).

[BPG+10] Barmettler, P., Punk, M., Gritsev, V., Demler, E., and Altman, E. Quantum quenches in the anisotropic spin-1/2 Heisenberg chain: Different approaches to many-body dynamics far from equilibrium. *New J. Phys.* **12** (5), 055017 (2010).

[BS07a] Bortz, M. and Stolze, J. Exact dynamics in the inhomogeneous central-spin model. *Phys. Rev. B* **76** (1), 014304 (2007).

[BS07b] Bortz, M. and Stolze, J. Spin and entanglement dynamics in the central-spin model with homogeneous couplings. *J. Stat. Mech.* **2007** (6), P06018 (2007).

[BS11] Bortz, M. and Stolze, J. Private communication (2011).

[BSW09] Barthel, T., Schollwöck, U., and White, S. R. Spectral functions in one-

dimensional quantum systems at finite temperature using the density matrix renormalization group. *Phys. Rev. B* **79** (24), 245101 (2009).

[CBB07] Chen, G., Bergman, D. L., and Balents, L. Semiclassical dynamics and long-time asymptotics of the central-spin problem in a quantum dot. *Phys. Rev. B* **76** (4), 045312 (2007).

[CDDS10] Cywiński, L., Dobrovitski, V. V., and Das Sarma, S. Spin echo decay at low magnetic fields in a nuclear spin bath. *Phys. Rev. B* **82** (3), 035315 (2010).

[CHHC06] Cappellaro, P., Hodges, J. S., Havel, T. F., and Cory, D. G. Principles of control for decoherence-free subsystems. *J. Chem. Phys.* **125** (4), 044514 (2006).

[CJ00] Cummins, H. K. and Jones, J. A. Use of composite rotations to correct systematic errors in NMR quantum computation. *New J. Phys.* **2** (1), 6 (2000).

[CL04] Coish, W. A. and Loss, D. Hyperfine interaction in a quantum dot: Non-Markovian electron spin dynamics. *Phys. Rev. B* **70** (19), 195340 (2004).

[CL06] Coish, W. A. and Loss, D. Quantum computing with spins in solids. *arXiv e-print* (2006). `arXiv:cond-mat/0606550`.

[CLJ03] Cummins, H. K., Llewellyn, G., and Jones, J. A. Tackling systematic errors in quantum logic gates with composite rotations. *Phys. Rev. A* **67** (4), 042308 (2003).

[CLNDS08] Cywiński, L., Lutchyn, R. M., Nave, C. P., and Das Sarma, S. How to enhance dephasing time in superconducting qubits. *Phys. Rev. B* **77** (17), 174509 (2008).

[CLYA07] Coish, W. A., Loss, D., Yuzbashyan, E. A., and Altshuler, B. L. Quantum versus classical hyperfine-induced dynamics in a quantum dot. *J. Appl. Phys.* **101** (8), 081715 (2007).

[CP54] Carr, H. Y. and Purcell, E. M. Effects of diffusion on free precession in nuclear magnetic resonance experiments. *Phys. Rev.* **94** (3), 630 (1954).

[DDR03] Dobrovitski, V. V. and De Raedt, H. A. Efficient scheme for numerical simulations of the spin-bath decoherence. *Phys. Rev. E* **67** (5), 056702 (2003).

[DH06] Deng, C. and Hu, X. Analytical solution of electron spin decoherence through hyperfine interaction in a quantum dot. *Phys. Rev. B* **73** (24), 241303 (2006).

[DH08] Deng, C. and Hu, X. Electron-spin dephasing via hyperfine interaction in a quantum dot: An equation-of-motion calculation of electron-spin correlation functions. *Phys. Rev. B* **78** (24), 245301 (2008).

[DiV00] DiVincenzo, D. P. The physical implementation of quantum computation. *Fortschr. Phys.* **48** (9-11), 771 (2000).

[DKSV04] Daley, A. J., Kollath, C., Schollwöck, U., and Vidal, G. Time-dependent density-matrix renormalization-group using adaptive effective Hilbert spaces. *J. Stat. Mech.* **2004** (4), P04005 (2004).

[dLWR+10] de Lange, G., Wang, Z. H., Ristè, D., Dobrovitski, V. V., and Hanson, R. Universal dynamical decoupling of a single solid-state spin from a spin bath. *Science* **330** (1), 60 (2010).

[DMK03] Das, R., Mahesh, T., and Kumar, A. Experimental implementation of Grover's search algorithm using efficient quantum state tomography. *Chem. Phys. Lett.* **369** (1), 8 (2003).

[DPS04] Dukelsky, J., Pittel, S., and Sierra, G. Colloquium: Exactly solvable Richardson-Gaudin models for many-body quantum systems. *Rev. Mod. Phys.* **76** (3), 643 (2004).

[DRZ+09] Du, J., Rong, X., Zhao, N., Wang, Y., Yang, J., and Liu, R. B. Preserving electron spin coherence in solids by optimal dynamical decoupling. *Nature* **461** (7268), 1265 (2009).

[dSDS03a] de Sousa, R. and Das Sarma, S. Electron spin coherence in semiconductors: Considerations for a spin-based solid-state quantum computer architecture. *Phys. Rev. B* **67** (3), 033301 (2003).

[dSDS03b] de Sousa, R. and Das Sarma, S. Theory of nuclear-induced spectral dif-

fusion: Spin decoherence of phosphorus donors in Si and GaAs quantum dots. *Phys. Rev. B* **68** (11), 115322 (2003).

[EHWvB+04] Elzerman, J. M., Hanson, R., Willems van Beveren, L. H., Witkamp, B., Vandersypen, L. M. K., and Kouwenhoven, L. P. Single-shot read-out of an individual electron spin in a quantum dot. *Nature* **430** (6998), 431 (2004).

[EN02] Erlingsson, S. I. and Nazarov, Y. V. Hyperfine-mediated transitions between a Zeeman split doublet in GaAs quantum dots: The role of the internal field. *Phys. Rev. B* **66** (15), 155327 (2002).

[EN04] Erlingsson, S. I. and Nazarov, Y. V. Evolution of localized electron spin in a nuclear spin environment. *Phys. Rev. B* **70** (20), 205327 (2004).

[Fau13] Fauseweh, B. Private communication (2013).

[FB07] Fischer, J. and Breuer, H.-P. Correlated projection operator approach to non-Markovian dynamics in spin baths. *Phys. Rev. A* **76** (5), 052119 (2007).

[FBN+08] Ferraro, E., Breuer, H.-P., Napoli, A., Jivulescu, M. A., and Messina, A. Non-Markovian dynamics of a single electron spin coupled to a nuclear spin bath. *Phys. Rev. B* **78** (6), 064309 (2008).

[Fer30] Fermi, E. Über die magnetischen Momente der Atomkerne. *Z. Phys.* **60** (5), 320 (1930).

[FPU12] Fauseweh, B., Pasini, S., and Uhrig, G. S. Frequency-modulated pulses for quantum bits coupled to time-dependent baths. *Phys. Rev. A* **85** (2), 022310 (2012).

[Fri06] Friedrich, A. *Time-Dependent Properties of One-Dimensional Spin-Systems: A DMRG-Study*. Ph.D. thesis, RWTH Aachen (2006).

[FS13a] Faribault, A. and Schuricht, D. Integrability-based analysis of the hyperfine-interaction-induced decoherence in quantum dots. *Phys. Rev. Lett.* **110** (4), 040405 (2013).

[FS13b] Faribault, A. and Schuricht, D. Spin decoherence due to a randomly fluctuating spin bath. *Phys. Rev. B* **88** (8), 085323 (2013).

[FTP+05] Facchi, P., Tasaki, S., Pascazio, S., Nakazato, H., Tokuse, A., and Lidar, D. A. Control of decoherence: Analysis and comparison of three different strategies. *Phys. Rev. A* **71** (2), 022302 (2005).

[FW05] Feiguin, A. E. and White, S. R. Time-step targeting methods for real-time dynamics using the density matrix renormalization group. *Phys. Rev. B* **72** (2), 020404 (2005).

[Gai01] Gaite, J. Angular quantization and the density matrix renormalization group. *Mod. Phys. Lett. A* **16** (17), 1109 (2001).

[Gai03] Gaite, J. Entanglement entropy and the density matrix renormalization group. *arXiv e-print* (2003). `arXiv:quant-ph/0301120`.

[Gau76] Gaudin, M. Diagonalisation d'une classe d'Hamiltoniens de spin. *J. Phys. France* **37** (10), 1087 (1976).

[Gau83] Gaudin, M. *La Fonction d'Onde de Bethe*. Masson, Paris (1983).

[GDT+09] Galassi, M., Davies, J., Theiler, J., Gough, B., Jungman, G., Alken, P., Booth, M., and Rossi, F. *GNU Scientific Library Reference Manual*. Network Theory Limited, third edition (2009). `http://www.gnu.org/software/gsl/`.

[GES+09] Greilich, A., Economou, S. E., Spatzek, S., Yakovlev, D. R., Reuter, D., Wieck, A. D., Reinecke, T. L., and Bayer, M. Ultrafast optical rotations of electron spins in quantum dots. *Nature Phys.* **5** (4), 262 (2009).

[GKL04] Golovach, V. N., Khaetskii, A. A., and Loss, D. Phonon-induced decay of the electron spin in quantum dots. *Phys. Rev. Lett.* **93** (1), 016601 (2004).

[GKSS05] Gobert, D., Kollath, C., Schollwöck, U., and Schütz, G. Real-time dynamics in spin-1/2 chains with adaptive time-dependent density matrix renormalization group. *Phys. Rev. E* **71** (3), 036102 (2005).

[GMD02] Galindo, A. and Martín-Delgado, M. A. Information and computation: Classical and quantum aspects. *Rev. Mod. Phys.* **74** (2), 347 (2002).

[Gro96] Grover, L. K. A fast quantum mechanical algorithm for database search. In

Proceedings of the twenty-eighth annual ACM symposium on Theory of Computing, STOC '96, pages 212–219. ACM, New York, NY, USA (1996).

[Gro97] Grover, L. K. Quantum mechanics helps in searching for a needle in a haystack. *Phys. Rev. Lett.* **79** (2), 325 (1997).

[GYS+06] Greilich, A., Yakovlev, D. R., Shabaev, A., Efros, A. L., Yugova, I. A., Oulton, R., Stavarache, V., Reuter, D., Wieck, A., and Bayer, M. Mode locking of electron spin coherences in singly charged quantum dots. *Science* **313** (5785), 341 (2006).

[HA14] Hackmann, J. and Anders, F. B. Spin noise in the anisotropic central spin model. *Phys. Rev. B* **89** (4), 045317 (2014).

[Hac13] Hackmann, J. Private communication (2013).

[Hae76] Haeberlen, U. *High Resolution NMR in Solids: Selective Averaging*. Advances in magnetic resonance: Supplement 1. Academic Press, New York, first edition (1976).

[Hah50] Hahn, E. L. Spin echoes. *Phys. Rev.* **80** (4), 580 (1950).

[HGB+08] Hernandez, F. G. G., Greilich, A., Brito, F., Wiemann, M., Yakovlev, D. R., Reuter, D., Wieck, A. D., and Bayer, M. Temperature-induced spin-coherence dissipation in quantum dots. *Phys. Rev. B* **78** (4), 041303 (2008).

[Hig02] Higham, N. J. Computing the nearest correlation matrix - a problem from finance. *IMA J. Numer. Anal.* **22** (3), 329 (2002).

[HKP+07] Hanson, R., Kouwenhoven, L. P., Petta, J. R., Tarucha, S., and Vandersypen, L. M. K. Spins in few-electron quantum dots. *Rev. Mod. Phys.* **79** (4), 1217 (2007).

[HL97] Hochbruck, M. and Lubich, C. On Krylov subspace approximations to the matrix exponential operator. *SIAM J. Numer. Anal.* **34** (5), 1911 (1997).

[HL99] Hochbruck, M. and Lubich, C. Exponential integrators for quantum-classical molecular dynamics. *BIT* **39** (4), 620 (1999).

[HWM+11] Holzner, A., Weichselbaum, A., McCulloch, I. P., Schollwöck, U., and von Delft, J. Chebyshev matrix product state approach for spectral functions. *Phys. Rev. B* **83** (19), 195115 (2011).

[JGP+04] Jelezko, F., Gaebel, T., Popa, I., Domhan, M., Gruber, A., and Wrachtrup, J. Observation of coherent oscillation of a single nuclear spin and realization of a two-qubit conditional quantum gate. *Phys. Rev. Lett.* **93** (13), 130501 (2004).

[Jon11] Jones, J. A. Quantum computing with NMR. *Prog. Nucl. Magn. Reson. Spectrosc.* **59** (2), 91 (2011).

[Kan98] Kane, B. E. A silicon-based nuclear spin quantum computer. *Nature* **393** (6681), 133 (1998).

[KBM12] Karrasch, C., Bardarson, J. H., and Moore, J. E. Finite-temperature dynamical density matrix renormalization group and the drude weight of spin-1/2 chains. *Phys. Rev. Lett.* **108** (22), 227206 (2012).

[KDH+04] Kroutvar, M., Ducommun, Y., Heiss, D., Bichler, M., Schuh, D., Abstreiter, G., and Finley, J. J. Optically programmable electron spin memory using semiconductor quantum dots. *Nature* **432** (7013), 81 (2004).

[KL05] Khodjasteh, K. and Lidar, D. A. Fault-tolerant quantum dynamical decoupling. *Phys. Rev. Lett.* **95** (18), 180501 (2005).

[KL07] Khodjasteh, K. and Lidar, D. A. Performance of deterministic dynamical decoupling schemes: Concatenated and periodic pulse sequences. *Phys. Rev. A* **75** (6), 062310 (2007).

[KLG02] Khaetskii, A. V., Loss, D., and Glazman, L. Electron spin decoherence in quantum dots due to interaction with nuclei. *Phys. Rev. Lett.* **88** (18), 186802 (2002).

[KLG03] Khaetskii, A., Loss, D., and Glazman, L. Electron spin evolution induced by interaction with nuclei in a quantum dot. *Phys. Rev. B* **67** (19), 195329 (2003).

[KMB+08] Kuopanportti, P., Möttönen, M., Bergholm, V., Saira, O.-P., Zhang, J.,

and Whaley, K. B. Suppression of $1/f^{\alpha}$ noise in one-qubit systems. *Phys. Rev. A* **77** (3), 032334 (2008).

[KN00] Khaetskii, A. V. and Nazarov, Y. V. Spin relaxation in semiconductor quantum dots. *Phys. Rev. B* **61** (19), 12639 (2000).

[KN01] Khaetskii, A. V. and Nazarov, Y. V. Spin-flip transitions between Zeeman sublevels in semiconductor quantum dots. *Phys. Rev. B* **64** (12), 125316 (2001).

[KNV08] Koppens, F. H. L., Nowack, K. C., and Vandersypen, L. M. K. Spin echo of a single electron spin in a quantum dot. *Phys. Rev. Lett.* **100** (23), 236802 (2008).

[Lan50] Lanczos, C. An iteration method for the solution of the eigenvalue problem of linear differential and integral operators. *J. Res. Natl. Bur. Stand.* **45** (4), 255 (1950).

[LBMW03] Leibfried, D., Blatt, R., Monroe, C., and Wineland, D. Quantum dynamics of single trapped ions. *Rev. Mod. Phys.* **75** (1), 281 (2003).

[LD98] Loss, D. and DiVincenzo, D. P. Quantum computation with quantum dots. *Phys. Rev. A* **57** (1), 120 (1998).

[Lev08] Levitt, M. H. *Spin Dynamics: Basics of Nuclear Magnetic Resonance*. John Wiley & Sons Ltd., Chichester, second edition (2008).

[LJL+10] Ladd, T. D., Jelezko, F., Laflamme, R., Nakamura, Y., Monroe, C., and O'Brien, J. L. Quantum computers. *Nature* **464** (7285), 45 (2010).

[LRV04] Latorre, J. I., Rico, E., and Vidal, G. Ground state entanglement in quantum spin chains. *Quant. Inf. Comput.* **4** (1), 48 (2004).

[LYS10] Liu, R.-B., Yao, W., and Sham, L. Quantum computing by optical control of electron spins. *Adv. Phys.* **59** (5), 703 (2010).

[Mag54] Magnus, W. On the exponential solution of differential equations for a linear operator. *Comm. Pure Appl. Math.* **7** (4), 649 (1954).

[MdSZW06] Möttönen, M., de Sousa, R., Zhang, J., and Whaley, K. B. High-fidelity one-qubit operations under random telegraph noise. *Phys. Rev. A* **73**, 022332 (2006).

[MER02] Merkulov, I. A., Efros, A. L., and Rosen, M. Electron spin relaxation by nuclei in semiconductor quantum dots. *Phys. Rev. B* **65** (20), 205309 (2002).

[MG58] Meiboom, S. and Gill, D. Modified spin-echo method for measuring nuclear relaxation times. *Rev. Sci. Instrum.* **29** (8), 688 (1958).

[MMN05] Manmana, S. R., Muramatsu, A., and Noack, R. M. Time evolution of one-dimensional quantum many body systems. *AIP Conf. Proc.* **789** (1), 269 (2005).

[MN98] Matsumoto, M. and Nishimura, T. Mersenne Twister: A 623-dimensionally equidistributed uniform pseudo-random number generator. *ACM Trans. Model. Comput. Simul.* **8** (1), 3 (1998).

[MSS01] Makhlin, Y., Schön, G., and Shnirman, A. Quantum-state engineering with Josephson-junction devices. *Rev. Mod. Phys.* **73** (2), 357 (2001).

[MTA+06] Morton, J. J. L., Tyryshkin, A. M., Ardavan, A., Benjamin, S. C., Porfyrakis, K., Lyon, S. A., and Briggs, G. A. D. Bang-bang control of fullerene qubits using ultrafast phase gates. *Nature Phys.* **2** (1), 40 (2006).

[MTL08] Maze, J. R., Taylor, J. M., and Lukin, M. D. Electron spin decoherence of single nitrogen-vacancy defects in diamond. *Phys. Rev. B* **78** (9), 094303 (2008).

[NC10] Nielsen, M. A. and Chuang, I. L. *Quantum Computation and Quantum Information*. Cambridge University Press, Cambridge, tenth anniversary edition (2010).

[NM05] Noack, R. M. and Manmana, S. R. Diagonalization- and numerical renormalization-group-based methods for interacting quantum systems. *AIP Conf. Proc.* **789** (1), 93 (2005).

[ON02] Osborne, T. J. and Nielsen, M. A. Entanglement, quantum phase transi-

tions, and density matrix renormalization. *Quantum Inf. Process.* **1** (1-2), 45 (2002).

[Pas13] Pasini, S. Private communication (2013).

[PFKU08] Pasini, S., Fischer, T., Karbach, P., and Uhrig, G. S. Optimization of short coherent control pulses. *Phys. Rev. A* **77** (3), 032315 (2008).

[PKRU09] Pasini, S., Karbach, P., Raas, C., and Uhrig, G. S. Optimized pulses for the perturbative decoupling of a spin and a decoherence bath. *Phys. Rev. A* **80** (2), 022328 (2009).

[PKU11] Pasini, S., Karbach, P., and Uhrig, G. S. High-order coherent control sequences of finite-width pulses. *Europhys. Lett.* **96** (1), 10003 (2011).

[PKWH99] Peschel, I., Kaulke, M., Wang, X., and Hallberg, K. A. (Editors). *Density-Matrix Renormalization - A New Numerical Method in Physics*, volume 528 of *Lecture Notes in Physics*. Springer, Berlin, first edition (1999).

[PQ08] Pryadko, L. P. and Quiroz, G. Soft-pulse dynamical decoupling in a cavity. *Phys. Rev. A* **77** (1), 012330 (2008).

[Pre98] Preskill, J. Reliable quantum computers. *Proc. R. Soc. Lond. A* **454** (1969), 385 (1998).

[PS08] Pryadko, L. P. and Sengupta, P. Second-order shaped pulses for solid-state quantum computation. *Phys. Rev. A* **78** (3), 032336 (2008).

[PTVF07] Press, W. H., Teukolsky, S. A., Vetterling, W. T., and Flannery, B. P. *Numerical Recipes: The Art of Scientific Computing*. Cambridge University Press, Cambridge, third edition (2007).

[PU08] Pasini, S. and Uhrig, G. S. Generalization of short coherent control pulses: extension to arbitrary rotations. *J. Phys. A* **41** (31), 312005 (2008).

[Sch07] Schmidt, E. Zur Theorie der linearen und nichtlinearen Integralgleichungen. *Math. Ann.* **63** (4), 433 (1907).

[Sch04] Schmitteckert, P. Nonequilibrium electron transport using the density matrix renormalization group method. *Phys. Rev. B* **70** (12), 121302 (2004).

[Sch05a] Schollwöck, U. The density-matrix renormalization group. *Rev. Mod. Phys.* **77** (1), 259 (2005).

[Sch05b] Schwabl, F. *Quantenmechanik*. Springer, Berlin, sixth edition (2005).

[Sch08] Schneider, C. *Dekohärenzphänomene im anisotropen Gaudin-Modell*. Diploma thesis, Technische Universität Dortmund (2008).

[Sch11] Schollwöck, U. The density-matrix renormalization group in the age of matrix product states. *Ann. Phys.* **326** (1), 96 (2011).

[SFPU12] Stihl, C., Fauseweh, B., Pasini, S., and Uhrig, G. S. Modulated pulses compensating classical noise. *ArXiv e-prints* (2012). `arXiv:quant-ph/1210.4311`.

[Sho94] Shor, P. Algorithms for quantum computation: Discrete logarithms and factoring. In *35th Annual Symposium on Foundations of Computer Science, 1994 Proceedings*, pages 124–134 (1994).

[Sho97] Shor, P. Polynomial-time algorithms for prime factorization and discrete logarithms on a quantum computer. *SIAM J. Comput.* **26** (5), 1484 (1997).

[SKL03] Schliemann, J., Khaetskii, A., and Loss, D. Electron spin dynamics in quantum dots and related nanostructures due to hyperfine interaction with nuclei. *J. Phys.: Condens. Matter* **15** (50), R1809 (2003).

[SKL+06] Skinner, T. E., Kobzar, K., Luy, B., Bendall, M. R., Bermel, W., Khaneja, N., and Glaser, S. J. Optimal control design of constant amplitude phase-modulated pulses: Application to calibration-free broadband excitation. *J. Magn. Reson.* **179** (2), 241 (2006).

[SMP02] Saykin, S., Mozyrsky, D., and Privman, V. Relaxation of shallow donor electron spin due to interaction with nuclear spin bath. *Nano Lett.* **2** (6), 651 (2002).

[SP05] Sengupta, P. and Pryadko, L. P. Scalable design of tailored soft pulses for coherent control. *Phys. Rev. Lett.* **95** (3), 037202 (2005).

[SR94] Silver, R. and Röder, H. Densities of states of mega-dimensional Hamiltonian matrices. *Int. J. Mod. Phys. C* **5** (04), 735 (1994).

[SRU13] Stanek, D., Raas, C., and Uhrig, G. S. Dynamics and decoherence in the central spin model in the low-field limit. *Phys. Rev. B* **88** (15), 155305 (2013).

[SS08] Stolze, J. and Suter, D. *Quantum Computing. A Short Course from Theory to Experiment.* Wiley-VCH, Weinheim, second edition (2008).

[Ste96a] Steane, A. Error correcting codes in quantum theory. *Phys. Rev. Lett.* **77** (5), 793 (1996).

[Ste96b] Steane, A. Multiple-particle interference and quantum error correction. *Proc. R. Soc. Lond. A* **452** (1954), 255 (1996).

[Sti12] Stihl, C. *Optimierung von Pulsen zur Entkopplung eines Spins von klassischem Rauschen: Amplituden- und Frequenzmodulation gegen Dephasierung und Dekohärenz*. Diploma thesis, Technische Universität Dortmund (2012).

[Sti13] Stihl, C. Private communication (2013).

[Stü08] Stübner, R. *Dekohärenz im inhomogenen Gaudin-Modell*. Diploma thesis, Technische Universität Dortmund (2008).

[Stü12] Stübner, R. Private communication (2012).

[TEK84] Tal-Ezer, H. and Kosloff, R. An accurate and efficient scheme for propagating the time dependent Schrödinger equation. *J. Chem. Phys.* **81** (9), 3967 (1984).

[Tyc83] Tycko, R. Broadband population inversion. *Phys. Rev. Lett.* **51** (9), 775 (1983).

[Uhr07] Uhrig, G. S. Keeping a quantum bit alive by optimized π-pulse sequences. *Phys. Rev. Lett.* **98** (10), 100504 (2007). *Erratum*: Phys. Rev. Lett. **106** (12), 129901 (March 2011).

[Uhr09] Uhrig, G. S. Concatenated control sequences based on optimized dynamic decoupling. *Phys. Rev. Lett.* **102** (12), 120502 (2009).

[Uhr13] Uhrig, G. S. Private communication (2013).

[UO30] Uhlenbeck, G. E. and Ornstein, L. S. On the theory of the Brownian motion. *Phys. Rev.* **36** (5), 823 (1930).

[VC05] Vandersypen, L. M. K. and Chuang, I. L. NMR techniques for quantum control and computation. *Rev. Mod. Phys.* **76** (4), 1037 (2005).

[vDP02] von Delft, J. and Poghossian, R. Algebraic Bethe ansatz for a discrete-state BCS pairing model. *Phys. Rev. B* **66** (13), 134502 (2002).

[VL98] Viola, L. and Lloyd, S. Dynamical suppression of decoherence in two-state quantum systems. *Phys. Rev. A* **58** (4), 2733 (1998).

[VSB+01] Vandersypen, L. M. K., Steffen, M., Breyta, G., Yannoni, C. S., Sherwood, M. H., and Chuang, I. L. Experimental realization of Shor's quantum factoring algorithm using nuclear magnetic resonance. *Nature* **414** (6866), 883 (2001).

[War13] Warburton, R. J. Single spins in self-assembled quantum dots. *Nature Mater.* **12** (6), 483 (2013).

[WCCDS12] Witzel, W. M., Carroll, M. S., Cywiński, L., and Das Sarma, S. Quantum decoherence of the central spin in a sparse system of dipolar coupled spins. *Phys. Rev. B* **86** (3), 035452 (2012).

[WDS06] Witzel, W. M. and Das Sarma, S. Quantum theory for electron spin decoherence induced by nuclear spin dynamics in semiconductor quantum computer architectures: Spectral diffusion of localized electron spins in the nuclear solid-state environment. *Phys. Rev. B* **74** (3), 035322 (2006).

[WDS07] Witzel, W. M. and Das Sarma, S. Multiple-pulse coherence enhancement of solid state spin qubits. *Phys. Rev. Lett.* **98** (7), 077601 (2007).

[WdSDS05] Witzel, W. M., de Sousa, R., and Das Sarma, S. Quantum theory of spectral-diffusion-induced electron spin decoherence. *Phys. Rev. B* **72** (16), 161306 (2005).

[WF04] White, S. R. and Feiguin, A. E. Real-time evolution using the density matrix renormalization group. *Phys. Rev. Lett.* **93** (7), 076401 (2004).

[WFL10] West, J. R., Fong, B. H., and Lidar, D. A. Near-optimal dynamical decoupling of a qubit. *Phys. Rev. Lett.* **104** (13), 130501 (2010).

[Whi92] White, S. R. Density-matrix formulation for quantum renormalization-groups. *Phys. Rev. Lett.* **69** (19), 2863 (1992).

[Whi93] White, S. R. Density-matrix algorithms for quantum renormalization-groups. *Phys. Rev. B* **48** (14), 10345 (1993).

[Whi96] White, S. R. Spin gaps in a frustrated Heisenberg model for CaV_4O_9. *Phys. Rev. Lett.* **77** (17), 3633 (1996).

[Whi98] White, S. R. Strongly correlated electron systems and the density matrix renormalization group. *Phys. Rep.* **301** (1-3), 187 (1998).

[Whi05] White, S. R. Density matrix renormalization group algorithms with a single center site. *Phys. Rev. B* **72** (18), 180403 (2005).

[Wil75] Wilson, K. G. The renormalization group: Critical phenomena and the Kondo problem. *Rev. Mod. Phys.* **47**, 773 (1975).

[WL13] Wang, Z.-Y. and Liu, R.-B. No-go theorems and optimization of dynamical decoupling against noise with soft cutoff. *Phys. Rev. A* **87** (4), 042319 (2013).

[WN92] White, S. R. and Noack, R. M. Real-space quantum renormalization groups. *Phys. Rev. Lett.* **68** (24), 3487 (1992).

[WWAF06] Weisse, A., Wellein, G., Alvermann, A., and Fehske, H. The kernel polynomial method. *Rev. Mod. Phys.* **78** (1), 275 (2006).

[WYD13] Witzel, W. M., Young, K., and Das Sarma, S. Converting a real quantum bath to an effective classical noise. *ArXiv e-prints* (2013). `arXiv:cond-mat.mes-hall/1307.2597`.

[YL08a] Yang, W. and Liu, R.-B. Quantum many-body theory of qubit decoherence in a finite-size spin bath. *Phys. Rev. B* **78** (8), 085315 (2008).

[YL08b] Yang, W. and Liu, R.-B. Universality of Uhrig Dynamical Decoupling for suppressing qubit pure dephasing and relaxation. *Phys. Rev. Lett.* **101** (18), 180403 (2008).

[YL09] Yang, W. and Liu, R.-B. Quantum many-body theory of qubit decoherence in a finite-size spin bath. II. Ensemble dynamics. *Phys. Rev. B* **79** (11), 115320 (2009).

[YLS07] Yao, W., Liu, R. B., and Sham, L. J. Restoring coherence lost to a slow interacting mesoscopic spin bath. *Phys. Rev. Lett.* **98** (7), 077602 (2007).

[ZDAH+06] Zhang, W., Dobrovitski, V. V., Al-Hassanieh, K. A., Dagotto, E., and Harmon, B. N. Hyperfine interaction induced decoherence of electron spins in quantum dots. *Phys. Rev. B* **74** (20), 205313 (2006).

[ZDM+13] Zwanenburg, F. A., Dzurak, A. S., Morello, A., Simmons, M. Y., Hollenberg, L. C. L., Klimeck, G., Rogge, S., Coppersmith, S. N., and Eriksson, M. A. Silicon quantum electronics. *Rev. Mod. Phys.* **85** (3), 961 (2013).

[ŽFDS04] Žutić, I., Fabian, J., and Das Sarma, S. Spintronics: Fundamentals and applications. *Rev. Mod. Phys.* **76** (2), 323 (2004).

[ZHL12] Zhao, N., Ho, S.-W., and Liu, R.-B. Decoherence and dynamical decoupling control of nitrogen vacancy center electron spins in nuclear spin baths. *Phys. Rev. B* **85** (11), 115303 (2012).

[ZWL11] Zhao, N., Wang, Z.-Y., and Liu, R.-B. Anomalous decoherence effect in a quantum bath. *Phys. Rev. Lett.* **106** (21), 217205 (2011).

Published Results

Parts of the results presented in this thesis were already published in the following reference:

> Stanek, Daniel, Raas, Carsten, and Uhrig, Götz S..
> Dynamics and decoherence in the central spin model in the low-field limit.
> *Phys. Rev. B* **88** (15), 155305 (2013).

Danksagung

Im Folgenden möchte ich bei Leuten bedanken, die mich bei der Anfertigung dieser Arbeit unterstützt und mich in den letzten Jahren begleitet haben.

Als erstes bedanke ich mich sehr herzlich bei meinem Betreuer Herrn Prof. Dr. Götz S. Uhrig für die Vergabe des Themas und die intensive Betreuung. Durch sein Engagement und seine umfangreichen Fachkenntnisse war unsere Zusammenarbeit für mich stets eine große Freude.

Herrn Prof. Dr. Frithjof B. Anders und Herrn Prof. Dr. Holger Fehske danke ich herzlich für die Begutachtung dieser Dissertation.

Ein besonderer Dank gilt Herrn Dr. Carsten Raas für die zahlreichen Diskussionen über DMRG und die geduldige Beantwortung meiner vielen Fragen. Auch bei Hard- und Software Problemen konnte ich stets mit seiner Unterstützung rechnen.

An unterschiedlichen Stellen dieser Arbeit sind zur Verifikation meiner eigenen Resultate und zur Durchführung von Simulationen Ergebnisse anderer Arbeiten eingeflossen. Für die Bereitstellung dieser Daten bedanke ich mich bei Dr. Michael Bortz, Johannes Hackmann, Dr. Stefano Pasini, Christopher Stihl, Prof. Dr. Joachim Stolze und Robert Stübner.

Bei der Durchsicht dieser Arbeit haben Nils Drescher, Benedikt Fauseweh, Holger Krull und Dr. Carsten Raas mitgeholfen. Für ihr Engagement bedanke ich mich herzlich.

Allen aktuellen und ehemaligen Mitgliedern der Arbeitsgruppe danke ich für das stets sehr angenehme und kollegiale Arbeitsklima. Insbesondere gilt dieses für Nils Drescher, Benedikt Fauseweh, Gregor Foltin, Mohsen Hafez, Simone Hamerla und Holger Krull, mit denen ich mir in den letzten Jahren zumindest zeitweise ein Büro geteilt habe.

Bei meiner Familie und meinen Freunden bedanke ich mich für den Rückhalt in den vergangenen Jahren. Insbesondere gilt dieser Dank meinen Eltern, die mich stets gefördert und bei all meinen Vorhaben unterstützt haben.

Zum Schluss möchte ich mich bei der NRW Forschungsschule „Forschung mit Synchrotronstrahlung in den Nano- und Biowissenschaften“ und der Studienstiftung des deutschen Volkes bedanken. Ohne ihre finanzielle Unterstützung wäre die Anfertigung dieser Arbeit nicht möglich gewesen. Der Studienstiftung des deutschen Volkes danke ich auch für die vielfältige ideelle Förderung, die stets eine interessante Abwechslung zum Promotionsalltag war.

Je mehr man den Quanten nachjagt, desto besser verbergen sie sich.

(Albert Einstein)